UNIVERSITY OF SOUTHAMPTON

Faculty of Engineering, Science and Mathematics
School of Ocean and Earth Science

Joint Seismic and Electrical Measurements of Gas Hydrates in Continental Margin Sediments

By
Michelle H. Ellis

A Thesis Submitted in Fulfilment of the Degree of Doctor of Philosophy in the School of Ocean and Earth Science of the University of Southampton.

February 2008

This work is dedicated to Janet and Arthur Davies

Abstract

Gas hydrates are well known to affect the physical properties of the sediments in which they reside. They can dramatically increase the seismic P-wave velocity of a sediment by cementing grains together. Also they can cause a significant increase in the electrical resistivity of sediment by partially replacing conducting pore fluids and blocking pore throats. Gas hydrates form a significant fraction of current hydrocarbon reserves and have great importance for seafloor slope stability and climate change. Estimates for the distribution and volume of gas hydrate trapped in the upper few hundred metres of continental margin sediments vary widely. This is due to the inability of techniques employed in previous studies to quantify accurately hydrates *in situ*.

This work develops a joint seismic/electrical effective medium model of hydrate in marine sediments, and validates this model through laboratory measurements on sediment samples. The seismic approach combines a Self Consistent Approximation (SCA) and Differential Effective Medium (DEM), which allows a bi-connected effective medium to be modelled and also allows the shape and alignment of the grains to be taken into account. The electrical approach is based on estimates of changes in path length taken by an electrical current through idealized sediments consisting of ellipsoidal grains. This method has advantages over the traditional Archie's method because is it able to model the effects of grain aspect ratio and anisotropy. Hydrate is added into both seismic and electrical models in either a load-bearing or non load bearing manner. A joint interpretation method is developed for the seismic and electrical models whereby two variables can be determined from co-located velocity and resistivity measurements. The joint seismic and electrical approach offers several advantages as the two methods give different, but complementary, information on the nature of the hydrate and sediment.

The individual models and the joint interpretation are tested against porosity, resistivity and velocity measurements made on artificial sediments created in the laboratory with known physical properties. Gas hydrate, at saturations from 0-30%, is artificially formed in the sediment samples from free gas and dilute brine. The models are also applied to data

collected during Integrated Ocean Drilling Program Expedition 311 offshore Vancouver Island to determine hydrate saturations. The models predict mean gas hydrate saturations of between 2-20%, toward the lower end of previous estimates, although there are significant lateral and vertical variations. In some cases, and particularly at one site, there is a significant discrepancy in hydrate saturations derived from the separate seismic and electrical models. The joint approach is applied to co-located data points in these areas and is able to successfully provide a consistent result by altering both the hydrate saturation and the aspect ratio of the grains. Thus, by jointly interpreting seismic and electrical data, a better understanding of hydrate bearing sediment can be achieved.

Contents Page

Acronyms

BHSZ	Base of the gas Hydrate Stability Zone
BSR	Bottom Simulating Reflector
CMAC	Compton Mass Attenuation Coefficients
CSEM	Controlled Source Electro Magnetic
DEM	Differential Effective Medium
EM	Electro-Magnetic
EWE	Empirical Weighted Equation
FFT	Fast Fourier Transform
GHASTLI	Gas Hydrate And Sediment Test Laboratory Instrument
GHRC	Gas Hydrate Resonance Column
GHSZ	Gas Hydrate Stability Zone
GRAPE	Gamma Ray Attenuation Evaluator
HS	Hashin-Shtrikman
IODP	Intergrated Ocean Drilling Program
IPTC	Instrumented Pressure Testing Chamber
IR	InfraRed
IW	Interstitial Waters
LWD	Logging While Drilling
MAD	Moisture and Density
mbsf	metres below seafloor
MSCL	Multi Sensor Core Logger
MST	Multi Sensor Track
NMR	Nuclear Magnetic Resonance
NOCS	National Oceanography Centre, Southampton

OBS	Ocean Bottom Seismometer
ODP	Ocean Drilling Program
P-T	Pressure and Temperature
RBIT	Resistivity at the BIT
RDAV	Deep Button Resistivity
RING	Ring Resistivity
RMAV	Medium Button Resistivity
RMS	Root Mean Squared
RSAV	Shallow Button Resistivity
SCA	Self Consistent Approximation
SEM	Scanning Electron Microscope
STP	Standard Temperature and Pressure
THF	TetraHydroFuran
TPB	Three Phase Biot theory
TPEM	Three-Phase Effective Medium theory
USGS	United Stated Geological Survey

Symbols

Symbol	**Description**
a	ellipse major semi-axis
A	CrosS-sectional area of the sediment
A_c	Area of contact
A_e	Ellipsoid crosS-sectional area
a_m	Correction of the intermolecular forces
b	Ellipse minor semi-axis (in the y direction)
B	Adiabatic compressibility
b_m	Volume occupied by one mole of molecules
B_r	Adiabatic compressibility of the r-th component
c	Ellipse minor semi-axis (in the z direction
C	Effective elastic tensor
c_1 and c_2	Interconnection constants (Schmeling, 1986)
C_b	Backgorund Chorinity
C_h	Chorinity of the pore fluids
C_l	Chorinity
C_o	Coordination number
D	Distance between electrodes
d	Diameter
d	Thickness of the sediment
D	Degree of anisotropy
d_c	Calibration block thickness
d_L	Total Liner thickness
d_R	Recorded displacement
e	Eccentricity
E	Young's modulus
f	Confining force
F	Formation factor
F_{fluid}	Fraction of the path length un-deviated
F_{grain}	Fraction of the path length deviated

Symbol	**Description**
f_t	Tangential force
g	Geometric factor
G_{ave}	Average geometric factor
I	Current
I_0	Intensity of the gamma beam after passing through the air gap and core liner
I_g	Intensity of the gamma beam after passing through the air gap and core liner and sediment
k	Permeability
l	Length
L	Mean free path length
l_1	Path length
l_{1ave}	Average path length
l_2	Vertical path length
l_{2ave}	Average vertical path length
l_p	Maximum path length
m	Cementation exponent
M	Hill's modulus average
m_{est}	Estimated cementation coefficient
m_h	Mass of 1 mole of methane gas
mol	Number of moles of gas
mol_c	Corrected (for methane solubility) number of moles required to form a given hydrate saturation
M_r	Modulus of the r-th component
M_R	Reuss's effective modulus
M_v	Voigt's effective moudulus
M_w	Molar mass of water
n	Number of direct connections to an inclusion
N	Total number of inclusions
N_{AVO}	Avogadro's number
n_g	Number of molecules
n_{max}	Maximum number of interconnections
n_v	Number density
N_w	Number of water molecules

Symbol	**Description**
n_w	Number of water molecules in a unit cell
p	Pressure
P	Geometric factor to describe inclusion shapes (SCA and DEM models)
P_4	Fourth rank tensor
P_h	Pressure at which hydrate forms
P_i	Probability of interconnection
Q	Geometric factor to describe inclusion shapes (SCA and DEM models)
r	Radius
R	Resistance
r_f	Ratio of the fluid
r_h	Ratio of the hydrate
r_m	Ratio of the matrix
R_n	Resistance from narrow spaced electrodes
R_w	Resistance from wide spaced electrodes
S	Salt in one litre of water after hydrate formation
s	Saturation factor
S	arc length for an ellipse
S_b	Weight of salt in 1 kg of water prior to hydrate formation
S_c	Effective collision crosS-section
S_h	Hydrate saturation
S_n	Normal Stiffness
S_w	Water saturation
S_τ	Tangential stiffness
T	Temperature
t	Tortuosity factor
T	Tensor
T_h	Temperature at which hydrate forms
t_L	Pulse delay time
T_o	Temperature (0^oC) in degrees kelvin
t_R	Recorded pulse travel time
u	Normal displacement (or shortening increment)
U	Universal gas law constant

Symbol	**Description**
V	Volume
V	Volume concentration
V	Volume of one inclusion
v	Viscosity
V_{cell}	Volume of unit cell
V_e	Volume of an Ellipsoid
Vel	Velocity
V_f	Volume of methane dissolved in the pore fluids just before hydrate formation
V_h	Volume of hydrate in sample
V_m	Volume of methane
V_{mp}	Volume of free methane gas before hydrate formation
V_p	P-wave velocity
$V_{p.f}$	P-wave velocity of fluid
$V_{p.m}$	P-wave velocity of the matrix
V_{p1}	P-wave velocity calculated using the Three Phase Time average equation
V_{p2}	P-wave velocity calcuated using the Wood extended equation
$V_{p\infty}$	P-wave velocity as frequency approaches infinity (Biot theory)
V_{pd}	Potential difference
V_{pf}	P-wave velocity of the pore fluid
V_{ph}	P-wave velocity of hydrate
V_{pm}	P-wave velocity of the matrix
V_s	S-wave velocity
V_t	Total volume of material
V_w	Volume of water in sample after hydrate formation
W	Weighting factor (Empirical weighted equation)
W_h	Mass of hydrate
W_{SE}	Weight of salt exspelled from hydrate
W_{sw}	Weight of salt in the water before the salt has been expelled from the hydrate
W_{TS}	Total weight of salt in water after hydrate formation
W_w	Weight of water in a sample after hydrate formation
W_{wh}	Mass of water contained in hydrate

Symbol	**Description**
α	Aspect ratio
β	Volumetric fraction of the fluid
β_1	Volume fraction of component 1
β_2	Volume fraction of component 2
β_G	Grain volume fraction
β_{G1}	Adjusted grain volume fraction
β_H	Volume fraction of gas hydrate
β_{H1}	Adjusted gas hydrate volume fraction
β_i	Volume fraction of the inclusion
β_m	Volume fraction of the solid matrix
β_w	Volume fraction of the pore fluids
γ	Cement distribution
γ	Natural gamma ray count
ΔT	Travel Time
ζ	Fluid flow
η	Co-efficient of friction
κ	Bulk modulus
κ^-	HS lower bound bulk modulus
κ^+	HS upper bound bulk modulus
κ_1	Bulk modulus of component 1
κ_2	Bulk modulus of component 2
κ_{cc}	Effective bulk modulus calculated using the contact cementation model
κ_{dem}	Bulk modulus (using the differential effective medium method)
κ_{dry}	Bulk modulus of a dry rock frame
$\overline{\kappa}_f$	Bulk modulus of a fluid hydrate mix
κ_f	Bulk modulus of the fluid
κ_G	Bulk modulus calculated using Gassman's equation
κ_h	Bulk modulus of hydrate
κ_{hf}	Bulk modulus of the hydrate frame
κ_{HM}	Effective shear modulus calculated by the Hertz and Mindlin contact method
κ_i	Bulk modulus of the inclusion
κ_m	Bulk modulus of the matrix

Symbol	**Description**
κ_n	Largest bulk modulus among the κ of the n phases.
κ_r	Bulk modulus of the rth component
κ_s	Smallest bulk modulus among the κ of the n phases;
κ_s	Smallest bulk modulus among all the bulk modulus of the n phases
κ_{sc}	Self consistent effective bulk modulus
κ_{sf}	Bulk modulus of the solid matrix frame
κ_w	Bulk modulus of water
κ_W	Wood's effective bulk modulus
μ	Shear modulus
μ^-	HS lower bound shear modulus
μ^+	HS upper bound shear modulus
μ_1	Shear modulus of component 1
μ_2	Shear modulus of component 2
μ_c	Compton mass attenuation coefficient of the sediment
μ_{cc}	Effective shear modulus calculated using the contact cementation model
μ_{dem}	Shear modulus (using the differential effective medium method)
μ_{dry}	Shear modulus of a dry rock frame
μ_{eff}	Effective shear modulus (Hertz and Mindlin model)
μ_G	Shear modulus calculated using Gassman's equation
μ_{hf}	Shear modulus of the hydrate matrix
μ_{HM}	Effective shear modulus calculated by the Hertz and Mindlin contact method
μ_i	Shear modulus of the inclusion
μ_m	Shear modulus of the matrix
μ_n	Largest shear moduli among μ of the n phases.
μ_r	Shear modulus of the rth component
μ_s	Smallest shear modulus among shear moduli of the n phases;
μ_{sc}	Self consistent effective shear modulus
μ_{sf}	Shear modulus of the solid matrix frame
ξ	Fluid flow rate
ρ	Resistivity
ρ_B	Bulk resistivity
ρ_f	Resistivity of fluid

Symbol	**Description**
ρ_{geo}	Resistivity of geometrically altered HS bound
ρ_{gm}	Geometric mean resistivity (Greer, 2001)
ρ_{GPL}	Geometric Path length effective resistivity
$\rho_{GPL,block}$	Geometric Path length effective resistivity where hydrate blocks the pores
$\rho_{GPL,non\text{-}block}$	Geometric Path length effective resistivity where hydrate does not block the pores and instead floats in the pore space
ρ_H	Resistivity of gas hydrate
$\rho_{HS,conductive}$	Resistivity of conductive HS bound
$\rho_{HS,resistive}$	Resistivity of resistive HS bound
ρ_{iso}	Effective medium resistivity using Krajew (1957) equations
ρ_m	Resistivity of intermediate medium
ρ_{max}	Maximum resistivity
ρ_{min}	Minimum resistivity
ρ_o	Resistivity of a fully saturated medium
ρ_s	Resistivity of the solid grains
ρ_t	Formation resistivity
ρ_w	Resistivity of pore fluid
ς	Weight percentage of water in the hydrate
σ_f	Conductivity of the fluid
σ_{geo}	Conductivity of geometrically altered HS bound
σ_{gm}	Geometric mean conductivity (Greer, 2001)
$\sigma_{HS\ conductive}$	Upper or conductive HS bound of conductivity
$\sigma_{HS\ resistive}$	Lower or resistive HS bound of conductivity
σ_{iso}	Effective medium conductivity using Krajew (1957) equations
σ_m	Conductivity of the medium
σ_o	Specific conductivity of the solid
τ	Tangential displacement
υ	Poisson's ratio
φ	Porosity
φ_c	Critical Porosity
φ_r	Porosity of the r-th component
χ	Density
χ_1	Density of component 1

Symbol	**Description**
χ_{12}	Induced mass
χ_2	Density of Component 2
χ_{bulk}	Bulk density
χ_f	Density of the fluid
χ_f	Density of the pore fluids
χ_g	Grain density
χ_h	Density of hydrate
χ_m	Density of the matrix
χ_o	Density of the solid
χ_w	Density of water
ψ	Lithification rate
ω	Average number of contacts per grain in a sphere pack (Contact cementation model)

DECLARATION OF AUTHORSHIP

I, Michelle H. Ellis declare that the thesis entitled

Joint Seismic and Electrical Measurments of Gas Hydrates in Continental Margin Sediments

and the work presented in the thesis are both my own, and have been generated by me as the result of my own original research. I confirm that:

- this work was done wholly or mainly while in candidature for a research degree at this University;
- where any part of this thesis has previously been submitted for a degree or any other qualification at this University or any other institution, this has been clearly stated;
- where I have consulted the published work of others, this is always clearly attributed;
- where I have quoted from the work of others, the source is always given. With the exception of such quotations, this thesis is entirely my own work;
- I have acknowledged all main sources of help;
- where the thesis is based on work done by myself jointly with others, I have made clear exactly what was done by others and what I have contributed myself;
- none of this work has been published before submission, or [delete as appropriate] parts of this work have been published as: [please list references]

Signed: ……..

Date:…….

Acknowledgements

I would like to express my thanks to all those who have helped me throughout this research project.

First, I would like to thank my parents for all their love, support and encouragement during the last four years.

My sincere gratitude to my supervisors Tim Minshull, Angus Best and Martin Sinha for all their advice, support and guidance through out the duration of this project.

I would like to thank Jeremy Sothcott for all his help in the Laboratory and the adaptation of the pressure rig. Without his help none of the laboratory measurements would have been possible. I would also like to thank Nadia Frerichs for designing and building the electrical switching box.

I acknowledge NERC Ocean Margins Link project for funding this PhD project and IODP for funding my participation on Expedition 311. I would also like to thank Shyam Chand and Anthony Greer for supplying various versions of SCA, DEM and combined SCA/DEM codes at the beginning of the project.

I also thank all those I travelled and worked with during IODP Expedition 311 especially project co-chiefs Michael Reidel and Tim Collett and my physical properties colleagues Phil, Hiroko and Anne.

Lastly I would like to thank my partner, Simon, for all his support during the good and the bad times especially during the write up of this thesis and for proof reading most of it. I would also like to thank him for making the code run faster and the endless cups of tea.

Chapter 1. Gas Hydrates

1.1 Aims and objectives

This Thesis ultimately aims to develop a method to quantify gas hydrate saturation from electrical resistivity and seismic velocity measurements. To do this the nature of gas hydrate must be investigated and its effects on the physical properties of the sediments explored. In this chapter I will introduce and give an overview of natural gas hydrates. The chapter starts by explaining the crystal structure, stability, and worldwide distribution of gas hydrates. The chapter then moves on to explain why gas hydrates are important. Next, the chapter describes the different methods of hydrate growth and their effect on the electrical and seismic properties of gas hydrate bearing sediments. The chapter then describes the current method of detecting natural gas hydrate in sediment from geophysical and geological methods. Lastly, laboratory methods used to make and measure the physical properties with their associated problems are introduced. The chapter ends by giving an outline of the rest of the Thesis.

1.2 What are gas hydrates?

Gas hydrates are naturally occurring clathrates, which form when water freezes in the presence of other gases at temperatures above 0^{o}C. A clathrate is a compound formed by the inclusion of molecules of one kind (the guest molecule) within the crystal lattice of another (the host). The term hydrate is used when the molecules making up the crystal lattice are water (H_2O) and the guest molecules are a gas (Figure 1.1).

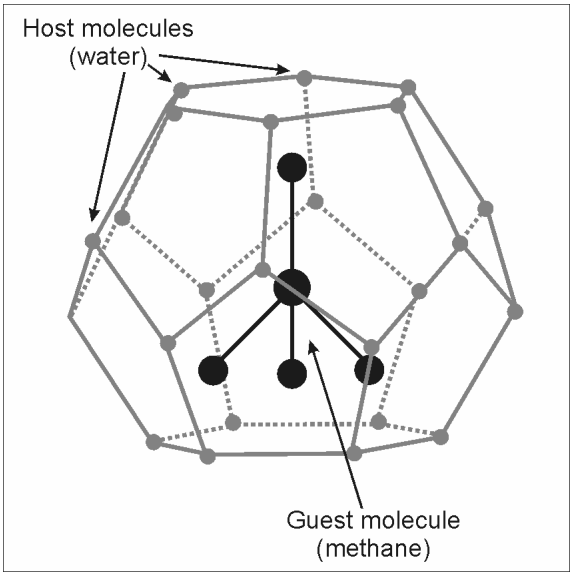

Figure 1.1 Structure of methane gas hydrate (adapted from Sloan, 1998).

1.2.1 Crystal structure

The crystal lattice structure of gas hydrate is a tetra-hedral arrangement of water molecules held together by hydrogen bonds. It is very similar in structure to ice, although it is slightly more rigid and the bond angles are slightly different. Within the crystal lattice there are cavities which are stabilized by a guest molecule trapped within them. A key characteristic of clathrates is that there is no chemical bonding between the host and guest molecules (Pellenbarg & Max, 2000). Gas hydrates come in 3 crystallographic lattice structure types: body centred cubic (structure I), diamond cubic (structure II) and hexagonal (structure H) (Sloan, 1998). Each of the lattice structure types has a variety of cavity configurations. Examples of the cavity configurations found in natural hydrates are shown in Figure 1.2. The structure of the hydrate is strongly dependent on the type of guest molecules available to fill the cavities. Small molecules such as methane (CH_4), carbon dioxide (CO_2) and hydrogen sulphide (H_2S) form Structure I hydrate. Structure II hydrates tend to be formed from slightly larger molecules such as propane and isobutane. Structure H hydrates contain two sizes of cage within the lattice. Small molecules are contained in the small cages and larger molecules such as the heavier hydrocarbons in the larger cages. Therefore two types of guest molecules are needed to form structure H hydrate. Naturally occurring hydrate guest molecules are predominantly methane (CH_4); Structure I methane hydrate accounts for more than 99% of all recovered gas hydrates (Kvenvolden, 1995). Ethane (C_2H_6) and

propane (C_3H_8) hydrates have also been found in small but significant quantities in the Gulf of Mexico (Brooks *et al*., 1984) and the Caspian Sea (Ginsburg *et al*., 1992). These structure II hydrates are problematic for the oil industry as they form very readily in oil pipe lines if there is any water present. There are only a few examples of naturally occurring structure H hydrate in sediment; examples have been documented in the Gulf of Mexico (Sassen and McDonald, 1994) and on the Cascadia Margin (Lu *et al.*, 2007).

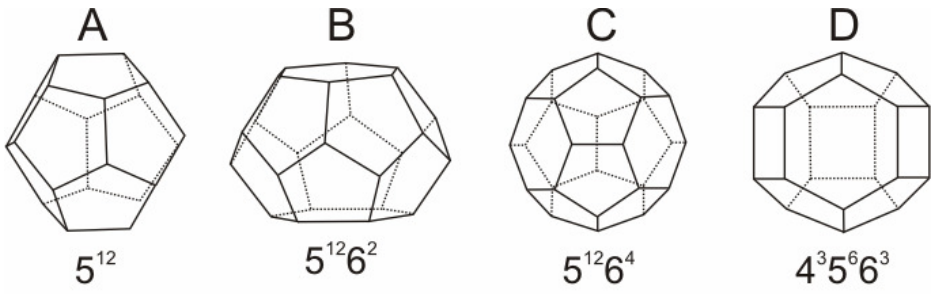

E

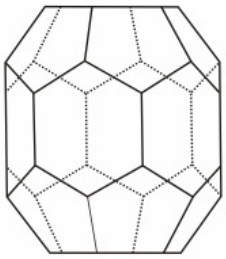

F

Cavity Structure	Structure I	Structure II	Structure H
5^{12}	2	16	3
$5^{12}6^2$	6	-	-
$5^{12}6^4$	-	8	-
$4^35^66^3$	-	-	2
$5^{12}6^8$	-	-	1

Figure 1.2 Cavity structures of gas hydrates. (A) Pentagonal Dodecahedron (B) Tetrakaidecahedron (C) Hexakaidecahedron (D) Irregular Dodecahedron (E) Icosahedron. Redrawn from Sloan, 1998 (A-C after Jeffrey and McMullan, 1967, D and E after Lederhos *et al*., 1992). (F) Table indicating the number of cavities per unit cell that each type of hydrate contains.

1.3 Formation and distribution of gas hydrates

1.3.1 Global distribution of gas hydrates

The occurrence of gas hydrate in sediment is controlled predominantly by the interaction of high hydrostatic pressure and low ambient temperatures. The lower limit is determined by the local geothermal gradient, which can vary over the planet. The conditions required for gas hydrate to be stable exist over 90% of the ocean bottom (Makogon, 1981). Hydrates can also be found in permafrost areas where temperatures are very low. However

it is known that hydrates are not always present where they are stable. This is due to the lack of methane supply in the areas. For a hydrate to form, 90% of the clathrate cavities need to be filled. Hydrate formation is therefore limited to areas where there are significant sources of methane. In the oceans these tend to occur along the continental margins. Figure 1.3 shows a map of locations where hydrate has been found or inferred. Areas that have been the subject of extensive study for gas hydrates include Blake Ridge (offshore South Carolina, US), Cascadia margin (accretionary prism west of Oregon, Washington and Vancouver Island), the Gulf of Mexico, offshore Norway and the Canadian Arctic permafrost.

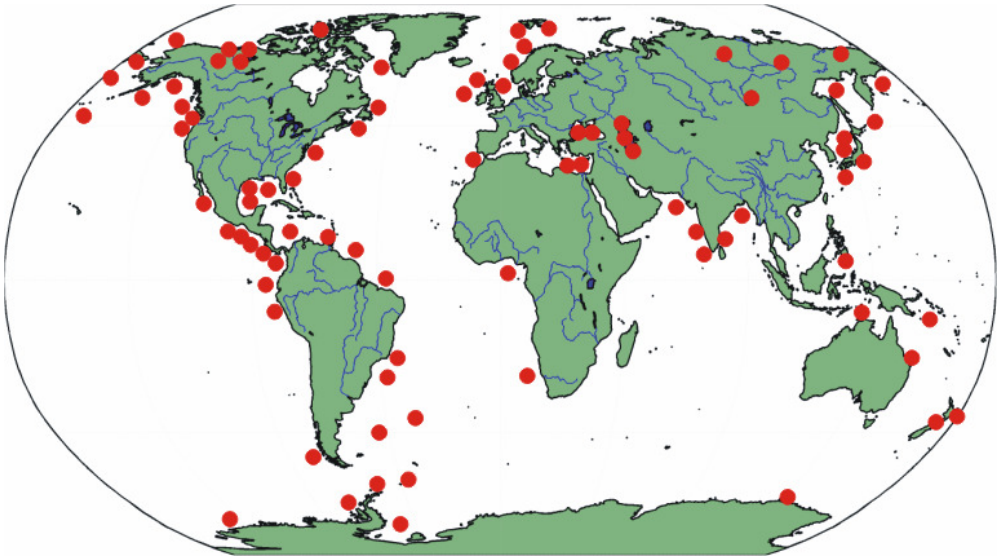

Figure 1.3 World-wide distribution of gas hydrate determined from samples and inferred from seismic data (Kvenvolden, 1998; Kvenvolden & Lorenson, 2001).

1.3.2 Stability and vertical distribution of gas hydrates

Gas hydrate is only stable at certain pressure and temperature conditions which are dependent on the type of gas molecules present. Figure 1.4 shows the stability curve for different gas filled hydrates created with values obtained from the CSMHYD program (Sloan, 1998). Stability exists in the areas below the line. If these conditions are not present the hydrate will dissociate into water and free gas. The stability of gas hydrates is primarily dependent on the ambient temperature, pressure and the availability of the guest molecules. Other controls on the gas/hydrate phase boundary include the composition of the gas

mixture. The presence of other gases (inhibitors such as methanol) and ionic impurities in the water can depress the stability zone (Kvenvolden, 1998).

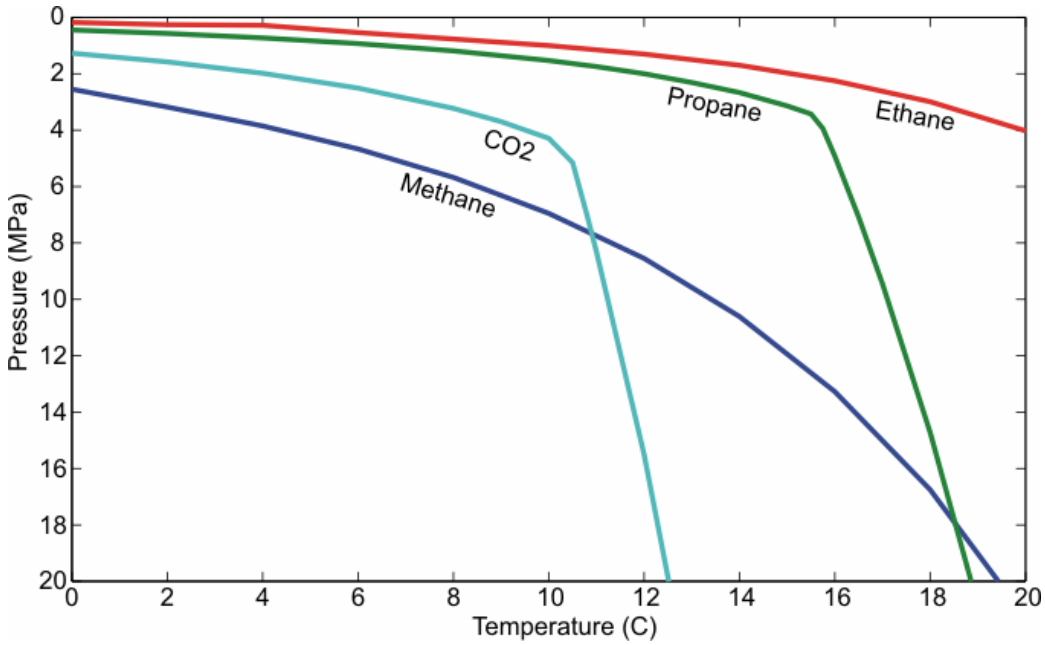

Figure 1.4 Hydrate stability curve for gas hydrates with different guest molecules (methane, propane, ethane and carbon dioxide). Hydrate is stable in the areas below the lines.

Figure 1.5 shows a schematic diagram of the Gas Hydrate Stability Zone (GHSZ) controlled by temperature, which increases with depth below the sea floor, and depth (pressure). The GHSZ extends well into the water column. Although hydrate formation in the water column is technically possible, any that does form would rise due to buoyancy and dissociate as the pressure decreases. Gas hydrates rarely form in seawater because methane concentrations are very low due to the low solubility of methane. The only hydrate that does form in the water column is around gas bubbles escaping from the sea floor.

The next two paragraphs come principally from a review of gas hydrate by Dillon & Max (2000). In many studies of gas hydrates in the field, the highest concentration of gas hydrate occurs just above the base of the GHSZ. This indicates that the methane is formed beneath the stability zone and then migrates upwards. It is believed that hydrate can form a seal, preventing the flow of methane further upward and preventing the formation of hydrate in the shallower sediments. This effect can cause free gas to pool beneath the GHSZ. If the methane is derived from biogenic sources either the methane is

produced below the stability zone or more likely it is formed high in the sediment column and then recycled down (Dillon & Max, 2000). It should be noted that maximum hydrate saturation at the base of the GHSZ does not always occur. An example can be seen in the sediments off Vancover Island which were investigated during IODP expedition 311 (Riedel *et al.,* 2006).

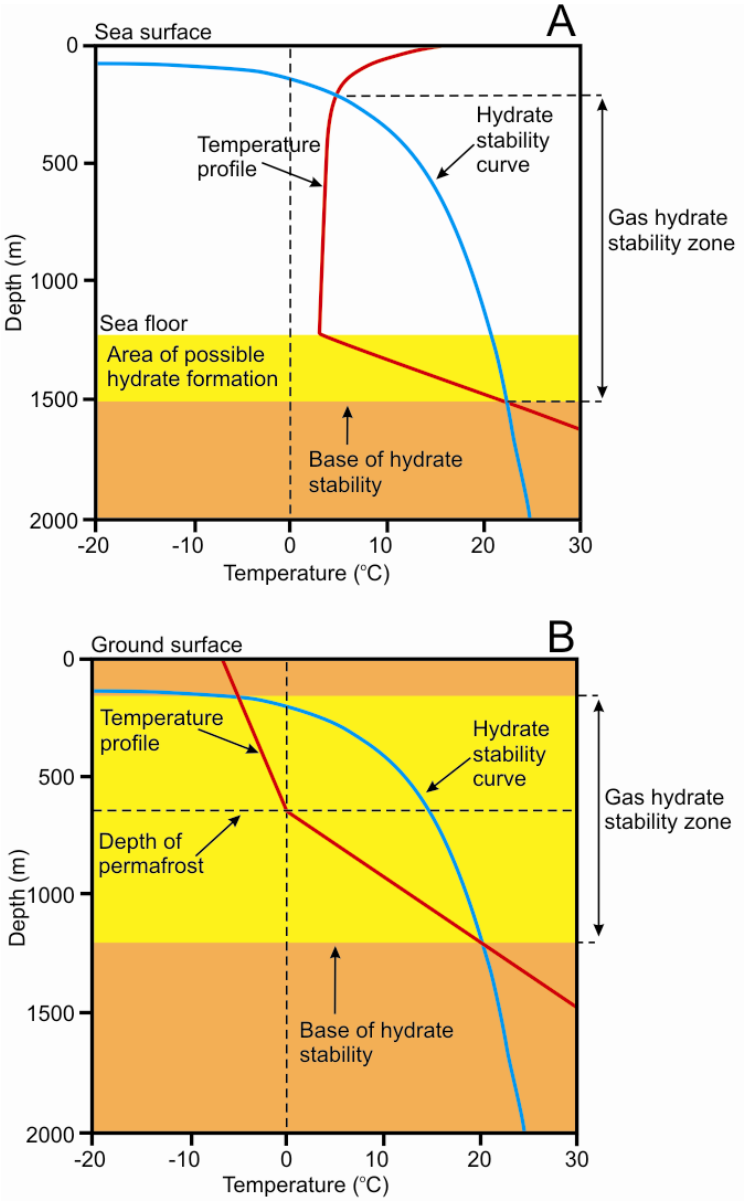

Figure 1.5 Gas hydrate stability zone in (A) oceanic sediments and (B) thick permafrost (adapted from Kvenvolden, 1988). Hydrate formation can occur in areas where the temperature profile is to the left of the stability curve.

In many continental margin settings there is active deposition of sediment. The geothermal gradient tends to remain the same over time. Therefore a patch of sediment or hydrate will effectively see the stability zone migrate up past it as deposition continues. A point will come when the hydrate will dissociate, releasing gas. If present in sufficient quantities, this gas will migrate up through the sediment column due to its low density and collect at the base of the stability zone (Dillon & Max, 2000).

Most gas found in hydrate is methane and is inferred to be microbially derived (Wellsbury & Parks, 2000). Such methane is formed from bacterial activity at low temperatures within the sediments in the GHSZ. Methane and other heavier hydrocarbons can also be derived from organic-carbon-rich sediments at depth and migrate upwards into the hydrate stability zone. Thermogenic methane is produced from the breakdown of organic matter and is therefore formed deep within the sediments below the stability zone and is related to hydrocarbon provinces. For hydrate to form in significant concentrations a continuous source of methane is needed. Because thermogenic methane is not formed within the stability zone it must be transported in. This transport usually occurs through faults and fractures (Hyndman & Davies, 1992). A C_1/C_2 ratio (C_1 is methane and C_2 represents the higher hydrocarbons) is usually used to determine whether methane is microbial or thermogenic. High C_1/C_2 ratios of 10^3 to 10^5 suggest that the methane was biogenic in origin, whereas low C_1/C_2 ratios of less than 100 generally indicate thermogenic methane (Matsumoto *et al*., 2000).

1.4 Reasons for interest

1.4.1 An economic source of hydrocarbon

Hydrates are a huge untapped reservoir of hydrocarbons. A given volume of hydrate can contain as much as 184 times the volume of gas at standard temperature and pressure (STP). Estimates of the total global amount of hydrocarbon trapped in hydrates indicate that the volume exceeds the amount of methane in conventional gas reserves (Kvenvolden, 1998). The amount of hydrocarbon in hydrate has been widely debated and many estimated global methane volumes have been put forward covering a range of three orders of magnitude (Table 1.1).

	Methane mass (Gt)		Methane volume STP (m^3 $\times 10^{13}$)	
	Terrestrial	Oceanic	Terrestrial	Oceanic
Trofimuk *et al*. (1977)	31.4	2750-1380	5.7	500-2500
Dobrynin *et al.* (1981)	18700	4180000	3400	760000
McIver (1981)	17.05	17050	3.1	3100
Meyer (1981)	7.7	17000	1.4	3100
McDonald (1990)	407	11000	74	2000
Kvenvolden & Claypool (1988)	-	22000	-	4000
Kvenvolden (1988)	-	11000	-	2000
Makogon (1990)	55	5500	10	1000
Gornitz & Fung (1994)	-	14520	-	2640
Harvey & Huang (1995)	800	24000	145	4360
Milkov (2003)	-	2200	-	400
Klauda & Sandler (2005)	-	74400	-	12000
Milkov (2005)	-	1375	-	250

Table 1.1 Global estimates of methane gas trapped in gas hydrates and its volume at standard temperature and pressure (STP).

Methane contained in hydrate is potentially a huge untapped energy resource. Unfortunately, because hydrate is a solid and widely dispersed, recovering it would be problematic on an industrial scale. Several methods have been put forward for gas recovery from in-situ gas hydrates by Collett (2000). (1) The sediments and hydrate could be heated to a point outside the stability field. Sloan (1998) showed that using hot water and steam floods it would be possible to produce gas at sufficient rates to make it recoverable. However the cost of using this method would not be economical. (2) Inject the system with inhibitors to change the point at which the hydrates are stable. Possible inhibitors include methanol and glycol, but again the economic cost of using such chemicals would be prohibitive. (3) Depressurize the hydrates to a point below hydrate equilibrium. This is the most economical method of recovering the gas, however extraction may be hampered by the formation of ice and reformation of hydrate because hydrate dissociation is an endothermic reaction (Collett, 2000).

1.4.2 Geohazards

Slope failure could be triggered by hydrate dissociation. The strength of sediment is affected by the presence of gas hydrate. Should either the pressure decrease, for example due to a change in sea level, or the temperature increase, the hydrate would become unstable and dissociate (Paull *et al.,* 2000). In this situation, the solid hydrate becomes a liquid and a gas at the base of the hydrate. The pore pressures may increase due to the release of gas and water. If the water and gas cannot be channelled away a zone of weakness with low shear strength may be produced. In this zone of weakness, failure of the sediment can occur due to gravitational loading or seismic activity. Slope failure can lead to debris flows, turbidity flows, slides and slumps. Examples of slope failures possibly linked to hydrates can be seen on the continental slopes and rises of south West Africa, on the USA Atlantic continental slope (Schmuck & Paull., 1993), and the Norwegian continental margin (Bugge *et al*., 1987).

1.4.3 Climate change

Hydrates may have a huge impact on global climate. The current amount of methane gas in the atmosphere is about 4.9×10^{15} g (Kvenvolden, 1998). This concentration is increasing by approximately 1.0% per year (Watson *et al*., 1990). Methane is radiatively active, that is it has the ability to trap the infrared radiation emitted by the earth's surface, and is therefore a greenhouse gas similar to CO_2. Although methane has a short residence time in the atmosphere (~10 years), it has a global warming potential 20 times greater than the equivalent weight of CO_2. Any large influx of methane into the atmosphere will have and may have already caused big changes in the global climate (Haq, 1998; Raynaud *et al.,* 1998). The amount of methane trapped in gas hydrate is perhaps 3000 times greater than the amount currently in the atmosphere. Destabilization of continental slope methane hydrates would potentially introduce significant amounts of methane into the water column and the atmosphere. In the higher latitudes methane in the permafrost would be emitted directly into the atmosphere. Either situation would significantly impact the atmospheric composition and therefore the radiative properties of the atmosphere that affects global climate. The methane emitted can also be then oxidized into water and carbon dioxide both in the water column and in the atmosphere. CO_2 is a dominant contributor to the atmospheric greenhouse forcing. It is also feared that the present day climate change will

cause gas hydrate to destabilize in the permafrost areas. The release of methane may itself lead to global warming, causing a positive feed back due to the release of more methane.

1.5 Morphology

Gas hydrates tend to form in four morphologies within the sediment (Malone, 1985): disseminated hydrate within the pore structure; nodules; veins; and massive hydrate. The morphological form that the hydrate takes will have a very strong effect on the physical properties of the hydrate bearing sediments (see Section 1.6). Malone (1985) suggested that hydrates grow from disseminated hydrate to massive as the hydrate volume fraction increases. However it is now understood that the hydrate morphology is dependent on the lithology that it grows in (Clennell *et al*., 1999; Ginsberg *et al*., 2000; Kleinberg *et al*., 2003).

Hydrate veins tend to occur in sediments with a relatively low permeability such as clays and carbonates. In such sediments the gas and fluid flow through the sediment is impeded and fluids tend to move through fractures and fissures. It is in these structures that the hydrate forms.

Hydrate nodules tend to form in lithologies containing mainly clays and silts. Clays and silts have very few nucleation sites for hydrate to form on and around due to the high capillary forces and small pore sizes. Although flow through the sediment is reduced the methane can diffuse through the sediment until it reaches a point where nucleation can occur. Because there are few nucleation points the nodules can grow large (several cm).

Massive hydrate forms in areas where the rate of methane flux is very high. In the deep sediments the hydrate forms throughout the pore structure. Higher in the sediment column the overburden effective stress is exceeded by the pressure of the hydrates and gas bubbles, allowing them to push away the sediment grains (Torres *et al*., 2004). This allows the hydrate crystals to grow larger than the previously available pore spaces and form massive hydrate.

Disseminated hydrate preferentially forms in coarse sediments such as sands (Ginsberg *et al*., 2000; Trehu *et al*., 2002; Riedel *et al*., 2006). Fluid and gas can flow relatively easily through such sediments and there are plenty of nucleation sites available allowing hydrate to form throughout the sediment. In disseminated hydrate the location within the pore structure where the hydrate forms is very important because it will have a strong effect on the physical properties of the hydrate bearing sediments. Four possible

growth habits for such hydrate have been put forward by Dvorkin (2000): (a) it may form in the pore space as small grains; (b) it may form grains as part of the load bearing structure; (c) it may form on and around the grains cementing them together; or (d) it may spot weld, forming a cement between the grains (Figure 1.6). Unfortunately hydrate in cores does not usually survive the coring process (especially if the hydrate is disseminated), so hydrate growth habits are hard to determine from field samples.

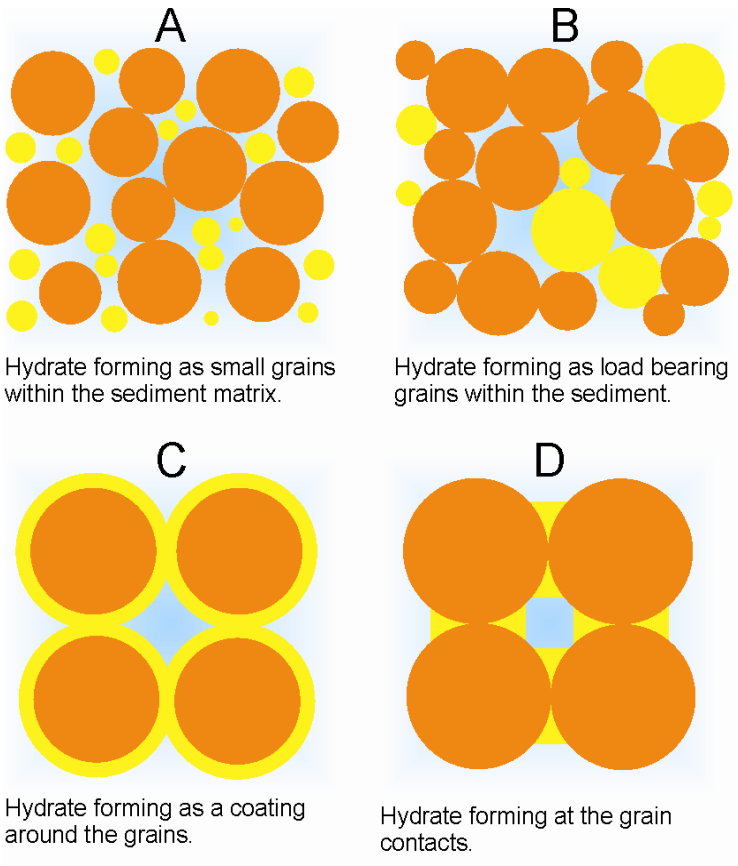

Figure 1.6 Proposed growth habits for disseminated hydrate (yellow) in sediment (orange) saturated with pore fluid (blue) modified from Waite *et al.* (2004): (A) gas hydrate forms small grains or inclusions within the sediment frame; (B) Hydrate forms as load bearing grains within the sediment matrix; (C) hydrate forms a coating around the sediment grains cementing them together; (D) hydrate forms at the grain contact only and cements the grains together.

There have only been a few studies to determine how disseminated hydrate forms in porous media. Tohidi *et al.* (2001) presented a micromodel to visually establish where hydrate forms. Their method involved forming hydrate between two plates of glass which had been etched to simulate a sediment. Hydrate was formed from free gas and distilled water, and their experiment showed that the hydrate collected in the pore spaces and

formed as small grains. Clennell *et al*. (1999) and Henry *et al*. (1999) produced theoretical models for hydrate growth based on capillary pressures and thermodynamics. From these studies it was determined that hydrate would be inhibited from growing in fine sediment because of the high capillary pressures in such sediments. Hydrate could grow in coarser sediments, preferentially forming in the larger pores. Deep sea nuclear magnetic resonance (NMR) has been used by Kleinberg *et al*. (2003) to determine the growth habit of hydrate in sandstones underwater. Hydrate was created by bubbling methane through a sandstone at or near the sea floor. The system was left open to simulate the dynamics of the natural system. This study concluded that hydrate formed in the larger pores within the sandstone, confirming the predictions of Clennell *et al*. (1999). While these studies have all shown hydrate growing in the pore spaces, Berge *et al.* (1999), using CCl_3F hydrate, indicate that hydrate is pore filling only at low hydrate saturations; at saturations above 35% it becomes cementing. Priest *et al.* (2005) made hydrate in loose sand and also suggest that hydrate forms at the grain contacts cementing the grains at saturations as low as 3-5%.

1.6 Seismic and electrical properties of sediments containing gas hydrates

1.6.1 Seismic velocity

Seismic velocity is known to increase in sediments containing gas hydrates. The gas hydrate replaces some of the pore fluids making the sediment stiffer and it can also cement the grains of the sediment together causing the bulk and shear moduli to increase. Theoretically the degree of the velocity increase is dependent on the amount of hydrate formed and the morphology of the hydrate.

Hydrate veins

Hydrate veins increase the strength of the sediment by forming a stiff structure within the sediment. The presence of hydrate veins therefore increases seismic velocity through the sediments and this increase is controlled by the gas hydrate saturation and the surface area to volume ratio of the veins. In a sediment where the ratio is small, the number of veins will be low and the increase in the strength of the sediment due to the hydrate is small (Priest, 2004). If a system has the same volume fraction of hydrate but the ratio is large, then the number of veins would be higher and the increase in strength would be greater. High degrees of anisotropy in sediments can be caused by the alignment of the veins. Such

examples can be seen on Hydrate Ridge, 100 km offshore Oregon (US) (Kumar, 2006). The fissures and fractures in which the hydrate forms can be caused by regional structural strain leading to the general alignment of the veins.

Hydrate nodules

The increase in seismic velocity is relatively low if hydrate forms as nodules. Hydrate nodules will have the same effect as if the sediment contained an inclusion of strong material (such as drop stones). The change in seismic velocity will almost completely be due to the replacement of the pore waters with solid hydrate. Anisotropy may be caused by the shape and alignment of the nodules formed. However, hydrate nodules tend to form with aspect ratios close to 1 and therefore any hydrate induced anisotropy will be low.

Disseminated hydrate

Disseminated hydrate is proposed to form with one of four different growth habits (Figure 1.6; Dvorkin, 2000). Each proposed growth habit will have a different effect on the physical properties of the hydrate bearing sediments. If the hydrate forms in the pore space (Figure 1.6 A), the effect on the velocity and strength of the sediment will be low. The only change will be due to the replacement of the pore fluids. The velocity change will be greater if the hydrate forms part of the load bearing structure (Figure 1.6 B), in which case the hydrate will be connected to other grains. If the hydrate coats the grains (Figure 1.6 C) it will cement the grains together producing a stiffer structure and result in higher seismic velocities. The highest theoretical seismic velocities relative to hydrate saturation would be produced if the hydrate forms at the grain contacts (Figure 1.6 D). Any anisotropy in sediments containing disseminated hydrate is not generally caused by the hydrate but by the alignment of the sediment grains.

1.6.2 Electrical resistivity

When an electrical current is passed through a fluid saturated sediment, the current predominantly flows through the conducting pore fluids. Hydrate, which is far more resistive that the pore fluids, can replace these fluids causing the resistivity of the bulk sediment to increase. Hydrate may also block the pore throats and restrict the current flow. The amount of resistivity increase is also dependent on the morphology of the hydrate. For example, a certain percentage of hydrate sitting in the pore space will not increase the

resistivity of the bulk sediment to the same degree as if that same percentage is blocking the pore throats.

Hydrate veins

Similar to the case for seismic velocity, hydrate veins will cause an increase in electrical resistivity. The electrical current will preferentially travel through the pore fluid. If the current must travel across a hydrate vein it will cause a resistive barrier which the current must either go through or around. If the current travels in the same direction as the vein there will be little change in the resistivity of the sediment. Therefore if hydrate veins are aligned electrical anisotropy may result.

Hydrate nodules

Hydrate nodules will have a small effect on the resistivity of the sediment, as any change caused will be due to the replacement of pore fluids. Nodules do not block pores or form large electrical barriers.

Disseminated hydrate

If hydrate forms in the pore fluids (Figure 1.6A) or as grains in the load bearing structure (Figure 1.6B) the resistivity effect will be small since only a fraction of the conducting pore fluid will be replaced. If the hydrate coats the grains or forms at the pore contacts it is possible that the hydrate will block the pore throats causing the pore spaces to become isolated. The current is therefore forced to travel through some of the highly resistive hydrate causing the resistivity of the sediment to be much higher than in the other cases.

Evidence and detection of gas hydrates

1.6.3 Hydrate sampling

Hydrate has been recovered by drilling cores at many locations (Figure 1.7). Massive hydrate and hydrates that have formed nodules often survive the drilling process. Disseminated hydrate is usually not recovered in cores because it dissociates due to the core warming before it gets to the surface, which prevents reliable hydrate saturations from being determined.

Figure 1.7 Gas hydrate retrieved from coring on Integrated Ocean Drilling Program (IODP) Leg 311 on the Cascadia Margin. (A) and (B) show nodules of hydrate from cold vent site U1328; (C) shows coarse sand with gas hydrate filling pore spaces from site U1326 (photos taken during Leg 311 by expedition scientists).

The presence of gas hydrate can be inferred from sedimentary cores even if the hydrate is no longer present. As sediment is brought up to the surface the hydrate starts to dissociate releasing water and gas. The sediment is confined in the core liners and often develops gaS-expansion cracks (Kvenvolden & Lorenson, 2001). Also the fine grain sediments may appear fluidized due the release of water (Figure 1.8)

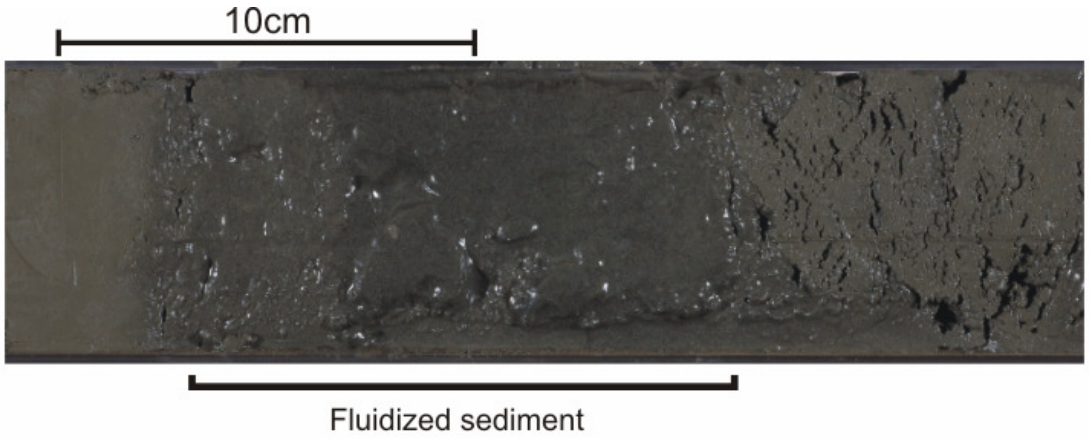

Figure 1.8 Sediment core from IODP Leg 311 showing fluidization of the sediment due to hydrate dissociation (adapted from Riedel *et al.,* 2006).

Pressure coring allows sediment to be cored and retrieved at in-situ pressure with minimal disturbance to the sediment. If such a technique is employed, hydrate may be brought to the surface intact. IODP Pressure cores are usually 1 m in length and 4.3 cm in diameter and the pressure corer can be used at pressures of up to 69 MPa (Riedel *et al.*, 2006). Such a system has been used on Ocean Drilling Program (ODP) Leg 163 on Blake

Ridge (Paull *et al*., 1996); Leg 201 on the Peru margin (Dickens *et al*., 2003); and Leg 204 on hydrate ridge (Trehu *et al*., 2002); on IODP Leg 311 on the Cascadia Margin (Riedel *et al*., 2006); and on the Indian Government's National Gas Hydrate Program (NGHP) Expedition 01 (Holland *et al*., 2006; Schultheiss *et al*., 2006).

Once the cores have been retrieved they can be stored for transfer to land based laboratories while maintaining in-situ pressure. On the expeditions listed above a series of non-destructive measurements were taken on the core before a degassing experiment was performed. The non-destructive measurements included x-ray imaging to determine hydrate distribution in the core (Figure 1.9), density and P-wave velocity. Degassing experiments were performed on the pressure cores to determine the volume of gas within the sediment. From this volume, the volume fraction of hydrate in the sediment can be calculated.

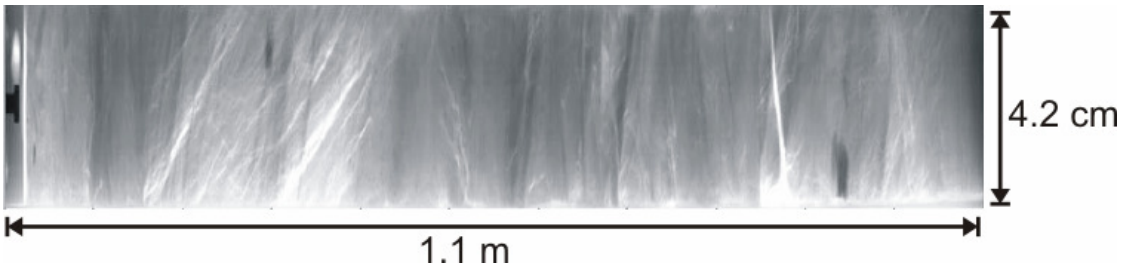

Figure 1.9 Pressure core x-ray from NGHP Expedition 01 showing veins of hydrate (white) cross cutting the core (adapted from Schultheiss *et al*., 2006).

The dissociation of hydrate is an endothermic process and as a result the temperature can be lower in the section of the core where hydrate was present (Kastner *et al*., 1995). Techniques have been developed to thermally map the cores. On ODP Leg 164 thermocouple probes were used along the length of the core to determine the temperature (Paull *et al*., 1996). On ODP Leg 204 this technique was improved with the use of an Infrared (IR) camera to scan the temperature distribution along the cores. IR allows rapid identification of hydrate before further dissociation occurs. Hydrate volume fraction can be estimated from the processed image, providing the thermal history of the core is known (Weinberger *et al*., 2005)

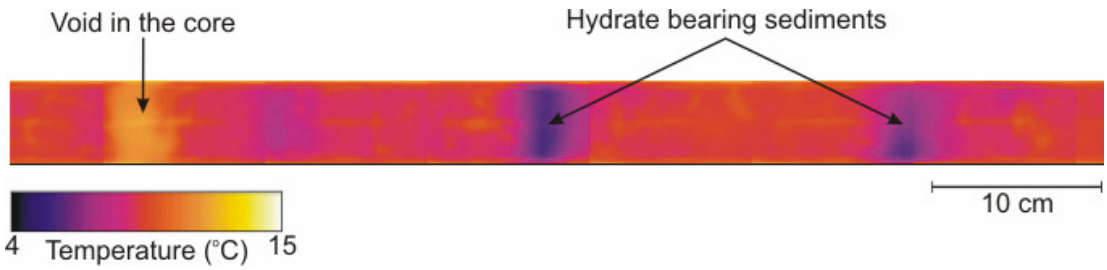

Figure 1.10 An IR image of a core from IODP Leg 311. Hydrate bearing sections appear blue (cold), voids in the core are warm and appear yellow (adapted from Riedel *et al.*, 2006).

Core analyses from the Blake Ridge (Ginsberg *et al.*, 2000) and Cascadia margin (Riedel *et al.*, 2006) use anomalies in the chlorinity of the pore fluid to give an indirect measurement of hydrate concentration. Fresh water markers have also been used to indicate the presence of hydrate. During the hydrate formation process, salt is excluded from the hydrate structure (Zatsepina & Buffett, 1998). The resulting highly saline pore fluids generally diffuse or advect away (Ussler & Paull, 2001). When the hydrate bearing sediment is cored and brought up to the surface the hydrate dissociates and releases fresh water (Figure 1.11). Therefore the pore fluid chemical composition will generally included a lower chorinity and salinity when hydrate has been present.

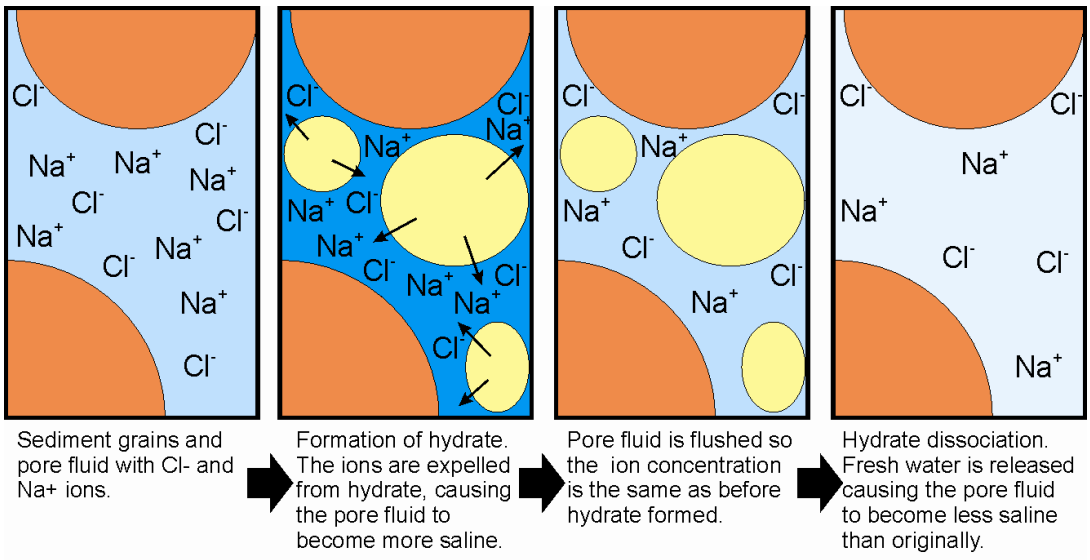

Figure 1.11 Representation of fluid freshening caused by the presence and dissociation of hydrate. Orange represents grains of sediment, blue the pore fluids and yellow the gas hydrate.

Pore fluid chlorinity, as well as indicating the presence of hydrate, also allows the hydrate saturation (S_h) to be calculated. Malinverno *et al.* (2006) present a method that relates the baseline chlorinity (C_b, the general background chorinity of the pore fluid where hydrate is not present) to the chlorinity of the pore fluid where hydrate formed (C_h):

$$S_h = \frac{w(C_b - C_h)}{C_h + w(C_b - C_h)}, \tag{1.1}$$

where

$$w = \frac{\chi_w N_{AVO} V_{cell}}{M_w n_w} \tag{1.2}$$

Parameter χ_w is the density of water, N_{AVO} is Avogadro's number (6.022×10^{23} mol^{-1}), V_{cell} is the volume of a unit cell (Type I), M_w is the molar mass of the water and n_w is the number of water molecules in a unit cell (Type I). This method does not take into account any salt trapped in the hydrate structure (Yuan *et al.*, 1996).

1.6.4 Hydrate detection by borehole logging

As previously mentioned, it is difficult to retrieve hydrate samples from the subsurface intact for laboratory study because the gas hydrate is unstable and prone to dissociate. Down hole logging measurements are therefore a powerful method of making measurements in hydrate bearing sediments. Logging allows the physical properties of the hydrate in sediment to be measured in-situ with minimal disturbance to the material. Logging has long been used by the oil industry to investigate hydrocarbon bearing formations, and a wide variety of downhole instruments have been developed to measure different physical properties. These include caliper, gamma ray, spontaneous potential, resistivity, sonic velocity, formation density and neutron porosity.

There are two methods of downhole logging currently in use. Wireline logging is undertaken by lowering an instrument into the borehole after it has been drilled. The instrument makes measurements while it is pulled upwards through the strata and sends the data back to the surface along a high speed communication cable (Goldberg *et al.*, 2000). This method has the advantage of collecting data continuously through the sediment column. Measurements can be made at depth intervals as small as 15 cm. One problem with wireline logging is that it cannot make measurements in the top of the sediment column, just below the sea bed. This part of the borehole tends to be unstable and a rigid

drill pipe casing must be placed in the first 80-100 m below the seafloor to provide stability (Goldberg *et al*., 2000). Measurements cannot be made through the casing. Recent technological developments allow measurements to be made while the borehole is being drilled. This technology is known as Logging While Drilling (LWD). It has the advantage over conventional drilling followed by logging in that measurements are made at the top of the sediment column, and it can make measurements in boreholes that are not drilled vertically. Both wireline logging and LWD methods can make resistivity, gamma ray and density measurements. However the resolution of LWD is currently not good enough to make velocity measurements in hydrate bearing sediments and in this situation standard wireline tools still need to be used (Goldberg, 1997). Another advantage of LWD over wireline is that measurements are made almost immediately after the material is drilled, when the physical properties of the sediment have had very little time to change. The drilling of sediments containing hydrate may lead to some dissociation of the hydrate or a change in gas concentration which could seriously affect the wireline results (Goldberg *et al*., 2000).

Sonic velocity logs, which measure P- and S-wave velocity, have been used to identify hydrate bearing sediments. Hydrate causes the P-wave velocity of the sediments to increase when present. Downhole logs can also determine the presence of free gas such as that which underlies the base of the hydrate stability zone. Sonic velocity logs can be used not only to detect the presence of hydrate but also to estimate the hydrate saturation of the sediments if the relationship between hydrate saturation and velocity is known.

Resistivity logs are routinely used by the hydrocarbon industry to determine oil and gas saturations of sediments. Resistivity can also be used to determine the hydrate saturation of sediments. It is common to relate formation resistivity to hydrocarbon concentration using a relationship based on Archie's (1942) equations. The resistivity of the pore fluids is needed for the interpretation of the resistivity logs and this can usually be obtained from core samples, if available, by measuring the chlorinity (Ginsberg *et al.*, 2000; Riedel *et al*., 2006). A problem with resistivity logs is that both hydrate and free gas are resistive, making it difficult to distinguish between them. Figure 1.12 shows the porosity, resistivity and velocity data collected by wireline logging on the Cascadia Margin on IODP Leg 311 (Riedel *et al*., 2006) in which the hydrate bearing zone can be identified in both the resistivity and the velocity logs. Table 1.2 gives some common values of physical properties recorded using downhole logging methods.

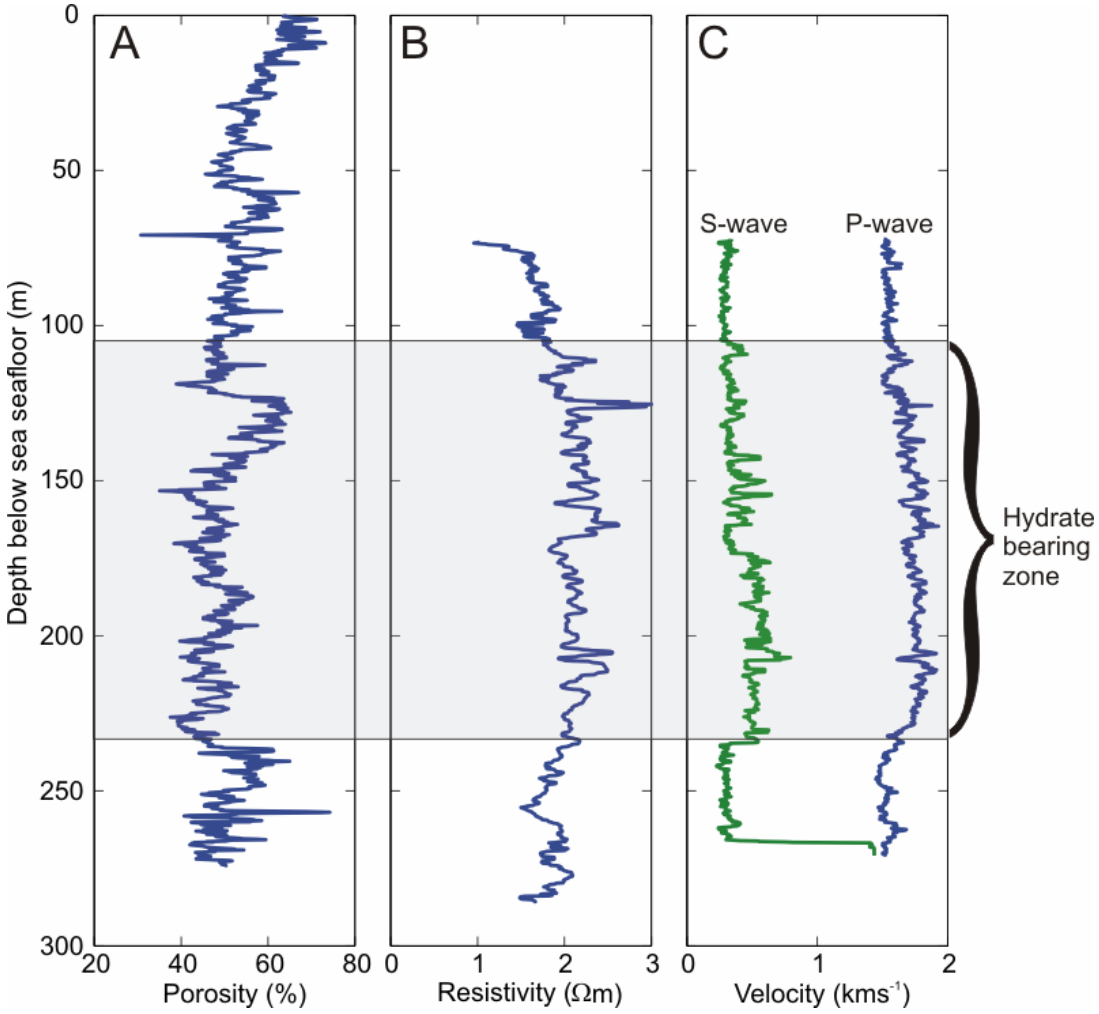

Figure 1.12 Logging results from IODP Leg 311, site U1327 showing a hydrate bearing zone. (A) LWD porosity log (determined from the density log, see Chapter 7); (B) wireline resistivity log; (C) wireline P- and S-wave velocity logs.

Both sonic velocity and resistivity logs should be interpreted together with porosity logs and, if available, temperature values, core samples etc. Hydrate will not be the only variable within the strata. Porosity has a huge effect on the physical properties of the sediment. Significant effort is put into making sure porosity values obtained from porosity logs are correct. For example, porosity measurements made from cores are often used to calibrate and check the log measurements (Riedel *et al.*, 2006). Temperature affects the resistivity of the material as well as the velocity. Changes in the composition of the sediment may also effect the physical properties.

	Massive Hydrate	Hydrate bearing Sediment	Water saturated Sediment	Gas bearing Sediment
V_p (km S^{-1})	3.2-3.6	1.7-3.5	1.5-2.0	1.4-1.6
V_s (km S^{-1})	1.6-1.7	0.4-1.6	0.75-1.0	0.4-0.7
ρ (Ω m)	150-200	1.5-175	1.0-3.0	1.5-3.5
χ (g cm^{-3})	1.04-1.06	1.7-2.0	1.7-2.0	1.1-1.5
φ (%)	20-50	35-70	35-70	50-90
γ (API)	10-30	30-70	50-80	30-80

Table 1.2 Common ranges of physical properties obtained from downhole logging (after Goldberg *et al*., 2000). V_p is P-wave velocity, V_s is S-wave velocity, ρ is resistivity, χ is density, φ is porosity and γ is natural gamma ray count.

1.6.5 Remote geophysical methods

Most gas hydrates in the field are inferred through seismic reflection profiling and the detection of the bottom-simulating-reflector (BSR). The BSR is believed to mark the interface between the hydrate bearing sediments and the free gas trapped in the sediments below. The BSR is caused by the high acoustic impedance contrast between the high velocity hydrate layer and the low velocity free gas layer. The existence of a BSR is dependent on free gas, and therefore hydrates may exist in the sediment without a BSR being present (Holbrook, 1996). Due to the pressure and temperature dependence of hydrate stability, the BSR often mimics the seafloor topography and can crosscut the stratigraphic horizons (Shipley *et al*., 1979; Paull *et al*., 1996; Bünz & Mienert, 2004). The BSR is often inferred to be the base of the hydrate stability zone (BHSZ). It has also been noted that within hydrate layers the sediments sometimes show low reflection amplitudes compared to sediments below the BSR. This "blanking" has been attributed to the reduction of impedance contrasts caused by the hydrate forming a cement in the pores of the sediments (Anstey, 1991; Lee *et al*., 1993); although other studies indicate that blanking is controlled by the acoustic characteristics of the hydrate bearing sediments (Holbrook *et al.,* 1996; Holbrook, 2001, Vanneste *et al.,* 2001). The relationship between blanking and the presence of hydrate is not yet fully understood (Chand & Minshull, 2003).

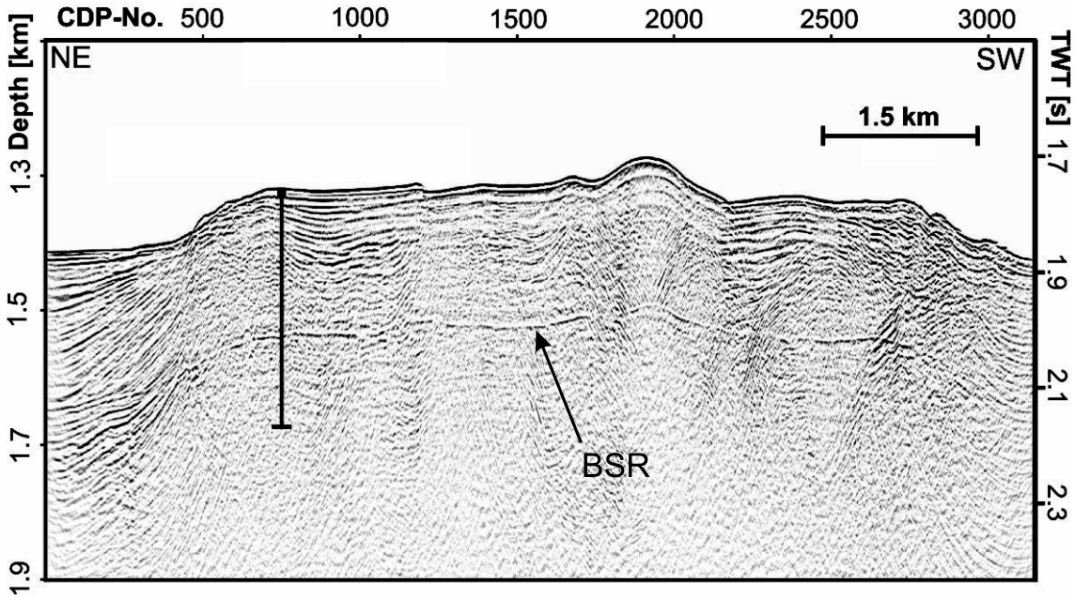

Figure 1.13 A multichannel seismic reflection profile from the Cascadia Margin showing the BSR following the seabed topography (modified from Collett *et al*., 2005).

Although identifying a BSR is the most common method of hydrate detection it is unable to give any information about the hydrate saturations of the sediments (Westbrook *et al*., submitted). Travel time and waveform inversion of multi-channel seismic and Ocean Bottom Seismometer (OBS) data can be used to obtain P- and S-wave seismic velocities of sediments, which may then be used to estimate hydrate saturations (Singh *et al*., 1993; Minshull *et al*., 1994; Minshull *et al.,* in press.; Westbrook *et al*., submitted). OBS surveys have several advantages over multichannel seismic data. Unlike other seismic surveys, the OBS is in contact with the sea floor and does not move until the survey is completed and it is retrieved. Often four-component receivers are used which permit both P- and S- wave velocities to be determined (e.g. Westbrook *et al.,* 2005). Analysis of converted S-waves along varying source-receiver azimuths can be performed to investigate anisotropy (e.g. Haacke & Westbrook, 2006). OBS derived velocities have the advantage over boreholes because both vertical and lateral velocities can be obtained - although these do not have the vertical resolution of velocities obtained by logging (Minshull *et al.,* in press).

Although there are good remote geophysical methods of measuring P- and S-wave velocities within hydrate bearing sediments, determining the gas hydrate saturation within those sediments is difficult. P- and S-wave velocities are dependent on many other parameters such as porosity, sediment composition and the hydrate morphology.

Controlled Source Electromagnetic (CSEM) sounding is a relatively new marine method of inferring the presence of hydrate in sediment from its resistivity signature. The CSEM technique exploits the resistive nature of the hydrate. The technique involves transmitting an EM field into the sediment, and this produces secondary fields associated with resistivity anomalies. A series of receivers in contact with the seafloor record the resultant field. CSEM has mainly been developed to investigate fluid presence and flow in basalts (Evans *et al*., 1991; MacGregor *et al*., 2000; Greer *et al*., 2002) and hydrocarbon reservoirs (Eidesmo *et al.,* 2002; Ellingsrud *et al.,* 2002; Constable *et al*., 2006). Edwards (1997) first considered using CSEM to investigate hydrates. CSEM has the advantage over downhole logging methods of being able to measure the resistivity of sediments without disturbing them, although borehole resistivity logs are still often used to ground truth CSEM data. While the current CSEM technique cannot provide the structural information that seismic profiling can, it can provide a more direct measure of hydrate saturation (Weitemeyer *et al,* 2006). It may also be able to identify hydrate in areas where no BSR can be identified (Yuan & Edwards, 2000; Schwalenberg *et al*., 2005).

1.7 Laboratory measurements of physical properties

Because of the problems of retrieving intact hydrate samples intact from a sediment core, most experimental research has concentrated on hydrate grown in the laboratory. Laboratory experiments are important because they can help our understanding of hydrate physical properties in a controlled environment. In particular they can provide data to test methods of modelling physical properties, which are needed for interpreting field measurements in terms of hydrate content.

1.7.1 Forming hydrate in the laboratory

In order to form hydrate in the laboratory, an apparatus needs to be set up in which hydrate will be stable. Laboratory experiments generally involve methods to both cool and place confining pressure on the system. The next problem is how to form the hydrate. The solubility of methane in water is very low. It is technically possible for hydrate to form from dissolved gas without free gas present (Remple & Buffett, 1998). However a question remains as to whether gas hydrate can nucleate when formed from dissolved gas. Tohidi *et al*. (2001) attempted to form gas hydrate from dissolved methane, but were unsuccessful.

They suggested that the pressures may not have been high enough. Most workers have therefore used a free gas phase for hydrate formation. When using free gas, hydrate growth occurs at the interface between the gas and the water, forming a barrier between the gas and the water. Hydrate formation will continue but at a reduced rate as the methane will still be able to diffuse across the barrier. There have been a number of methods that attempt to accelerate the hydrate formation by breaking the barrier (Englezos *et al.*, 1987; Handa, 1986).

For many experiments carbon dioxide is used instead of methane, for several reasons. Carbon dioxide yields the same Structure I gas hydrate and forms at a lower pressures (Figure 1.4). Other studies have used the water soluble hydrate former tetrahydrofuran (THF) (Pearson *et al.*, 1986; Kunerth *et al.*, 2001; Tohidi *et al.*, 2001). THF has the advantage that it is much easier to form hydrate from solution, but it forms a Structure II hydrate. If the aim of the laboratory work is to compare the properties of the laboratory formed hydrate with that of natural hydrate, methane hydrate will give more reliable results.

1.7.2 Hydrate formed in a porous media

Gas hydrates are generally dispersed in a sediment and it is therefore useful to grow hydrate in a porous medium to observe the effects it has on the sediment. This has generally involved hydrate being formed within silt or sand or some combination of the two (Stoll *et al.*, 1979; Winters *et al.*, 2000; Winters *et al.*, 2004; Waite *et al.*, 2004; Priest *et al.*, 2005) or in a sandstone or siltstone (Kleinberg *et al.*, 2003).

Much of the initial work on hydrates in a porous medium was accomplished by Stoll (Stoll *et al.*, 1971; Stoll & Bryan, 1979), who formed hydrate by passing a stream of methane through a column of sand. In the earliest work (Stoll *et al.*, 1971) a significant proportion of the gas became trapped within the medium because the hydrate formed blockages. The approach was later adapted to produce either pure hydrate or hydrate and sand without the trapped gas. The medium was stirred using rotational and translational motion until a slurry of hydrate had formed (Stoll & Bryan, 1979). The whole medium was then compacted. This allowed all the methane and water to form hydrate and prevent any gas being trapped. Both Stoll *et al.* (1971) and Stoll *et al.* (1979) formed 2-phase media. However in nature it is more usual to find a third phase, gas or water, also present.

Winters *et al*. (2000) and Waite *et al*. (2004) formed hydrate in the Gas Hydrate And Sediment Test Laboratory Instrument (GHASTLI) developed by the United States Geological Survey (USGS) at Woods Hole to test the physical properties of the hydrate bearing sediments. The instrument has been used to analyse both natural cores and laboratory grown hydrates. The GHASTLI method allows either water or gas to be present along with the hydrate and sand. The method involves starting with a completely water saturated Ottawa sand. A confining pressure is placed on the sample although the pressure and temperature (P-T) conditions are outside that required for hydrate stability. Methane is then percolated up through the sample until it has replaced a certain volume of water. The temperature of the sample is then dropped until the P-T conditions are in the hydrate stability zone. Hydrate is then left to form and stabilize which may take several days (Waite *et al*., 2004). No stirring of the sediment is used to accelerate the process, making it more representative of natural hydrate bearing sediments.

Priest (2004) and Priest *et al*. (2005) produced a 3-phase medium consisting of hydrate, gas and water. Their method, originally developed by Stern *et al.,* (1996), involves mixing ice, formed from distilled and de-aired water, with Leighton Buzzard sand. The ice and sand mixture is allowed to melt, tamped into a mould and then refrozen. The frozen mixture is flooded with methane, pressure is applied, and left to form hydrate. This method produces a gas saturated hydrate bearing sediment.

Yun *et al.* (2005) and Yun *et al.* (2007) investigate large strain mechanical properties of Tetrahydrofuran (THF) –hydrate bearing sediments. THF has several advantages over methane formed hydrate. THF hydrate has similar thermo-mechanical properties as structure II hydrate. It is completely miscible in water and is therefore not diffusion controlled as is the case with methane. It means that a free gas phase dose not have to be used. This means that its formation more closely resembles natural gas hydrate formation. Natural methane hydrate is often thought to form from aqueous phase methane (Buffett & Zatsepina, 2000). However methane is not very soluble in water which means long specimen preparation times if aqueous phase methane is desired (Yun *et al.,* 2005). THF shortens the time required to prepare a hydrate sample.

1.7.3 Hydrate distribution and quantification

Two problems with forming hydrate in a porous medium are determining what the hydrate saturation is, and controlling the hydrate distribution. Determining hydrate saturation is

important when trying to quantify the effects the hydrate has on the sample. Priest *et al.* (2005) calculate the hydrate saturation by measuring the amount of water in the system. Winters *et al*. (2000) calculate the hydrate saturation of the sample by measuring the volume of water that is pushed out of the sample by the injection of methane, and by assuming that all the remaining water is turned to hydrate. Winters *et al.* (2004) and Waite *et al*. (2004) calculate the hydrate saturation by measuring the volume expansion that occurs when the hydrate dissociates. Controlling the distribution of hydrate throughout a sample has proved more problematic. In most laboratory cases a homogeneous hydrate distribution is required. If the distribution is not homogeneous it may alter the results of any physical properties measurements made on the sample. Priest (2004) used a riffle box to mix sand and ice to ensure an homogeneous distribution of the hydrate. Other methods assume that the capillary forces on the gas and water mixture will cause the hydrate to form uniformly throughout the sample.

1.7.4 Physical property measurements on hydrate bearing sediments

Measuring the physical properties of a hydrate bearing sediment is problematic because the measuring system must be able to maintain the pressure and temperature required to keep the hydrate stable. The GHASTLI system (Winters *et al*., 2000; Winters *et al*., 2004; Waite *et al.*, 2004) can measure P-wave velocity, shear strength, hydraulic conductivity and electrical resistivity. The sample is contained in a flexible membrane with top and bottom end caps which contain acoustic transducers and gas and water flow ports. The system can be put under up to 25 MPa of pressure. Transmitted P-wave velocity is measured using 0.5-1 MHz transducers located on the backside of each end cap. Resistivity is measured using four equally spaced resistivity probes. The current is passed through the outer electrodes and the voltage is measured using the inners ones.

Priest (2004) used an adapted “Stokoe” resonant column (Stokoe *et al*., 1999) to measure P- and S-wave velocities as well as attenuation at frequencies relevant to marine seismic investigations. The Gas Hydrate Resonant Column (GHRC), developed at the University of Southampton, can make measurements on field and laboratory samples. The velocities are determined from the frequency of vibration at resonance of the sediments using flexural and torsional excitation.

Resistivity measurements have proved to be the most problematic to obtain. This is primarily because the majority of hydrate samples made in the laboratory are gas saturated.

The resistivity of the samples is therefore extremely high. They are also not equivalent to field samples which are more water saturated. Making measurements on field samples does not completely solve the problem. Samples that have been collected from the field have often partly dissociated even if they are placed in liquid nitrogen immediately.

Yun *et al.* (2006) have developed a method for measuring the physical properties of hydrate bearing sediments from pressure cores. These samples have never been depressurized and the hydrate has not dissociated. Their samples were retrieved from the Gulf of Mexico and then transferred into Georgia Tech's Instrumented Pressure Testing Chamber (IPTC) while maintaining pressure. A series of probes are used to measure P- and S-wave velocity, electrical resistivity and undrained shear strength. Results show that the IPTC data are much closer to those obtained from the velocity log than conventional core measurements, although the S-wave velocity was still lower than the logs. Yun *et al.*'s (2006) explanation for the velocity discrepancy was that the S-wave velocity is strongly dependent on the skeletal stiffness of the sediment which was affected by the coring process. Despite these effects the method looks promising. However, no data were provided by Yun *et al.* (2006) on the hydrate saturation or porosity of the samples, which would be useful for modelling. When used to validate models, laboratory grown hydrate does have the advantage over field samples because the variables, such as porosity and sediment composition, are easier to control and measure.

1.8 Aim of this thesis

Gas hydrates have been shown to be a complex substance. They are found all over the world in a variety of sediments. Detecting gas hydrates in-situ has been accomplished through drilling, logging and seismic and EM surveying, however predicting the amounts of hydrate has proved more difficult. It is clear that hydrates may be an important factor in climate change and the stability of ocean sediments. Gas hydrates are known to affect the physical properties of the sediments that they reside in. Seismic velocity and resistivity are both known to increase due to the presence of hydrate, and the amount of increase is dependent on the hydrate saturation as well as the morphology of the hydrate within the sediments. This thesis aims to produce a method for quantifying the gas hydrate saturation in marine sediments using seismic and electrical properties. Using both the electrical and the seismic properties in a joint interpretation approach allows different but complementary information on the sediment to be used to determine litholgical parameters

with greater accuracy. The theoretical models will be tested against laboratory data, and used to estimate the gas hydrate saturation of sediments drilled and cored on IODP Leg 311.

Organisation of Thesis

Chapter 2 introduces the concepts of an effective medium and effective medium theory. It details the principal seismic effective medium methods which determine the overall seismic properties of a medium from the individual constituent properties. Archie's law is also introduced for estimating the electrical resistivity of clastic sediments. The chapter concludes with the principal methods of gas hydrate saturation estimation using effective medium methods. This chapter also discusses the effective medium methods which would be the most appropriate for the joint interpretation method.

Chapter 3 discusses in more depth than Chapter 2 the Self Consistent Approximation (SCA), the Differential Effective Medium (DEM) methods and the combined SCA/DEM method for the elastic properties of two-phase (pore fluid and grain) media. Lastly it explains the development of the method by altering the critical porosity. It then extends the adapted SCA/DEM method to three phases (pore fluid, grain and hydrate) using the method of Jakobsen *et al.* (2000).

In Chapter 4 an electrical effective medium modelling algorithm is developed based on the Hashin-Shrikman conductive bound, a geometrical factor, and electrical path length. The geometrical factor is based on the aspect ratio of the sediment grains and is independent of grain size and porosity. The path length is dependent on the porosity of the sediment and aspect ratio of the grains but is also independent of the grain size. The electrical effective medium theory is then extended to include a hydrate phase. The theory is developed in such a manner as to be compatible with the three-phase seismic effective medium methods.

To validate both the electrical and seismic effective medium methods a set of laboratory experiments were designed. Chapter 5 explains how and why the laboratory experiments were designed and presents the results. Two sets of experimental results are presented, one with and one without hydrate.

In Chapter 6 the laboratory data presented in Chapter 5 are compared to the effective medium models developed in Chapters 3 and 4. Once this has been accomplished, a joint interpretation method is developed and also tested against the laboratory data. The joint interpretation method is developed for both two-phase and three-phase effective media.

In Chapter 7 the individual effective medium theories developed in Chapter 3 and 4 are used to determine the hydrate saturation of sediments measured during the Integrated Ocean Drilling program (IODP) expedition 311. The joint interpretation method, developed in chapter 6, is then used to determine the hydrate saturation and aspect ratios of the sediments from co-located data points. This helps to determine the reason why the hydrate saturations from the individual methods do not always match.

Chapter 8 presents a summary of the thesis and provides final conclusions.

Chapter 2. Effective Media and Hydrate Quantification from Physical Properties

2.1 Introduction

This chapter reviews some of the principal methods for relating the physical properties of the individual constituents of a medium to the overall effective physical properties. This review forms the background from which to decide which methods should be used in the final joint seismic and electrical model. This chapter will also investigate some of the current methods used to quantify hydrate fraction in sediment.

An effective medium is a theoretical medium which has the same overall physical properties, such as seismic velocity and electrical resistivity, as a physical medium which is composed of more than one constituent (e.g. sediment). In general when physical property measurements are made on sediments it is the bulk properties that are measured. These sediments are composed of many different constituents each of which will have their own different physical properties. In this chapter an effective medium model is defined as a model which relates the overall physical properties of a medium to the individual constituent properties. This definition includes methods which include empirical constants as well as those which are purely physical.

This chapter reviews first seismic then electrical effective medium theory, initially for two-phase effective medium models that are developed for a sediment consisting of single grain type and fluid. The models are then extended to three-phases to incorporate the additional hydrate phase.

2.2 Seismic effective medium theory

Effective medium theory reproduces many of the observed characteristics of sedimentary rocks, such as bulk and shear modulus. There are many theories and models that have been used to determine the elastic properties of an effective medium. Some only provide upper and lower bounds to the elastic properties, while others attempt to give an exact solution.

Most of the methods described here require the bulk and shear modulus of the individual components to be known. The shear modulus (μ) is the ratio of shear stress to

shear strain and is sometimes known as the modulus of rigidity. The bulk modulus (κ) is the ratio of hydrostatic stress to volumetric strain and is sometimes known as the compressibility modulus. Bulk and shear moduli are related to seismic P-wave (compressional wave) velocity (V_p) and S-wave (shear wave) velocity (V_s) by:

$$V_p = \sqrt{\frac{\kappa + 4/3\,\mu}{\chi}}, \tag{2.1}$$

$$V_s = \sqrt{\frac{\mu}{\chi}}, \tag{2.2}$$

where χ is the density of the material[1]. Most effective medium models calculate the overall effective moduli of the composite. Such models will be presented in this thesis in terms of moduli. There are several effective medium models that are usually calculated and presented in the literature in terms of velocity, and these models will be presented in this thesis in terms of velocity. These velocities can be related to the bulk modulus and shear modulus by the equations above. It is assumed that the wavelength of a seismic wave passing though the medium is much larger than the size of any inclusions and wavelength dependent effects are neglected.

In order to calculate the value of the elastic modulus of a multi phase effective medium, three principal quantities need to be specified:

1. The volume fraction of the different phases,
2. The elastic moduli of the phases,
3. The geometric details of how the phases are related to one another. This is the most difficult to determine.

Values of density, shear modulus and bulk modulus for glass beads (used in the two-phase experiments, see Chapter 5) and brine are used in the models presented in this chapter. Moduli and density values used for glass beads and brine are given in Appendix A. If only the volume fraction and the elastic moduli are given then only the upper and the lower bounds of the elastic properties can be predicted. For any given volume fraction of a mixture, the effective medium elastic moduli should fall between these bounds. The simplest bounds are the Voigt (1928) and Reuss (1929) bounds.

[1] The symbol ρ is generally used in geophysics for both electrical resistivity and density. To avoid confusion the symbol ρ will be used for electrical resistivity and χ will be used for density throughout this thesis.

2.2.1 Voigt Model

Voigt's Model (1928) is an isostrain model, which averages the stress of a single crystal in terms of the given strain over all possible lattice orientations (Figure 2.1). The model assumes that the strain is uniform throughout the aggregate. The calculated effective modulus is an upper bound. However real isotropic mixtures can never be as stiff as the Voigt bound unless the medium is only composed of one material. The Voigt model is given by:

$$M_{\mathrm{V}} = \sum_{r=1}^{n} \varphi_r M_r \,, \tag{2.3}$$

where:

M_V = Voigt's effective modulus (which can be either bulk or shear modulus);

M_r = Modulus of the r-th component;

φ_r = Volume fraction of the r-th component of n phases.

2.2.2 Reuss and Wood Models

Reuss' model (1929) is an isostress model (Figure 2.1). It assumes that all the constituents have an equal stress throughout the model. The model calculates a lower effective modulus bound. When all the constituents are gases or liquids, which have a shear modulus of zero, then the Reuss model gives the effective moduli (M_R) exactly:

$$\frac{1}{M_R} = \sum_{r=1}^{n} \frac{\varphi_r}{M_r}. \tag{2.4}$$

Both the Reuss and the Voigt models require that the effective medium be isotropic. If the medium is highly anisotropic, or highly heterogeneous, then the models fail. Both the Reuss and Voigt models also assume that each of the constituents is linear and elastic.

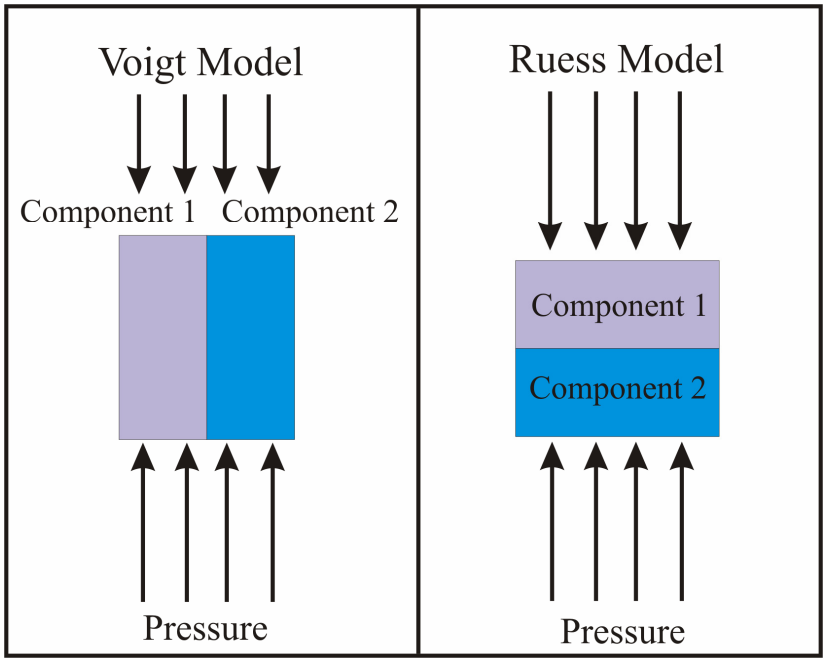

Figure 2.1 Schematic diagram of the Voigt (isostrain) and Reuss (isostress) models for a two-phase effective medium (redrawn from Wang & Nur, 1992). In the Voigt model the deformation of both components is the same but the force applied may not be equal. In the Reuss model the force or stress applied to each component is the same but the deformation may not be equal.

Wood (1930) noted that the adiabatic compressibility of a mixture of fluids is equal to the sum of the compressibility of the individual components weighted by their volume fraction. This gives the equation

$$B = \sum_{r=1}^{n} \varphi_r B_r \,, \tag{2.5}$$

where B is the overall adiabatic compressibility of the fluid mixture, B_r is the adiabatic compressibility of the r-th component and φ_r is the volume fraction of the r-th component. This maybe rewritten in terms of bulk modulus:

$$\frac{1}{\kappa_w} = \sum_{r=1}^{n} \frac{\varphi_r}{\kappa_r} \,. \tag{2.6}$$

Equation 2.6 is derived on an isostress basis and can be used to evaluate the bulk modulus of a dilute suspension, where the grains do not touch. The Wood (1930) equation, Equation 2.6, and the Reuss (1929) equation, Equation 2.4, are essentially the same when analysing the bulk modulus of an effective medium. However the assumptions for each

model are different. Wood's equation was developed for dilute suspensions where only bulk modulus exists. Whereas the Reuss model was developed for crystal aggregates in which both bulk and shear modulus could be analysed. Because a suspension of grains in a fluid will not pass a shear wave, Wood (1941) rewrote Equation 2.6 in terms of V_p:

$$\frac{1}{\chi V_p} = \frac{\varphi}{\chi_f V_{pf}^{\ 2}} + \frac{1-\varphi}{\chi_m V_{pm}^{\ 2}}, \tag{2.7}$$

where φ is the fractional volume of fluid in the total volume of the sample, i.e. the porosity; V_{pf} and V_{pm} are the P-wave velocity of the fluid and the rock matrix respectively; and χ, χ_f and χ_m are the densities of the overall effective medium, the fluid and the matrix respectively. The Wood equation 2.7 fits measured data of liquid mixtures, emulsions and dilute suspensions very well (Wang & Nur, 1992).

2.2.3 Hill's average approach

The upper and the lower effective modulus bounds of the Voigt and Reuss models on their own cannot be used to determine the elastic properties of a rock. Hill (1952) shows mathematically that the bulk and shear modulus should lie between the bounds of Voigt and Reuss. Hill's approach is to average the upper and lower effective moduli produced by the Reuss and the Voigt models (see Figure 2.2 and Figure 2.3),

$$M = \frac{1}{2}\left(M_{\mathrm{V}} + M_R\right), \tag{2.8}$$

where M is Hill's average effective modulus. Hill's approach does not have any direct physical meaning but can be used when no other information is given or no other method is available (Wang & Nur, 1992). Wang & Nur (1992) show that Hill's average gives a good approximation of the bulk moduli for sandstones with porosities between 5% and 20%. However, as the porosity increases Hill's average overestimates the effective moduli.

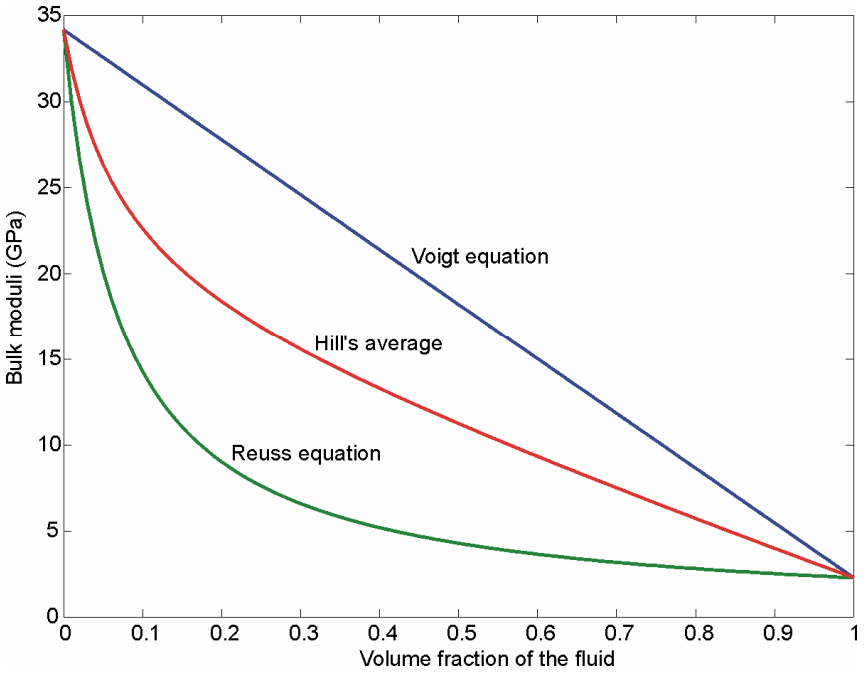

Figure 2.2 Bulk moduli of a glass beads and water composite calculated from the Voigt (1928), Reuss (1929) and Hill (1952) equations.

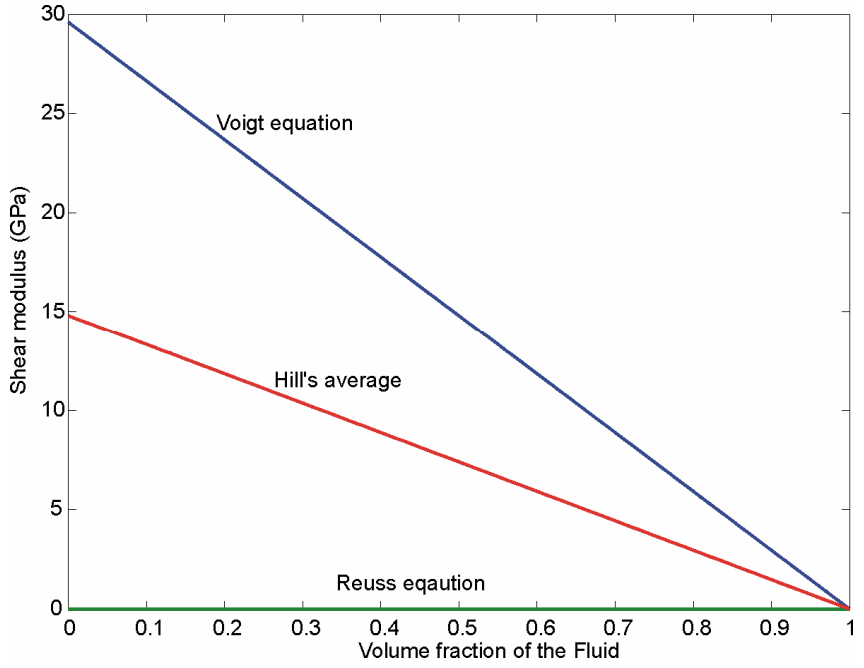

Figure 2.3 The shear moduli of a mixture of glass beads and water calculated from the Voigt (1928), Reuss (1929) and Hill (1952) equations. Because of the way the effective medium is calculated by the Reuss equation, any composite that contains fluid will give a lower bound shear modulus of zero.

2.2.4 Wyllie Time Average Equation

Wyllie *et al.* (1956; 1958) developed a simple equation in which the effective velocity is the sum of the transit times in each phase and is referred to as the time average equation:

$$\frac{1}{V_p} = \frac{\varphi}{V_{pf}} + \frac{1-\varphi}{V_{pm}}, \tag{2.9}$$

where V_{pf} and V_{pm} are the P-wave velocity of the fluid and the matrix respectively. The physical interpretation of this method is a rock or sediment that is made up of alternating layers of the two phases, perpendicular to the direction of the seismic wave (Figure 2.4). Because of this a shear wave cannot pass through the medium if there is any fluid.

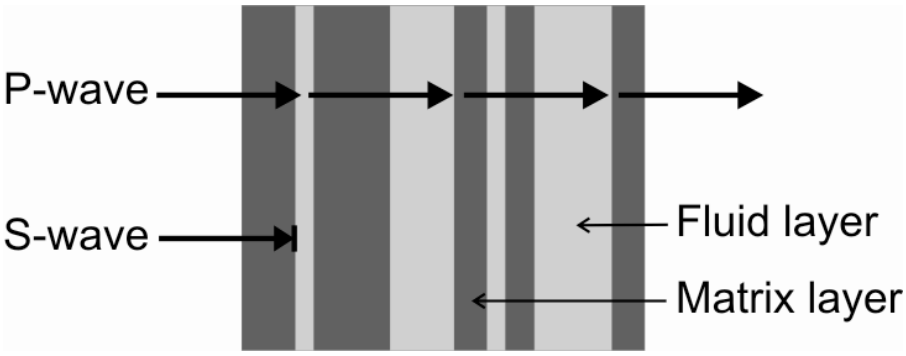

Figure 2.4 Physical interpretation of the medium calculated by the Wyllie *et al.* (1956) Time Average Equation.

Equation 2.9 is often applied when the lithology and pore fluid information are unknown. Wang & Nur (1992) show that the Time Average Equation causes large errors in the final compressional velocity, that the model oversimplifies and that it does not work for rocks containing fluids of low velocities, and in general should not be used when $V_{p.f} \leq 1.0$ kmS-^{1}. Vugular pores, often seen in limestones, tend to be spherical and incompressible and cause V_p to be insensitive to pore fluid saturation and the equation will therefore underestimate velocity. Pores formed by fractures tend to be small in volume, elongated and highly compressible, causing the V_p to be very sensitive to the pore fluid saturation, so that in this case Equation 2.9 will over estimate the porosity. In general, for a water saturated sediment, the Time Average Equation underestimates V_p in cleaner sandstones and overestimates V_p in shaley sandstones and soft sands (Wang & Nur, 1992).

2.2.5 The Hashin-Shtrikman (HS) bounds

Hashin & Shtrikman (1963) calculate bulk and shear modulus in terms of upper and lower bounds. The physical interpretation of the Hashin-Shtrikman (HS) method is of an effective medium which is comprised of a space filled with spheres. Each sphere is comprised of a core of component one with a shell of component two (Figure 2.5). The volume fraction of each component in every sphere is the same as the total volume fraction of that component in the medium. If the material with the higher moduli forms the shell of the sphere, the effective modulus will be that of the upper bound. The lower bound is produced when the stiffer material forms the core of the sphere.

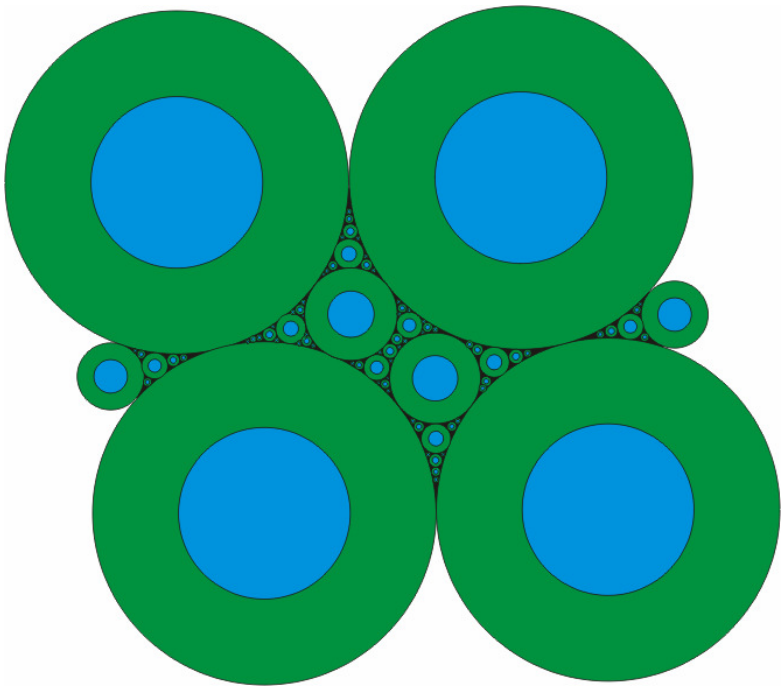

Figure 2.5 The physical interpretation of the Hashin & Shtrikman (1963) effective medium with two components forming the core and shell of a series of spheres (redrawn from Mavko *et al*., 1998). The components can be interchanged to produce the upper and lower bounds. The HS bounds (Figure 2.6 and Figure 2.7) are calculated from Equations 2.10-21.

When the shear modulus is equal to zero the lower bound of the bulk modulus is equal to that of the Reuss bound, which exactly describes the moduli of a suspension of grains in a pore fluid. The HS bounds assume that both the medium and each of the constituents are isotropic and elastic.

Bulk modulus is given by:

$$\kappa^{-} = \kappa_s + \frac{A}{1 + a_1 A_1}, \tag{2.10}$$

$$\kappa^{+} = \kappa_n + \frac{A_n}{1 + a_n A_n}, \tag{2.11}$$

where,

$$a_1 = \frac{3}{3\kappa_s + 4\mu_s}, \tag{2.12}$$

$$a_n = -\frac{3}{3\kappa_n + 4\mu_n}, \tag{2.13}$$

$$A_1 = \sum_{r=2}^{n} \frac{\varphi_r}{\frac{1}{\kappa_r - \kappa_s} - a_1}, \tag{2.14}$$

$$A_n = \sum_{r=1}^{n-1} \frac{\varphi_r}{\frac{1}{\kappa_r - \kappa_n} - a_n}, \tag{2.15}$$

where,

κ_s = smallest bulk modulus among the κ of the n phases;

κ_n = largest bulk modulus among the κ of the n phases;

κ_r = bulk modulus of the r^{th} component;

κ^{-} = lower bound bulk modulus;

κ^{+} = upper bound bulk modulus.

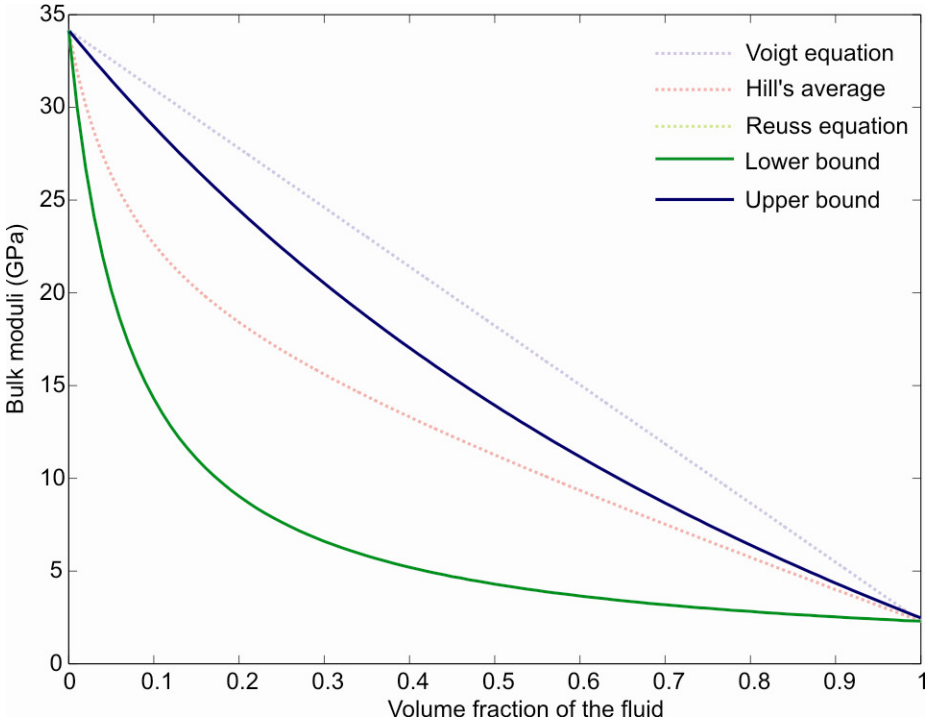

Figure 2.6 Upper and lower bounds for bulk moduli calculated from Hashin & Shtrikman (1963) (Equations 2.10 and 2.11) for a composite of glass beads and brine. The Voigt, Hill and Reuss equations are also plotted for comparison. The Reuss and the HS Lower bound give the same results when a solid is mixed with a liquid but the results are not the same when both components are solid.

Shear modulus is given by:

$$\mu^{-} = \mu_s + \frac{B_1}{2(1 + b_1 B_1)}, \tag{2.16}$$

$$\mu^{+} = \mu_n + \frac{B_n}{2(1 + b_n B_n)}, \tag{2.17}$$

where

$$b_1 = -\frac{3(\kappa_s + 2\mu_s)}{5\mu_s(3\kappa_s 4\mu_s)}, \tag{2.18}$$

$$b_n = -\frac{3(\kappa_n + 2\mu_n)}{5\mu_n(3\kappa_n 4\mu_n)}, \tag{2.19}$$

$$B_1 = \sum_{r=2}^{n} \frac{\varphi_r}{\frac{1}{2(\mu_r - \mu_s)} - b_1}, \tag{2.20}$$

$$B_n = \sum_{r=1}^{n-1} \frac{\varphi_r}{\frac{1}{2(\mu_r - \mu_s)} - b_n}, \tag{2.21}$$

where:

μ_s = smallest shear modulus among μ of the n phases;

μ_n = largest shear modulus among μ of the n phases;

μ_r = shear modulus of the rth component;

μ^- = lower bound shear modulus;

μ^+ = upper bound shear modulus.

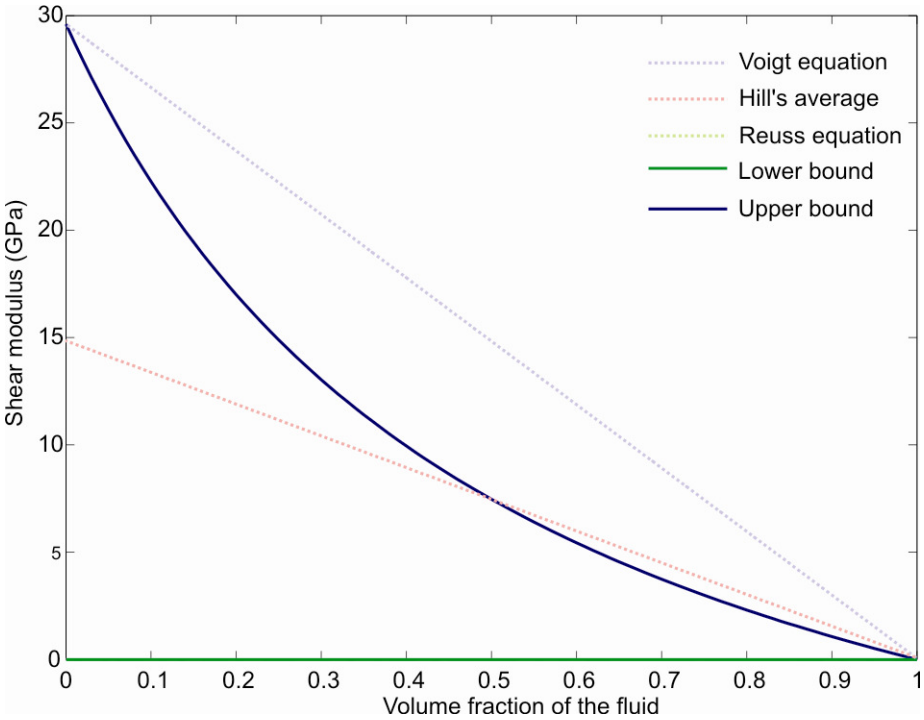

Figure 2.7 Upper and lower bounds for shear moduli calculated from Hashin & Shtrikman (1963) (Equation 2.16 and 2.17) for a composite of glass beads and brine. Note the lower bound has a value of zero for all fluid volume fractions. The Voigt, Hill and Reuss equations are also plotted for comparison. The Reuss and the HS Lower bound give the same results when a solid is mixed with a liquid but the results are not the same when both components are solid.

The HS bounds are similar to the Voigt and Reuss models in that they give upper and lower bounds for the bulk modulus and shear modulus. However these bounds are narrower than the Voigt and Reuss bounds (Figure 2.6 and Figure 2.7) and are therefore considered to be more useful for many applications.

2.2.6 Self Consistent Approximation (SCA)

The bounds produced by the Hashin & Shtrikman (1963) and the Voigt, Reuss and Hill equations are too far apart to give reliable predictions for the effective bulk and shear moduli of an effective medium. By adding in some specific inclusion shapes, the values of the moduli can be estimated with greater accuracy. The assumption of the Self Consistent Approximation (SCA) is that the orientation of an inclusion's stress or strain is the same as the overall stress or strain. This assumption means that each of the inclusions is treated as an individual isolated inclusion within a uniform matrix. This matrix is assumed to have the same elastic properties as the effective medium as a whole. The elastic moduli of the medium are as yet unknown. This replacement of the background material approximates the interaction of the inclusions. The effective bulk and shear moduli are coupled together in the SCA equations which have to be solved by iteration to determine each modulus separately.

Hill (1965) developed a Self Consistent method for embedding spherical grains within a matrix. These grains are statistically dispersed throughout the medium and allowed to interact with each other. This approach allows the medium to have permeability as well as porosity. Hill's (1965) SCA equations are given by:

$$\frac{\beta_1}{\kappa_{SC}-\kappa_2}+\frac{\beta_2}{\kappa_{SC}-\kappa_1}=\frac{a}{\kappa_{SC}}, \tag{2.22}$$

$$\frac{\beta_1}{\mu_{SC}-\mu_2}+\frac{\beta_2}{\mu_{SC}-\mu_1}=\frac{b}{\mu_{SC}}, \tag{2.23}$$

where,

$$a=3-5b=\frac{\kappa_{SC}}{\kappa_{SC}+4/3\,\mu_{SC}}. \tag{2.24}$$

Subscripts 1 and 2 indicate each of the constituents and SC indicates the effective medium; β is volume fraction; μ and κ are the shear modulus and bulk modulus.

Hill's model can only be used for spherical inclusions. A number of SCA methods have been developed to allow for more complex inclusion shapes. These including

methods by Wu (1966), Berryman (1980), Willis (1977) and Budiansky (1965). One very important effect of the SCA is that as porosity increases it passes through a bi-connected phase, i.e. at certain inclusion volume fractions both the inclusion and the matrix are fully interconnected with each other. This bi-connectivity occurs when the inclusions constitute between 40% and 60% of the effective medium (Sheng, 1990).

SCA methods are primarily used to calculate the effective properties of water saturated sediments and to calculate the elastic moduli of the dry frames of rocks. There are a number of assumptions and limitations associated with SCA (Wang & Nur, 1992; Mavko *et al.*, 1998). These include:

- The constituents and the effective medium are linear, isotropic and elastic. The effective medium will therefore also be homogeneous and isotropic.
- The inclusion shapes are idealized. The inclusions are spheroidal and only the aspect ratio can change. There are however a number of special inclusion shapes which can also be added into the medium (see Chapter 3).
- All the inclusions must have the same shape. Therefore the medium cannot contain inclusions with different aspect ratios.
- At very low porosities the inclusions become isolated and no longer interact with each other.

2.2.7 Differential Effective Medium (DEM)

The DEM method models an effective medium by starting with a medium composed of a single material, to which inclusions with a known geometric shape are incrementally added. After each incremented addition of the inclusion the effective medium bulk and shear moduli are recalculated. This process continues until the desired volume fraction of each constituent is reached. A typical DEM method is given by Berryman (1992):

$$(1-\beta_2)\frac{d}{d\beta_2}[\kappa_{dem}(\beta_2)] = (\kappa_2 - \kappa_{dem})P_2(\beta_2), \tag{2.25}$$

$$(1-\beta_2)\frac{d}{d\beta_2}[\mu_{dem}(\beta_2)] = (\mu_2 - \mu_{dem})Q_2(\beta_2), \tag{2.26}$$

where κ_{dem} and κ_2 are the bulk moduli of the effective medium and the inclusion respectively; μ_{dem} and μ_2 are the shear modulus of the effective medium and the inclusion respectively; β_2 is the volume fraction of the inclusion; P and Q are geometric factors that describe the shape of the inclusion (formulae for theses are given in chapter 3).

In the DEM method the components are not treated symmetrically. Therefore if a calculated effective medium starts with component 1 and component 2 is incrementally added, it will not predict the same results as if it had started with component 2 and component 1 was incrementally added, even if the volume fractions of the two components are the same in the final effective medium. The DEM method preserves the microstructure of the starting medium (Sheng, 1990). It follows that if the starting medium is component 1 it will remain interconnected at all porosities and component 2 will remain isolated. A more in-depth explanation of DEM is given in Chapter 3. Assumptions used in the DEM method include (Wang & Nur, 1992; Mavko *et a*l, 1998):

- The individual constituents are isotropic and homogeneous.
- The process of adding in incremental amounts of a material is a thought process only and does not describe the evolution of a real rock.
- The inclusions are idealized and therefore may not truly represent inclusions in real rocks.

2.2.8 Contact models

Contact theory was developed mainly to investigate the elastic properties of granular materials such as unconsolidated sands. Such models are based on relating the normal (S_n) and tangential (S_τ) contact stiffness of two spherical grains to the effective elastic properties of the medium. The normal stiffness is defined as the ratio of a confining force (f) increment to the shortening (u) of a sphere radius (r). The tangential stiffness is defined as the ratio of a tangential force (f_t) increment to the increment of the tangential displacement of the centre relative to the contact region (τ) (Mavko *et al.*, 1998). Normal and tangential stiffnesses are given by:

$$S_n = \partial f \big/ \partial u, \tag{2.27}$$

$$S_\tau = \partial f_t \big/ \partial \tau. \tag{2.28}$$

For a medium composed of random packed spheres the bulk modulus and shear modulus are given by:

$$\kappa = \frac{C_o(1-\varphi)}{12\pi r} S_n, \tag{2.29}$$

$$\mu = \frac{C_o(1-\varphi)}{20\pi r}(S_n + 1.5S_\tau), \tag{2.30}$$

where C_o is the coordination number. The coordination number is the average number of spheres each sphere is in contact with. Although this number will be dependent on the type of packing (cubic, hexagonal etc.) for a random dense pack C_o will be approximately 9 (Mavko *et al.*, 1998).

Although there are a number of contact models they are all based on either the Hertz (1881) or Mindlin (1949) models (Figure 2.8).

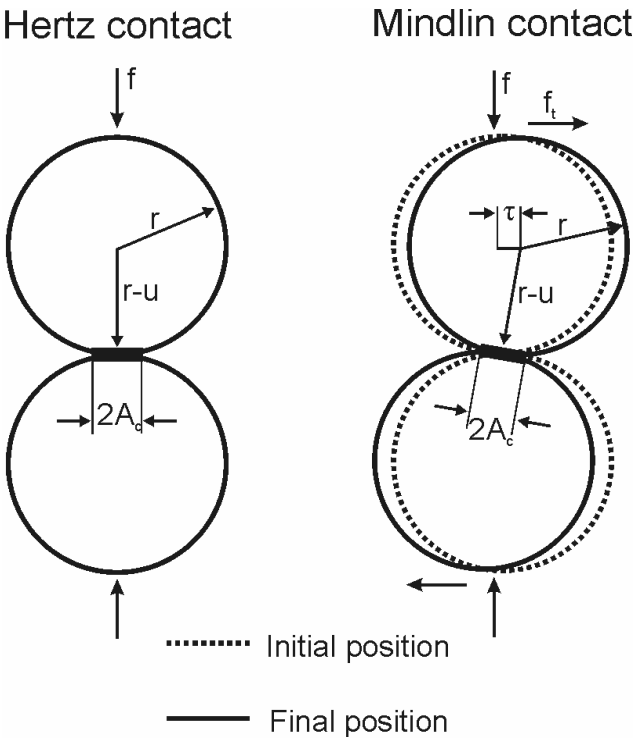

Figure 2.8 Schematic diagram showing the Hertz and Mindlin contact models (adapted from Wang & Nur, 1992).

Hertz model

In the Hertz model only compressional force is applied to the grains. There is no tangential force and therefore there is no tangential displacement between the grains. For two identical elastic spheres the radius of the contact area (A_c) is given by:

$$A_c = \left[\frac{3\left(1-\nu^2\right)rf}{4E}\right]^{1/3} = \left[\frac{3(1-\nu)rf}{8\mu}\right]^{1/3}, \qquad (2.31)$$

where E is the Young's modulus and υ is the Poisson's ratio of the grain material. The normal displacement is given by:

$$u = \frac{2A_c^{\,2}}{r} = \frac{2}{R}\left[\frac{3(1-\nu)rf}{8\mu}\right]^{2/3}, \tag{2.32}$$

therefore the normal contact stiffness becomes:

$$S_n = \frac{4\mu A_c}{1-\nu}. \tag{2.33}$$

If the force being applied to the packing is a result of hydrostatic pressure (p) then:

$$f = \frac{4\pi r^2 p}{C_o(1-\varphi)}, \tag{2.34}$$

the contact area then becomes:

$$A_c = r\left[\frac{3\pi(1-\nu)}{2C_o(1-\varphi)\mu}p\right]^{1/3}, \tag{2.35}$$

and the effective bulk modulus is given by:

$$\kappa = \left[\frac{C_o^{\,2}(1-\varphi)^2\mu^2}{18\pi^2(1-\nu)^2}p\right]^{1/3}. \tag{2.36}$$

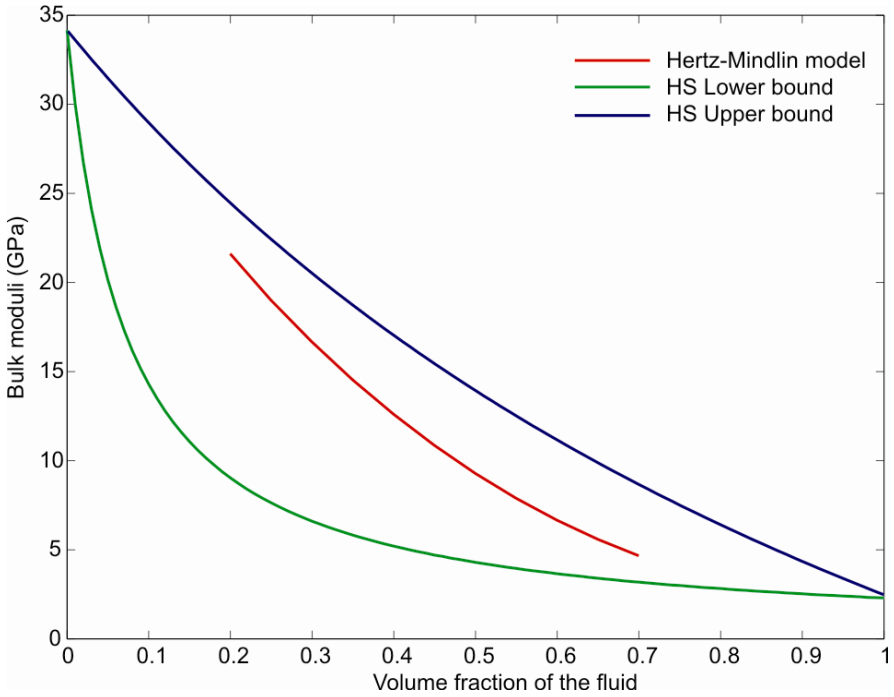

Figure 2.9 Comparison of the HS Upper and Lower bounds for bulk modulus and the Hertz-Mindlin contact model for a composite consisting on glass beads and brine. The Hertz-Mindlin model is calculated at atmospheric pressure. The coordination numbers used are those given in Mavko *et al.*, 1998. However the coordination numbers are only given for fluid volume fractions between 0.2 and 0.7 and hence the bulk modulus is only calculated between these volume fractions.

Mindlin model

Mindlin (1949) developed a model in which there is both compressional force and a tangential force applied to the spheres causing tangential displacement between the grains. The model assumes that there is no slip at the grain contacts and therefore the normal displacement and the normal contact stiffness remain the same as in the Hertz model (Equation 2.33). The tangential displacement (τ) is given by:

$$\tau = \frac{3\eta f(2-\nu)\left[1-\left(1-f_t/\eta f\right)^{2/3}\right]}{8\mu A_c}. \tag{2.37}$$

where η is the coefficient of friction. The shear stiffness is given by:

$$S_\tau = \frac{8A_c\mu}{1-\nu}. \tag{2.38}$$

The bulk modulus will remain the same as in the Hertz model (Equation 2.36) and the shear modulus becomes:

$$\mu_{eff} = \frac{5-4\nu}{5(2-\nu)}\left[\frac{3C_o{}^2(1-\varphi)^2\mu^2}{2\pi^2(1-\nu)^2}p\right]^{1/3}. \tag{2.39}$$

Both the Hertz and the Mindlin models can be used for granular sediment such as sands. Both models also assume that the strains applied to the grains are small and that the grains are isotropic, elastic and linear. The grains must always be spherical, the same size and composed of the same material. The medium cannot contain any pore fluids. Pore fluids may be added using Gassmann's equations (Section 2.2.9).

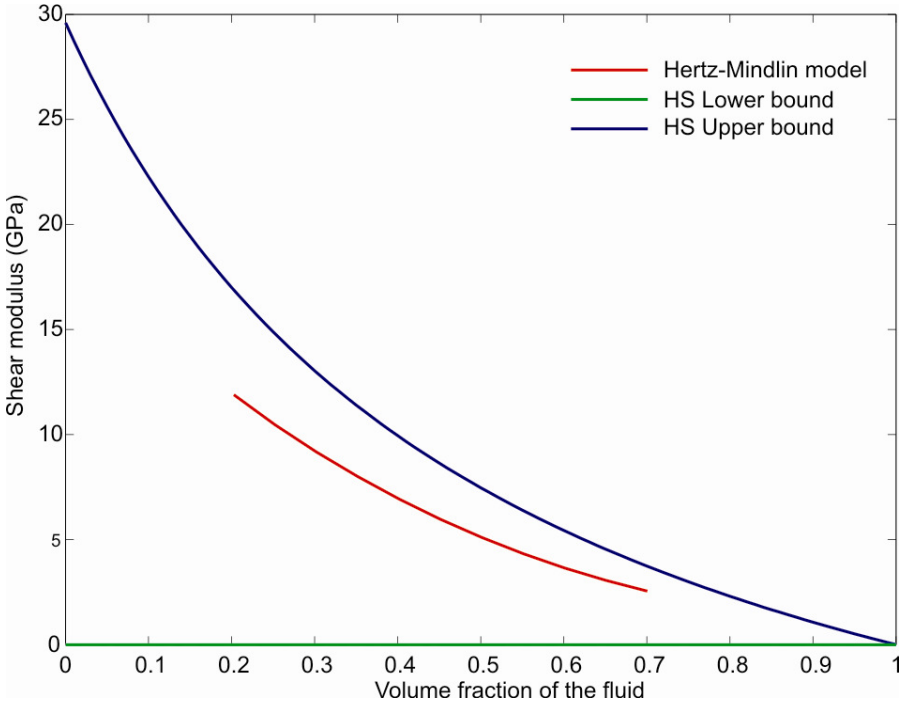

Figure 2.10. Comparison of the HS Upper and Lower bounds for shear modulus and the Hertz-Mindlin contact model a composite consisting on glass beads and brine. The Hertz-Mindlin model is calculated at atmospheric pressure. The coordination numbers used are those given in Mavko *et al.*, 1998. However the coordination numbers are only given for fluid volume fractions between 0.2 and 0.7 and hence the shear modulus is only calculated between these volume fractions.

2.2.9 Wave propagation theories

Wave propagation theories calculate the seismic P-wave and S-wave velocities of saturated porous rocks in terms of their dry rock properties. Velocities may be determined from any of the above methods using equations 2.1 and 2.2 and an effective density which is given by

$$\chi = \beta_1\chi_1 + \beta_2\chi_2 \qquad (2.40)$$

where β_1 and β_2 are the volume fraction of component 1 and 2 and χ_1 and χ_2 are the components densities respectively. In addition two further major theories of wave propagation are Gassmann's equation and Biot theory.

Gassmann's equation

Gassmann's (1951) equation predicts the seismic P- and S-wave velocity of a fluid saturated rock from that of a dry rock. If a porous rock is saturated with a fluid and a

seismic wave propagates through it then a pore pressure change is induced. This pore pressure change will resist the compression and act to stiffen the rock. Gassmann's (1951) equation predicts the resulting increase in effective bulk modulus, compared to a dry rock without pore fluid, as:

$$\kappa_G = \kappa_{dry} + \frac{\left(1 - \kappa_{dry} / \kappa_m\right)^2}{\frac{\varphi}{\kappa_f} + \frac{1-\varphi}{\kappa_m} - \frac{\kappa_{dry}}{\kappa_m^2}}, \tag{2.41}$$

where κ_G is the bulk modulus of the rock using Gassmann's equation, κ_{dry} is the bulk modulus of the dry rock frame, κ_f and κ_m are the bulk moduli of the fluid and the rock matrix respectively, and φ is the porosity of the rock. Since the shear modulus of a fluid is zero, the shear modulus of the rock is unaffected by fluid saturation and therefore;

$$\mu_G = \mu_{dry}, \tag{2.42}$$

where μ_G is Gassmann's shear modulus of the fluid saturated rock and μ_{dry} is the shear modulus of the dry rock.

Unfortunately Gassmann's equation cannot be used without prior knowledge of certain components. μ_{dry} and κ_{dry} must be known before any calculations can take place. They are often determined by measuring the seismic velocity through dry rock laboratory samples. If the rock matrix is composed of a single material then κ_m will simply be the bulk modulus of that material. However, if the matrix is composed of more than one material with different bulk moduli then κ_m will have to be calculated using other effective medium theories, or else it must be assumed. An error in the saturated velocity as calculated using Gassmann's equation is often caused by incorrect κ_m, κ_{dry}, μ_m, or μ_{dry} values. Uncertainties in these parameters limit the use of Gassmann's equation, but nevertheless it is still widely used for fluid substitution problems, particularly in the petroleum industry.

Gassmann's equation makes a number of assumptions (Wang & Nur, 1992; Mavko *et al.*, 1998);

- The porous rock is homogenous and isotropic.
- All of the minerals making up the rock frame must have the same shear modulus and bulk modulus. If the frame is made up of a variety of materials then an effective bulk modulus for the entire rock frame must be calculated before Gassmann's equation can be used.

- There can be no isolated pores; all the pore spaces must be interconnected. However unlike for HS bounds, the solid frame may be also interconnected.
- The pore spaces are filled with a frictionless fluid or gas (i.e. the viscosity of the saturating fluid is negligible).
- The pore spaces are fully saturated with fluid.
- The solid-fluid system is closed (undrained) and therefore the stress caused by a propagating seismic wave does not cause any significant flow of fluid through the rock. In laboratory experiments this means that the rock sample under investigation must be sealed so that no fluid flows out of the sample.
- The relative motion of fluid and rock is negligible when compared to the motion of the rock itself as the seismic wave propagates through it and therefore the seismic wave must have a long wavelength. If the seismic wavelength is too short, then relative motion of the solid frame and the fluid is large and the wave becomes dispersive. Ultrasonic laboratory measurements on samples (i.e., using short wavelengths) will be poorly predicted from Gassmann's equation.
- The pore fluid does not interact with the solid in such a way as to change the shear rigidity of the frame and therefore there is no chemical or physical interaction between the frame and the pore fluids. In real rocks, fluid usually does interact with the matrix and change the surface energy of the solid frame causing it to harden or soften.

Biot theory

Whereas Gassmann's equation is only valid for low frequency seismic waves Biot (1956, 1962) developed a series of wave equations which are valid at all frequencies. As for Gassmann's equation, Biot's equations relate the seismic velocity of a dry rock to the seismic velocity of a fully saturated rock. As wave frequency approaches zero, Biot's equation reduces to Gassmann's equation. As the frequency approaches infinity, V_p and V_s are given by:

$$V_{p\infty}(fast, slow) = \left\{ \frac{\Delta \pm \left[\Delta^2 - 4\left(\chi_{11}\chi_{22} - \chi_{12}{}^2\right)\left(IJ - K^2\right)\right]^{1/2}}{2\left(\chi_{11}\chi_{22} - \chi_{12}{}^2\right)} \right\}^{1/2}, \qquad (2.43)$$

$$V_s = \left(\frac{\mu_{dry}}{\chi - \varphi \chi_f t^{-1}} \right)^{1/2}, \tag{2.44}$$

where:

$$\Delta = I\chi_{22} + J\chi_{11} - 2K\chi_{12}, \tag{2.45}$$

$$I = \frac{(1-\varphi)\left(1-\varphi-\kappa_{dry}/\kappa_s\right)\kappa_s + \left(\frac{\varphi\kappa_s\kappa_{dry}}{\kappa_f}\right)}{1-\varphi-\kappa_{dry}/\kappa_s + \varphi\kappa_s/\kappa_f} + \frac{4}{3}\mu_f, \tag{2.46}$$

$$K = \frac{\left(1-\varphi-\frac{\kappa_{dry}}{\kappa_s}\right)\varphi\kappa_s}{1-\varphi-\frac{\kappa_{dry}}{\kappa_s}+\frac{\varphi\kappa_s}{\kappa_f}}, \tag{2.47}$$

$$J = \frac{\varphi^2\kappa_s}{1-\varphi-\frac{\kappa_{dry}}{\kappa_s}+\frac{\varphi\kappa_s}{\kappa_f}}, \tag{2.48}$$

$$\chi_{11} = (1-\varphi)\chi_s - (1-t)\varphi\chi_f, \tag{2.49}$$

$$\chi_{22} = t\varphi\chi_f, \tag{2.50}$$

$$\chi_{12} = (1-t)\varphi\chi_f, \tag{2.51}$$

$$\chi = \chi_s(1-\varphi) + \chi_f\varphi, \tag{2.52}$$

where κ_{dry} and μ_{dry} are the effective bulk modulus and shear modulus respectively of the dry rock frame, κ_s is the bulk modulus of the mineral making the rock frame, κ_f is the effective bulk modulus of the pore fluids. χ_s and χ_f are the mineral and fluid densities. χ_{12} is the induced mass resulting from the inertial drag caused by the relative motion of the solid frame to the pore fluid, t is the tortuosity parameter which is always greater than one and is a purely geometric factor. For pores shaped like parallel cylindrical tubes, t equals 1 (the minimum value). For sandstones t lies between 2 and 3 (Wang and Nur, 1990).

The two solutions given by the Equation 2.43 for the P-wave velocity correspond to the 'fast' and 'slow' P-waves. The fast P-wave is the compressional body wave which is the most easily observed in the laboratory and field experiments. The slow P-wave is a highly dissipative wave where the solid and fluid motions are out of phase (Wang & Nur, 1992).

There are a number of assumption and limitations for using Biot's equations, some of which are the same as Gassmann's equation (Wang & Nur, 1992; Mavko *et al.*, 1998):

- The rock is macroscopically homogeneous and isotropic.
- The minerals forming the frame all have the same shear and bulk modulus.
- The rock is fully saturated.
- All of the pores are interconnected and have a fairly uniform size and distribution.
- The wave length of the seismic wave passing through the medium, even in the high frequency limit, is appreciably larger than the grains making up the rock frame.
- There is relative motion between the rock matrix and pore fluids but it follows Darcy's law for flow. Darcy (1856) experimentally showed that the fluid flow rate is linearly related to the pressure gradient in a fluid saturated porous medium and is represented by:

$$\xi = -\frac{k}{v}\frac{\partial p}{\partial x}, \tag{2.53}$$

  where ξ is the fluid flow rate in the x direction, k is the permeability of the medium, v is the viscosity of the fluid and p is the pressure.
- Thermal effects due to dissipation of energy during wave propagation are neglected.
- The pore fluid does not chemically interact with the rock matrix causing softening or hardening of the rock frame.

2.3 Seismic methods of hydrate quantification

The previous section described a number of methods of relating the physical properties of the individual constituents of a medium to its effective seismic properties. These are important when trying to analyze field and laboratory data. Such methods either allow the porosity to be determined, or constrain the constituents making up the sediments, depending on the data available. Most of the methods assume that there are two components making up the medium. Adding hydrate into such systems adds a third phase. A number of the methods have been adapted to predict the physical properties of hydrate bearing sediments. Descriptions of the most widely used effective medium methods for quantifying hydrate in sediments (Chand *et al.,* 2004) are given below.

2.3.1 Empirical Weighted Equation (EWE)

The Empirical Weighted Equation was developed by Lee *et al.* (1996) and uses a combination of Wyllie's (1958) time average equation and Wood's (1941) weighted equation. Wyllie's time average equation (Section 2.2.4), originally developed for two-phase media, was extended to three-phases by Timur (1968) and Pearson *et al.* (1983). The three-phase time average equation is given by Pearson *et al.*, 1983 as:

$$\frac{1}{V_{p1}} = \frac{\varphi(1-S_h)}{V_{p.f}} + \frac{\varphi S_h}{V_{p.h}} + \frac{(1-\varphi)}{V_{p.m}}. \qquad (2.54)$$

where V_{p1} is the P-wave velocity of final effective medium of the 3-phase composite. S_h is the hydrate saturation, $V_{p.h}$, $V_{p.f}$ and $V_{p.m}$ are the P-wave velocity of hydrate, pore fluid and matrix respectively.

The Wood equation (section 2.2.2) was extended to three phases by Nobes *et al.* (1983) where P-wave velocity (V_{p2}) is given as:

$$\frac{1}{\chi V_{p2}} = \frac{\varphi(1-S_h)}{\chi_f V_{p.f}^2} + \frac{\varphi S_h}{\chi_h V_{p.h}^2} + \frac{(1-\varphi)}{\chi_m V_{p.m}^2}. \qquad (2.55)$$

where χ_f, χ_h and χ_m are the densities of the pore fluid, hydrate and matrix respectively. Lee *et al.* (1996) mix the two methods (Equation 2.54 and 2.55) using a weighting factor (W) and a lithification rate (ψ) to give:

$$\frac{1}{V_p} = \frac{W\varphi(1-S_h)^{\psi}}{V_{p2}} + \frac{1-W\varphi(1-S_h)^{\psi}}{V_{p1}}. \qquad (2.56)$$

When $W>>1$ the calculated P-wave velocity tends towards Wood's solution; when $W<<1$ the calculated P-wave velocity tends towards Wyllie's solution. Both W and ψ have no physical meaning and Lee *et al.* (1996) determined the values by fitting Equation 2.56 to velocity and porosity log data for non-hydrate bearing sediments. W and ψ can be adjusted to fit any data set. Unfortunately this means that the weighted equation can only be used if all the sediment under investigation is of a similar type. If the lithology varies a lot the Empirical Weighed Equation will give poor results.

Lee *et al.,* (1996) determined the S-wave velocity by assuming that the P- to S-wave velocity ratio of the hydrate-bearing sediment is proportional to the weighted average of the P- to S-wave velocity ratio of the constituent components of the sediments. This is given as;

$$V_s = V_p\left(r_m(1-\varphi) + r_h\varphi S_h + r_f\varphi(1-S_h)\right) \qquad (2.57)$$

Where r_m, r_h and r_f are the S-wave to P-wave velocity ratios of the matrix, hydrate and fluid respectively. Because a fluid cannot transmit a shear wave the $r_f \varphi(1-S)$ term can be dropped.

2.3.2 Three-Phase Effective Medium Theory (TPEM)

The Three-phase effective medium theory (TPEM) was developed by Ecker *et al.* (1998) and is based on the contact models (Section 2.2.8). TPEM comes in two forms: the first method is non-cementing, with the hydrate located either in the pore spaces or on the grains away from the grain contacts (Figure 2.11). In the second method, the cementation model, the hydrate forms on the grains causing the frame to stiffen (Figure 2.12). The TPEM methods presented below were developed by Dvorkin *et al.,* (1994; 1999; 2000) and Dvorkin & Nur (1996).

Three Phase Contact Model

The bulk and shear modulus of the dry frame is calculated using the Hertz and Mindlin equations for contact theory (Section 2.2.8) for a critical porosity (φ_c). The critical porosity has been determined to be approximately 0.36-0.4 (Nur *et al.,* 1998), representing the point at which a composite of spheres and fluid becomes grain supported and ceases to be a suspension. An adapted lower HS bound is then used to calculate the shear modulus and bulk modulus at all porosities below the critical porosity:

$$\kappa_{dry} = \left[\frac{\varphi/\varphi_c}{\kappa_{HM} + \frac{4}{3}\mu_{HM}} + \frac{1-\varphi/\varphi_c}{\kappa_m + \frac{4}{3}\mu_{HM}} \right]^{-1} - \frac{4}{3}\mu_{HM}, \tag{2.58}$$

$$\mu_{dry} = \left[\frac{\varphi/\varphi_c}{\mu_{HM} + Z} + \frac{1-\varphi/\varphi_c}{\mu_m + Z} \right]^{-1} - Z, \tag{2.59}$$

Where,

$$Z = \frac{\mu_{HM}}{6}\left(\frac{9\kappa_{HM} + 8\mu_{HM}}{\kappa_{HM} + 2\mu_{HM}} \right). \tag{2.60}$$

For porosities above the critical porosity the HS upper bound is used (Dvorkin & Nur, 1996).

$$\kappa_{dry} = \left[\frac{(1-\varphi)/(1-\varphi_c)}{\kappa_{HM} + \frac{4}{3}\mu_{HM}} + \frac{(\varphi-\varphi_c)/(1-\varphi_c)}{\frac{4}{3}\mu_{HM}} \right]^{-1} - \frac{4}{3}\mu_{HM}, \qquad (2.61)$$

$$\mu_{dry} = \left[\frac{(1-\varphi)/(1-\varphi_c)}{\mu_{HM} + Z} + \frac{(\varphi-\varphi_c)/(1-\varphi_c)}{Z} \right]^{-1} - Z. \qquad (2.62)$$

Where κ_{HM} and μ_{HM} are the bulk and shear moduli calculated from the Hertz and Mindlin contact method. κ_m and μ_m are the bulk and shear moduli respectively of the minerals that form the dry frame, and are calculated from Hill's (1952) average. The dry frame is then saturated with fluid using the Gassmann's equation to given the final sediment fluid medium. The hydrate may form either as part of the frame or as part of the fluid, with only the bulk modulus being affected (Figure 2.11).

If hydrate forms on the grains of the sediment but does not cement the grains then it can be treated as an extra mineral in the frame. The bulk and shear moduli of the frame can be calculated using Hill's equation (Equation 2.5) including the extra mineral.

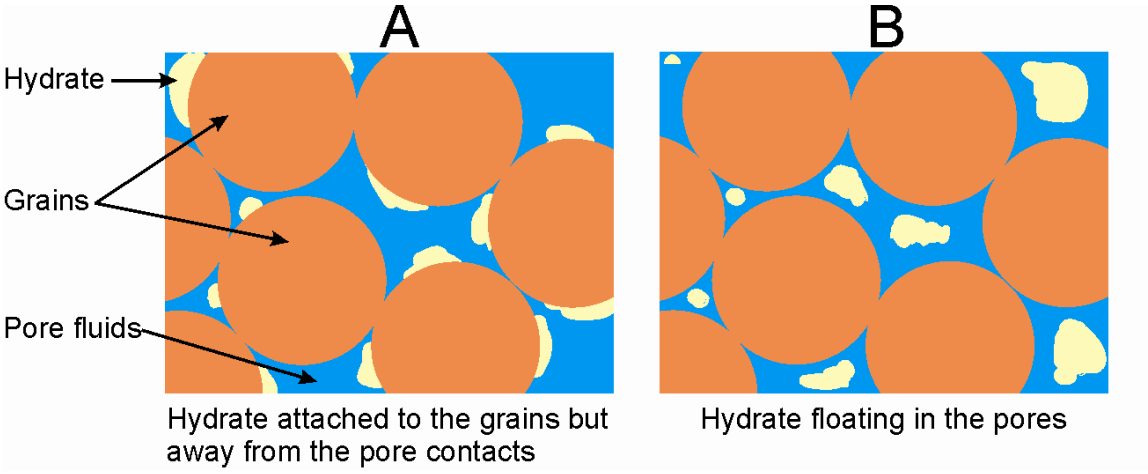

Figure 2.11 Schematic diagram showing where the hydrate forms within the sediment structure using the TPEM contact method. (A) Hydrate forming on the grains away from the pore contacts. (B) Hydrate forming in the pore fluid.

If hydrate forms part of the pore fluid then only the moduli of the fluid are affected and not the moduli of the frame. The hydrate is assumed to be homogeneously distributed through the pore space. Reuss (1929) defines the effective bulk modulus of the fluid hydrate mix ($\bar{\kappa}_f$) to be:

$$\bar{\kappa}_f = \left[\frac{S_h}{\kappa_h} + \frac{1-S_h}{\kappa_f} \right]. \qquad (2.63)$$

$\bar{\kappa}_f$ is then used instead of the bulk moduli of the pore fluid to saturate the dry frame. The shear modulus is not affected by the hydrate phase because the Reuss Equation always predicts a value of zero for a mixture of fluid and solid. The model is only appropriate for a medium where hydrate does not fill the whole of the pore space, i.e. $S_h < 1$ (Dvorkin *et al.*, 2000). This model in theory applies even if there is only a very thin film of liquid around the grains.

Contact cementation model

If hydrate forms a cement between the grains it will stiffen the frame. Theoretically hydrate may form either at the contacts of the grains or it may envelop the grains (Figure 2.12). The shape of the remaining pore space is dependent on how the hydrate forms.

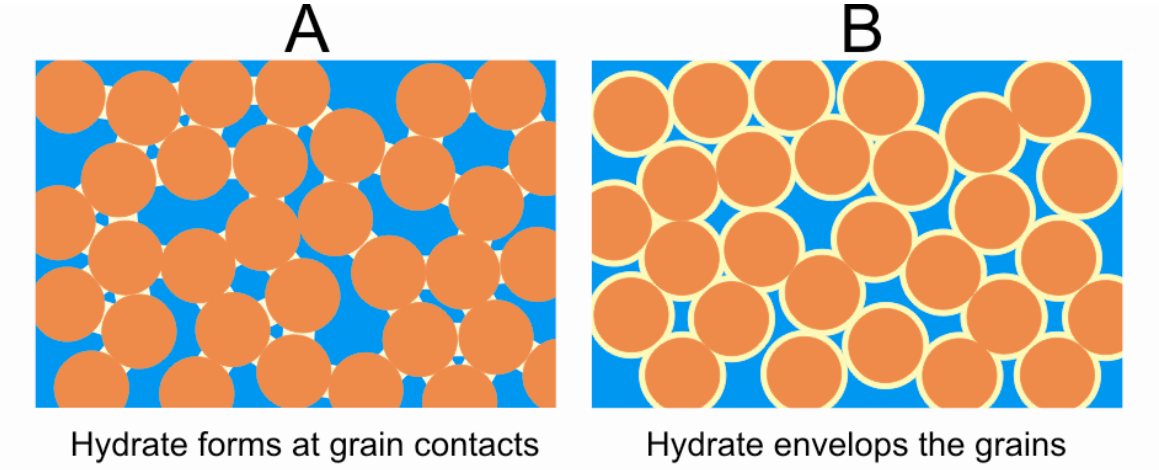

Figure 2.12 Two methods of cementing sediment grains (orange) with hydrate (yellow). (A) Hydrate forms at the grain contacts only. (B) Hydrate forms as a shell around the grains.

Dvorkin *et al.* (1994) and Dvorkin & Nur (1996) calculate the dry frame bulk modulus (κ_{cc}) and shear modulus (μ_{cc}) respectively by:

$$\kappa_{cc} = \frac{C_o(1-\varphi_c)}{6}\left(\kappa_c + \tfrac{4}{3}\kappa_h\right)S_n, \qquad (2.64)$$

$$\mu_{cc} = \frac{3}{5}\kappa_{cc} + \frac{3C_o(1-\varphi_c)}{20}\mu_h S_\tau. \qquad (2.65)$$

S_n and S_τ are solutions to integral equations and approximate solutions are given by Dvorkin & Nur (1996). S_n and S_τ are both dependent on the cement distribution parameter (γ). γ takes different forms depending on where on the grains the hydrate forms. For hydrate forming just at the grain contacts:

$$\gamma = 2\left[\frac{\varphi_c - \varphi}{3C_o(1-\varphi_c)}\right]^{1/4}. \quad (2.66)$$

If hydrate forms by enveloping the grains:

$$\gamma = \left[\frac{2(\varphi_c - \varphi)}{3(1-\varphi_c)}\right]^{1/2}. \quad (2.67)$$

In most studies of hydrate, the hydrate is not believed to form cement, but forms in the pore space, especially at low saturation. If the hydrate forms as part of the pore fluids the shear modulus is not affected. However in nature hydrate bearing sediments do show a relative increase in S-wave velocity. Also this method assumes that the grains are spheres. No anisotropic response can be modelled using this contact method. While an isotropic assumption may be acceptable for sand, it cannot always be used for clay rich sediments. However there have been a number of studies where the TPEM has been used for clay rich, high porosity sediments (Chand *et al*., 2004; Petersen *et al*., 2007; LeBlanc *et al*., 2007; Sultan *et al*., 2007). In most studies a coordination number of 9 is used which is the original value given by Helgerud *et al*. (1999) for spherical grains. However this value should be used with care because the coordination number can vary from 8 to 12 and is very dependent on the clay content of the sediments (Marion *et al.*, 1992; Blangy *et al.,* 1993) and the sediment porosity (Mavko *et al.*, 1998). Helgerud *et al.* (1999) determined the bulk and shear moduli of the grains from retrieved sediments cores. Where there is a mixture of mineral constituents Hill's (1952) average is used to determine a single value.

2.3.3 Three Phase Biot theory (TPB)

Three phase Biot theory (TPB) considers the existence of two solid phases and one fluid phase in the medium, as opposed to the 2-phase medium with one solid and one fluid phase. The method was developed by Carcione & Tinivella (2000) and Gei & Carcione (2003) based on theory for frozen porous media (Leclaire *et al.,* 1994). The generalized form of calculating the effective medium assumes that the medium is composed of two frames, a solid mineral frame and a hydrate frame, plus the fluid phase (Carcione *et al.,* 2005):

$$\mu_G = \mu_{sf} + \mu_{hf}\,, \quad (2.68)$$

$$\kappa_G = \kappa_{sf} + \kappa_{hf} + \left(1 - \frac{\kappa_{sf}}{\kappa_s} - \frac{\kappa_{sf}}{\kappa_h}\right)^2 M \,, \tag{2.69}$$

$$M = \left[\left(\beta_s - \frac{\kappa_{sf}}{\kappa_s}\right)\frac{1}{\kappa_s} + \frac{\beta_w}{\kappa_w} + \left(\beta_h \frac{\kappa_{hf}}{\kappa_h}\right)\frac{1}{\kappa_h}\right]^{-1}, \tag{2.70}$$

where subscripts *sf* and *hf* denote the solid frame and the hydrate frame respectively, *s*, *h* and *w* denote the solid, hydrate and pore fluid, and *G* denotes the final effective medium calculated using Gassmann's equation.

The Biot-type three phase theory has been used to determined the hydrate saturations in sediments on continental margins of NW Svalbard and the Storegga region of Norway (Carcione *et al.,* 2005; Westbrook *et al*., submitted). The bulk and shear rock frame and hydrate frame moduli (κ_{sf}, μ_{sf}, κ_{hf} and μ_{hf}) need to be determined before the TPB model can be applied to the moduli. Carcione *et al.* (2005) determines these moduli using a sonic log profile at full water saturation and the Kuster and Toksöz (1974) effective medium model. The frame moduli were calibrated using the mineral content of the sediment sampled with piston cores and drilled on ODP site 986 (Carcione *et al.,* 2005; Westbrook *et al.,* submitted). Poisson's ratio, also required to determine μ_{sf} , was estimated using ray-tracing travel time.

2.3.4 Combined SCA/DEM theory

The combined SCA/DEM method was developed by Jakobsen *et al.* (2000) using the method of Sheng (1990) and Hornby *et al.* (1994) extended for hydrate-bearing sediments. This method involves calculating the effective medium composed of two materials at a critical porosity. The critical porosity is defined as the point at which the effective medium is said to be bi-connected. Jakobsen *et al.,* (2000), Sheng (1990) and Hornby *et al.,* (1994) all used a value of 50% porosity as the critical porosity. The DEM is then used to add or remove porosity from the system to the desired porosity. The DEM method preserves the microstructure of the material so that the final medium will be bi-connected at all porosities. In the approach of Jakobsen *et al.* (2000) hydrate is added in one of two ways. It is either added into the pore fluid using the DEM method, or the starting material is composed of both hydrate and grain into which pore fluids are added (Figure 2.13). The choice of method allows hydrate to be either load bearing or not. If the hydrate is load bearing then the calculated bulk and shear moduli will be higher than if it

exists in the pore spaces. A possible problem with the load bearing model is that the hydrate becomes completely cementing at low hydrate saturations. Laboratory studies show that completely cementing hydrate is not valid at all hydrate saturations (Tohidi *et al*., 2001; Waite *et al.,* 2004). Chand *et al.* (2006) attempted to solve this by creating a model where hydrate forms as part of the pore space and as cement. This approach starts by determining the bulk and shear moduli of an effective medium without hydrate using the SCA method for an adjusted porosity. The load bearing hydrate is added using the DEM model by replacing the part of the matrix. The non-load-bearing hydrate is then added, also using the DEM model, by replacing the part of the pore fluids. This allows the hydrate to simulate partial cementation at low hydrate saturations. A more in-depth look at the SCA/DEM model will be given in Chapter 3.

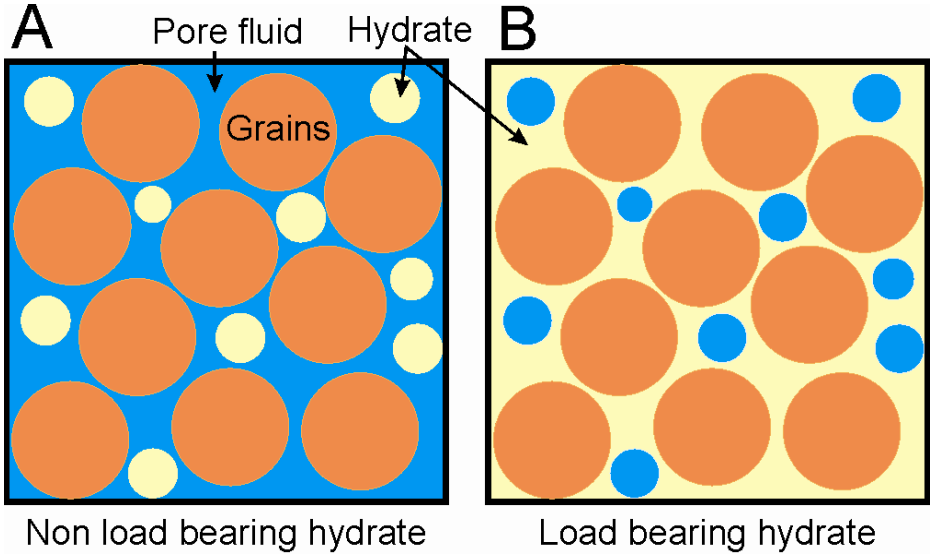

Figure 2.13 Schematic diagram of a 3-phase medium in which the hydrate is (A) non-load bearing and (B) load bearing as modelled by the combined SCA/DEM model. It should be noted that the grains in this figure should also be interconnected as well as the pore fluid in the non-load bearing diagram and the hydrate in the load bearing diagram. However it is difficult to represent a three-dimensional bi-connected medium with a two-dimensional diagram.

The SCA/DEM method was also adapted by Jakobsen *et al.* (2000) to model anisotropic effects of clay platelets as inclusions. The SCA/DEM was reformulated so that it can produce a fully anisotropic effective medium by aligning the inclusions. From this, an isotropic medium can be calculated by considering that the final effective medium is composed of blocks of the anisotropic material. Each of the blocks is then orientated so

that the overall bulk and shear moduli are isotropic. This method also allows partial alignment of the blocks to produce a more weakly anisotropic medium if required.

Variables in the SCA/DEM model that need to be determined before the method can be applied to geophysical data include aspect ratio, sediment clast composition, bulk and shear moduli of the grains and the critical porosity. The aspect ratio can be determined from the clay content of the sediments (Chand *et al*., 2006). The sediment clast composition is usually determined from sediment cores (Chand *et al*., 2004, 2006; Jakobsen *et al*., 2000). An advantage of the SCA/DEM method is that more than one mineral can be added into the effective medium. Therefore a single bulk and shear modulus value does not have to be determined from the mixture of minerals, each of which have their own moduli values. The critical porosity is often given as 0.5 (Sheng 1990, 1991; Hornby *et al.,* 1994; Jakosben *et al.,* 2000) however other values have been used (Chand *et al*., 2006).

Section 2.2 has introduced various effective medium approaches to calculate the effective bulk and shear modulus of a multi component medium. A discussion of the best method to use for a joint electrical and seismic method is given at the end of the chapter in Section 2.5.

2.4 Electrical Effective Medium Theories

Having reviewed elastic effective medium models in the preceding section, effective medium models for the electrical properties of multi-phase materials shall now review be reviewed.

2.4.1 Archie's equations

Archie's (1942) equation is currently the most widely used method of electrical resistivity interpretation. Archie (1942) showed experimentally that the resistivity of clean sandstone is proportional to the resistivity of the brine saturating the sandstone. The proportionality constant is known as the formation factor (F) and defined as:

$$F = \frac{\sigma_f}{\sigma_o} = \frac{\rho_o}{\rho_f}, \tag{2.71}$$

where σ_f is conductivity of the pore fluid, σ_o is the conductivity of the medium when it is fully saturated with the conducting fluid, and ρ_f and ρ_o are the resistivities of the fluid and the fully saturated medium respectively. F depends only on the properties of the solid material framework and not on the constituents of the pore spaces.

Archie (1942) relates the formation factor of a saturated sandstone to its porosity using an empirical relationship:

$$F = t\varphi^{-m}, \tag{2.72}$$

where m and t are empirical constants. t represents the tortuosity factor of the system, m is the cementation exponent, and φ is the porosity. Tortuosity generally takes a value in the range 0.6-1. The cementation exponent can vary between 1.3 and 2.5 for most sedimentary rocks and is determined by the type and degree of cementation holding the rocks together. For sandstones, m generally has a value between 1.8 and 2 (Archie 1942) but for artificial and natural unconsolidated sands or glass beads m ranges between 1.25 and 1.3 (Archie, 1942; Wyllie *et al.,* 1953; Atkins *et al.,* 1961; Jackson *et al.,* 1978). Equations 2.71 and 2.72 can be combined to give:

$$\rho_o = F\rho_f = t\varphi^{-m}\rho_f \tag{2.73}$$

Archie's Equation has been further extended for application in the hydrocarbon industry, for the case when the pore spaces are not fully saturated with a conductive aqueous fluid:

$$\rho_B = \frac{1}{S_f{}^n}\rho_o = \frac{1}{S_f{}^n}F\rho_f = t\varphi^{-m}S_f{}^{-n}\rho_f \tag{2.74}$$

where S_f is the saturation of the pore spaces with the conductive fluid, ρ_B is the effective resistivity of the medium and n is the saturation exponent. This method assumes that the remainder of the pore space is filled with a more resistive phase (e.g. oil or gas). n is a measure of how the resistive phase in the pore space effects the resistivity of the conductive pore fluids.

While Archie's law is a powerful method of interpretation, it can be forced to fit most data sets by altering the empirical constants. Figure 2.14 shows the wide range of resistivities that Archie's formula can calculate just by varying the cementation exponent.

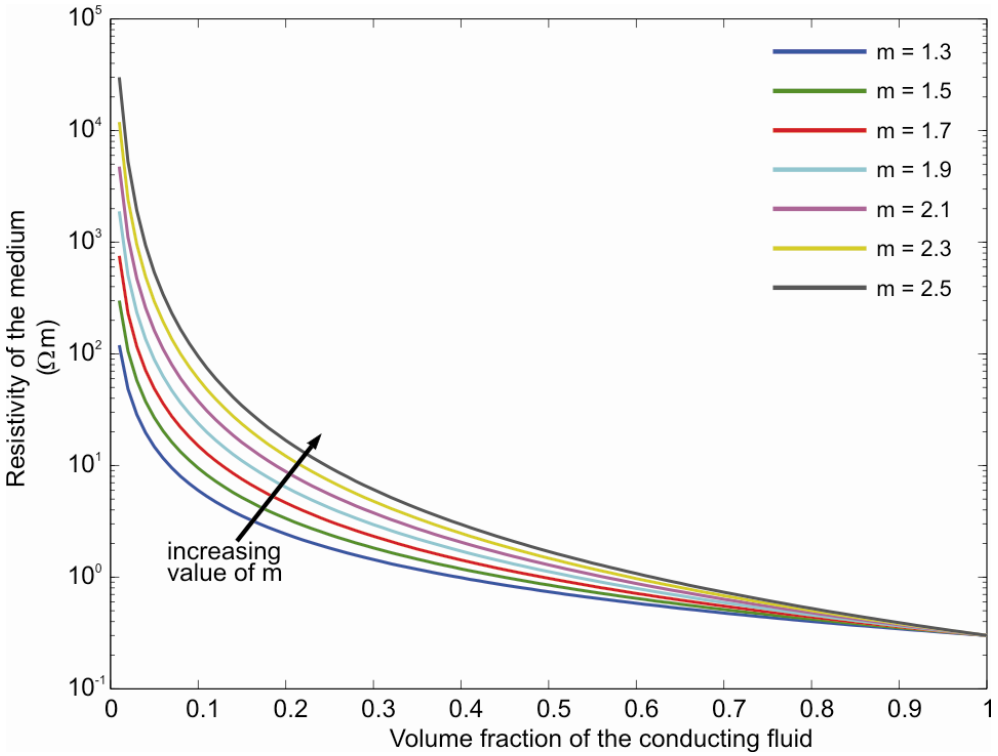

Figure 2.14 Resistivity of a fully saturated fluid solid mixture calculated using Archie's law for a series of models where *t* is equal to 1 and the resistivity of the fluid is 0.3 Ωm and m ranges from 1.3 to 2.5.

2.4.2 Clay models

There have been several attempts to determine the effective resistivity of sediments which contain a significant clay fraction. Archie's (1942) equation is generally limited to clean sands where the grains forming the matrix are highly resistive. Clay minerals are phyllosilicates and can exhibit a net negative charge over the grain surfaces. This negative change attracts cations towards the surface of the clay grain causing a double–layer conductance (Figure 2.15; Bassiouni, 1994). Clay grains have a huge surface are a compared to their volume, causing the double–layer conductance to have a large influence on the effective resistivity of the sediment. Bussian (1983) reviews 3 methods and also presents a method in which both the pore fluids and the grain matrix contribute to the total conductivity of the sediment.

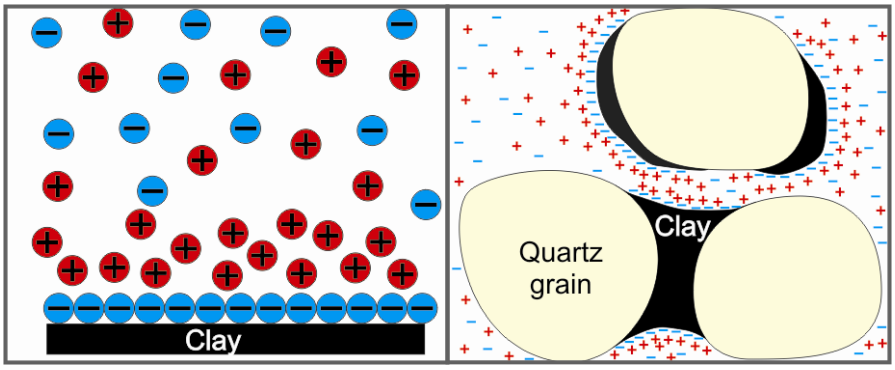

Figure 2.15 Schematic of electric double layer model (left) and charge distribution in shaly sand (right; modified from Bassiouni, 1994)

The three-resistor model

The three-resistor model was proposed by Wyllie and Southwick (1954). The model is based on assuming that the final effective resistivity can be represented by three elements in series (Figure 2.16). These are (1) the resistivity of the grains, (2) the resistivity of the pore fluids (3) the resistivity or the grain and the fluid in series with each other. This can be given mathematically as:

$$\frac{1}{\rho_o} = \frac{1}{X\rho_r} + \frac{1}{Y\rho_f} + \frac{1}{W\rho_f + Z\rho_r} \tag{2.75}$$

where W,X,Y,Z are geometrical factors, ρ_o is the final effective resistivity, ρ_f is the resistivity of the fluid and ρ_r is the resistivity associated with the rock matrix.

The Waxman and Smits model

The Waxman and Smits (1968) model (Figure 2.16) is based on 3 assumptions. (1) The electrical resistance of a shaly sand can be represented by two resistive elements in series. The first element represents the pore fluid conductivity and the 2nd the conductivity associated with the matrix. This can be given as:

$$\frac{1}{\rho_o} = \frac{X}{\rho_r} + \frac{Y}{\rho_f} \tag{2.76}$$

ρ_r is determined from:

$$\rho_r = \Lambda_+ Q_v \tag{3.77}$$

where Λ_+ is equivalent cation conductance and Q_v is the concentration of cations. (2) The current path through the pore fluid is the same as though the cation exchange ions and therefore $X=Y$. It follows that the two conduction mechanisms must use the same water

(Bussian, 1983). (3) The conductivity attributed to the matrix is dependent on the conductivity of the pore fluids. Equation 2.76 can therefore be written as:

$$\frac{1}{\rho_o} = \left(\frac{1}{\rho_g} + \frac{1}{\rho_f} \right) \varphi^{-m} \tag{2.78}$$

From analysis of shaly sands Waxman and Smits (1968) found that, as in Archie's equation:

$$\varphi^{-m} = F = \frac{\rho_o}{\rho_f} \tag{2.79}$$

where F is the formation factor of the sediment.

The dual water model

The dual water model was proposed by Clavier *et al.* (1984) and is similar to the Waxman and Smits (1968) model. In the dual water model Clavier *et al.* (1984) assumes that there are two kinds of water. The first of the two waters components is the clay water. Its resistance is controlled by the cation exchange ions and is centred near the clay surface. This clay water is spatially separated from the second water type, the main pore waters, and therefore $X \neq Y$ (Figure 2.16).

Bussian model

The Bussian (1983) model for shales is based on the work of Bruggeman (1935) and Hanai (1960, 1961). The Bruggeman-Hanai model assumes that the effective medium is composed of one component immersed in another. In this model both of the components have some conductance, i.e. the matrix does not have infinite resistivity as is assumed by Archie's equation. Bussian developed the model by including a conducting lattice like matrix immersed in the fluid to represent the interconnection of the clays (Figure 2.16). Similar to the dual water method, Bussian assumes that there are two kinds of water present. However unlike the dual water method, the current path may pass through both kinds of water. For the low frequency case Bussian (1983) gives the effective resistance as:

$$\frac{1}{\rho_o} = \sigma_o = \sigma_f \varphi^m \left(\frac{1 - \sigma_r / \sigma_f}{1 - \sigma_r / \sigma_o} \right) \tag{2.80}$$

where m is the cementation factor and is empirically determined from core samples. σ_o is the effective conductivity or the formation, σ_f is the conductivity of the fluid and σ_r is the conductivity of the rock matrix.

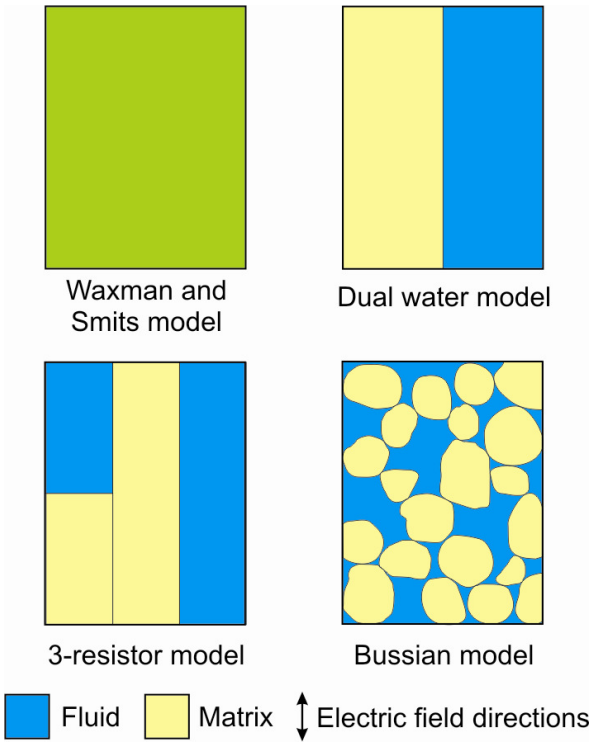

Figure 2.16 Geometrical schematics of clay electrical effective medium models (redrawn from Bussian 1983).

Berg (1995) model

Berg (1995) also used the Bruggeman-Hanai model to determine the water saturation (S_f) of hydrocarbon bearing shale sediments. The Bruggeman-Hanai equation at low frequency is given as:

$$\varphi = \left(\frac{\sigma_f}{\sigma_o}\right)^{\frac{m-1}{m}} \left(\frac{\sigma_o - \sigma_r}{\sigma_f - \sigma_r}\right). \tag{2.81}$$

To develop Bruggeman-Hanai equation to three phases Berg (1995) makes two principal assumptions: (1) the sediments are water wet. Therefore the hydrocarbon can be treated as part of the matrix and is dispersed through the continuous pore fluid phase. (2) The hydrocarbon has no conductivity. To determine the conductivity of the grain matrix with the hydrocarbon Berg (1995) treats them as resistors in parallel and the final matrix conductivity (σ_d) is given as:

$$\sigma_d = \frac{\sigma_r(1-\varphi)+\sigma_h(\varphi-\varphi S_f)}{(1-\varphi S_f)} \tag{2.82}$$

where σ_h is the conductivity of the hydrocarbon. To include hydrocarbon in the matrix the Bruggeman-Hanai equation changes to:

$$S_f\varphi = \left(\frac{\sigma_f}{\sigma_o}\right)^{\frac{m-1}{m}}\left(\frac{\sigma_o-\sigma_d}{\sigma_f-\sigma_d}\right). \tag{2.83}$$

Figure 2.17 shows the change in resistivity with porosity and hydrocarbon saturation of an effective medium using the Berg (1995) method. It shows the resistivity increases with increasing hydrocarbon saturation and decreasing porosity. This trend reverses at very high hydrocarbon saturations because the hydrocarbon has infinite resistivity and the grain matrix does not.

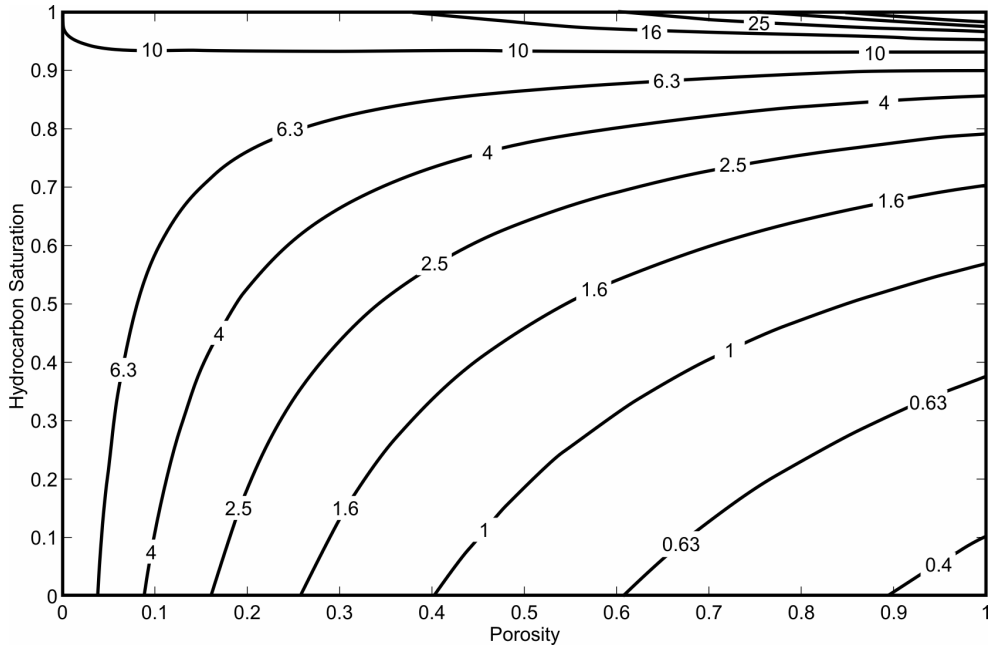

Figure 2.17 Change in resistivity with hydrocarbon saturation and porosity using the Berg (1995) model where m = 1.25, ρ_f =0.35 (Ωm) and ρ_r = 10 (Ωm).

2.4.3 Electrical methods of hydrate quantification

Archie's law has long been successfully used for analysing the resistivity of sediments including those bearing hydrocarbons. For this reason Archie's law has become the primary method of determining hydrate saturation from resistivity. The effect of the

hydrate is generally modelled as a reduction in the porosity and therefore hydrate saturation is related to the bulk resistivity (Hyndman *et al.,* 1999) by:

$$\rho_E = t\rho_f \left[(1 - S_h)\varphi\right]^{-m}, \tag{2.84}$$

where ρ_E is the resistivity of the whole medium and S_h is the hydrate saturation on the pore spaces. This is basically the extended Archie's Equation (Equation 2.74) rewritten with the n exponent set to 1. An example of the application of this is given in Figure 2.18.

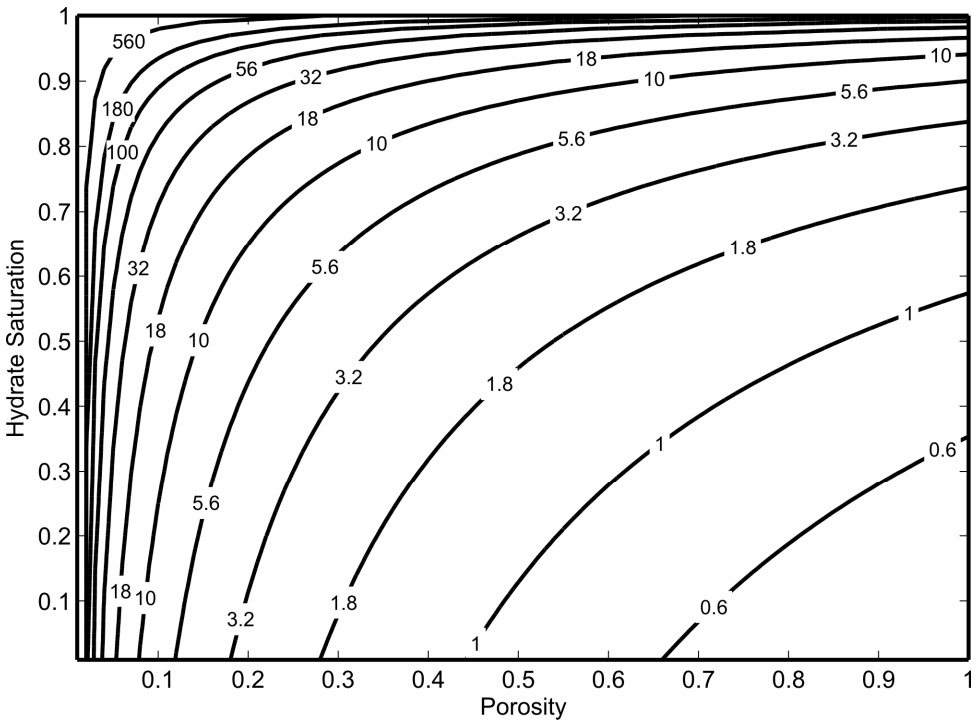

Figure 2.18 Change in resistivity (Ωm) with hydrate saturation and porosity calculated using Equation 2.75 and where m=1.25, t=1 and ρ_f=0.35 Ωm.

Paull *et al*. (1996), Collett (1998) and Collett & Ladd (2000) include the extra empirical factor n, to describe the effect of the different growth habits of hydrate on the sediments. The bulk resistivity of a hydrate bearing sediment is given as:

$$\rho_E = t\rho_f \varphi^{-m} (1 - S_h)^{-n}. \tag{2.85}$$

If n is large the hydrate obstructs the electrical current to a high degree. The hydrate is most likely forming at the grain contacts and causing the pore throats to be blocked. If the value of n is small the effect of the hydrate is low and it is probably forming in the pore spaces.

To be able to apply this method to laboratory or field data three components must be known: effective resistivity, porosity and pore fluid resistivity. The effective resistivity and the porosity of the sediment are usually obtained from down-hole logs. The resistivity of the pore fluid is more problematic to obtain, but it is very important because most of the electrical current will pass through the fluid and therefore the overall resistivity of the sediment will depend strongly on the resistivity of the fluid. Pore fluid resistivity is often derived from the salinity of the pore waters of cores. Fofonoff (1985) provides a relationship between the salinity of seawater, using in-situ temperature and pressure, to the resistivity of the aqueous pore fluids.

2.5 Summary and Discussion

2.5.1 Seismic methods

The aim of this thesis is to develop a joint seismic and electrical data interpretation method. Therefore one of the seismic models must be selected for use within the joint method. To do this some criteria need to be established for the final seismic model.

The seismic model must be able to describe a sediment. Most of the methods described above only assume that the effective medium is a composite of two or more individual materials. The use of inappropriate geometries between the phases mean that the effective medium calculated is not always suitable for a sediment. The final effective medium needs to allow both phases to be interconnected (bi-connected) at all volume fractions of those phases. One of the phases must be fluid to represent the pore fluid in a sediment. The composition of hydrate bearing sediments ranges from clay to sand. The grains therefore range in size and shape. Ideally the different shapes of sediment grains of different lithologies should also be described.

The joint model is being developed to interpret field data from boreholes and geophysical surveys. The inputs for the models should be readily available from these types of data. Therefore models with no empirical coefficients will be preferable.

This chapter has reviewed a large number of seismic effective medium models. The simplest of these models predict the shear and bulk modulus of an effective medium without any of the microstructure being expressed. These included the Voigt (1928) upper bound, Reuss (1929) lower bound, Hill's (1952) average, Wood's (1930) equation and the

Wyllie (1956) time average equation. Each of these methods relates the effective bulk and shear moduli to the bulk and shear moduli of the individual components by different methods of averaging the individual components, except for the time average equation, which deals with velocities. The Wyllie model does represent a specific microstructure, but it assumes that the medium is composed of alternate layers of each constituent and is therefore unsuitable for modelling a sediment. These models are also unable to model different grain shapes.

The HS upper and lower bounds go slightly further and calculate the effective moduli when one component is totally interconnected and the other is isolated. Although the microstructure is expressed, the model is unsuitable for a sediment because only one phase is interconnected. The HS bounds cannot model changes in grain shape; however, the lower bound does model spherical grains because the calculated effective medium is composed of many spheres.

The SCA and the DEM methods determine the effective bulk and shear moduli of a medium from the individual components and the geometric relation between those components. Both methods embed inclusions of one material, which maybe a variety of shapes, within another material. By changing the shapes of the inclusions, different types of sediments can be modelled. The SCA goes through a bi-connected stage at porosities of 40-60% but not at other porosities, and should not be used at porosities greater than 60%. This is a problem because many clay-rich sediments have porosities greater than 60%. The DEM allows the micro-structures to be modelled but it is completely dependent on the starting medium. If the starting medium is solid and fluid inclusions are added, the solid will remain interconnected at all porosities and the fluid will remain isolated. Therefore one or other of the phases is always interconnected and the other is isolated at all porosities preventing the DEM to represent bi-connected sediment. There is however a method that combines the SCA and the DEM which allows the medium to be bi-connected at all porosities.

The contact method relates the normal and the tangential stiffness of two spheres to predict the effective modulus. Two models have been developed. The Hertz model only relates the compression force applied to the grains to the overall medium and can therefore only predict the effective bulk moduli. The Mindlin method relates compression and tangential force to the effective moduli. For the bulk modulus this becomes the same as the Hertz method but it can also calculate the shear modulus. The final effective medium is a

medium composed of spherical grains which can easily represent sediment. There are though several problems with this method. The first is that it can only be used for spherical grains. While this makes it suitable for sediment composed of sands, it is unusable for clays. The final medium is dry and the sediment we want to model is saturated with fluid. The method also assumes a coordination number which is derived empirically.

Biot and Gassmann methods determine the effective bulk and shear moduli of a fluid or gas saturated medium from the dry rock properties. This is achieved by determining the increase in pore pressure, which stiffens the rock, as a seismic wave propagates through the medium. The essential difference between Biot and Gassmann equations is Gassmann is only valid at the low frequency limit for seismic waves whereas Biot theory is valid at all frequencies. The major problem with the Biot and Gassmann approaches is that they assume that the dry rock frame moduli are already known. Unless laboratory measurements are available, this component cannot be determined. The Biot and Gassmann methods have been combined with contact models which can calculate the dry rock frame properties.

Chand *et al.* (2004) made a comparison of the major methods used to quantify hydrates in marine sediments. They concluded that all the methods produce comparable results for sediments where no hydrate is present. However the methods produce highly variable results for hydrate bearing sediments. Each of the methods was compared with resistivity derived hydrate saturations from the same areas. The SCA/DEM method consistently produces similar hydrate saturations to those calculated from the resistivity. The EWE, TPEM and TPB predicted hydrate saturations consistent with those derived from resistivity for some datasets but not for others. The inconsistent results may be due to poor choice of the empirical constants within each method.

None of the methods above can perfectly model a sediment composed of grains of solid within a fluid. However the SCA and the DEM are probably the most suitable, for the following reasons. Both the SCA and the DEM are able to model a range of sediment types from clays through to sand, unlike any of the other methods. They also require no empirical constants. A method has been described for using a combination of the SCA and DEM that allows both the two phases to be bi-connected at all porosities (Sheng, 1990). However the SCA/DEM method combines the SCA with the DEM via some empirical constants, which are discussed in Chapter 3. The SCA/DEM method has also been successfully used to quantify hydrate saturations in hydrate bearing sediments, assuming

that the porosity of the sediments is already known (Jakobsen *et al.*, 2000). A joint seismic and electrical model has already been successfully developed for basalts using a SCA/DEM combination (Greer, 2001). Chapter 3 gives a more in depth explanation of the individual SCA and DEM methods and how they can be combined for the joint model. It also gives an explanation of how hydrate can be included in the model.

2.5.2 Electrical methods

Archie's (1942) law is the dominant method of interpreting electrical resistivity data especially in well log interpretation. Its advantages are that it is a simple method to interpret electrical data. The empirical constants within the equation can be varied such that it can fit almost any data set. Formation factor versus porosity curves can be determined for different lithologies and these are used extensively in the hydrocarbon industry.

Archie's law is unfortunately an empirical equation and as such the constants m and t cannot be physically justified. Also a large data set is usually needed to determine these constants, although rough values have been determined for different types of sediments. The addition of hydrate to Archie's law requires use of a further empirical constant (n). Because the constants in Archie's law can be freely varied, it can be forced to fit almost any data set which may lead to some incorrect interpretation of data. The clay models developed by Wyllie and Southwick (1954), Waxman and Smits (1968), Clavier (1984), Bussian (1983) and Berg (1995) are able to account for the conductance of clay particles in the sediment however they all suffer from the same problem as Archie's equation. All the models require at least one empirically derived constant to account for the grains geometrical arrangement. Several of the models require multiple empirical constants. This makes these models unsuitable for the work developed in this thesis.

The aim of this thesis is to produce a joint seismic and electrical model and therefore both the seismic and the electrical models must be compatible. The seismic model to be used in the joint approach will be based on a purely physical method therefore the electrical model should be also physically based. There is no obvious mapping between Archie's law and seismic effective medium methods. Therefore an alternative electrical effective medium method must be sought.

2.6 Conclusion

A seismic effective medium technique, combined SCA/DEM, has already been developed which is suitable for the joint model with some adjustments (described in Chapter 3). This method calculates the effective moduli from the moduli of the individual components and the geometric relations of the constituents for a bi-connect medium. To model resistivity data, Archie's equation is not suitable because it is dependent on empirical constants. Therefore a model needs to be developed which is purely physical, with the same input parameters as the seismic method. This method would need to relate the effective resistivity of a medium to the resistivity of the individual components and a geometric factor to describe the shape of the grains.

Chapter 3. Seismic Effective Medium Model

3.1 Introduction

In the previous chapter a variety of methods were discussed for modelling the seismic effective moduli of sediments. The Self-Consistent Approximation (SCA) and the Differential Effective Medium (DEM) methods were determined to be the most appropriate for unconsolidated clastic sediments because the geometric details of the phases can be modelled and the models are purely physical with no empirical constants. Quantities that need to be specified in the SCA and DEM models include: the volume fraction of each of the constituents, the elastic moduli of each of the constituents and the shape of the inclusions. Both the SCA and the DEM methods assume that the size of the inclusions is much smaller than the wavelength of the seismic wave passing through the sediment. It is also assumed that as the wave passes through the medium no fluid flow is induced. All the inclusions have the same shape and are idealized to simple shapes such as spheres and ellipsoids. The physical properties of each of the constituents are also assumed to be linear, isotropic and elastic.

This chapter discusses the SCA and DEM methods in greater depth than the previous chapter. It also describes a method of combining the two models to produce a single method in which each of the phases remains interconnected at all porosities. This ability to model a bi-connected medium is important because both the fluid and the solid grains in uncemeted sediments containing ellipsoidal clasts will remain interconnected at all porosities apart from 0% and 100%. The chapter concludes with a discussion of how hydrate may be added into the combined SCA and DEM model in both load and non-load bearing manners. As with chapter 2 all the graphical depictions of the models assume that the solid matrix is composed of glass beads and the pore filling fluid is brine. The density, bulk and shear moduli values for these components are given in Appendix A.

3.2 Self-Consistent Approximations (SCA)

A two phase medium is assumed to be composed of inclusions contained within a background matrix. As a seismic wave passes through the medium the inclusions will be deformed, i.e. change in shape and size. Eshelby (1957) developed a method to calculate

the elastic deformation of a single inclusion embedded in an infinite background medium. This was then related to the effective moduli of the whole medium when there is a distribution of the inclusions throughout the background material. The Eshelby (1957) method assumes that there is no interaction between the inclusions and is therefore only valid for dilute distributions of inclusions.

As the density of the inclusions increases the inclusions start to interact with each other and calculating the effective moduli becomes more complicated. SCA methods (Hill, 1965; Wu, 1966; Willis, 1977; Berryman, 1980) extend the Eshelby (1957) method to higher inclusion concentrations. The SCA method still uses the solution for the deformation of a single inclusion in a uniform matrix. However, the matrix is assigned the elastic properties of the as yet to be solved effective medium allowing the interaction of the inclusion to be approximated. The bulk and shear moduli are therefore coupled together and must be solved by iteration.

3.2.1 Wu (1966) Self-Consistent Approximation

Wu's (1966) method is typical for a SCA model and can be expressed as the estimate of the elastic moduli for a two-phase medium (matrix and inclusions):

$$\kappa_{SC} = \kappa_m + \beta_i(\kappa_i - \kappa_m)P_i\,, \tag{3.1}$$

$$\mu_{SC} = \mu_m + \beta_i(\mu_i - \mu_m)Q_i\,, \tag{3.2}$$

where:

κ_{SC} = Bulk modulus of the aS-yet-unknown effective medium;

μ_{SC} = Shear modulus of the aS-yet-unknown effective medium;

β = Volume fraction;

P and Q are coefficients for specific inclusion shapes;

subscripts m and i denote the matrix and the inclusions respectively. When the inclusions are not spheres they are assume to be randomly orientated and distributed throughout the effective medium.

The Wu (1966) method, unlike the Hill (1965; described in chapter 2) method, allows a variety of inclusion shapes to be modelled although all the inclusions must have

the same shape. Wu (1966) gives the relevant geometric coefficients required for computing P and Q as:

$$P = \frac{1}{3} T_{iijj}, \tag{3.3}$$

$$Q = \frac{1}{5}\left(T_{ijij} - \frac{1}{3} T_{iijj} \right), \tag{3.4}$$

Where the tensor T_{ijkl} relates the uniform far-field strain to the strain within the ellipsoidal inclusion (Wu, 1966):

$$T_{iijj} = \frac{3F_1}{F_2}, \tag{3.5}$$

$$T_{ijij} - \frac{1}{3} T_{iijj} = \frac{2}{F_3} + \frac{1}{F_4} + \frac{F_4 F_5 + F_6 F_7 - F_8 F_9}{F_2 F_4}, \tag{3.6}$$

and,

$$F_1 = 1 + A\left[\frac{3}{2}(f+\theta) - R\left(\frac{3}{2} f + \frac{5}{2}\theta - \frac{4}{3} \right) \right], \tag{3.7}$$

$$\begin{aligned} F_2 = {} & 1 + A\left[1 + \frac{3}{2}(f+\theta) - \left(\frac{R}{2} \right)(3f + 5\theta) \right] + B(3-4R) + \\ & \left(\frac{A}{2} \right)(A+3B)(3-4R)\left[f + \theta - R\left(f - \theta + 2\theta^2 \right) \right] \end{aligned}, \tag{3.8}$$

$$F_3 = 1 + A\left[1 - \left(f + \frac{3}{2}\theta \right) + R(f+\theta) \right], \tag{3.9}$$

$$F_4 = 1 + \left(\frac{A}{4} \right)\left[f + 3\theta - R(f-\theta) \right], \tag{3.10}$$

$$F_5 = A\left[-f + R\left(f + \theta - \frac{4}{3} \right) \right] + B\theta(3-4R), \tag{3.11}$$

$$F_6 = 1 + A\left[1 + f - R(f+\theta) \right] + B(1-\theta)(3-4R), \tag{3.12}$$

$$F_7 = 2 + \left(\frac{A}{4} \right)\left[3f + 9\theta - R(3f+5\theta) \right] + B\theta(3-4R), \tag{3.13}$$

$$F_8 = A\left[1 - 2R + \left(\frac{f}{2} \right)(R-1) + \left(\frac{\theta}{2} \right)(5R-3) \right] + B(1-\theta)(3-4R), \tag{3.14}$$

$$F_9 = A\left[(R-1)f - R\theta\right] + B\theta(3-4R), \tag{3.15}$$

with A, B and R given by:

$$A = \frac{\mu_i}{\mu_{SC}} - 1, \tag{3.16}$$

$$B = \frac{1}{3}\left(\frac{\kappa_i}{\kappa_{SC}} - \frac{\mu_i}{\mu_{SC}}\right), \tag{3.17}$$

$$R = \left[\frac{(1-2\upsilon_m)}{2(1-\upsilon_{SC})}\right] = \frac{3\mu}{3\kappa + 4\mu}, \tag{3.18}$$

θ and f are given by:

$$\theta = \frac{\alpha}{(\alpha^2-1)^{3/2}}\left[\alpha(\alpha^2-1)^{1/2} - \cosh^{-1}\alpha\right] \text{ (For prolate spheroids)}, \tag{3.19}$$

$$\theta = \frac{\alpha}{(1-\alpha^2)^{3/2}}\left[\cos^{-1}\alpha - \alpha(1-\alpha^2)^{1/2}\right] \text{ (For oblate spheroids)}, \tag{3.20}$$

$$f = \frac{\alpha^2}{1-\alpha^2}(3\theta - 2), \tag{3.21}$$

where α is the aspect ratio. Because κ_{SC}, μ_{SC} and P, Q are interdependent the equations 3.1 and 3.2 are coupled and must be solved by simultaneous iteration. The equations 3.1-3.21 assume that the inclusions are spheroidal. For the special cases when the inclusions are needle (prolate, $\alpha \to 0$) or disk (oblate, $\alpha \to 0$), shaped Wu found:

For needle shaped inclusions:

$$\frac{\kappa - \kappa_1}{\kappa_2 - \kappa_1} = \frac{c_2}{3}\frac{3 + RA}{1 + (1-R)A + (3-4R)B}, \tag{3.22}$$

$$\frac{\mu - \mu_1}{\mu_2 - \mu_1} = \frac{c_2}{5}\left[\frac{2}{1 + A/2} + \frac{1}{1 + (1+R)A/2} + \frac{(1 - 4/3\,R)(A+3B)}{1 + (1-R)A + (3-4R)B}\right] + \frac{2 + (3-R)(A/2) + (3-4R)B}{\left[1 + (1+R)(A/2)\right]\left[1 + (1-R)A + (3-4R)B\right]}\frac{c_2}{5}. \tag{3.23}$$

For disk shaped inclusions:

$$\frac{\kappa - \kappa_1}{\kappa_2 - \kappa_1} = \frac{c_2}{3} \frac{3 + RA}{1 + A + (3 - 4R)B}, \tag{3.24}$$

$$\frac{\mu - \mu_1}{\mu_2 - \mu_1} = \frac{c_2}{5} \left[\frac{3 + A}{1 + A} + \frac{2 + \left(2 - \frac{4}{3} R\right) A + 2(3 - 4R)B}{1 + A + (3 - 4R)B} \right]. \tag{3.25}$$

3.2.2 Berryman (1980) Self-Consistent Approximation

The Berryman (1980) theory is related to the scattering theory approaches introduced by Zeller & Dederichs (1973), Korringa (1973) and Gubernatis & Krumhansl (1975) and follows on from the Kuster & Toksöz (1974) model. While the earlier approaches concentrate on the average stress and strain fields, Berryman (1980) deals directly with the displacement vector. This approach has the advantage that the analysis is reduced from tensor, to vector algebra which leads to a comparatively simple set of formulae.

Berryman's (1980) self-consistent method is a variation of the Kuster & Toksöz (1974) approach designed to minimize the effect of multiple scattering. The Kuster & Toksöz method considers a sphere which is embedded into an infinite background material. The sphere is composed of a composite of material, component 1 and component 2. The initial background is composed of only component 2 (Figure 3.1). Scattering within this medium will only depend on the volume fraction of component 1, assuming that there is no multiple scattering. When the concentration of component 1 is low the scattering from this medium is the same as replacing the composite sphere by a sphere of homogeneous material with the same elastic constants. Berryman (1980) noted that the Kuster & Toksöz (1974) model is only valid at low inclusion concentrations and that the results are not symmetric, i.e. if component 1 and component 2 are switched around then the final elastic moduli will not be the same even if the volume fractions of each component remain unchanged. Berryman considers a slightly different approach to allow high inclusion concentrations. Berryman also considers a sphere embedded in an infinite background medium, however the background medium is now composed of a material where the elastic properties can be freely varied. The embedded sphere is composed of inclusions of component 1 and component 2 and a matrix of the freely varying material

(Figure 3.1). The scattering experiment is repeated and the background material is varied until the low order scattering vanishes. At this point the background material has the same elastic properties as the composite sphere.

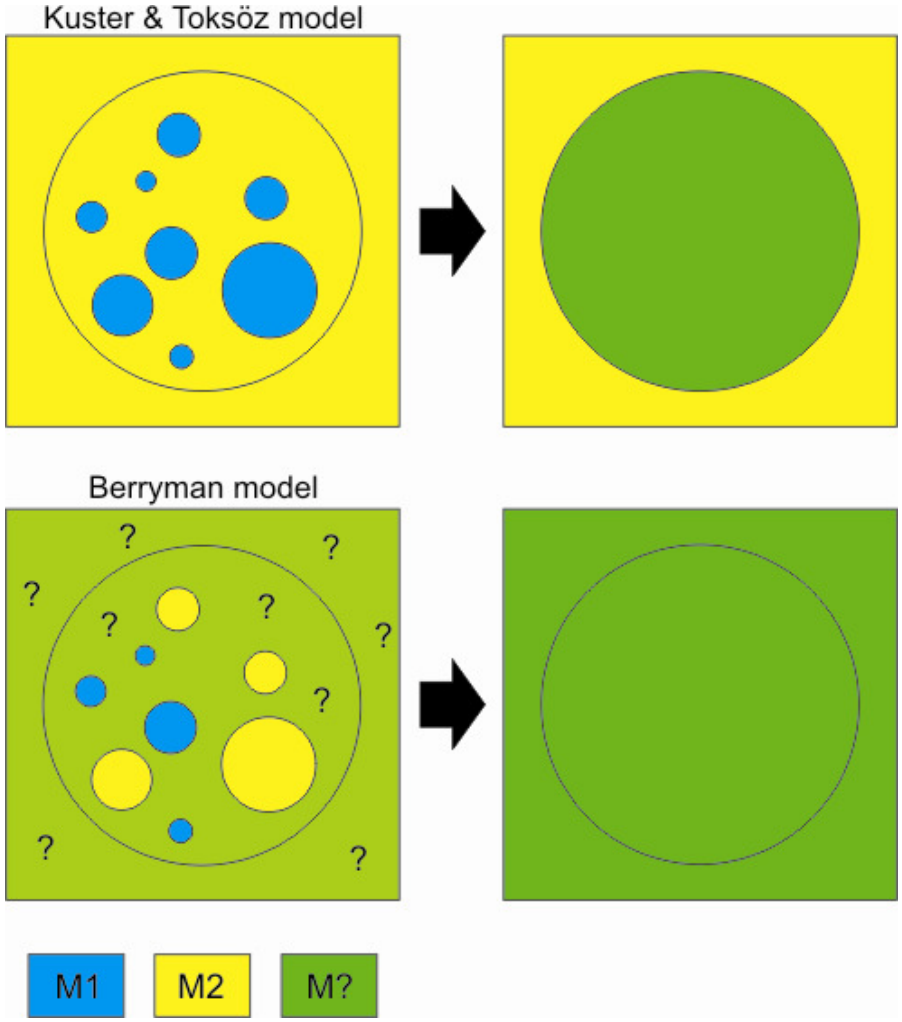

Figure 3.1 Schematic diagram of the model composite used by the Kuster and Toksöz (1974) model (top) and the Berryman (1980) SCA method (bottom) (adapted from Berryman 1980). The Kuster and Toksöz (1974) model is not a true self consistent approximation. M1 and M2 are the 2 components in the effective medium. M? is the unknown background material.

Berryman (1980) gives a general form of the self-consistent approximation for N-phase composites as:

$$\sum_{i=1}^{N} \beta_i \left(\kappa_i - \kappa_{SC}\right) P_i = 0, \tag{3.26}$$

$$\sum_{i=1}^{N} \beta_i (\mu_i - \mu_{SC}) Q_i = 0, \tag{3.27}$$

where β_i is the volume fraction of the i-th component; κ_i and κ_{SC} are the bulk moduli of the i-th component and self-consistent effective medium respectively. μ_i and μ_{SC} denote the shear moduli of the i-th component and the effective medium; P and Q are geometric coefficients given in Table 3.1.

Shape of the inclusions	P_i	Q_i
Spherical	$\dfrac{\kappa_m + \frac{4}{3}\mu_m}{\kappa_i + \frac{4}{3}\mu_m}$	$\dfrac{\mu_m + \zeta_m}{\mu_i + \zeta_m}$
Needle	$\dfrac{\kappa_m + \mu_m + \frac{1}{3}\mu_i}{\kappa_i + \mu_m + \frac{1}{3}\mu_i}$	$\dfrac{1}{5}\left(\dfrac{4\mu_m}{\mu_m + \mu_i} + 2\dfrac{\mu_m + \gamma_m}{\mu_i + \gamma_m} + \dfrac{\kappa_i + \frac{4}{3}\mu_m}{\kappa_i + \mu_m + \frac{1}{3}\mu_i}\right)$
Disk	$\dfrac{\kappa_m + \frac{4}{3}\mu_i}{\kappa_i + \frac{4}{3}\mu_i}$	$\dfrac{\mu_m + \zeta_i}{\mu_i + \zeta_i}$
Penny shaped cracks	$\dfrac{\kappa_m + \frac{4}{3}\mu_i}{\kappa_i + \frac{4}{3}\mu_i + \pi\alpha\vartheta_m}$	$\dfrac{1}{5}\left(1 + \dfrac{8\mu_m}{4\mu_i + \pi\alpha(\mu_m + 2\vartheta_m)} + 2\dfrac{\kappa_i + \frac{2}{3}(\mu_i + \mu_m)}{\kappa_i + \frac{4}{3}\mu_i + \pi\alpha\vartheta_m}\right)$

Where

$$\vartheta = \mu\frac{(3\kappa + \mu)}{3\kappa + 4\mu} \qquad \gamma = \mu\frac{(3\kappa + \mu)}{(3\kappa + 7\mu)} \qquad \zeta = \frac{\mu}{6}\frac{(9\kappa + 8\mu)}{(\kappa + 2\mu)}$$

Table 3.1. Geometric coefficient used in both the SCA and the Differential Effective Medium (DEM) approaches (Berryman, 1995). Subscripts *i* and *m* denote the inclusion and the background material.

The Berryman equations (3.26 and 3.27) agree with the self-consistent equations obtained by Hill (1965) and Budiansky & O'Connell (1976). The Berryman equations reproduce the known results for spherical inclusions. They also give equations that are completely symmetrical when the components are switched around unlike the models from Wu (1966) and Budiansky & O'Connell (1976).

3.2.3 Willis Self Consistent Approximation

Willis (1977) uses the SCA method to determine the overall elastic moduli and thermal conductivity properties of a composite material. Willis uses the stiffness tensors (*C*), which allow both isotropic and anisotropic effects to be calculated, unlike the Berryman (1980) and Wu (1966) methods. Willis' work is a generalization of the work by Walpole (1969). Walpole (1969) considers the elastic moduli of a composite in the limited cases where the inclusions are needle or disk shaped. Walpole exploits the geometry of the inclusions, which allow the edge effects to be disregarded. His approach therefore cannot obtain the overall properties of a body containing cracks, in which the edge effects are vital. Willis' work (1977) is free of this limitation.

The Self-Consistent Approximation of Willis (1977) asserts that the effective elastic stiffness tensor *C* for the composite is given by the implicit equation:

$$C_{SCA} = \left\{ \sum_{i=1}^{n} \beta_i C_i Q_i \right\} \left\{ \sum_{j=1}^{n} \beta_j Q_j \right\}^{-1} \tag{3.28}$$

where

$$Q_i = \left[I + P_4(C)(C_i - C_{SCA}) \right]^{-1}, \tag{3.29}$$

β is the volume concentration of each component, P_4 is a fourth order tensor and I is the unit tensor for tensors of fourth order.

While the Willis (1977), Berryman (1980) and Wu (1966) SCA are all extensions of the work by Eshelby (1957), the Berryman and Wu SCA are simplified approximations and only deal with isotropic media. The Willis model is capable of dealing with both isotropic and anisotropic situations. The Berryman model produces some unusual results at porosities of 45% and above (Greer, 2001). The general trend is that the bulk modulus decreases as the aspect ratio decreases. However at porosities greater than ~ 45% this trend reverses and there is no physical explanation for such a reversal (Greer, 2001). The Wu and Willis models produce the same result for composites where the inclusions have an aspect ratio of one. However as the aspect ratio of the inclusions decrease the results start to differ (Figure 3.2 and Figure 3.3).

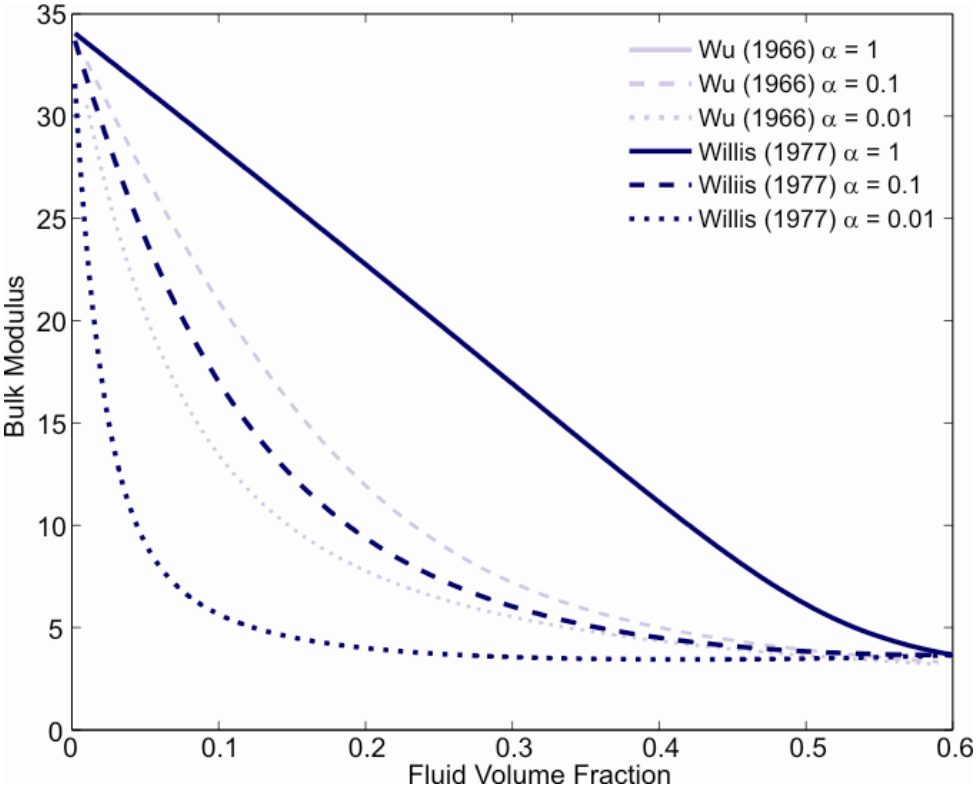

Figure 3.2 Wu (1966; dark blue) and Willis (1977; light blue) SCA bulk moduli for a two-phase effective medium composed of fluid and solid grains at different inclusion aspect ratios. When the aspect ratio of the inclusions is 1 the Wu and Willis bulk modulus is the same. The bulk modulus is only calculated up to porosities of 60% because the SCA is only valid to this point.

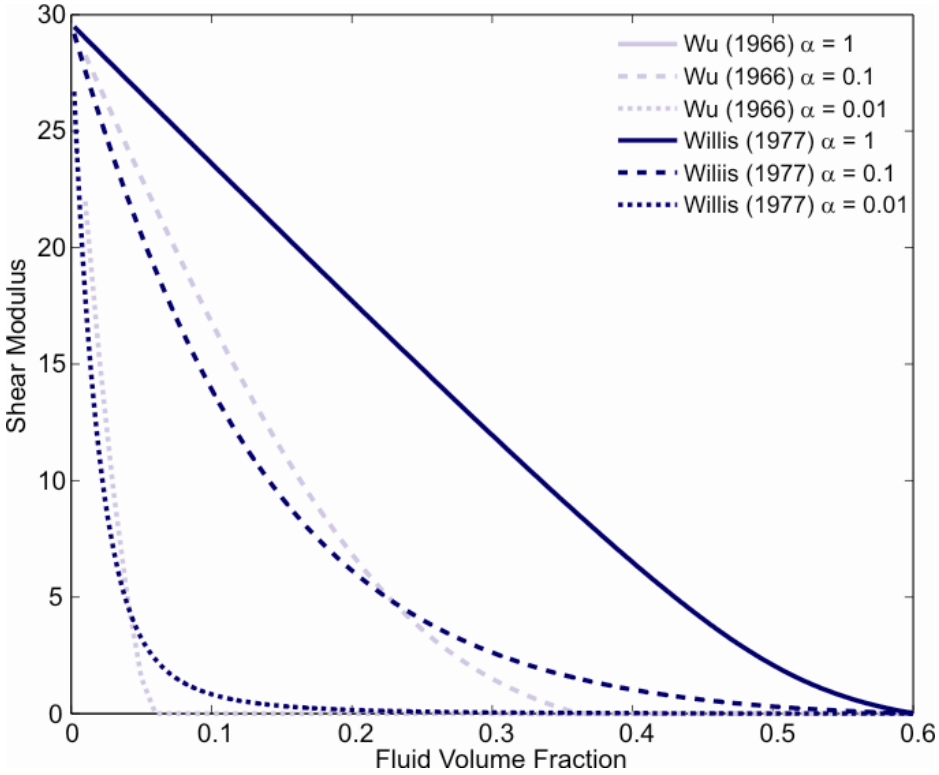

Figure 3.3 Wu (1966; dark blue) and Willis (1977; light blue) SCA shear moduli for a two-phase effective medium composed of fluid and solid grains at different inclusion aspect ratios. When the aspect ratio of the inclusions is 1 the Wu and Willis shear modulus is the same. The shear modulus is only calculated up to porosities of 60% because the SCA is only valid to this point.

A comparison between the SCA and the HS bounds (Hashin & Shtrikman, 1963; chapter 2) for spherical inclusions is shown in Figure 3.4 and Figure 3.5. The HS bounds are the upper and lower bound for the bulk and shear moduli of the sediment and should not be violated. However, the SCA calculated shear modulus does have a higher value than the upper HS bound for fluid volume fractions of less than ~0.3 (Figure 3.4). This is a known effect of the self-consistent theory and it is therefore only used for porosities of between 30% and 60% (Sheng 1990). The bulk modulus values do not violate the HS bounds over the full range of fluid volume fractions (Figure 3.5).

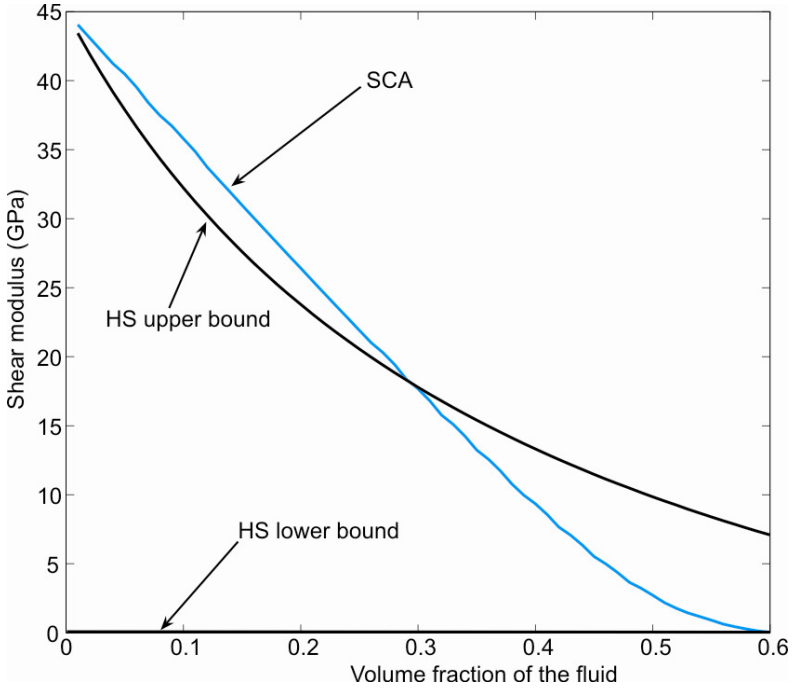

Figure 3.4 Shear modulus of a two phase medium composed of fluid and solid calculated using the SCA effective medium for spherical inclusions (blue line) and the HS upper and lower bound (black lines). The HS lower bound calculates a medium where the fluid phase is totally interconnected at all porosities causing the shear modulus to be zero. The SCA shear modulus exceeds the HS upper bound at fluid volume fractions of less than 0.3. The SCA is only valid for fluid volume fractions between 0.3 and 0.6 (Sheng, 1990).

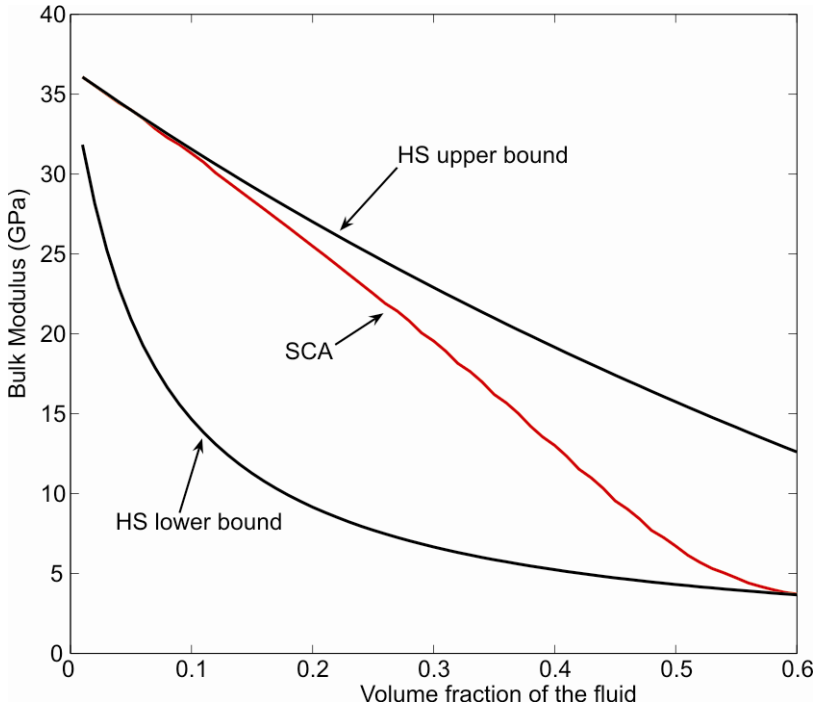

Figure 3.5 Bulk modulus for a two-phase medium of fluid and solid calculated using the SCA method for spherical inclusions (aspect ratio = 1): comparison of the SCA effective medium model with the HS upper and lower bounds for bulk modulus.

3.3 Differential Effective Medium (DEM)

The DEM theory (Cleary *et al*, 1980; Norris, 1985; Zimmerman, 1991; Berryman, 1992) models two-phase composites by incrementally adding inclusions of one phase (component 2) into a background phase (component 1). After each addition of component 2, the average elastic properties of this new medium are calculated. This medium now becomes the effective medium and the process is repeated. The inclusions of component 2 replace an equal volume of the effective medium keeping the total volume of the effective medium constant. The process is repeated until the desired proportion of the constituents is reached (Figure 3.6).

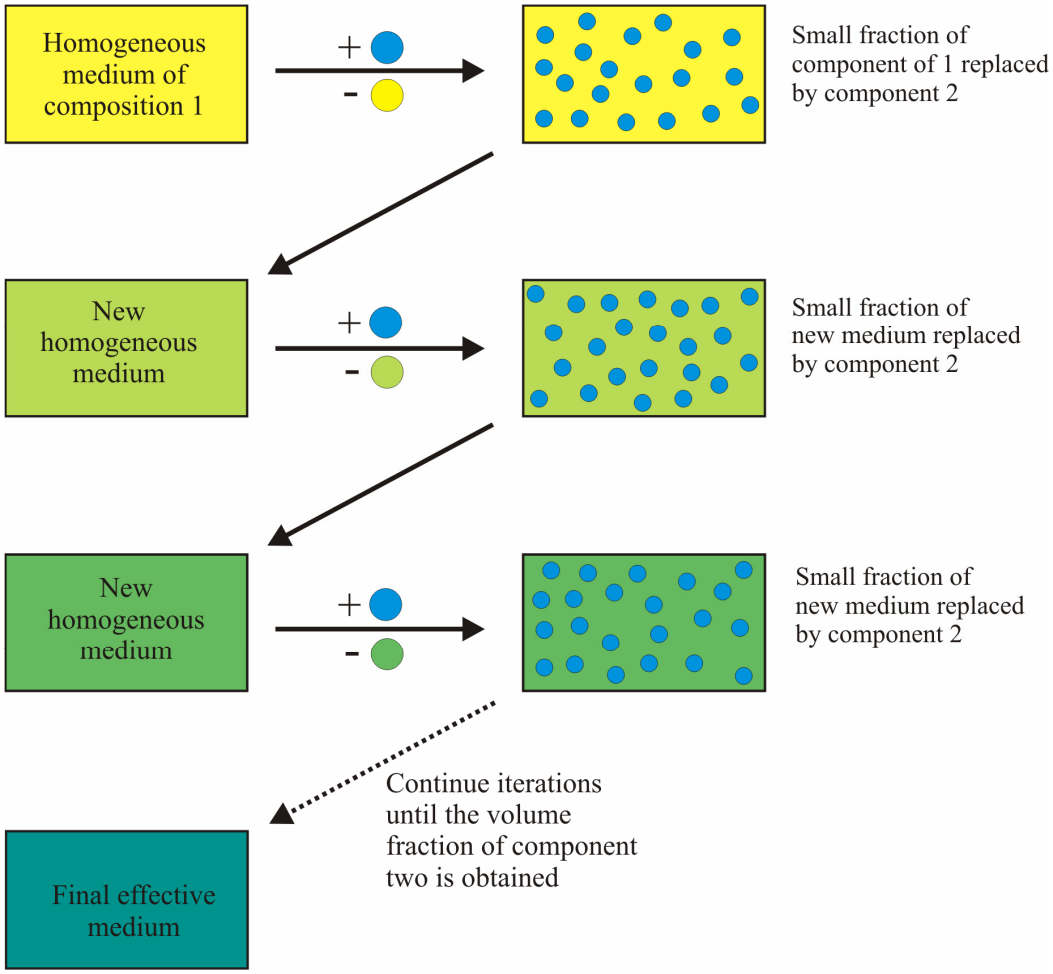

Figure 3.6 Schematic representation of the DEM process (adapted from Sheng, 1991)

The DEM does not treat each component symmetrically and the elastic properties of the final medium depend on the order in which the components are added, i.e. if the host is component 1 and inclusions of component 2 are added, the final effective medium produced will not have the same effective moduli as a system with the same relative proportions of component 1 and 2 where component 2 is the host medium and the inclusions are formed of component 1. In other words the effective moduli calculated for a composite medium depend on both the final volume fraction of the individual constituents and the construction path taken. This dependence on the construction path is due to the individual inclusions interacting elastically with one another through the background material although they are physically isolated from each other. Therefore if we start with a background composed of component 1 and add inclusions of component 2, the inclusions will remain isolated up to concentrations of 100% while component 1 is totally interconnected for all inclusion concentrations less than 100%.

Norris (1985) and Berryman (1992) assume that the inclusions of component 2, added at each iteration, replace the composite homogeneous medium from the previous iteration (Figure 3.6). Zimmerman (1984) makes the assumption that the inclusions of component 2 will replace only component 1, the original host material, at every iteration. Zimmermans's assumption leads to differential equations in which $d\beta/(1-\beta)$ is replaced with $d\beta$, that predict stiffer effective moduli than either Norris (1985) or Berryman (1992). At low inclusion concentrations the Zimmerman, Norris and Berryman models predict similar values but at concentrations above ~10% they diverge (Mavko *et al.*, 1998). For spherical inclusions the elastic moduli calculated by Zimmerman (1984) lie outside of the HS bounds (Mavko *et al.*, 1998). Berryman (1992) gives the DEM equations as (Figure 3.7 and Figure 3.8):

$$(1-\beta_2)\frac{d}{d\beta_2}[\kappa_{dem}(\beta_2)] = (\kappa_2 - \kappa_{dem})P_2(\beta_2), \tag{3.30}$$

$$(1-\beta_2)\frac{d}{d\beta_2}[\mu_{dem}(\beta_2)] = (\mu_2 - \mu_{dem})Q_2(\beta_2), \tag{3.31}$$

where β_2 is the concentration of component 2, κ_{dem} is the DEM effective bulk modulus, μ_{dem} is the DEM effective shear modulus and P and Q are geometric coefficients (Table 3.1). The initial conditions are defined as $\kappa_{dem}(0) = \kappa_1$ and $\mu_{dem}(0) = \mu_1$, where κ_1 and μ_1 are the bulk and shear moduli of the host material and κ_2 and μ_2 are the bulk and shear moduli of the inclusion material respectively.

The DEM equation may also be written in terms of the elastic stiffness tensor (C), which allows both isotropic and anisotropic effective media to be calculated. Hornby *et al.* (1994) give the DEM equations as:

$$\frac{d}{d\beta}C_{dem} = \frac{1}{1-\beta}(C_i - C_{dem})Q_i \tag{3.32}$$

$$Q_i = [I + P(C_i - C_{dem})]^{-1} \tag{3.33}$$

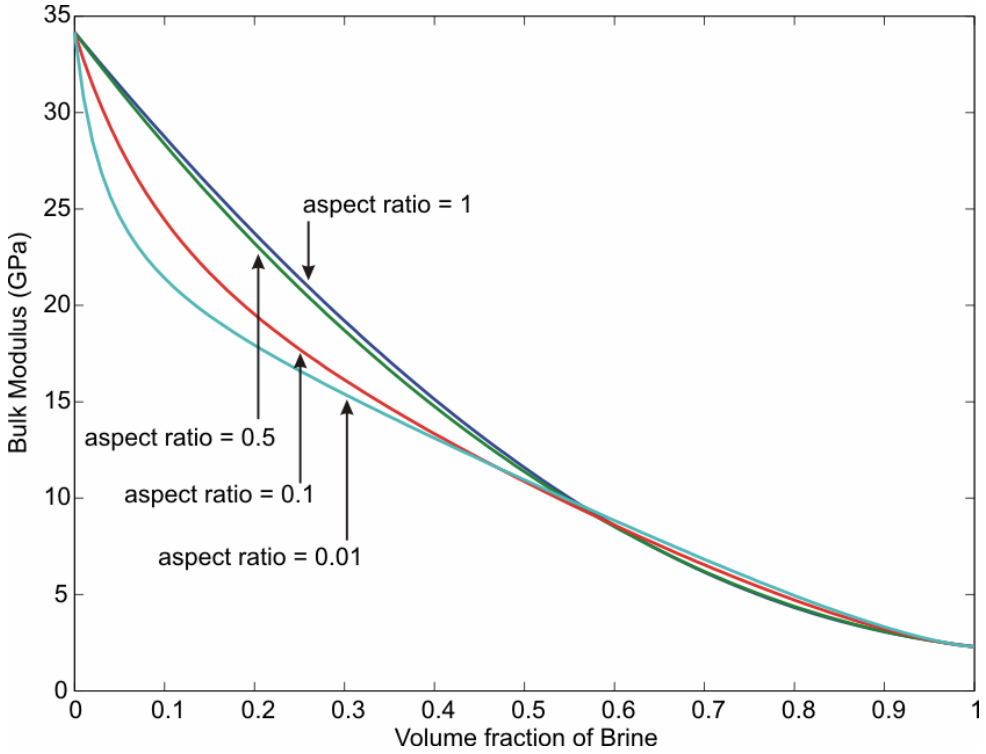

Figure 3.7 Bulk modulus versus brine volume fraction for an effective medium composed of glass beads and brine (values given in Appendix A), at aspect ratios varying from 0.01 to 1 calculated using the DEM method where the fluid is considered the matrix and the solid the inclusions.

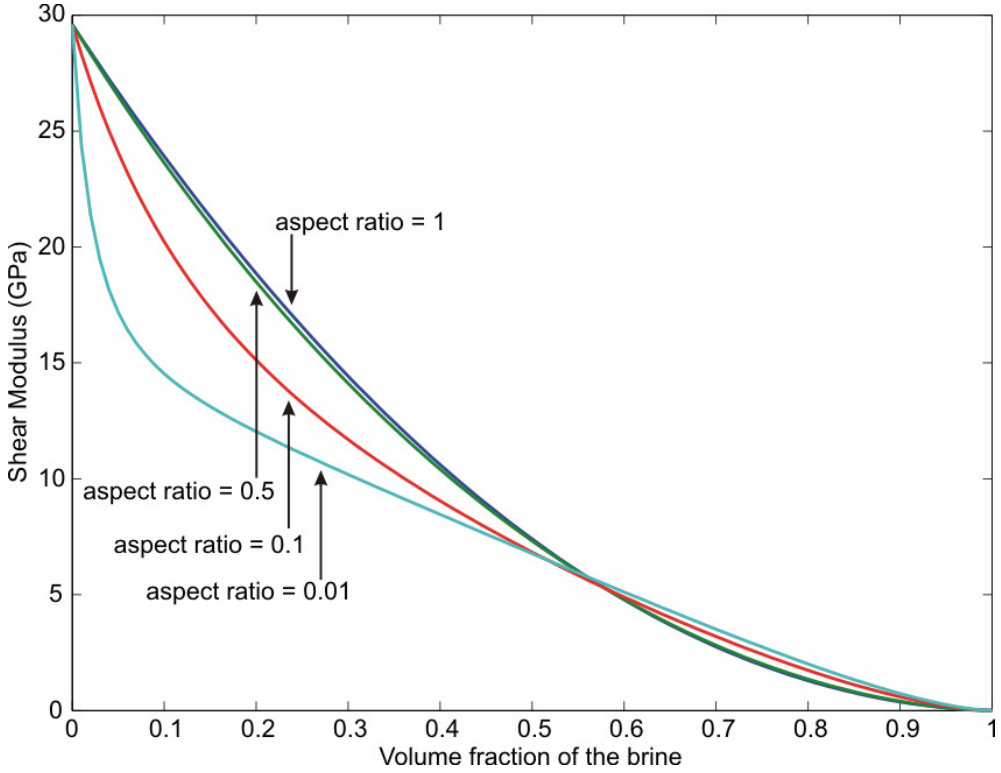

Figure 3.8 Shear modulus versus brine volume fraction for an effective medium composed of glass beads and brine (values given in Appendix A), at aspect ratios varying from 0.01 to 1 calculated using the DEM method where the fluid is considered the matrix and the solid the inclusions.

3.4 Combined SCA/DEM

The grains and pore fluid in clastic sediments are generally both fully interconnected at all realistic porosities. It is therefore necessary to use a bi-connected effective medium to model such sediments. If a sediment is assumed to be bi-connected at all porosities then individually neither the SCA nor the DEM can model it. The SCA is a bi-connected for porosities between 40% and 60% (Sheng, 1990, Berryman 1980), however sediment and sedimentary rock porosities can range from 0% to 70% and in some cases higher. The DEM method preserves the microstructure of its starting medium and therefore if the starting medium is a solid and inclusions of fluid are added, while the solid will remain interconnected the fluid will be isolated at all porosities and the sediments will never be bi-connected.

Sheng (1990) used a combination of the SCA and DEM to model a system in which the solid portion of the medium can be load bearing while the fluid portion remains totally interconnected. This method was developed for sandstones. It starts by calculating the effective bulk and shear moduli for a two phase medium at a specific porosity using the

SCA method. The starting porosity, at which the sediment is bi-connected, is known as the critical porosity (φ_c). The moduli calculated using the SCA method are entered into the DEM technique which then calculates the moduli at all other porosities. Since the DEM preserves the microstructure of its starting medium the final effective medium must also be interconnected at all porosities. Figure 3.9 and Figure 3.10 show the variations in bulk and shear moduli with changing porosity using the combined SCA/DEM method. These figures show that the porosity of the starting medium, calculated using the SCA and given to the DEM, has an enormous effect on the final effective moduli. Therefore choosing the critical porosity (φ_c) is very important.

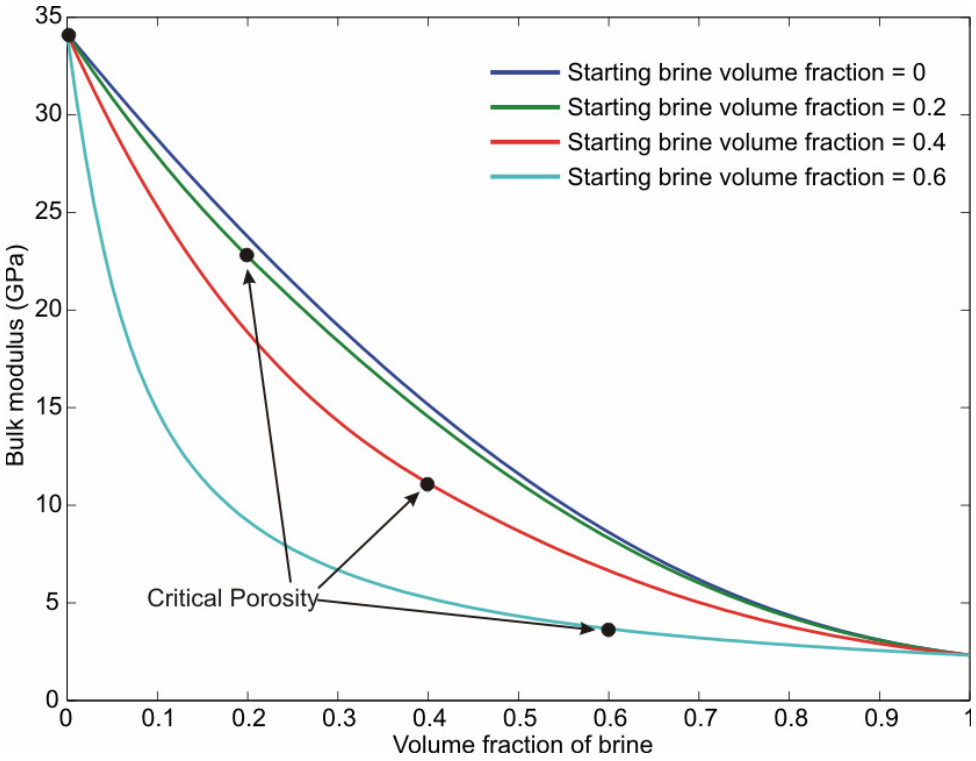

Figure 3.9 Bulk modulus values calculated using the combined SCA/DEM method for spherical inclusions and critical porosities of 0, 0.2 0.4 and 0.6. Black dots show the SCA starting porosities (critical porosities) passed to the DEM and used to calculate the modulus over the entire porosity range.

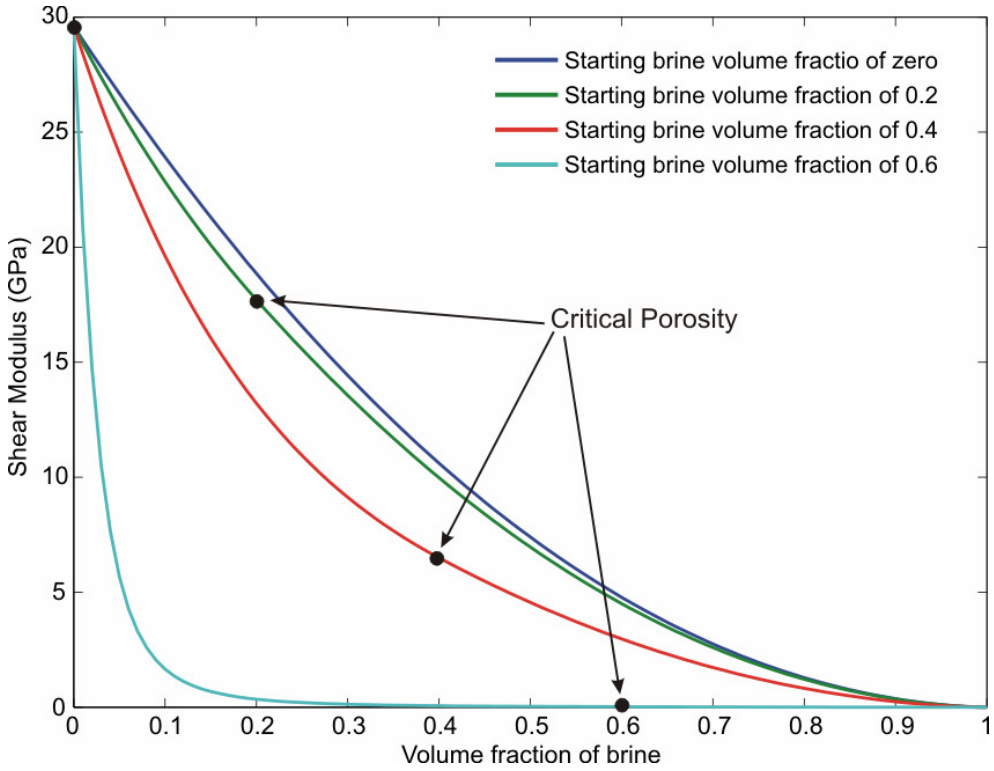

Figure 3.10 Shear modulus values calculated using the combined SCA/DEM method for spherical inclusions and critical porosities of 0, 0.2 0.4 and 0.6. Black dots show the SCA starting porosities (critical porosities) passes to the DEM and used to calculate the modulus over the entire porosity range.

3.4.1 Critical porosity

As is shown in the previous section the starting or critical porosity (φ_c) has a substantial effect on the moduli of the final medium. Sheng (1990, 1991) determined the critical porosity from Archie's (1942) equations for resistivity; the critical porosity is related to the tortuosity (t) and cementation (m) by:

$$t = \frac{3\varphi_c - 1}{2\varphi_c^{\,m}} \tag{3.34}$$

Sheng (1991) uses values of 1 for tortuosity and 2 for cementation. These are generally accepted values for calculating the resistivity of a clean sandstone and give a critical porosity of 0.5. For our purpose the Sheng method has two problems.

(1) We are trying to model sediment in general and not sandstone; an unconsolidated sediment has no cementation and therefore the value of m should range between 1.25 and 1.3, resulting in a critical porosity of 1 if t =1. This cannot be the case since there can be no bi-connection when there is no solid.

(2) Since Archie's is an empirical relation, the *t* and the *m* coefficients, while they do tell something about the nature of the medium, do not have direct physical meaning.

Comparing the P-wave velocities calculated using a critical porosity of 0.5 with velocities measured from experimental data (Figure 3.11) we can see that the combined SCA/DEM method predicts values that are ~0.75 kmS^{-1} too high at ~0.35 porosity. Therefore we need another method of determining the critical porosity which fits the data better and is not reliant on empirical constants.

Greer (2001) uses a version of the combined SCA/DEM method to calculate the effective medium moduli for fractured basalts. Greer defines the critical porosity as the point at which the effective medium loses shear strength, which is calculated by using the probability of interconnection developed by Schmeling (1986; Equations 4.10 and 4.11). One problem with Greer's method is that it is dependent on the ability to define the number of direct connections between inclusions at which point the system can be considered to be interconnected. This value of direct connections can range from 2 to 10 (Schmeling, 1983; O'Connell & Budiansky, 1977) and will therefore give different porosities at which the system becomes interconnected.

If we physically interpret the SCA method, inclusions of fluid are added into a matrix of solid. If the solid remains interconnected at all porosities then the medium should have some shear strength at all porosities. However when the shear modulus is calculated using the Willis (1977) SCA method (Figure 3.4), the point at which shear strength is lost occurs at a much lower porosity of ~60%. Hornby *et al.* (1994) and Sheng (1990) interpret the point at which the shear modulus falls to zero as the point at which the solid phase becomes isolated, thus preventing the transmission of a shear wave. Setting the critical porosity, according to the SCA method, at 60% provides a much better fit to the experimental data than using the 50% critical porosity suggested by Sheng (Figure 3.11). In terms of Archie's equation, tortuosity, calculated using Equation 3.49 for a critical porosity of 0.6 and assuming a cementation coefficient value of 1.25 (i.e., no cementation) is 0.757, well within the normal range of 0.35-4.78 (Bassiouni, 1994).

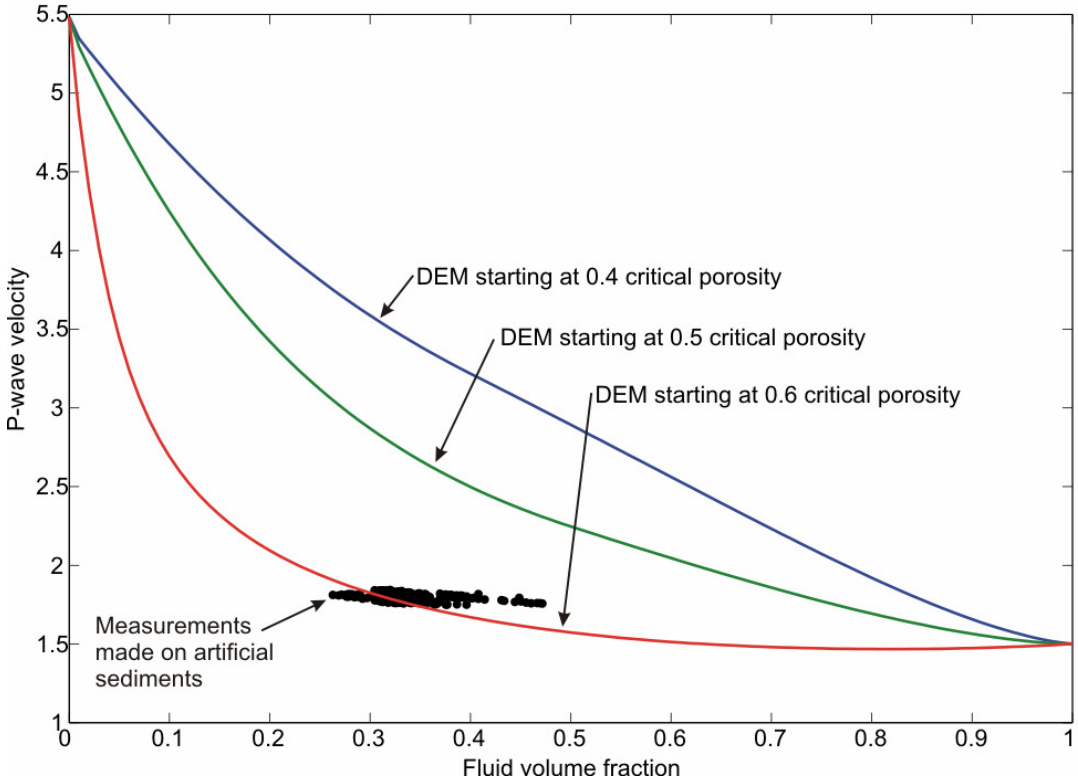

Figure 3.11 P-wave velocity versus fluid volume fraction calculated by the SCA/DEM models with different critical fluid volume fractions for inclusions with an aspect ratio of one. Black circles show P-wave velocities measured in the laboratory experiment (Chapter 5).

This combined SCA/DEM method is suitable for materials with low shear modulus such as uncemented sediments. The shear moduli of sediments are known to be low due to a low surface area of contact between the grains. However it would not be suitable for sandstones which would have higher shear moduli due to the cementation of the grains. Therefore for a sandstone Sheng's (1991) critical porosity of 0.5 is valid. However there is a continuum between uncemented sediments and consolidated rock. Therefore φ_c should decrease as the sediment becomes more consolidated. This work will only consider uncemented sediments.

Using a critical porosity of 0.6 in the SCA/DEM model means that we have departed from the approach of Jakobsen *et al*. (2000) and Chand *et al*. (2004) where a critical porosity of 0.5 was utilized.

3.4.2 Inclusion shapes

An important question to consider in the model is what shape the inclusions should take. Both Hornby *et al*. (1994) and Jakobsen *et al*. (2000) model the background material as the solid and the inclusions as the pore fluids. Determining the shape of the inclusions is difficult because real pore shapes in sediment are highly irregular due to the packing of the grains. However, the DEM and SCA methods idealize the shape of the inclusions. If the material forming the background and the inclusions are switched such that the fluid is modelled as the background and the solid grains become the imbedded inclusions, this problem is simplified. A scanning electron microscope photograph of glass beads (Figure 3.12A) shows the pore spaces between the beads to be very irregular in comparison, however the beads could easily be modelled as ellipsoids with an aspect ratio of 1. Real sediment grains (Figure 3.12B; Leighton Buzzard sand) are not perfect ellipsoids, but they are far more uniform in shape than the surrounding pore spaces. Based on these examples, a sediment composed primarily of sand could be modelled using a background medium of fluid and solid inclusions with an aspect ratio of 1.

Ocean sediments commonly contain a significant clay fraction. It would therefore be useful for a combined SCA/DEM method to be able to model clay as well as sand. Clay platelets have very low aspect ratios and are far smaller than sand grains (Figure 3.12C). The SCA and DEM models are both grain-size-independent so long as the size of the inclusion is significantly smaller than the wavelength of the transmitted seismic wave. Therefore the different sediment types can be modelled simply by changing inclusion aspect ratios. However this model does not include effects due to clay cohesive forces.

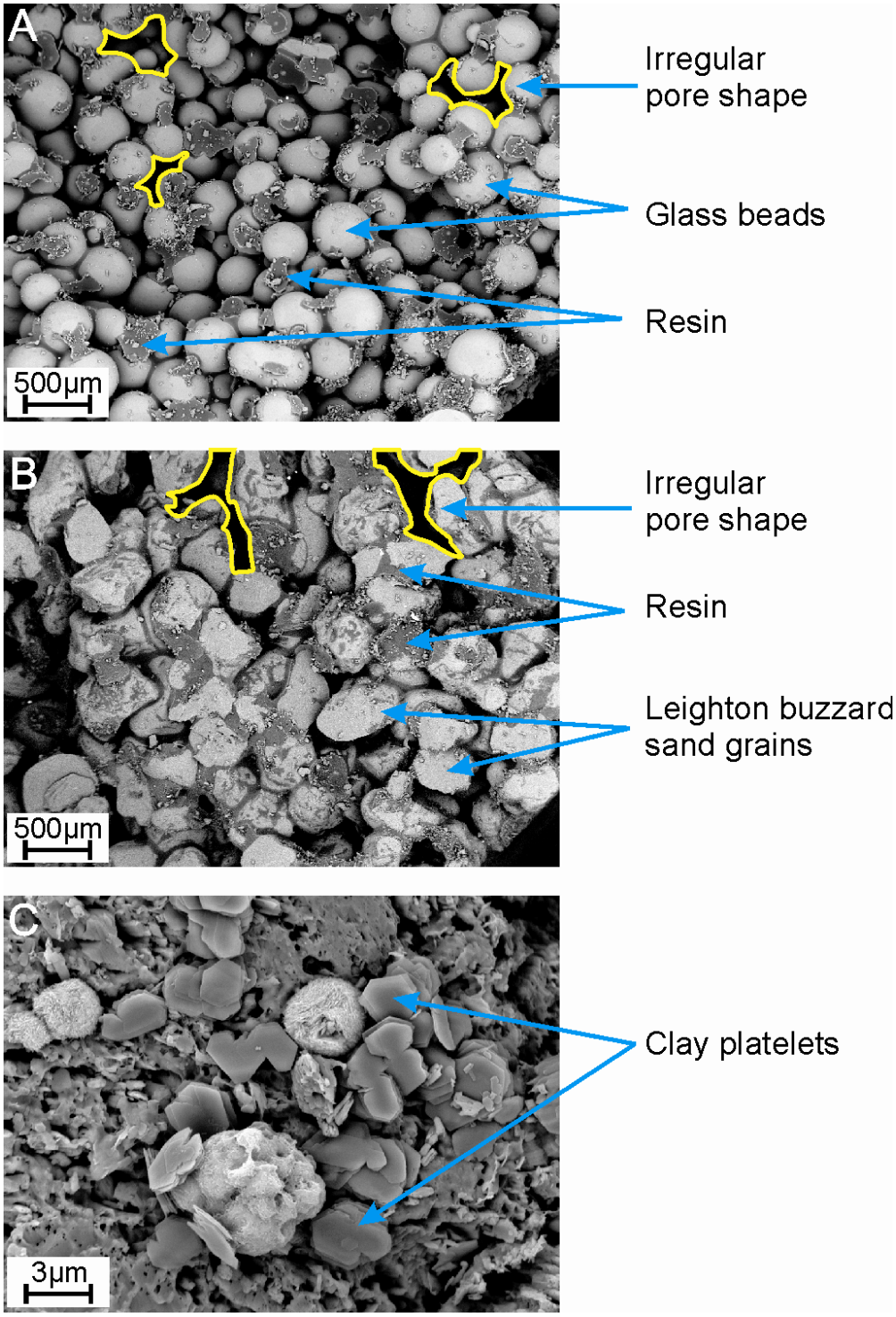

Figure 3.12 Scanning Electron Microscope (SEM) image of a variety of artificial and natural sediments showing the shape of the sediment grains and the intervening pore spaces. (A) Glass beads cemented with resin. (B) Leighton Buzzard sand cemented with resin. (C) Sandstone containing clay platelets.

3.5 Three-phase SCA/DEM modelling

A three-phase effective medium in the context of this thesis is one which contains the solid sediment phase and the pore fluid phase discussed so far, and also a hydrate phase. Hydrate saturation (S_H) is defined as the percentage of the porosity which is filled with hydrate. For example if we describe a sample to have 50% hydrate saturation then 50% of the pore space contains hydrate. We must therefore redefine porosity (φ) and fluid/brine volume fraction (β_f) which, with the two phase medium considered until now, have been used interchangeably. Porosity is defined to include hydrate. Volume fraction of fluid is defined to only include the fluid which does not contain hydrate. To continue our example, it follows that a sediment which is 50% grains and has a hydrate saturation of 0.5 will have a φ of 0.5 and a β of 0.25. Therefore:

$$\beta = \varphi(1 - S_H). \tag{3.35}$$

As described in Chapter 1, hydrate may form in the sediment in a variety of ways causing the seismic velocity to increase to different degrees. If the hydrate is located in the pore spaces then the system is said to be non-load-bearing. If the hydrate is part of the solid frame then the system is said to be load bearing. A method for adding hydrate to the two-phase SCA/DEM models is described by Jakobsen *et al*. (2000). The difference between his method and that used in this thesis is that we retain the critical porosity at the point just before shear strength is lost in the calculations.

3.5.1 Non-load bearing hydrate

To model non-load bearing hydrate the effective medium model is initially composed of just pore water and grains (Figure 3.13; Stage1). The effective medium is modelled using the 2-phase SCA/DEM method described earlier in this chapter, assuming that the fluid is the matrix and the solid grains are the inclusions. The critical porosity for such a system, when the grains have an aspect ratio of 1, is 0.6.

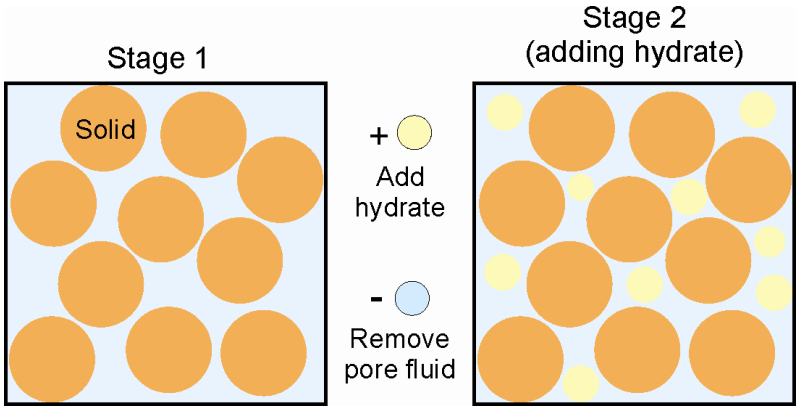

Figure 3.13 Schematic of the method used to calculate the effective moduli of a three-phase effective medium composed of hydrate (yellow), grain (orange) and pore fluid (blue) using the SCA/DEM method for non-load bearing hydrate. It should be noted that the grains in this figure should also be interconnected as well as the pore fluid, however this is difficult to represent in a two-dimensional diagram.

Hydrate is then added in small increments by the DEM method until the prescribed hydrate concentration is achieved (Figure 3.13; Stage 2). The hydrate only replaces the fluid phase, so amounts of fluid equal to the amount of hydrate added must be removed. The solid grain volume fraction remains the same. The hydrate has the same aspect ratio and orientation as the solid phase. The mathematical method is given in Appendix B.

The bulk and shear moduli for a three-phase system composed of glass beads, brine pore fluid and hydrate is shown in Figure 3.14. The hydrate has little effect on either the bulk or shear moduli until the saturation exceeds ~0.5. The effect of gas hydrate saturation is far more pronounced on the shear modulus, and is due to the combination of a high critical porosity pulling the shear modulus down to almost zero at high porosities and the hydrate existing between the grains. As with the Jakobsen *et al*. (2000) model the hydrate is given the same aspect ratio as the inclusions (i.e. the solid grains). In essence the hydrate simply forms a second set of inclusions within the model with different moduli to those of the first set. However the hydrate inclusions remain isolated from each other at all concentrations. Figure 3.15 shows the change in P- and S-wave velocities. In the S-wave velocity plot the velocity increases as porosity decreases at all hydrate saturations as expected. This trend does not occur in the P-wave velocity plot. In this plot for a given hydrate saturation the P-wave velocity decreases and then increases as porosity decreases. This is because velocity is dependent on both the effective moduli of the sediment and the bulk density. At high porosities the effect of the change in density is greater than the effect of the change in bulk and shear moduli.

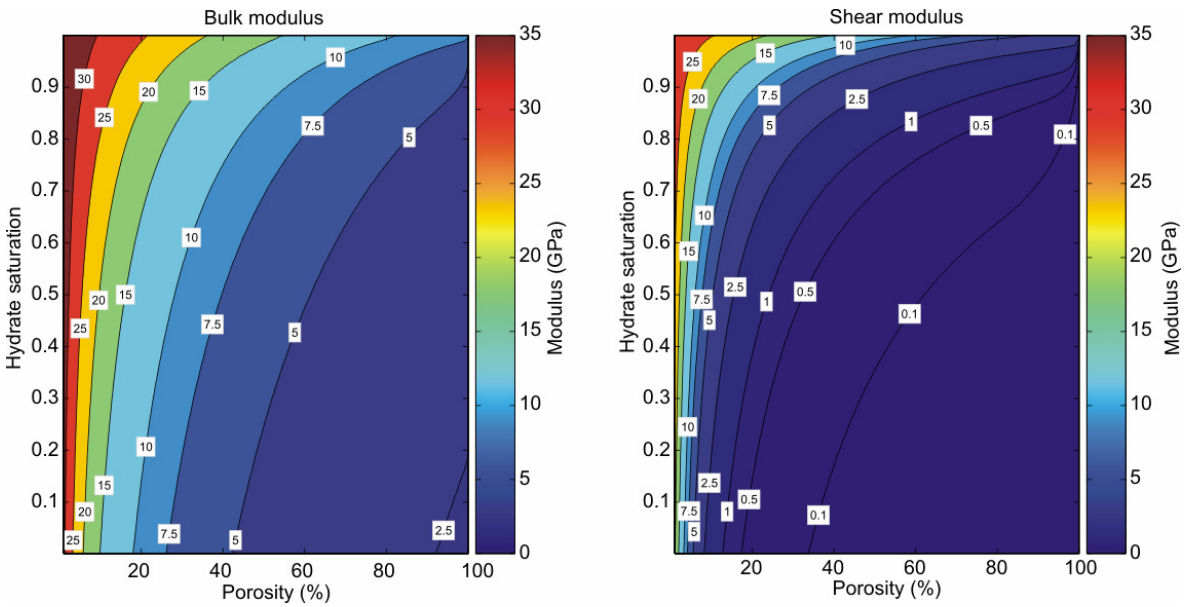

Figure 3.14 Variation of modulus with porosity and hydrate saturation for bulk (left) and shear (right) moduli, calculated using the SCA/DEM for non-load bearing hydrate. Physical properties for all three phases are given in Appendix A. Sediment grains and hydrate inclusions are spherical.

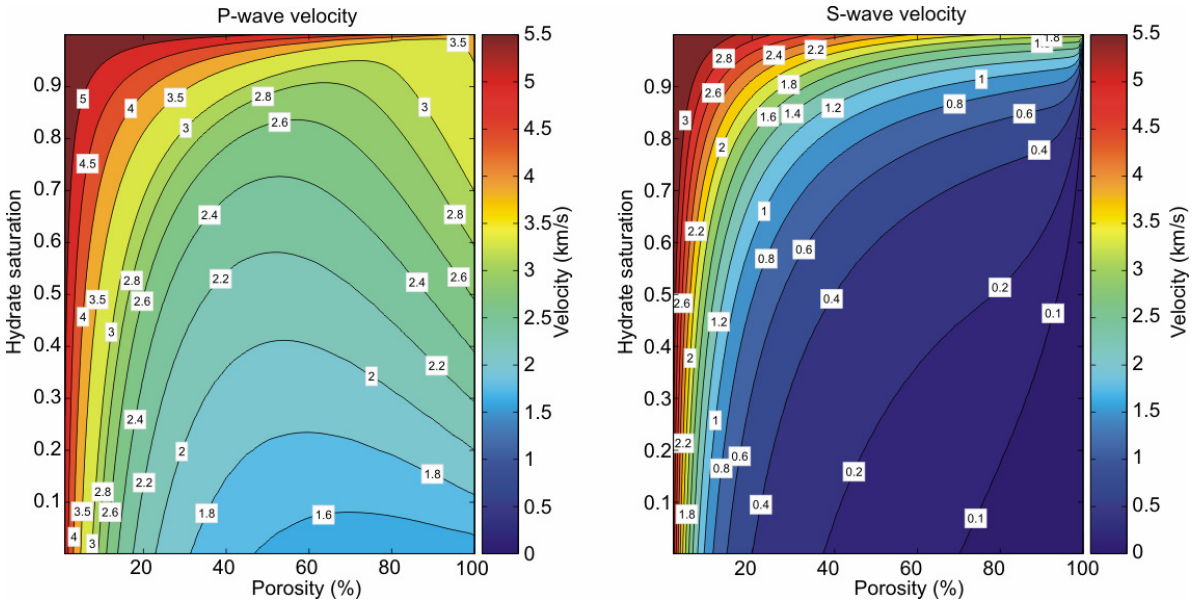

Figure 3.15 Variation of P-wave (left) and S-wave (right) velocity with porosity and hydrate saturation calculated using the SCA/DEM for non-load bearing hydrate. Sediment grains and hydrate inclusions are spherical.

3.5.2 Load bearing hydrate

To determine the effective moduli of a load bearing hydrate phase within the sediments we use the approach of Jakobsen *et al.* (2000). The method used to calculate the effective

moduli of a load bearing hydrate is similar to that for non-load bearing hydrate, except the roles of the hydrate and the pore fluids are reversed. The SCA/DEM method is first used to calculate the effective moduli of a medium containing hydrate and solid, with hydrate taking the place of the pore fluid in the background medium of the non-load bearing model. Choosing a critical porosity for this case is more difficult than for the non-load bearing hydrate case because hydrate has a non-zero shear modulus. The SCA effective medium moduli calculated for a hydrate and solid grain system shows that shear strength is not lost for any hydrate volume fraction (Figure 3.16). Since the grain and hydrate will always interact with each other there is no hydrate volume fraction at which the effective modulus equals that of the hydrate until the volume fraction of hydrate is 1. Therefore we choose to use the same critical porosity as used for the non-load bearing hydrate model, i.e. $\varphi_c = 0.6$ for an aspect ratio of 1.

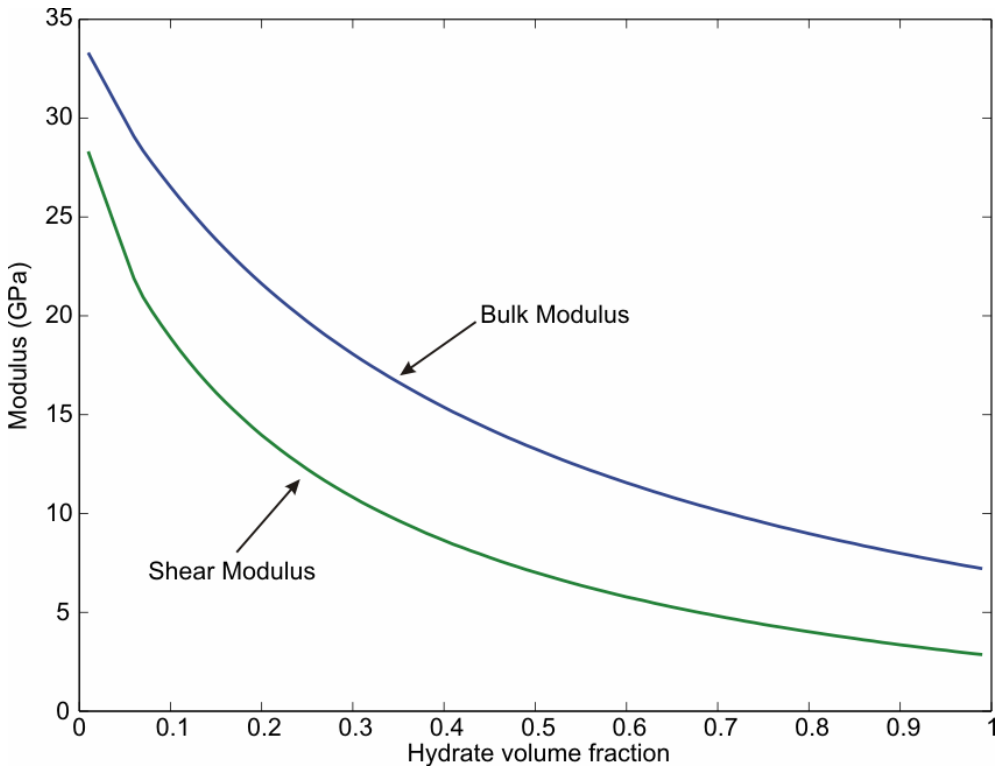

Figure 3.16 Shear and bulk moduli as a function of hydrate volume fraction for an effective medium composed of glass beads and hydrate, calculated using the SCA method.

The DEM is then used to calculate the effective moduli at all hydrate volume fractions, and fluid is added in small volumes by the DEM method. This method for calculating the load bearing hydrate system is shown schematically in Figure 3.17. The

mathematical equations are given in Appendix B. The pore fluid inclusions have the same aspect ratio as the grains and will remain isolated for all pore fluid volume fractions.

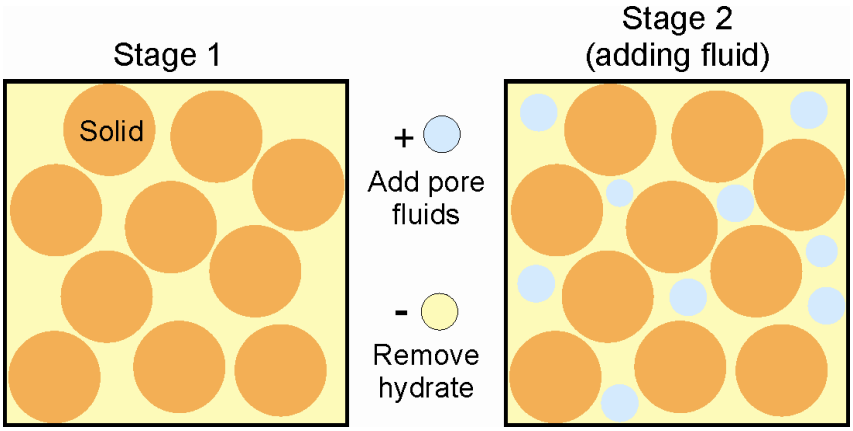

Figure 3.17 Schematic of the method used to calculate the effective modulus of a 3 phase effective medium composed of hydrate (yellow), grain (orange) and pore fluid (blue) using the SCA/DEM method for load bearing hydrate. The grains in this figure should also be interconnected as well the hydrate however this is difficult to represent in a two-dimensional diagram.

Both the shear modulus and the bulk modulus are much higher for the load bearing hydrate system (Figure 3.18) compared to the non-load bearing hydrate system (Figure 3.14).

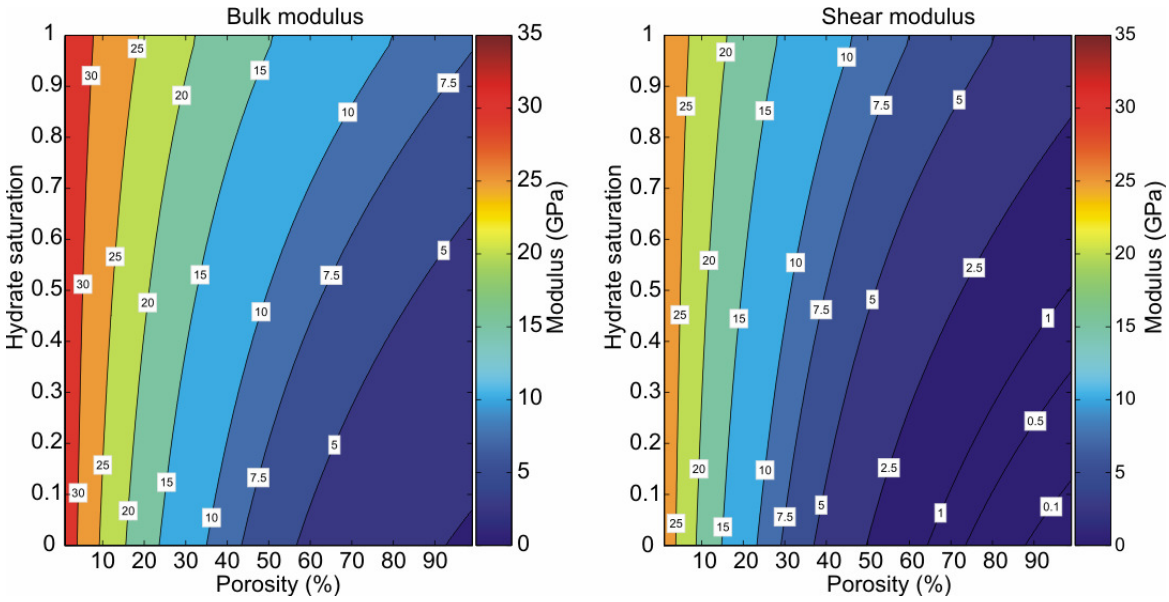

Figure 3.18 Variation of modulus with porosity and hydrate saturation for bulk (left) and shear (right) moduli, calculated using the SCA/DEM for load bearing hydrate. Physical properties for all three phases are given in Appendix A. Sediment grains and hydrate inclusions are spherical.

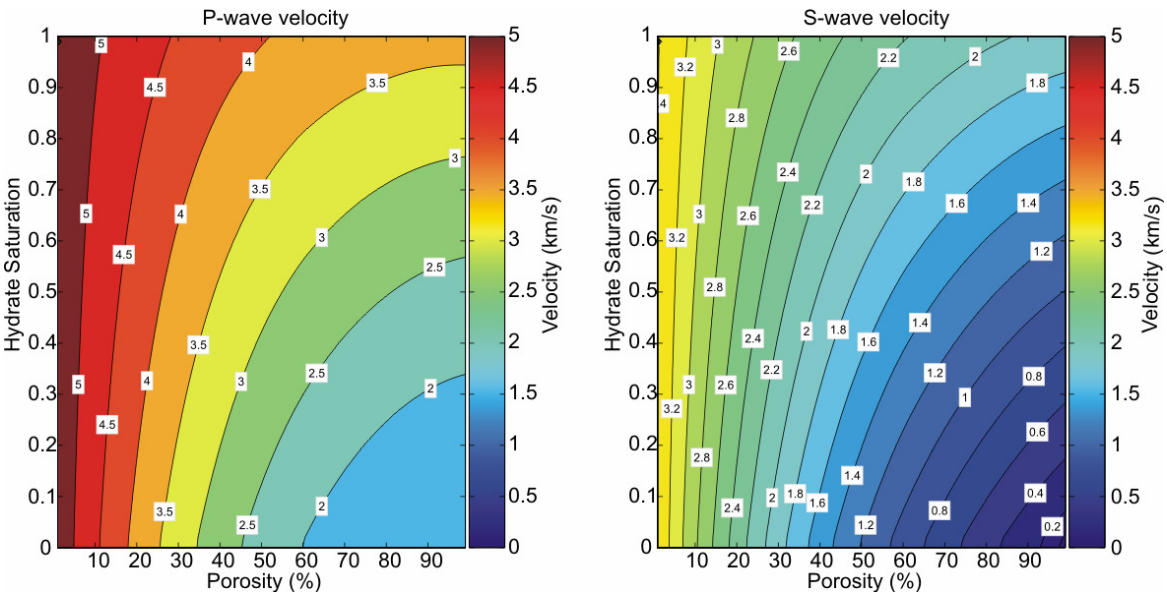

Figure 3.19 Variation of P- and S-wave velocity with porosity and hydrate, calculated using the SCA/DEM for load bearing hydrate. Sediment grains and hydrate inclusions are spherical.

3.6 Conclusion

There are a number of two-phase effective medium techniques that allow the bulk and shear moduli to be calculated. Most of these allow one phase to be interconnected and the other phase to be isolated. However, in uncemented sediments the grain and the fluid phases are both interconnected. The SCA method can model an effective medium where both phases are interconnected only for porosities between 40-60%. The DEM method calculates the moduli without changing the microstructure of the sediment. Therefore if the starting point for the DEM method is an effective medium calculated from the SCA where the fluid and the solid are both interconnected, then the effective moduli calculated by the combined method at all porosities will remain valid for the case of both phases being fully interconnected. The critical porosity for grains with no cementation has been determined to be 60%, the point at which the shear strength is lost from the SCA method. The model described is purely physical with no empirical constants and allows hydrate to be added in both a load bearing and non-load bearing manner. The location of the hydrate in the model has been shown to cause large differences in the calculated bulk and shear moduli, and consequently in the P- and S-wave velocities.

Chapter 4. Effective Resistivity

4.1 Introduction

Electric or electro-magnetic surveys of the sea floor provide valuable information about the macro and microscopic properties of the sediments or other materials beneath it. Resistivity is highly variable near the Earth's surface, covering a range of over 8 orders of magnitude. The resistivity of submarine sediments is primarily dependent on porosity, the salinity of the conducting pore fluids, the geometry of the pores and temperature. There are a range of techniques used for measuring the electrical properties of the Earth's interior. These include self potential, induced polarization, DC resistivity, magnetotellurics, magnetometric resistivity, controlled source electromagnetic surveying and many borehole logging techniques. The most common relationship for the interpretation of electrical data, especially in the petroleum industry, is Archie's (1942) law. A problem arising from all such interpretations is that Archie's law is empirical. To move away from this, we need a description of the effective (or bulk) resistivity of a medium in which the resistivities of the individual components, the volume fraction of the components, and the geometry of the individual components relative to each other are defined.

This chapter starts by describing some of the exisiting effective medium methods for determining the effective resistivity of a multi-component medium. The effective resistivity is defined as the overall macroscopic or bulk resistivity of a multi-component medium. It then describes the development of a numerical model for calculating the effective resistivity of a sediment based on the shape of the grains and the average distance between them. The chapter ends with two methods for including gas hydrate within the electrical model based on the morphology of the hydrate.

There are a number of different electrical effective medium models mentioned in this chapter. To help avoid confusion between them the symbols, type and terminology are given in Table 4.1.

Symbol	Type of model	Terminology
$\rho_{HS,conductive}$	Bound	HS Conductive bound
$\rho_{HS,resistive}$	Bound	HS Resistive bound
ρ_{iso}	Bound	Krajew resistive bound
ρ_{gm}	Effective medium model prediction	Geometric Mean effective resistivity
ρ_{geo}	Intermediate model prediction	Geometric effective resistivity*
ρ_{GPL}	Effective medium model prediction	Geometric Path Length effective resistivity*
$\rho_{GPL,nonblock}$	Effective medium model prediction	Geometric Path Length non-pore-blocking effective resistivity*
$\rho_{GPL,block}$	Effective medium model prediction	Geometric Path Length pore-blocking effective resistivity*

Table 4.1 Electrical effective medium model symbols, type and terminology. * indicates models that have been developed for this thesis.

4.2 Bounds

When estimating the effective resistivity of a mixture of phases, the volume fraction of each of the phases as well as the resistivity of the phases and the geometric arrangement of the phases relative to each other needs to be known. If the geometrical arrangement of the phases is not known then only the upper and lower bounds can be predicted.

4.2.1 Hashin-Shtrikman bounds

The Hashin-Shtrikman (HS) bounds (Hashin & Shtrikman, 1962) are effective conductivity bounds that give the narrowest possible bounds without defining the geometry between components of a two-phase medium. All the components within this medium are themselves isotropic and homogeneous. The upper bound represents the maximum conductivity the isotropic composite can have. This occurs when the fluid (conductive phase) is totally interconnected and the solid (resistive phase) is totally isolated. The HS lower or resistive bound represents the bound when the fluid phase is completely isolated and the solid phase is totally interconnected. No information is given about the geometry of the pores apart from that the system is required to be isotropic and the pores are either totally interconnected or totally isolated. The bounds (Figure 4.1) are given by:

$$\frac{1}{\rho_{HS,conductive}} = \sigma_{HS,conductive} = \sigma_f + (1-\beta)\left(\frac{1}{\sigma_s - \sigma_f} + \frac{\beta}{3\sigma_f}\right)^{-1}, \quad (4.1)$$

$$\frac{1}{\rho_{HS,resistive}} = \sigma_{HS,resistive} = \sigma_s + \beta\left(\frac{1}{\sigma_f - \sigma_s} + \frac{1-\beta}{3\sigma_s}\right)^{-1}, \quad (4.2)$$

where:

$\sigma_{HS,conductive}$ = upper or conductive HS bound of effective conductivity,

$\sigma_{HS,resistive}$ = lower or resistive HS bound of effective conductivity,

$\rho_{HS,conductive}$ = conductive HS bound of the effective resistivity,

$\rho_{HS,resistive}$ = resistive HS bound of the effective resistivity,

$\sigma_s = \frac{1}{\rho_s}$ = conductivity of the solid,

$\sigma_f = \frac{1}{\rho_f}$ = conductivity of the fluid,

β = volumetric fraction of the fluid (assumed to be equal to the porosity).

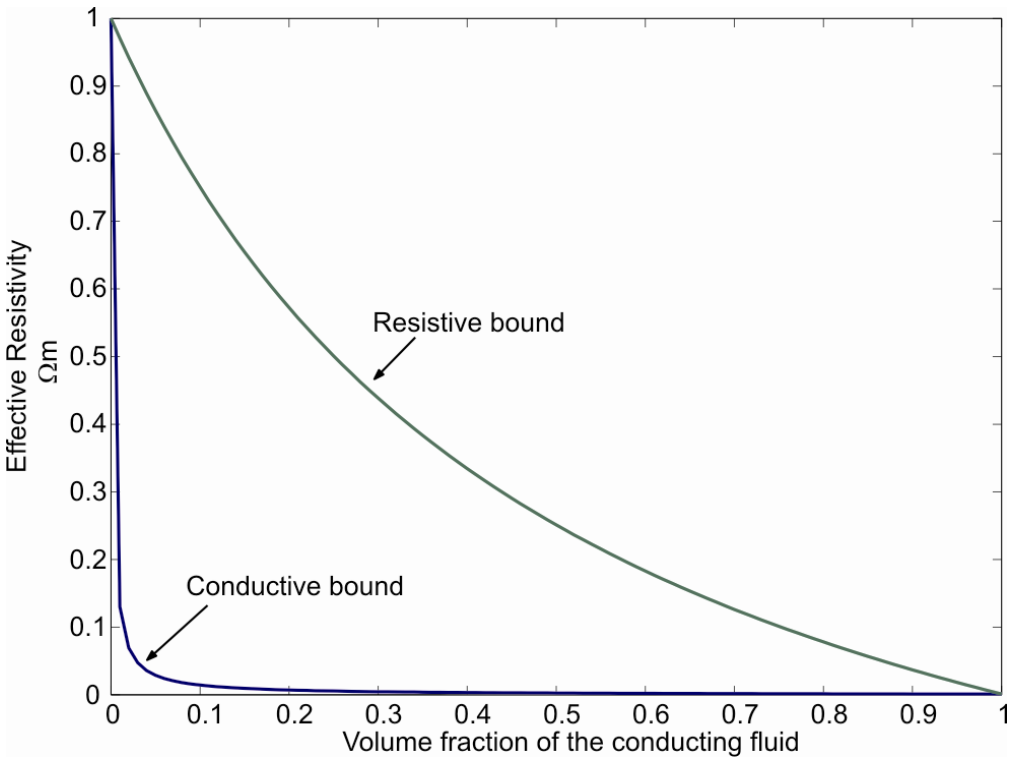

Figure 4.1 Upper and lower HS bounds of effective resistivity for a solid-fluid mixture. The solid phase has a resistivity of 1 Ωm and the fluid has a resistivity of 0.001 Ωm.

4.2.2 Semjonow and Krajew equations

An alternative to the HS resistive bound was given by Krajew (1957) based on equations derived by Semjonow (1948). All the fluid inclusions are assumed to be isolated (similar to the HS lower bound) and spheroidal, and the solid is totally interconnected. Unlike the HS bounds more information is given about the geometry of the pores. The Krajew bound of effective resistivity is given by:

$$\frac{1}{\rho_{iso}} = \sigma_{iso} = \frac{1}{3}(\sigma_1 + \sigma_2 + \sigma_3), \tag{4.3}$$

$$\sigma_{i=1,2,3} = \sigma_s \left(\frac{(1-\beta)(n_i - 1)\sigma_s + (n_i - (n_i - 1)(1-\beta))\sigma_f}{(n_i - 1 + \beta)\sigma_s + (1-\beta)\sigma_f} \right), \tag{4.4}$$

$$n_1 = n_2 = \frac{-2h^3}{h - (1+h^2)\tan^{-1} h}, \tag{4.5}$$

$$n_3 = \frac{-2h^3}{(1+h^3)(\tan^{-1} h - h)} \tag{4.6}$$

$$h = \sqrt{\alpha^{-2} - 1}, \tag{4.7}$$

where σ_{iso} is the bound on effective conductivity of the medium, ρ_{iso} is the bound on effective resistivity of the medium and α is the aspect ratio of the pores. Figure 4.2 shows how the resistivity bound versus the volume fraction of the conducting fluid changes with aspect ratio for a two-phase effective medium.

The Krajew resistive bound model predicts higher resistivities than the HS resistive bound when the aspect ratio of the pores is 1. Therefore the resistivity of an effective medium should lie between the HS conductive bound and the lower of the HS resistive bound or the Krajew bound. Which this will be will depend on the aspect ratio of the pores.

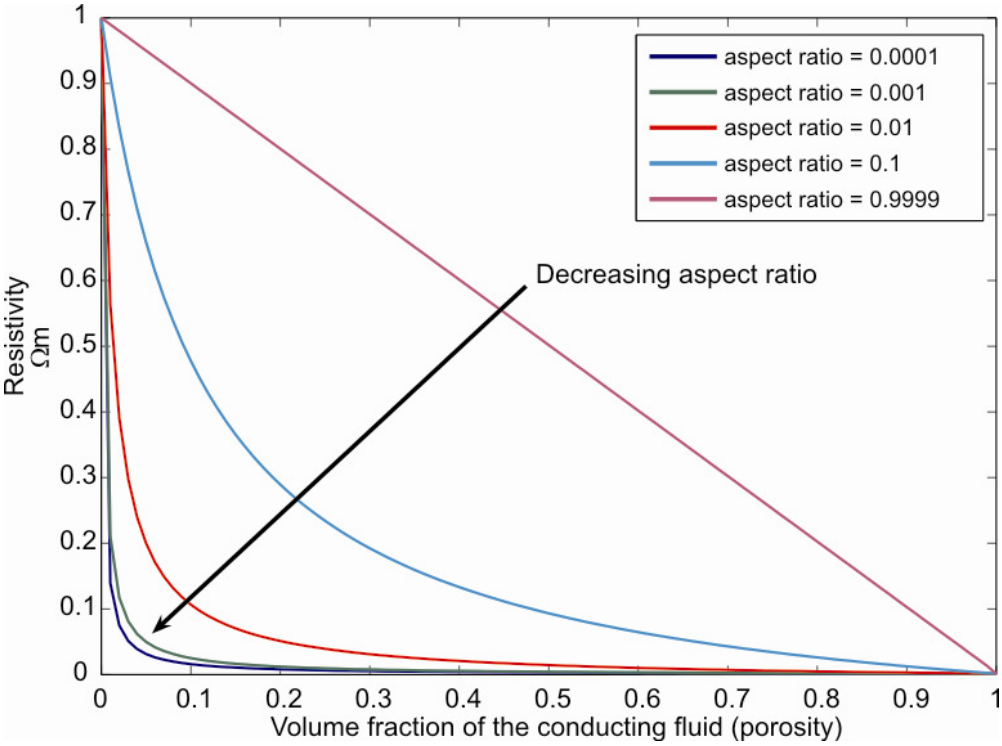

Figure 4.2 Krajew (1957) lower bound of effective resistivity versus volume fraction of the fluid in a solid-fluid mixture for different pore aspect ratios.

4.3 Partially interconnected systems

The previous effective resistivity models of a composite medium only deal with media in which the fluid phase is totally interconnected or totally isolated. In real systems both the solid and fluid phase may be partially interconnected.

4.3.1 Probability of interconnection

A method of calculating the probability of the interconnection is given by Schmeling (1986). The probability of interconnection between two adjacent pores is dependent on the porosity and the aspect ratio of the pore spaces. The higher the porosity and the smaller the aspect ratio of the pores then the greater the probability of interconnection. Schmeling's (1986) approach describes the probability (P_i) of finding i centres of neighbouring inclusions within the volume of one specific inclusion (V) as given by:

$$P_i = \left(\frac{V_t - V}{V_t}\right)^{N-i} \left(\frac{V}{V_t}\right)^{i} \left(\frac{N}{i}\right), \tag{4.8}$$

where V_t is the total volume of the material and N is the total number of inclusions. Schmeling used this approach to calculate the numbers of direct connections to neighbouring inclusions (n) as a function of fluid volume fraction (β) and aspect ratio (α). The approach is however time consuming and Schmeling approximated it to a semi-empirical formula with a standard deviation of about 2%:

$$n(\alpha,\beta) \approx c_1 + \left(\frac{c_2}{\alpha}\right)\beta\,, \tag{4.9}$$

where c_1 and c_2 are constants with the values of 5.65 and 1.72 respectively. When $n = 0$ the inclusions are totally isolated and when $n \geq n_{max}$ the inclusions are considered to be totally interconnected. n_{max} is the number of connections that each inclusion needs for the medium to be considered fully interconnected. The value of n_{max} therefore is critical. Schmeling (1983) determines that an appropriate value for n_{max} should lie between 4 and 10. O'Connell & Budiansky (1977) give crack densities with corresponding values of n of between 2 and 4. Therefore Schmeling (1986) uses $n_{max} = 4$ for a totally interconnected fluid. The probability of interconnection (Figure 4.3) is given by:

$$P_i(\alpha,\beta) = \begin{cases} n(\alpha,\beta)/n_{\max} & n \leq n_{\max} \\ 1 & n \geq n_{\max} \end{cases}. \tag{4.10}$$

The value P_i plotted in Figure 4.3 is strictly the probability that a single pore space interconnects with one or more of its neighbours. For a medium containing large numbers of pore spaces this can be taken as a probabilistic estimate of the proportion of pore spaces that are interconnected. Similarly, we can estimate probabilistically that a proportion (1-P_i) of pore spaces are isolated.

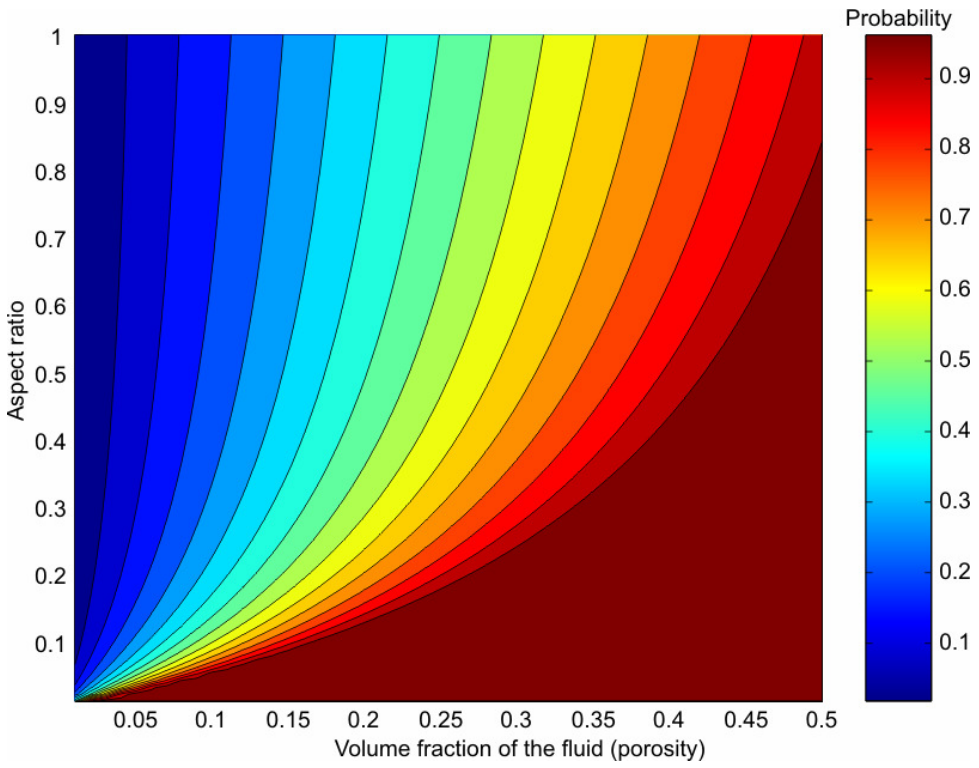

Figure 4.3 Contoured probability of interconnection for a two phase system (Equations 4.9 and 4.10 with n_{max} = 4) with varying volume fraction and pore space aspect ratio of the fluid phase.

4.3.2 Conductivity of a two-phase system with varying interconnection

Greer (2001) uses the HS conductive bound ($\sigma_{HS,\ conductive}$;Equation 4.1) and the Krajew resistive bound (σ_{iso}; equation 4.3), together with the probability of interconnection ($P_i(\alpha,\beta)$); Equation 4.10) to derive an estimate of the effective conductivity of a two-phase system, taking account of varying degrees of interconnection. When $P_i(\alpha,\beta)$ = 1 the conductivity is given by the HS conductive bound. When $P_i(\alpha,\beta)$ = 0 the conductivity is given by the Krajew resistive bound. If $0<P_i(\alpha,\beta)<1$ then a good approximation is given by a geometric mean between the two bounds (Greer, 2001; Figure 4.4):

$$\frac{1}{\rho_{gm}} = \sigma_{gm} = \sigma_{HS,conductive}^{\ P_i} \times \sigma_{iso}^{\ (1-P_i)}, \qquad (4.11)$$

where σ_{gm} is the estimated effective conductivity and ρ_{gm} is the estimated effective resistivity.

A problem with this approach is that it only calculates the resistivity for a system where the conductive inclusions are fluid and spheroidal. This limitation would be

acceptable for solid rock with fluid filled fractures, but a sediment rarely appears like this. To use this method for a sediment, the inclusion terms in the equations, which were originally assigned the values for fluid parameters, should instead be assigned the values for the solid parameters. If this is done the HS conductive bound effectively becomes the resistive bound and the Krajew resistive bound becomes a conductive bound ($\sigma_{iso,\ conductive}$). Unfortunately there is a problem using probability of interconnection when the solid is considered to be the inclusion because the probability of interconnection of the fluid cannot be calculated from the probability of the interconnection equations 4.9 and 4.10. These equations require the fluid pores to be spheroidal which they no longer are. Also if we consider a sediment filled with spheroidally shaped grains, the fluid should always be completely interconnected at all porosities. In that case the effective resistivity of the medium would be that of the HS conductive bound. Although for these reasons Greer's (2001) method of calculating the effective resistivity cannot be used for a porous sediment, the idea of navigating between two bounds can still be used.

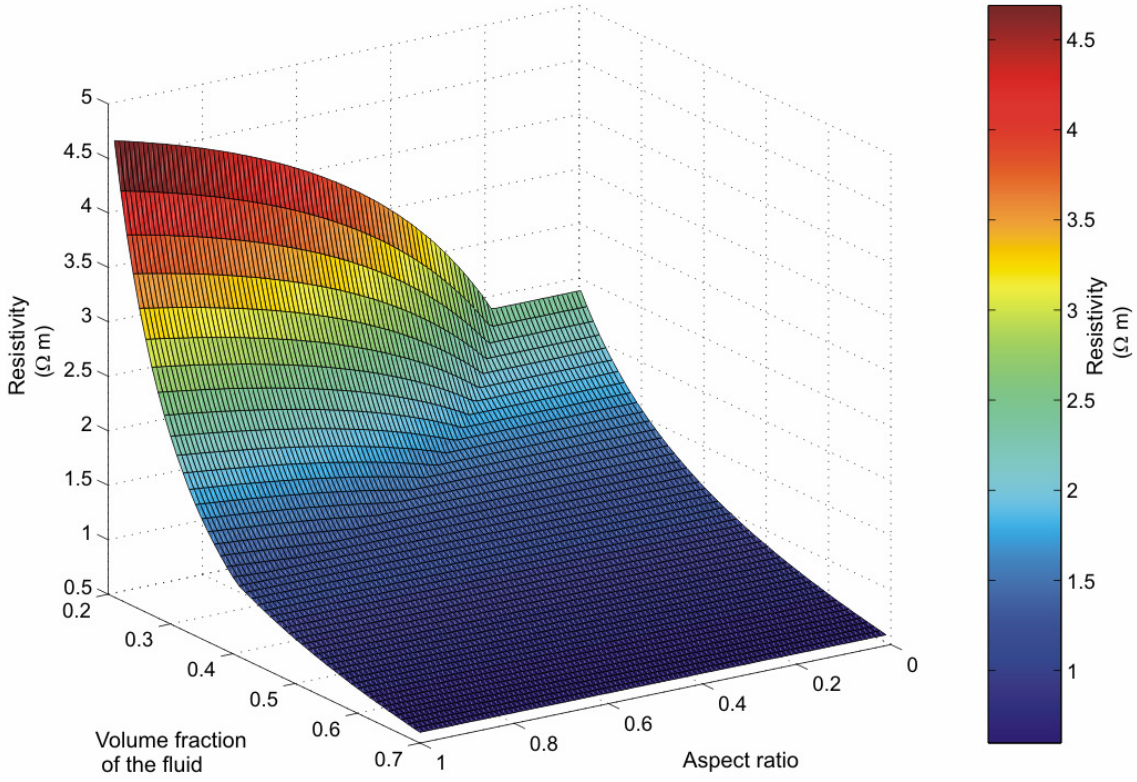

Figure 4.4. Effective resistivity of a two-phase system with spheroidal inclusions of conductive fluid for different aspect ratios and fluid volume fraction. The solid phase has an electrical resistivity of 3×10^{11} Ωm and the fluid phase of 0.36 Ωm. Resistivity is calculated using the geometric mean (Equation 4.11).

4.4 Average path length resistivity for a sphere (aspect ratio = 1)

The presence of grains in a fluid affects the resistivity in several ways: (1) The grains reduce the cross-sectional area of conduction through which the current must flow. This also means that the amount of current which must flow through the resistive phase is increased. This is accounted for in the HS bounds. (2) Since in general the current is no longer directly aligned with the ambient electric field there is an increase in the 'path-length' as the current will preferentially travel around the grains rather than through them. (3) The grain density influences the proportion of the path length which is deviated in order to travel around the grains and the proportion of the path length which is not deviated. This section will investigate the latter two points and will develop an effective medium model which takes into account all three points.

We start by investigating the influence on the effective resistivity of a sediment by the average increase in path length that the electric current has to take to get through the sediment. This can be represented as a geometric factor. Using the path a current takes through a formation to determine the effective resistivity has previously been investigated by Herrick and Kennedy (1994). Their model assumes that the formation can be represented as a solid volume (representing the matrix) with a series of tubes running through it representing the pores. A geometrical parameter can be calculated from the size, shape and number of tubes and then used to determine the effective resistivity of the formation. The problem with this method is that it cannot completely represent the complex pore geometry observed in sediments. Rather than trying to model the complex shapes of pores, the geometric factor developed in this thesis concentrates on estimating the change in current path caused by the grains. The electric current will take the shortest available route through the sediment but this is longer than the actual length of sediment because the current must go around the grains (Figure 4.5). In order to calculate the increase in path length the grains of a sediment are idealized. A sphere, an ellipsoid with an aspect ratio of one, is the simplest shape and can be used to model a sand. Assuming that the increase in path length is due to a spherically shaped grain, the increase can be up to 57% (geometric factor = $\pi/2$) causing the resistance of the fluid to increase by the same amount. This value assumes that the electric current hits at the apex of the sphere and travels around the grain to the point at which the current continues along the same path.

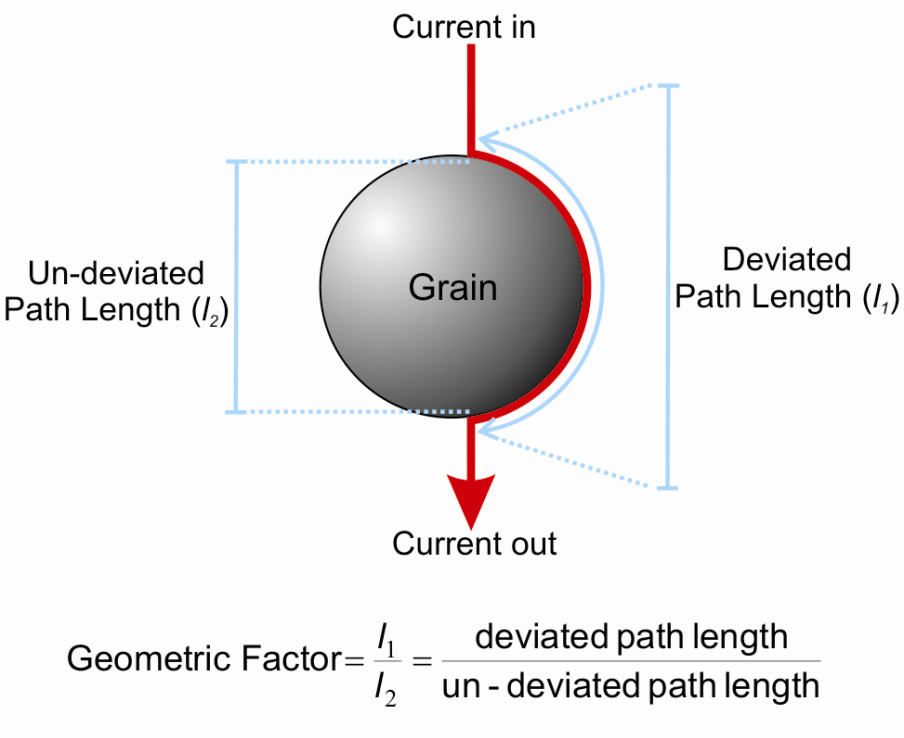

Figure 4.5. Diagram of a grain showing the increase in path length of a current as it passes around the grain.

4.4.1 Average increase in path length

Assuming that the current hits one of the grains the average increase in path length needs to be calculated. It is assumed that when the current encounters the grain it will travel around the grain until it reaches a point at which it can continue in the fluid along the same path. This allows the current to redistribute itself as it passes the grain (Figure 4.6). It also means that the current will travel a maximum of half of the way around the grain if it encounters the grain at the apex. Using this simple model we can assume that (1) a current path that does not directly encounter a grain will suffer no deviation. (2) The current path that encounters a grain is deviated around its circumference until it reaches the corresponding point on the other side.

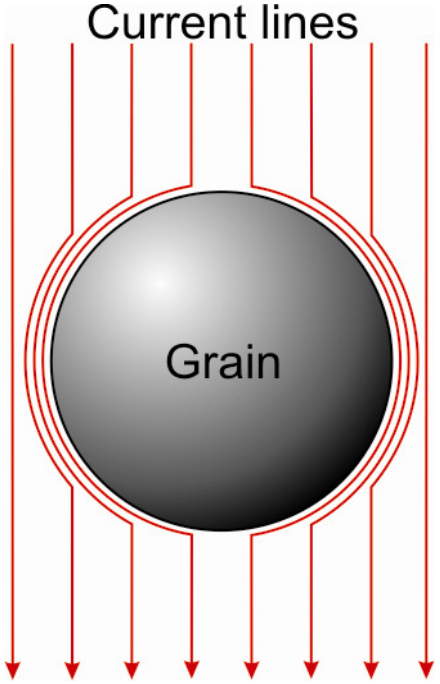

Figure 4.6 Deviation and redistribution of the electric current around a grain.

To calculate the geometric factor, the fractional increase in path length, both the deviated path length (l_1) and the un-deviated path length (l_2) first need to be calculated. Figure 4.7 shows the relationship between l_1 and l_2.

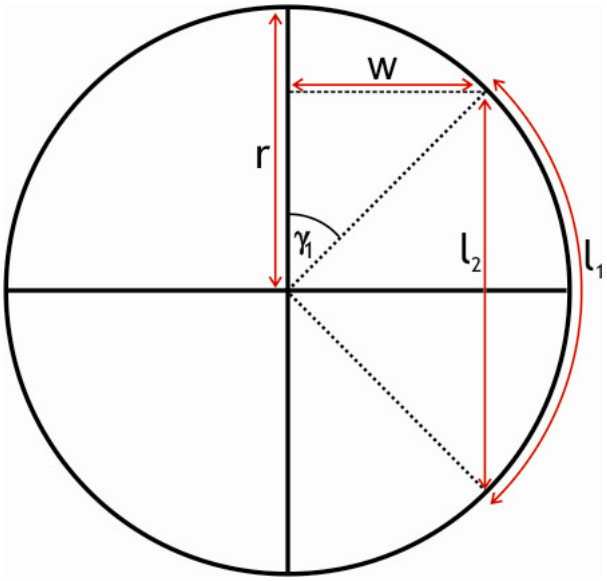

Figure 4.7 Schematic diagram of a spherical grain used to calculate the geometric factor in Equations 4.12-4.17.

In this case:

$$\text{deviated path length } (l_1) = 2\left[\frac{\pi r}{2} - r\gamma_1\right] = 2\left[\frac{\pi r}{2} - r\sin^{-1}\left(\frac{w}{r}\right)\right], \qquad (4.12)$$

$$\text{un-deviated path length } (l_2) = 2\sqrt{r^2 - w^2}\,, \qquad (4.13)$$

where:

$$w = r\sin\gamma_1 \qquad (4.14)$$

The geometrical factor (g) can then be calculated as follows:

$$\text{geometric factor } (g) = {}^{l_1}\!/_{l_2} = \frac{\frac{\pi r}{2} - r\gamma_1}{\sqrt{r^2 - (r\sin\gamma_1)^2}} = \frac{\frac{\pi}{2} - \gamma_1}{\sqrt{1 - \sin^2\gamma_1}}, \qquad (4.15)$$

Because both l_1 and l_2 are proportional to the radius the r's cancel out. The geometric factor is therefore independent of the size of the grain. This is an important result for the practical application of any effective medium model.

When viewed from above the grain appears as a circle, on which the current may hit at any point (Figure 4.8).

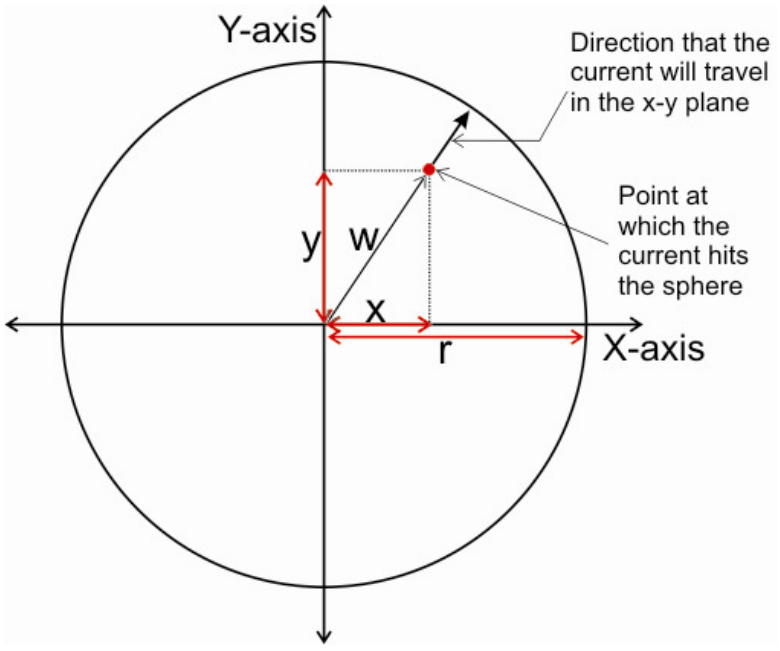

Figure 4.8 View of the grain from above (i.e. the current is travelling into the page).

To obtain the average geometric factor (G) the ratio must be calculated at every point over the grain's crosS-section.

$$G = l_{1ave} \Big/ l_{2ave} = \int_{x=0}^{r} \int_{y=0}^{\sqrt{r^2-x^2}} \frac{l_1}{l_2}.dydx = \frac{\int_0^r \int_0^{y=\sqrt{r^2-x^2}} l_1.dydx}{\int_0^r \int_0^{y=\sqrt{r^2-x^2}} l_2.dydx} \approx \frac{\sum_{x=0}^{x=r} \sum_{y=0}^{y=\sqrt{r^2-x^2}} l_1}{\sum_{x=0}^{x=r} \sum_{y=0}^{y=\sqrt{r^2-x^2}} l_2}, \quad (4.16)$$

where:

$$w = \sqrt{x^2 + y^2}\ . \quad (4.17)$$

x and y are the x and y coordinates of the point where the current hits the grain. l_{1ave} and l_{2ave} are the average l_1 and l_2 values over the entire sphere. Equation 4.16 is written in terms of x and y (Cartesian coordinates) rather than polar coordinates so that the sampling is even over the whole of the grain surface. Using polar coordinates causes the sampling to be denser at the apex than at the equator and the summation would have to be weighted to remove this. Equation 4.16 has been solved numerically with decreasing values of dx (=dy) until a stable solution of G is determined (Figure 4.9). For a sphere the geometric factor is 1.178 (4 s.f.).

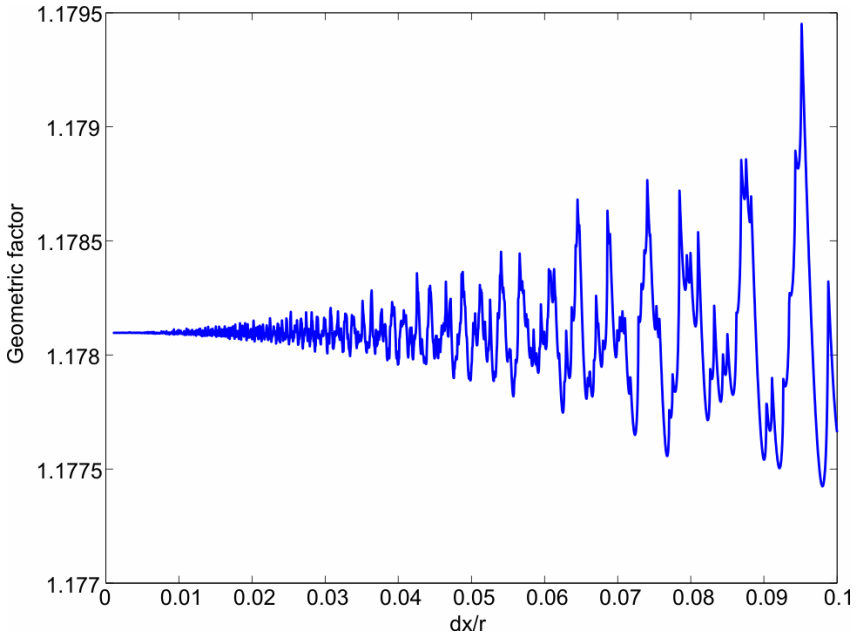

Figure 4.9 Stabilization of the average geometric factor (G) as dx (=dy) changes (Equation 4.16).

The geometric factor is then multiplied by the resistivity of the fluid, to give a new, higher, fluid effective resistivity which accounts for the extra distance travelled by the electrical current. This new fluid effective resistivity is then used with the HS conductive bound to give a new geometric effective resistivity of the medium (ρ_{geo}):

$$\frac{1}{\rho_{geo}} = \sigma_{geo} = \frac{\sigma_f}{G} + (1-\beta)\left(\frac{1}{\sigma_s - \frac{\sigma_f}{G}} + \frac{G\beta}{3\sigma_f}\right)^{-1} . \qquad (4.18)$$

4.4.2 Mean free path length

The geometric factor, as calculated, cannot simply be applied to the HS conductive bound at all porosities because this will always have the effect of increasing the estimated resistivity. This would cause the estimated resistivity of the medium to be greater than the resistivity of the fluid at 100% porosity. Therefore a method is needed to determine the percentage of the fluid to which the geometric factor must be applied, so that at 100% porosity the geometric factor is not applied.

It can be seen in Figure 4.10, that the current will spend a certain proportion of the total path length being deviated around the grains, with (1- that proportion) of the path length being un-deviated. The individual proportions will depend on the porosity of the sediment. Calculating the proportions of the total length that the current spends deviated and undeviated allows us to navigate between the geometrically altered bound and the conductive HS bound.

To calculate the average distance between the grains, an adapted version of the mean free path, which is used in the kinetic theory of gases to calculate the average distance between molecule collisions, can be used. The definition of the mean free path (L) is taken as the length (l) of a path divided by the number of collisions in that path. In kinetics this is given as:

$$L = \frac{1}{\sqrt{2} n_v S_c} , \qquad (4.19)$$

where n_v is the number density of particles and S_c is the effective collision crosS-section.

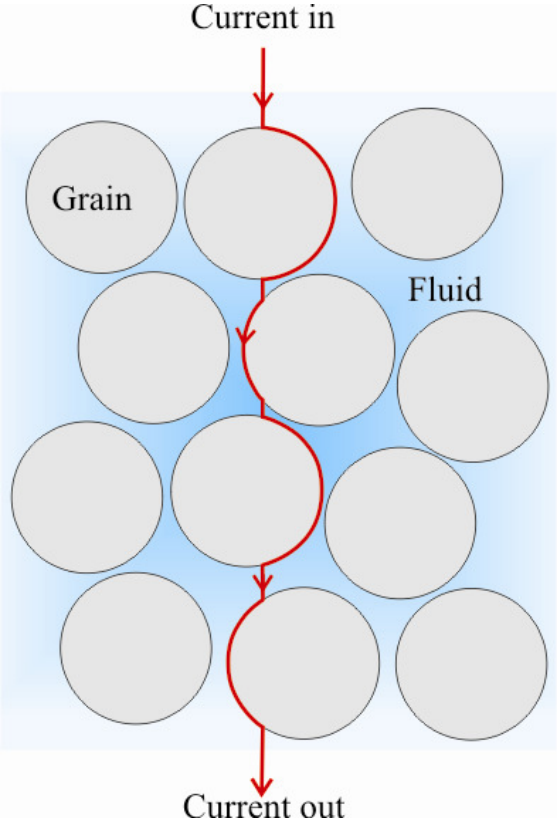

Figure 4.10 Path of electric current through a medium comprising resistive spherical grains and conductive fluid.

The $\sqrt{2}$ term in Equation 4.19 is included because in kinetics the molecules are considered to be moving. Since we are considering deposited sediments all of the grains are stationary and therefore this term can be left out. In kinetics the effective collision cross section (S_c) is given by πd^2 where d is the diameter of the molecules. It is assumed that both the molecules have volume. In the case of an electric current encountering a grain, the electric current element can be said to have infinitely small crosS-section and the collision cross section will therefore be solely dependent on the crosS-section of the grain (Figure 4.11). Therefore S_c will be given as πr^2.

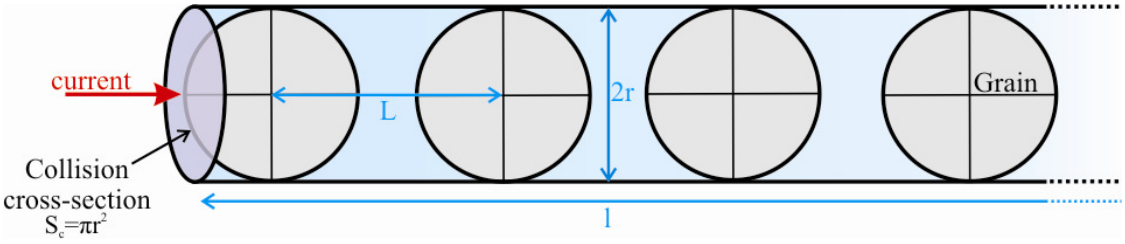

Figure 4.11 Schematic diagram using to calculate the mean free path (*L*) between spherical grains of radius *r*.

The number density (n_v) is given by:

$$n_v = \frac{\text{number of grains } (n_g)}{\text{volume they occupy}} = \frac{n_g}{\pi r^2 l}. \tag{4.20}$$

The mean free path (L) is then given by:

$$L = \frac{1}{\pi r^2 \dfrac{n_g}{\pi r^2 l}} = \frac{l}{n_g}, \tag{4.21}$$

and for a sediment with porosity β the number of grains (n_g) is given by:

$$n_g = \frac{\text{volume of all grains}}{\text{volume of a single grain}} = \frac{\pi r^2 l(1-\beta)}{\frac{4}{3}\pi r^3} = \frac{l(1-\beta)}{\frac{4}{3}r}. \tag{4.22}$$

Therefore for an imaginary electric current line passing through a sediment with porosity β:

$$L = \frac{l}{l(1-\beta)\Big/\frac{4}{3}r} = \frac{4r}{3(1-\beta)}. \tag{4.23}$$

In this equation L, the mean free path length, represents the mean distance between grain centres. L is plotted in Figure 4.12 and can be used to determine the deviated and un-deviated proportions of the total path length though a composite medium.

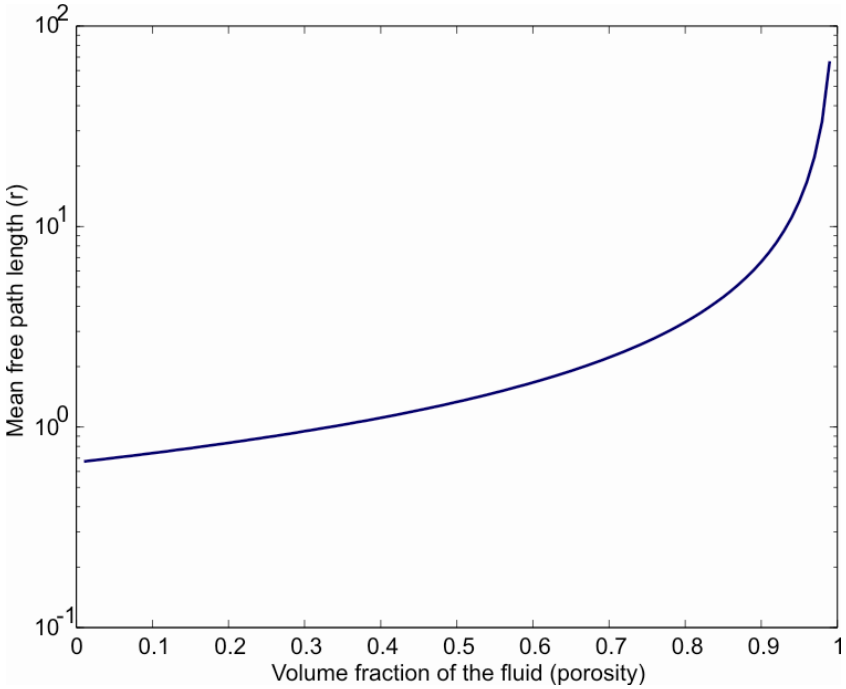

Figure 4.12 The mean free path length (Equation 4.23) of a medium containing spherical grains of radius *r*, versus porosity.

If we consider vertical current flow and grains of finite size then the geometric relationship between the average un-deviated path length (l_{2ave}), grain radius (r), and the mean free path (L) can be seen in Figure 4.13.

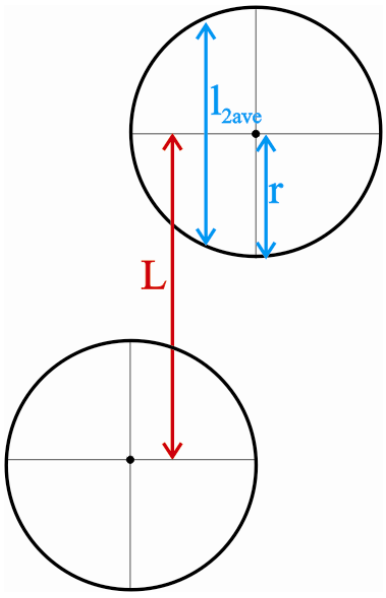

Figure 4.13 The relationship between *L*, *r* and l_{2ave}.

Using Equation 4.23 for L and Equation 4.16 for l_{2ave} we can calculate the proportions of the total path length that are deviated by grains and that pass undeviated through the fluid (F_{grain} and F_{fluid} respectively):

$$\text{Deviated proportion of total path length } (F_{grain}) = \frac{l_{2ave}}{L}, \qquad (4.24)$$

$$\text{Un-deviated proportion of the total path length } (F_{fluid}) = 1 - F_{grain}. \qquad (4.25)$$

Because both L and l_{2ave} are proportional to the radius of the grains, the deviated and un-deviated proportions are independent of the radius and only dependent on the porosity. Figure 4.14 shows the variations in these proportions over a range of porosities. It shows a linear relationship between the fraction of fluid and the deviated proportions of total path length. It can be seen that at 100% fluid the deviated proportion is zero and at 100% grain fill the current is always deviated.

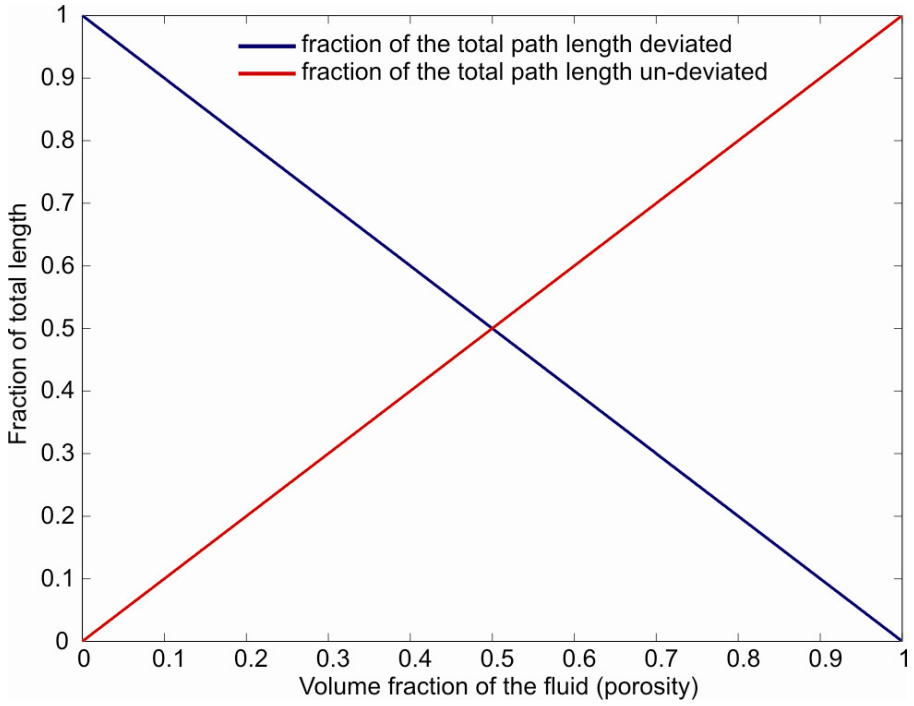

Figure 4.14 The fractions of the total path length that are deviated (blue line) and undeviated (red line) by encountering a grain as a function of fluid content (porosity).

The resulting proportions of deviated and undeviated path length can now be used to navigate between the HS conductive bound (Equation 4.1) and the geometrically altered HS conductive bound (ρ_{geo}, Equation 4.18):

$$\frac{1}{\rho_{GPL}} = \left(\frac{1}{\rho_{HS,conductive}} F_{fluid} \right) + \left(\frac{1}{\rho_{geo}} F_{grain} \right). \quad (4.26)$$

Where P_{GPL} is the geometric path length effective resistivity. The relationship between $\rho_{HS,conductive}$, ρ_{geo} and ρ_{GPL} can be seen in Figure 4.15. It can be seen that at 100% porosity, ρ_{GPL} and $\rho_{HS,conductive}$ are the same. As the porosity decreases, ρ_{GPL} leaves the HS bound and moves towards ρ_{geo}.

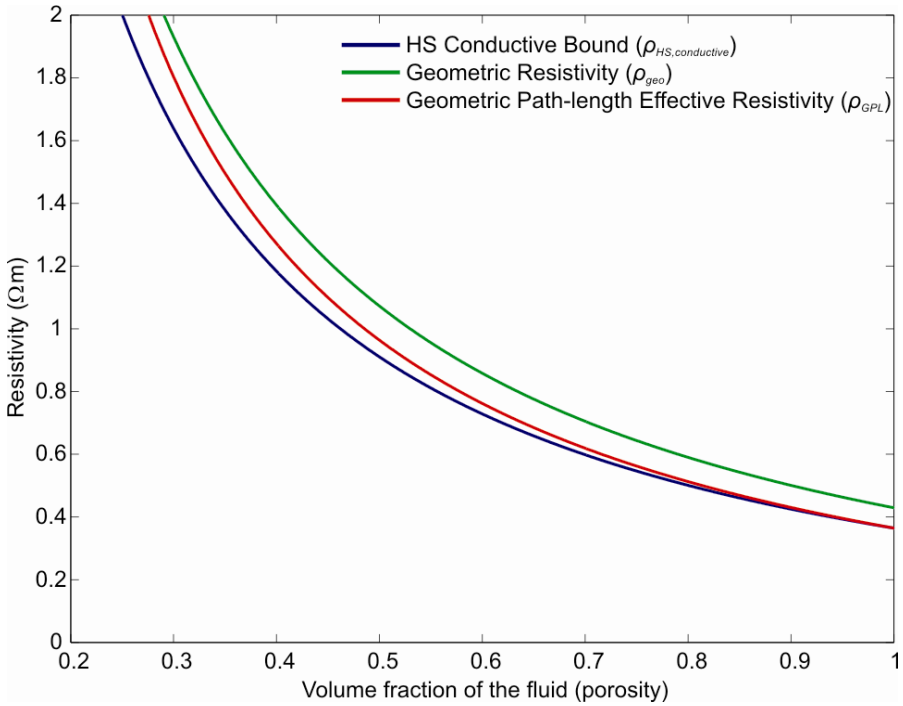

Figure 4.15 The relationship between the HS conductive bound ($\rho_{HS,conductive}$; blue), the Geometric resistive (ρ_{geo}; green) and the Geometric Path length effective resistivity (ρ_{GPL}; red). The fluid has a resistivity of 0.36 Ωm and the solid has a resistivity of 300 GΩm.

4.5 Average Path length resistivity for an ellipsoid (aspect ratio ≤ 1)

This simple model of using the geometric and path length factors to adjust the effective resistivity of a medium becomes more complicated when the aspect ratio of the grains is less than one. This is because instead of dealing with circles and spheres we are now dealing with ellipses and ellipsoids. The following equations define these shapes:

ellipse polar equation:

$$r = \frac{a(1-e^2)}{1+\cos\theta}, \tag{4.27}$$

where e is the eccentricity and is defined as:

$$e = \sqrt{1-\frac{a^2}{b^2}}, \tag{4.28}$$

a is the semi-major axis and b is the semi-minor axis (the relationship between the two can be seen in Figure 4.16 A). An ellipse can also be defined in Cartesian coordinates:

$$\frac{x^2}{a^2}+\frac{y^2}{b^2}=1. \tag{4.29}$$

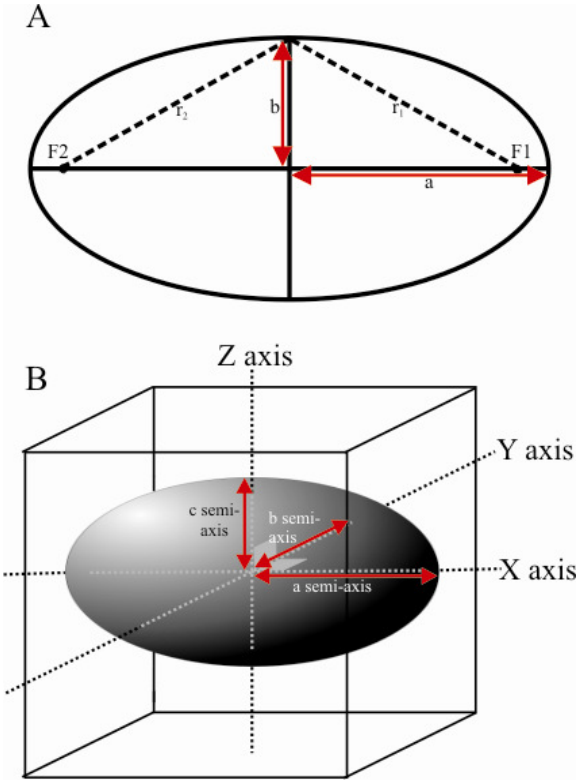

Figure 4.16 (A) An ellipse with a and b being the semi-major axis and the semi-minor axis respectively. F1 and F2 are the foci from which the sum of the distances to any point of the curve is equal to 2a. (B) An ellipsoid with its a, b and c semi-axes and their corresponding x, y and z Cartesian coordinates.

The equation for an ellipsoid is:

$$\frac{x^2}{a^2}+\frac{y^2}{b^2}+\frac{z^2}{c^2}=1, \tag{4.30}$$

where c is the 3rd semi-axis as seen in Figure 4.16 (B). In the case of an ellipsoid the a, b and c semi-axes are associated with the x, y and z Cartesian axes respectively. This allows

a, *b* and *c* to be any length depending on the grain shape, however the following equations shall be calculated where at least 2 of the axes have the same length.

4.5.1 Grain shape

Before the arc length can be determined the shape of the grains needs to be defined. In general there are two grain shapes: oblate and prolate. An oblate grain has two long axes and one short axis and is shaped like a pancake or the shape of the Earth. A prolate grain has two short axes and one long axis and is shaped like cigar. Once the shape is defined the orientation of the grains must be given. In the following cases the grains will be oriented so that the electric current is travelling parallel to the c-axis. Figure 4.17 shows both prolate and oblate grains in the most and least resistive orientations.

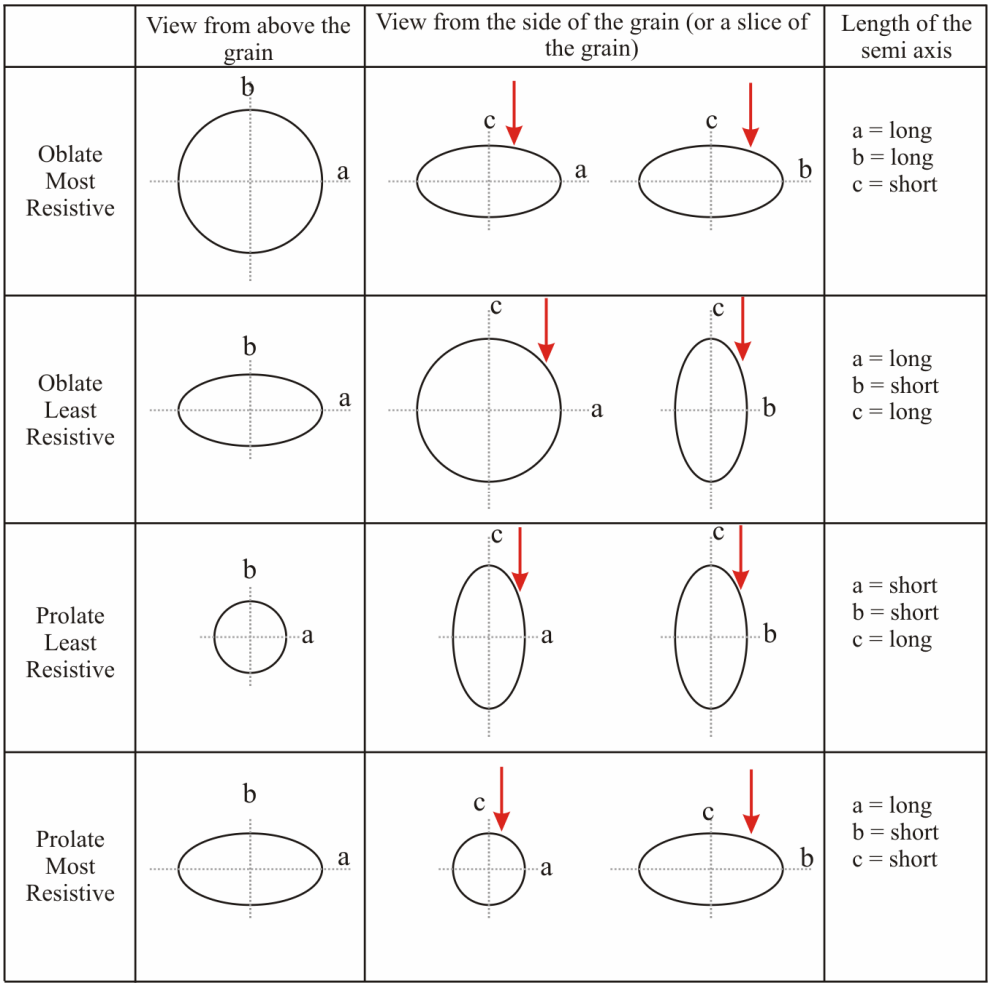

Figure 4.17 Ellipsoidal grains viewed from three different directions with their associated axes lengths. The red arrows indicate the direction of the electrical current.

4.5.2 Average path length

Once the length of the semi-axis has been defined the arc length (S) for that ellipsoid can be given as:

$$S = \int_q^p \sqrt{\left(\frac{dx}{dt}\right)^2 + \left(\frac{dy}{dt}\right)^2 + \left(\frac{dz}{dt}\right)^2}\, dt\,, \tag{4.31}$$

where p and q are the end points of the arc and t is a parametric value. In the case of the current encountering the grain p and q are the points where the current starts and ceases to be deviated. As in the case of a sphere the mean path length must be determined by averaging the path length over the whole of the grain. Equation 4.16, which was used in the case of the spherical grain, can be used again to determine G for an ellipsoidal grain. In this case:

$$l_1 = S\,, \tag{4.32}$$

and

$$l_2 = 2z\,. \tag{4.33}$$

z is given in Equation 4.30. Figure 4.18 shows the average geometric factor (G) for fully aligned grains as a function of aspect ratio. Values of the geometric factor are given in Appendix C. For grains aligned in the least resistive direction (i.e., the current is travelling parallel to the long axis) there is little variation between the prolate and the oblate grains. The major change in the geometric factor is associated with the oblate grain aligned in the most resistive direction. This grain alignment will cause the resistivity of the medium to increase dramatically as the aspect ratio of the grains decreases.

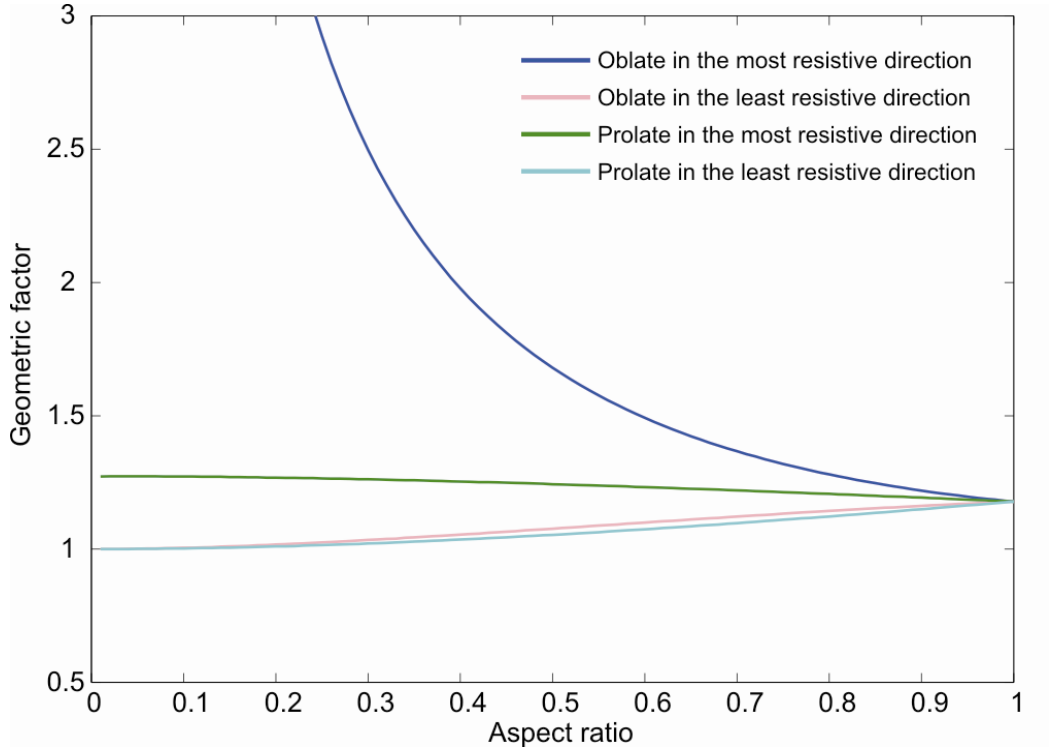

Figure 4.18 Variation of average geometric factor (*G*) for oblate and prolate ellipsoidal grains in both the conductive and resistive direction. Appendix C gives the average geometric factors (*G*) calculated for the different grain shapes and aspect ratios.

4.5.3 Mean path length

Once the average geometric factor G has been determined, the mean free path length L again needs to be calculated. This is slightly different to the mean free path of a sphere, because here the axes of the ellipsoid have different lengths. The crosS-sectional area and the volume of the ellipsoid are given by:

$$\text{Ellipsoid crosS-sectional area } (A_e) = ab\pi \,, \tag{4.34}$$

$$\text{Volume of an Ellipsoid } (V_e) = \tfrac{4}{3}\pi abc \,. \tag{4.35}$$

Equations 4.31–4.35 assume that the c-axis orientation is parallel to the direction of current flow. These equations can be worked through as was done in the case of the sphere (Equations 4.19-23) to give the mean free path of ellipsoidal grains:

$$L = \frac{4c}{6(1-\beta)}. \tag{4.36}$$

The resistivity of the effective medium can then be determined in the same way as for spherical grains (Equations 4.24-26). Appendix C gives the average geometric factors

and l_{2ave} values needed for these equations for a range of aspect ratios. Figure 4.19 and Figure 4.20 show the change in resistivity as aspect ratio and porosity change for both oblate and prolate grains respectively. The change in resistivity of an effective medium using the HS conductive bound is also given for comparison. It can be seen that there is a marked change in the effective resistivity between the HS conductive bound and the Geometric Path Length effective resistivity. The biggest change is seen with the oblate grain in the resistive orientation, where the resistivity increases dramatically as porosity and aspect ratio decrease.

4.5.4 Degree of anisotropy

The degree of anisotropy (D) can be used to compare the difference in resistivity between the different grain orientations and is calculated from:

$$D = \frac{2(\rho_{\max} - \rho_{\min})}{(\rho_{\max} + \rho_{\min})}, \tag{4.37}$$

where ρ_{max} is the resistivity of the medium for a particular aspect ratio and porosity where the grains are orientated in the resistive direction, ρ_{min} is the resistivity of the medium at the same aspect ratio and porosity in the conductive direction. If $D = 0$ then $\rho_{max} = \rho_{min}$ and the effective medium is isotropic. The greater the value of D the more anisotropic the medium is.

Figure 4.21 shows the change in degree of anisotropy for both oblate and prolate grains. It shows that for both oblate and prolate grains the degree of anisotropy increases as aspect ratio and porosity decrease. However the degree of anisotropy is approximately an order of magnitude greater for oblate grains compared to prolate grains. This indicates that the grain shape as well as the alignment of the grains has an important effect on the degree of anisotropy.

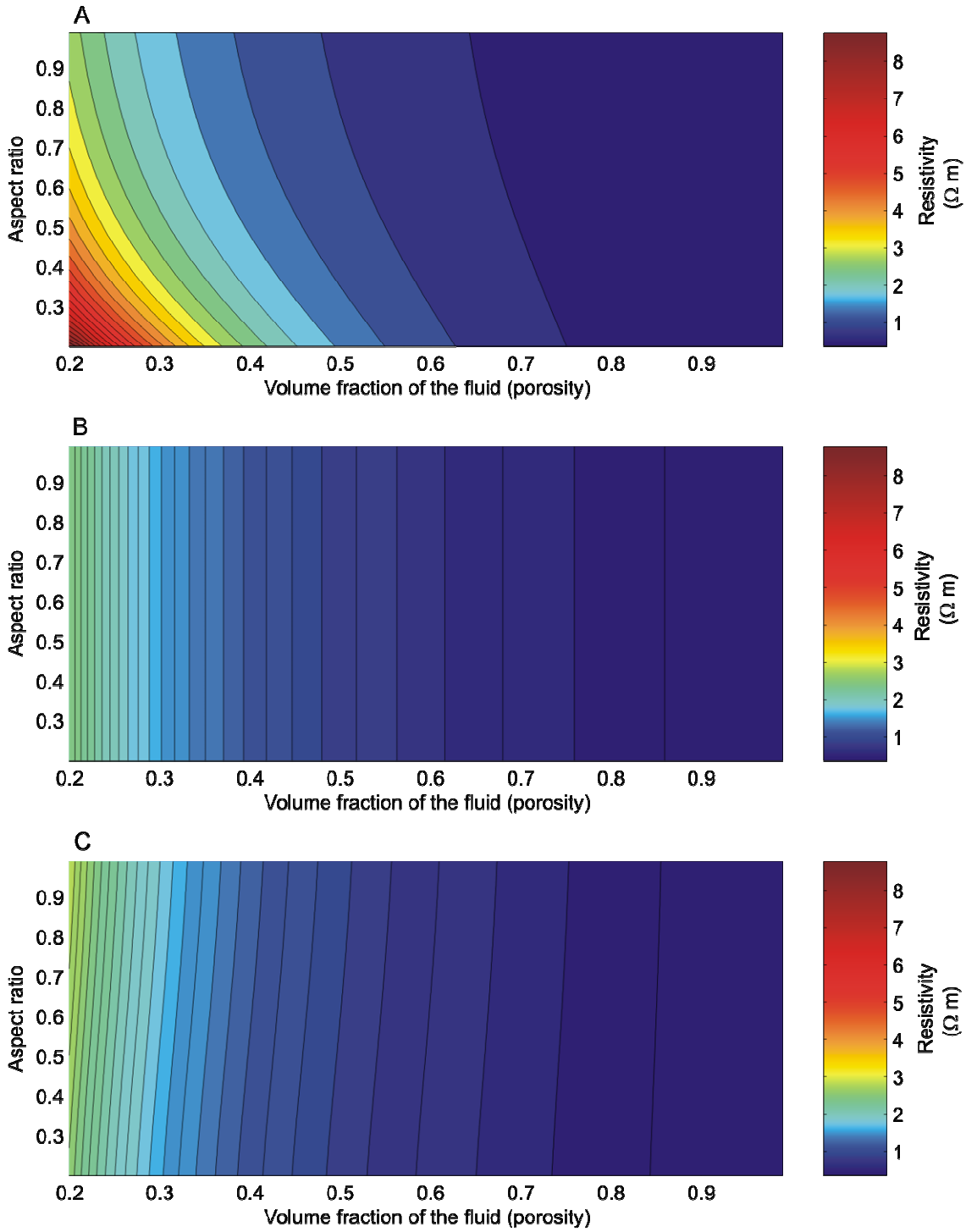

Figure 4.19. Contour plots of the Geometric Path Length effective resistivity as functions of grain aspect ratio and fluid volume fraction. (A) Effective resistivity for an effective medium of oblate grains in the resistive direction. (B) Effective resistivity of an effective medium calculated from the HS conductive bound without any geometric correction. (C) Effective resistivity of oblate grains in a conductive direction.

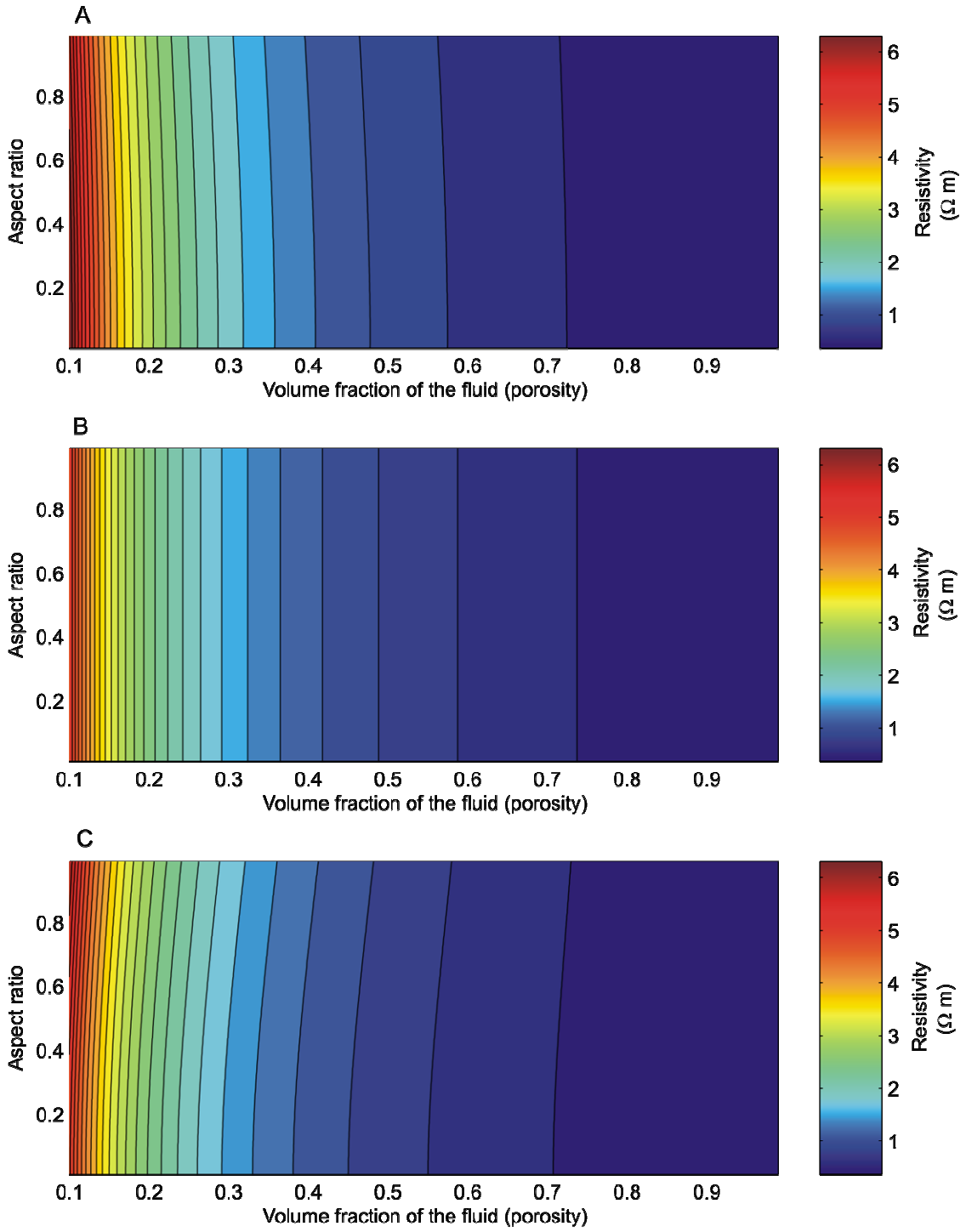

Figure 4.20 Contour plots of the Geometric Path Length effective resistivity as functions of grain aspect ratio and fluid volume fraction. (A) Effective resistivity for an effective medium of prolate grains in the resistive direction. (B) Effective resistivity of an effective medium calculated from the HS conductive bound without any geometric correction. (C) Effective resistivity of prolate grains in a conductive direction.

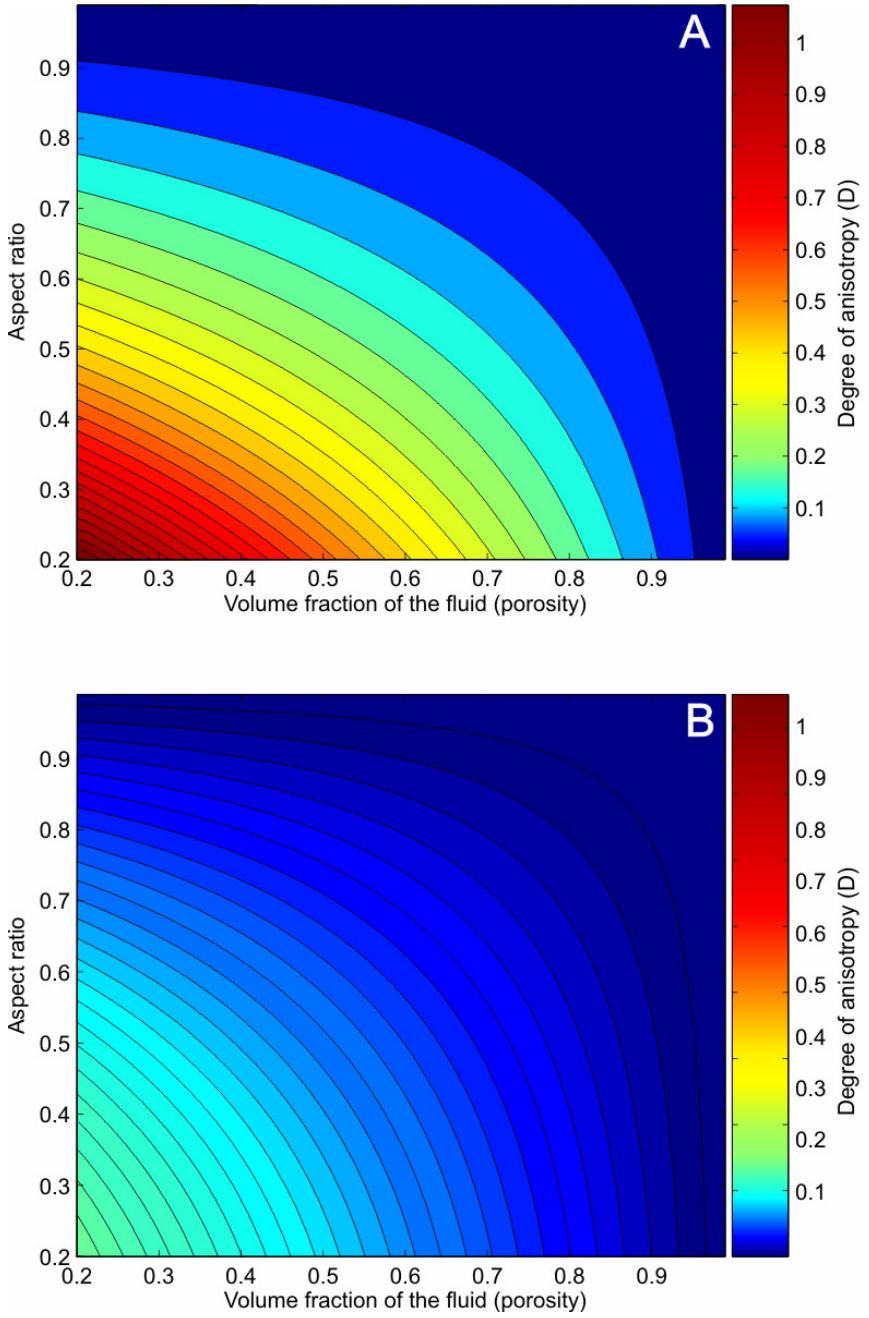

Figure 4.21 Variation in the degree of anisotropy with aspect ratio and fluid volume fraction for (A) oblate grains and (B) prolate grains.

4.6 Electrical Three-phase Modelling

As with the seismic modelling, hydrate can be added into the model in two ways. In the first case gas hydrate is modelled as isolated grains within the fluid. The resulting change in resistivity is due to the replacement of the conducting pore fluids only and not the blocking of pore throats. In the second case the hydrate replaces the pore fluids and blocks

pore throats so that the conducting fluid exists as isolated droplets within the medium. This causes higher resistivities than in the first case.

4.6.1 Hydrate in the pore spaces (non-pore blocking)

To model the case where hydrate sits in the pore spaces, the hydrate is modelled as a second set of grains within the effective medium. To obtain the final effective resistivity, the effective medium is modelled in two steps (Figure 4.22).

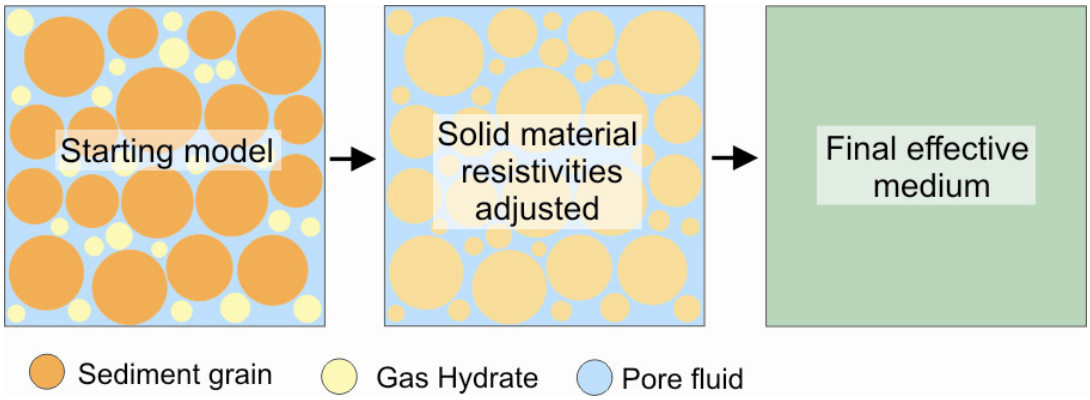

Figure 4.22 Schematic of the effective medium method used to calculate the effective resistivity for a system where hydrate floats in the pore fluid.

Step 1

As with the sediment grains the gas hydrate has a much higher resistivity than the fluid. The current will still primarily pass through the fluid and not the hydrate. Therefore we adjust the volume fraction of the solid grain to include that of the hydrate:

$$\beta_m = \beta_G + \beta_H = (S_H \times \varphi) + (1 - \varphi), \tag{4.36}$$

where β_m is the volume fraction of the solid in the medium, S_H is the hydrate saturation of the original pore spaces, φ is the porosity of the medium and β_G and β_H are the volume fractions of the solid grain and hydrate respectively. We now effectively have only one grain type in the effective medium. The resistivity of this grain type is based on the relative proportions of the hydrate and grain solid resistivities:

$$\rho_m = \frac{1}{\beta_G + \beta_H}(\beta_G \rho_G + \beta_H \rho_H), \tag{4.37}$$

where ρ_m is the resistivity of the grain/hydrate mixture, ρ_G and ρ_H is the resistivity of the solid (grains) and the hydrate respectively. This is a relatively simplistic approach to obtain

a grain/hydrate mixture resistivity and can be used because the final effective medium resistivity is quite insensitive to ρ_m.

Step 2

The three phase medium has now become a two phase medium and we can therefore use the 2-phase equations to calculate the final effective medium. $\rho_{HS,conductive}$ and ρ_{geo} are calculated by replacing σ_s with $1/\rho_m$ in Equations 4.1 and 4.18 respectively. The path length is calculated by replacing $(1-\beta)$ with β_m in Equation 4.23. Then to calculate the final effective medium resistivity ($\rho_{GPL,non\text{-}block}$) these values are inserted into Equations 4.24-4.26. Figure 4.23 shows the change in effective resistivity as the hydrate saturation increases. The equations for this method are written out in full in Appendix B.

This is the simplest method of adding hydrate into the effective medium. As expected the effective medium resistivity increases with hydrate saturation. Because this method is independent of the grain size it also models the case where the hydrate forms grains within the load bearing structure (Figure 1.6 B).

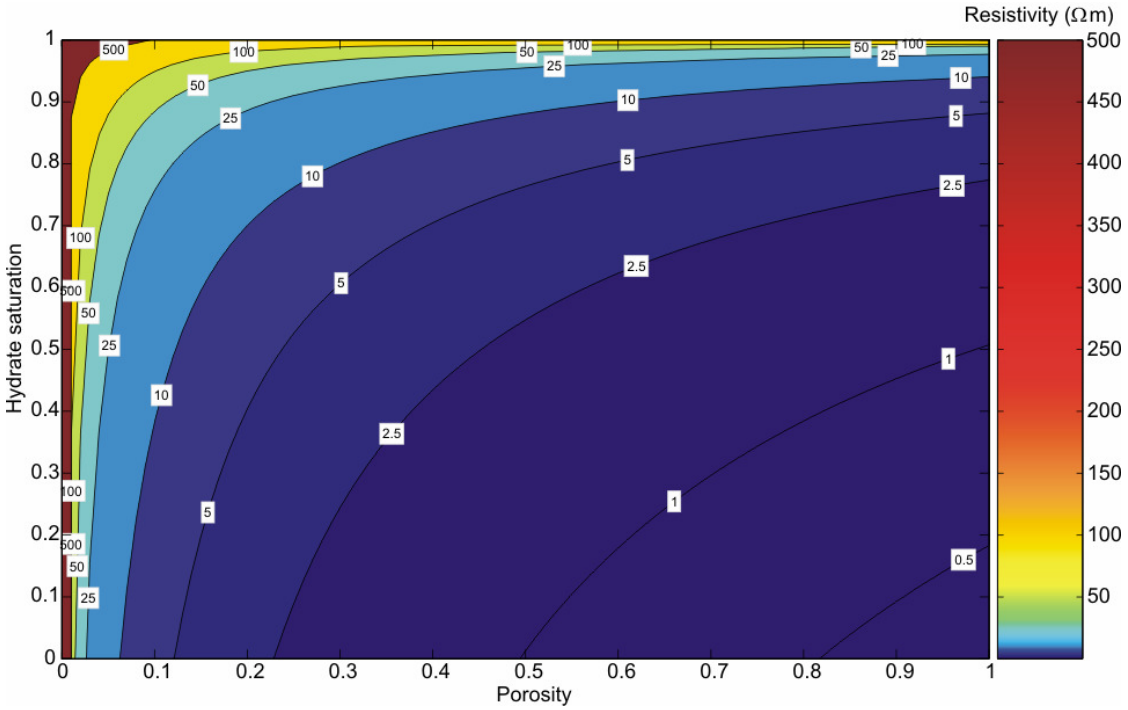

Figure 4.23 Contoured resistivity for a three-phase effective medium where hydrate sits in the pore spaces, calculated using Geometric Path Length non-pore-blocking effective resistivity model ($\rho_{GPL,non\text{-}block}$). The aspect ratio of the grains and hydrate is assumed to be 1. The fluid has a resistivity of 0.36 Ωm, the solid grains have a resistivity of 300 GΩm and the hydrate has resistivity of 200 Ωm.

4.6.2 Hydrate blocking the pores

An alternative effective medium model for the distribution of hydrate is one in which the hydrate blocks the connections between adjacent pore spaces. Modelling can again be achieved in two steps. First a two-phase effective medium is calculated in which only hydrate and grains exist, similar to the starting model of the load-bearing seismic model (section 4.6.1). Then fluid is added and the effective medium is recalculated (Figure 4.24).

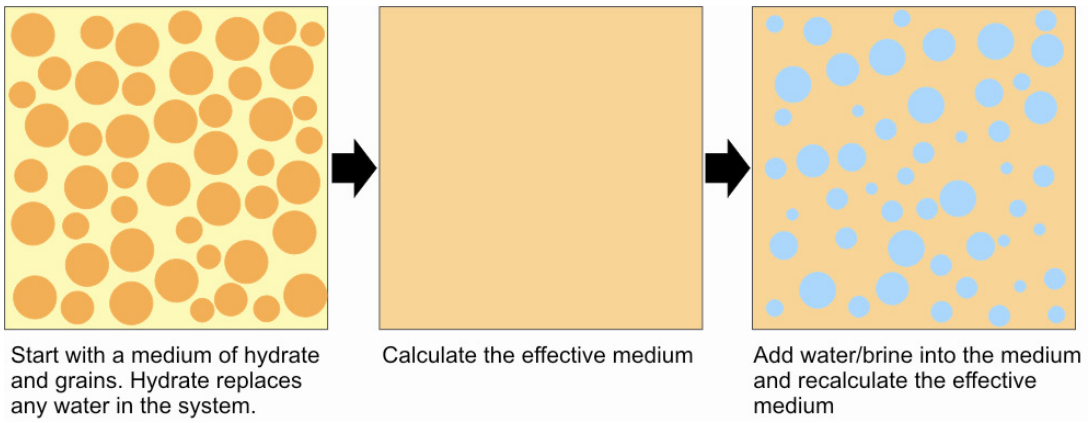

Figure 4.24 Schematic of the method used to calculate the effective resistivity of a three-phase system where the hydrate (yellow) blocks the pores.

Step 1

Although the resistivity of the hydrate is high compared to the pore fluids, it is many orders of magnitude lower than the grain (Appendix A). Therefore the electrical current will preferentially travel through the hydrate in the same manner as it travels through the fluid in the fluid/grain case. The fluid will be added later but the ratio of hydrate to grain must be that of the final effective medium when the fluid is added. Therefore the volume fractions needed for the hydrate/grain effective medium are given as:

$$\beta_H = \varphi S_H , \tag{4.38}$$

$$\beta_{H1} = \left(\frac{\beta_H}{\beta_H + \beta_G} \right), \tag{4.39}$$

$$\beta_{G1} = \left(\frac{\beta_G}{\beta_H + \beta_G} \right), \tag{4.40}$$

where β_H is the volume fraction of the hydrate, β_G is the volume fraction of the grain and β_{H1} and β_{G1} are the volume fractions of the hydrate and the grain respectively used in the initial hydrate/grain only model. The β_{H1} value replaces the fluid volume fraction (β) value

and ρ_H replaces ρ_f in the two-phase model (Equations 4.1, 4.18 and 4.23) to give ρ_{geo} and $\rho_{HS,conductive}$. Equations 4.24-4.26 are then worked through with these values allowing the hydrate/grain effective medium resistivity to be calculated.

Step 2

Random fluid drops are added into the hydrate/grain effective medium replacing both grain and hydrate. Unlike the case of solid grains, the fluid droplets do not cause the same geometric factor change in the resistivity of the hydrate/grain medium as in the fluid two-phase case. The electrical current will go straight through the fluid drops as opposed to deviating around them. Therefore the HS resistive bound (Equation 4.2) can be used to determine the effective resistivity of the medium where the matrix consists of the grain/hydrate mix and the isolated inclusions are composed of conducting pore fluid. This final effective medium resistivity is termed as the Geometric Path Length pore-blocking effective resistivity ($\rho_{GPL,block}$).

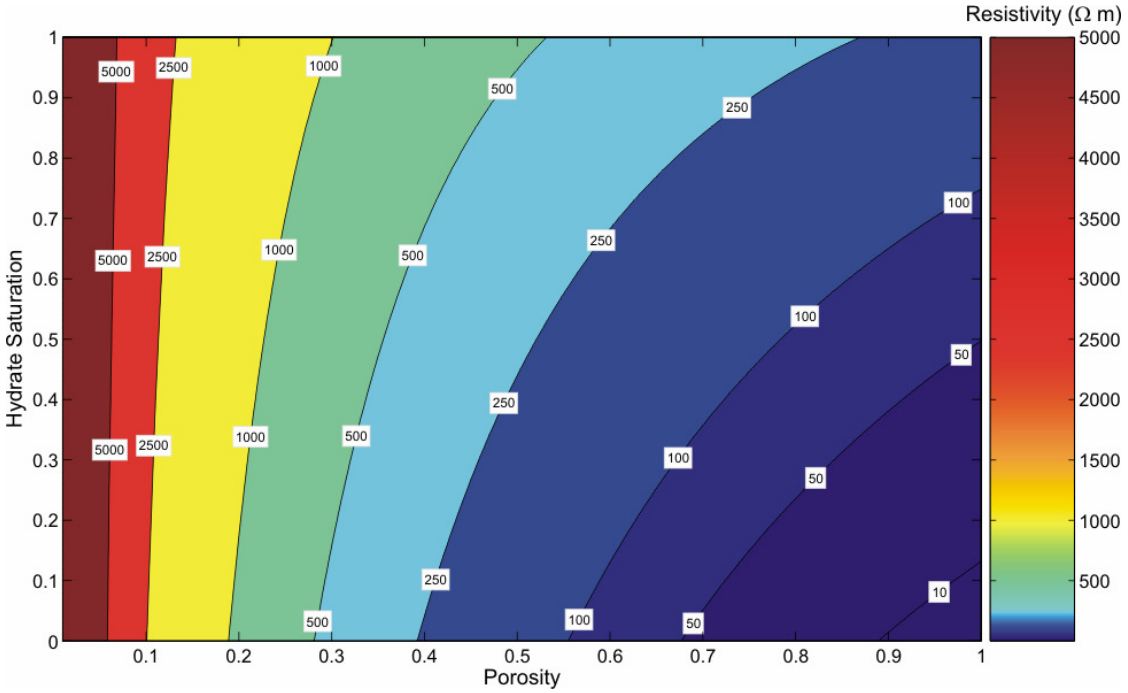

Figure 4.25 Contoured effective resistivity for a three-phase effective medium where hydrate blocks the pore spaces, calculated using the Geometric Path Length pore-blocking effective resistivity model The fluid has a resistivity of 0.36 Ωm, the solid grains have a resistivity of 300 GΩm and the hydrate has resistivity of 200 Ωm. Aspect ratio of the grains and fluid drops are 1.

4.7 Conclusion

There are few effective medium methods for calculating the effective resistivity of a medium based upon the geometric proportions of the component phases. The HS bounds model systems where the fluid is either totally isolated or totally interconnected. Greer's (2001) method takes the next step by introducing partially interconnected systems. However his method, while suitable for fractured crystalline rocks, is not appropriate for sediments. In sediments both the grain and the fluid are interconnected. Using a geometric factor and mean path length approach allows us to model such systems. The resistivity is only dependent on the porosity and aspect ratio of the grains, and not on the size of the grains. This approach also has the advantage that it can model resistivity anisotropy by aligning grains with an aspect ratio of less than one. It shows that the degree of anisotropy is not only dependent on the alignment of the grains but also on the grain shape.

Hydrate is added into the model in two ways, either as grains within the pore fluid or as cement blocking the pores so that the fluid is isolated. The two methods model effective media similar to the two seismic effective medium models for hydrates in Chapter 3. Both show increases in resistivity due to the presence of hydrate. The increase in resistivity due to gas hydrate is far greater when the hydrate blocks the pores than when it is in isolated grains within the pore fluid. However an intermediate model between the two end member types has not been developed which would allow partial interconnection between the hydrate and the pore fluids.

Chapter 5. Seismic and Electrical Laboratory Measurements

5.1 Introduction

Having developed seismic and electrical effective medium models, these models need to be validated. To achieve this, two separate experiments were designed and developed. The aim of the experiments was to make co-located seismic velocity and electrical resistivity measurements on sediments with known porosity and composition. This chapter describes the methods and results of these experiments. Comparison between the results and the effective medium models will be shown in Chapter 6.

The first experiment, described in Section 5.2, was developed to test the 2-phase versions of the effective medium models. Therefore, hydrate was not included in the design. It was important to ensure that the 2-phase effective medium models can model a 2-phase sediment because they form the base of the 3-phase models.

The second experiment, described in Section 5.3, was developed to include hydrate to test the 3-phase models. This experiment involved a completely different setup from the 2-phase experiment because hydrate requires both high pressures and low temperatures to form. These could not be achieved with the design of the first experiment. No dedicated laboratory equipment was available at NOCS to make physical properties measurements on hydrate bearing sediments. A pressure rig however was available and already setup to make velocity measurements using a pulse-echo system. This equipment was developed during the course of this work, by J. Sothcott, to include a cooling jacket to allow samples to be pushed into the hydrate stability zone. The rig was also adapted to include a ring of electrodes around the sample to allow resistivity and velocity to be measured at the same time.

5.2 Two Phase Experiment

The aim of this experiment was to make electrical resistivity and seismic velocity measurements on 2-phase sediments of known properties. The results could then be used to validate the 2-phase versions of the electrical and seismic effective medium models. Most real sediments are composed of many different types of grains each with their own

physical properties and grain shape. Because the aim of this work is to test a model where the grains are made up of only a single material it was decided that the sediment should be composed of only one grain type where the physical properties and the geometry of the grains were known. It was therefore decided that an artificial sediment core using glass beads with known physical properties should be used instead. An advantage with using artificial sediment was that the pore water resistivity could be controlled. According to the models the pore water resistivity is the biggest control in the overall resistivity of the effective medium. Therefore, being able to control its resistivity makes it easier to compare final effective resistivities to the predicted values from the electrical effective medium model.

Making the P-wave velocity measurements along the artificial sediment cores is relatively simple because they can be made using a Multi-Sensor Core Logger (MSCL; Section 5.2.3). Porosity measurements can also be made using the Gamma Ray Attenuation Porosity Evaluator (GRAPE) on the same equipment for a sediment with known grain and fluid densities. Unfortunately electrical resistivity measurements cannot be made using the MSCL. Therefore the core liner was modified with a series of electrodes running along the length of it. These could be used to measure resistivity along the length of the core at the same points that velocity was measured at (Section 5.2.2).

5.2.1 Sediment Preparation

Background

Available methods used to prepare loose sediment samples include pluviation (Figure 5.1), vibration and tamping. Pluviation provides reasonably homogeneous specimens (Rad & Tumay, 1985) and simulates a natural sedimentation processes that influences the degree of grain packing, based on the energy of the grains under pluviation and has therefore been used in this experiment. The procedure and equipment widely used for pluviating dry and wet sand was first documented by Kolbuszewski (1948). The general set-up for pluviating sand to produce artificial sediment can be seen in Figure 5.1. A glass cylinder is filled with water and a glass funnel is placed at the top and is sealed in. The seal also contains an outlet tube for excess water. The funnel contains a stopper to prevent the sediment from falling into the system until it is ready. Sand and water are placed in the funnel. The stopper is then removed and the sand and water are allowed to fall into the glass cylinder

and accumulate at the base of the cylinder. The fall height and the rate at which the sediment is allowed to fall determines the grain packing.

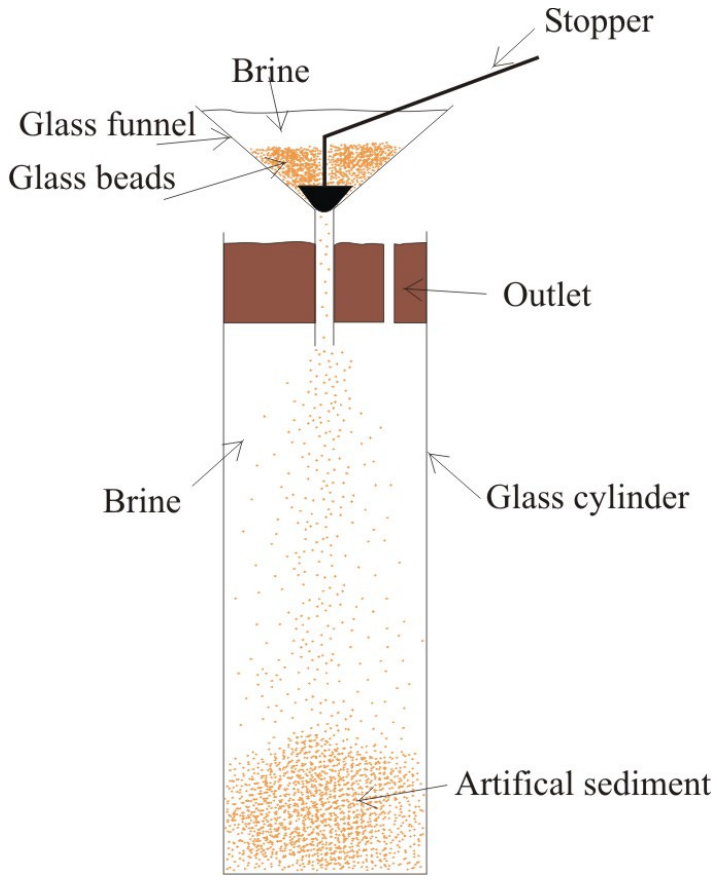

Figure 5.1 Kolbuszewski (1948) set-up for pluviation of sand.

Method

The method used to make these sediments is a modified version of the Kobuszewski's (1948) method. However in this experiment all the air needed to be removed from the water. Air can have a large effect on the resistivity of the samples by adding another high resistance component into the system. Also the container holding the sediment needed to be sealed at both ends and made in a non-conductive material for the resistivity measurements later. The general setup can be seen in Figure 5.2.

Apparatus

1. Sediment cell: This consists of a plastic tube (with high resistivity) with a diameter of 64mm cut to a length of approximately 50cm. Along the length of the tube a series of small holes were drilled into it at 2 cm intervals into which electrodes were placed and sealed in with resin. One end of the cell is sealed with a piston. This piston has an electrode drilled into it with a steel mesh attached to one side of it (a second one is needed later). The other end of the cell has a piston with a hole drilled through, through which a tube is placed.
2. De-airer and pump: this places a vacuum on the fluid to remove all the air.
3. Pluviation setup: a 2 metre high stand is set up with a desiccator base attached. Beneath the desiccator is a glass tube which is attached via a rubber tube. The other end of the glass tube is attached to the sediment cell with another tube. Clamps are placed at each of the rubber tubes to prevent the sediment falling until desired.
4. Glass beads. These are used to simulate the sediment grains. These came in four size ranges from the manufacture, 1000-450 μm, 500-250 μm, 250-150 μm and 100-24 μm (Table 5.1). The glass beads have an aspect ratio of 1 (i.e. they are spherical).

Size range	Sieve size (μm)	% Passing	90% glass beads between (μm)
1000-450	1000 850 425	100 90-100 0-20	425-850
500-250	500 425 250	100 90-100 1-10	250-425
250-150	300 250 150	100 90-100 0-10	150-250
100-24	100 63 45 24	99.8-100 83-97 67-88 20-40	3-80

Table 5.1 Glass bead size distribution, supplied by the manufacture (PotterS-Ballotini).

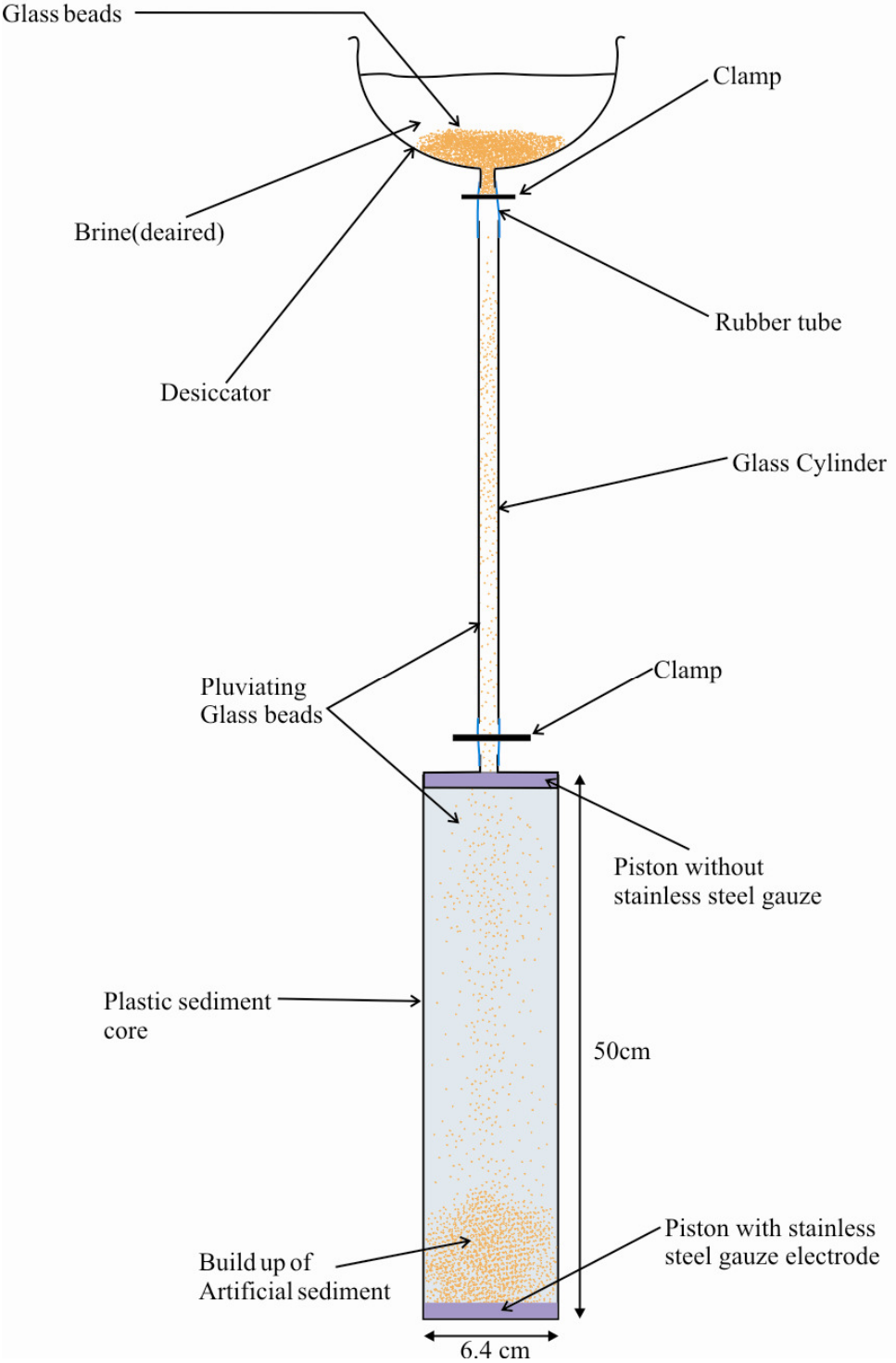

Figure 5.2 Setup for artificial homogeneous sediment core preparation using glass beads and de-aired brine.

Approximately 4 litres of distilled water was de-aired and into this salt was added to make brine (25g of NaCl per litre of water). The sediment cell was filled with the brine

and then attached to the pluviation apparatus. The rest of the system was filled with the brine. A clamp was fastened just below the desiccator into which enough glass beads were added to fill the sediment cell. The lid of the desiccator was attached and a vacuum was placed on the sediment/brine mixture. This removed any air which may have been entrapped when the glass beads were added. Then the clamp was removed and the glass beads were allowed to tumble down the glass tube and into the cell. This process took from one to three hours depending on the grain size used (longer for smaller grains). Once the sediment had filled the cell the system was clamped off and the top piston was replaced with a piston identical to the one at the base. This method produced a homogeneous sediment with the densest possible packing of the grains permitting repeatability of the experiment. The dense packing was also needed so that the samples could be transported without altering the packing and therefore the porosity.

When only one grain size is used with the densest possible packing then the porosity range is small. However we needed a range of porosities to test the models. In the Kolbuszewski (1948) setup, porosity was changed by altering the funnel size (i.e., how quickly the sediment was added) or the falling height in order to change the packing density. Similar techniques were used by Rad & Tummay (1985) and Cresswell *et al.* (1999). However these techniques are not really viable for this setup because the packing is not always at its maximum. Instead porosity of the sediment was altered by using a mixture of different grains sizes. The smaller grains sit inside the larger grains and therefore alter the porosity (Figure 5.3). Some of the core samples were prepared using a mixture of the grain size ranges. The grains from two different ranges were mixed together before being poured in to the desiccator. Using this technique it was possible to achieve a porosity range of 30 to 47%.

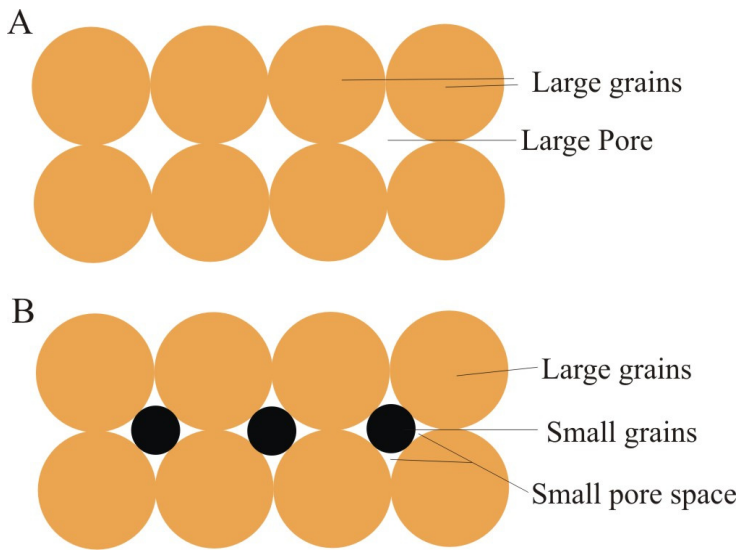

Figure 5.3 Diagram shows the different pore space sizes when only one grain size is used (A) and when two grain sizes are used (B).

Clay and silt sized grains could have been used to alter the porosity. Deep ocean sediments contain large amounts of clay so using it would have been appropriate. Sediments made out of clay can have porosities of up to 80% which would have also given a much wider range of porosity. However clay is very difficult to de-air and the consolidation time is very long (days instead of hours) so it was decided to work with only sand sized (2mm – 0.0625mm) grains. Six samples were made in total with varying grain sizes in each. Unfortunately 2 of the artificial sediment cores partially dried out because the sealing around the electrodes leaked. Therefore only the results of the other four will be presented. Table 5.2 gives information on the size of the grain sizes used in each of the samples.

Sample number	Grain sizes used in each sample
Sample 1	2 grain size ranges used An equal mixture of 1000-450µm and 250-150µm
Sample 2	2 grain sizes ranges used An equal mixture of 1000-450µm and 100-24µm
Sample 3	1 grain size used 250-150 µm
Sample 4	2 grain sizes ranges used An equal mixture of 1000-450µm and 250-150µm

Table 5.2 Sediment grain sizes in each of the samples.

5.2.2 Resistivity measurements

Background

Resistivity is one of the most variable physical properties in sediments. Most rock forming materials are insulators (high resistance) and it is the pore water that conducts the electrical current. Therefore most rocks conduct electricity by electrolytic rather than electronic processes. It follows that the porosity, permeability and the pore water composition are the major controls on the resistance of the composite. It should be noted however that some sediment grains, predominantly clays, exhibit double layer conductance when water saturated. In these cases the composition of the sediments is also important.

Method

Apparatus

1. Sediment cell (Described in Section 5.2.1)
2. Voltmeter
3. Temperature Probe
4. Ampmeter
5. Constant current source (0.1 – 10 mA, 220 Hz)

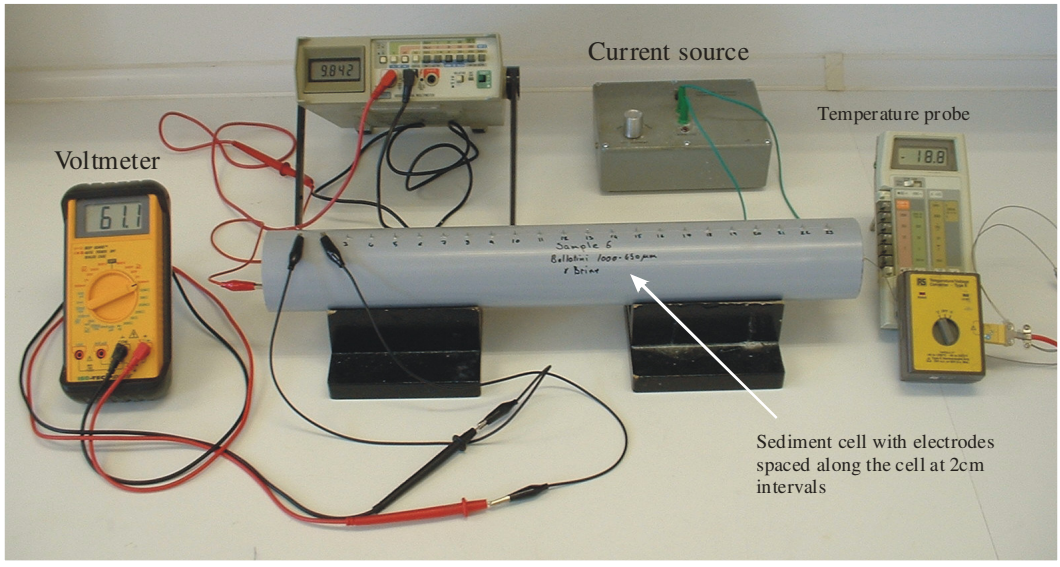

Figure 5.4 Picture of the electrical setup

A current of 10mA was passed through the sediment cell through electrodes at each end of the sediment cell. The electrodes have a steel mesh to distribute the current over the whole of the cell cross section and therefore minimize edge effects. The potential difference was measured between neighbouring electrodes along the length of the core spaced at 2cm. Temperature and current readings were also taken at the same time. A setup for the resistivity measurements can be seen in Figure 5.5.

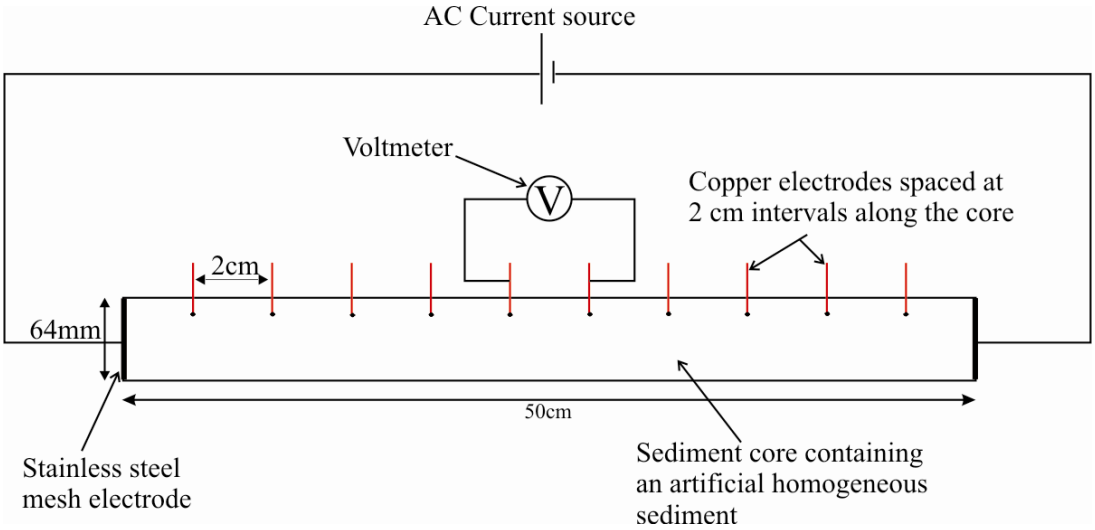

Figure 5.5 Schematic diagram for the setup of the resistivity measurements of the artificial sediment core.

Temperature effects

Temperature can have a large effect on the resistivity of the sample. To demonstrate this Sample 3 was cooled down to 5°C in the NOCS core store and then slowly allowed to warm up to room temperature. Resistivity was monitored during this process at two sets of electrodes to show the change caused by the increasing temperature. Figure 5.6 shows the resistivity decreasing as the temperature increases. It can be seen that the resistivity drops over 0.5 Ωm over a 15°C change in temperature. Therefore, a single degree of temperature change could lead to a 33 mΩm change in resistivity and could effectively double the errors of the resistivity measurements. Rather than trying to correct for the temperature changes in the samples, they were placed in the NOCS cold core store where the temperature is regulated at 5°C. Each of the samples was given a minimum of 24 hours to equilibrate to the surrounding temperature before taking a resistivity reading. A

temperature probe was inserted into the base of each sample to monitor the temperature of the samples while the measurements were made.

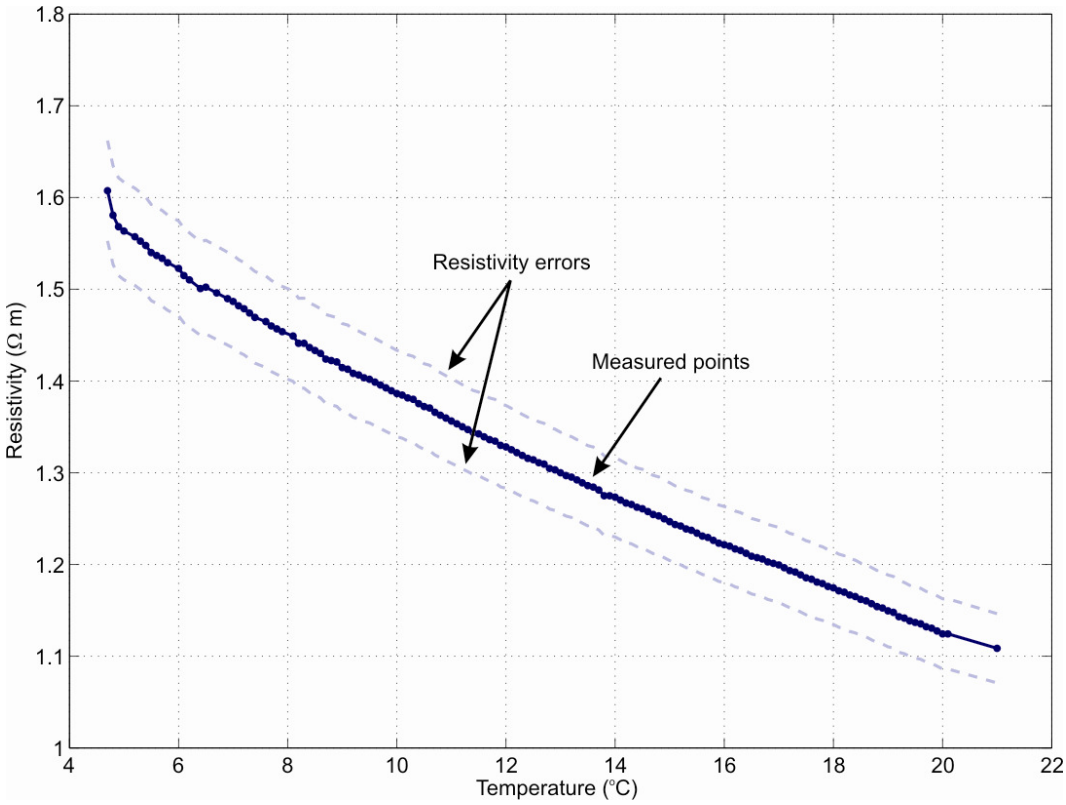

Figure 5.6 Graph showing the change in resistivity as Sample 3 was allowed to warm up from 5°C to room temperature (~21°C). Resistivities were measured at a single pair of electrodes and the porosity of the sediment was 39%.

5.2.3 Porosity and P-wave velocity measurements

Porosity and P-wave velocity measurements were both made using a non-destructive multi-sensor core logger (Figure 5.7). Measurements were made at 5mm intervals along the length of the core. The samples were run through the logger twice at different orientations to check that there was no grading in the sediment along its cross section.

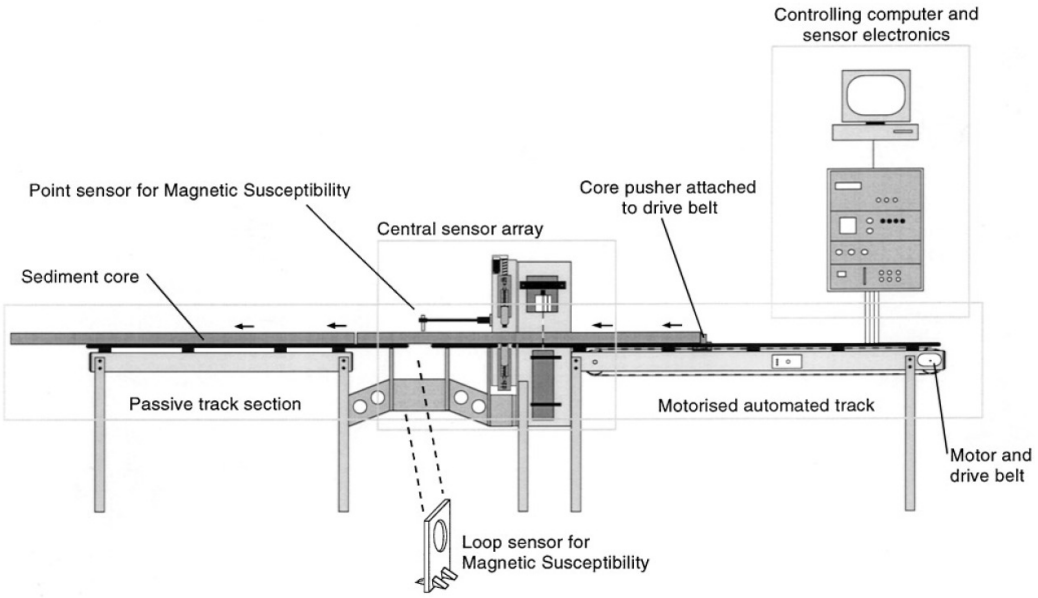

Figure 5.7 Schematic of NOCS Marine Sediment Core logger (after Gunn & Best, 1998).

P-wave velocity measurements

Velocity measurements were made using two vertically mounted compressional wave transducers on opposite sides of the core (see Figure 5.8). The transducer sends a 500-kHz pulse through the core at a repetition rate of 1kHz. The pulse is detected using a similar transducer receiver. The first negative amplitude excursion of the received waveform is detected using an automated system, and the travel time at the first break is recorded. Core thickness is measured by rectilinear displacement transducers attached to the P-wave transducer housing (Gunn & Best, 1998). The velocity is calculated using,

$$V_p = \frac{(d_c + d_R - d_L)}{(t_R - t_L)}, \tag{5.1}$$

where

d_c=calibration block thickness,

d_R = the recorded displacement,

d_L = the total liner thickness,

t_R = recorded pulse travel time,

t_L = the pulse delay time.

Velocity errors are caused by the changes in the liner wall thickness, the delay time error (±0.53%), thickness deviation (precision ±0.1 mm) and travel time (precision ±50 ns). The

absolute errors increase with velocity of the sediment. A relativity high sediment velocity (~2000 mS-^{1}) leads to absolute errors of ±0.59% (Best & Gunn, 1999).

Porosity measurements

The bulk density of the cores is measured using the standard gamma-ray attenuation method. A radiation source is located vertically above the core and a scintillation counter beneath (Figure 5.8). Gamma rays from a CS-137 source are released by opening an aperture in the lead container. Two apertures exist, producing gamma ray beams of 2mm or 5mm. The number of scintillations are counted over a given time, 2 or 5 seconds (Gunn & Best, 1998). Gamma ray measurements were made with a 5mm beam for 5 seconds. The bulk density was then calculated from (Evans 1965);

$$\chi_{bulk} = \frac{1}{\mu_c d} \ln\left(\frac{I_0}{I_g}\right), \tag{5.2}$$

where,

χ_{bulk}=Bulk density (g/cm^3).

μ_c= Compton mass attenuation coefficient of the sediment (cm^{2}g^{-1}).

d=Thickness of the sediment (cm).

I_g=intensity of the gamma beam after passing through the air gap, core liner and the sediment (cps).

I_0=intensity of the gamma beam after passing through the air gap and the core liner (cps).

The main problem with this technique is the fact that Compton Mass Attenuation Coefficients (CMAC) vary with lithology. To overcome this problem careful calibration is needed using different thicknesses of water and aluminium which represent the extremes of CMAC in most sediments. This results in errors of bulk density for a sediments of typically 0.07 g/cm^3 (Best & Gunn, 1999). Porosity of the sediment can then be calculated from the bulk density and the density of the individual components, assuming uniform grain density,

$$\beta = \frac{\chi - \chi_o}{\chi_f - \chi_o}, \tag{5.3}$$

where,

χ_f = density of the fluid (Brine)

χ_o = density of the solid (glass beads)

β = volume fraction of the fluid (porosity).

Using this method to measure porosity the porosity errors are typically 3.6%.

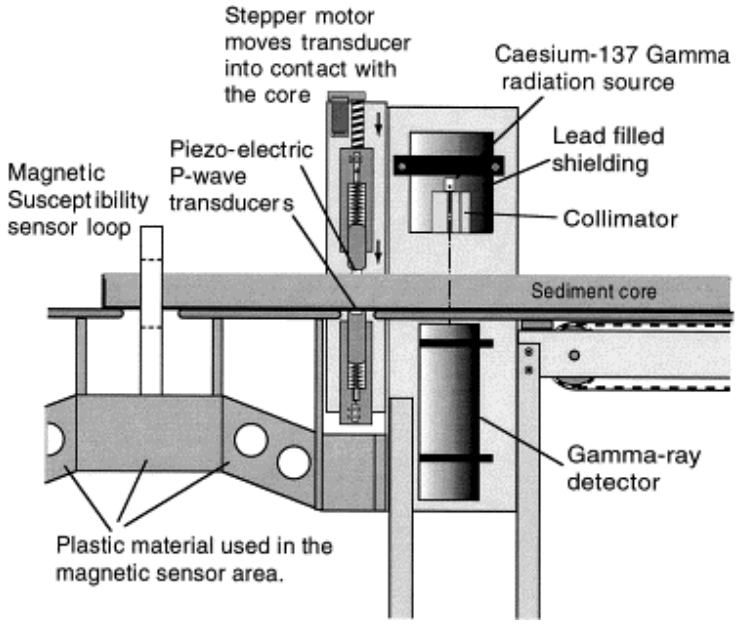

Figure 5.8. Schematic of the sensor array of the core logger (after Gunn & Best, 1998).

5.2.4 Results

The purpose of this section is to present the measured data and look into the homogeneity of the samples and how this may affect the velocity, porosity and resistivity. Comparisons between the measured data and the effective medium models will be presented in Chapter 6. The four successful samples all had porosity, P-wave velocity and resistivity measurements made as a function of position along the core (Figure 5.9).

Porosity

The pluviation technique produced porosities in the range 30%-47% for the 4 samples. This seems to be the maximum change in porosity that can be obtained by simply varying sand grain sizes. It may be possible to reduce porosity further by applying a confining pressure. This however was not deemed necessary in order to test the effective medium models. Figure 5.9 shows the change in the porosity along the length of the cores.

Figure 5.9 shows that the porosity does vary along the length of the samples. Sample 3, which was composed of one grain size, shows the least amount of variation. The others show larger porosity changes along the samples. This difference between the samples probably indicates that grains did not mix evenly during the pluviation causing the

different porosities. Therefore the samples are not as homogeneous as desired along the samples. All the samples were measured at least twice in different orientations. The results from these samples show that the porosity was approximately the same in each direction indicating that the samples are homogeneous across the crosS-section.

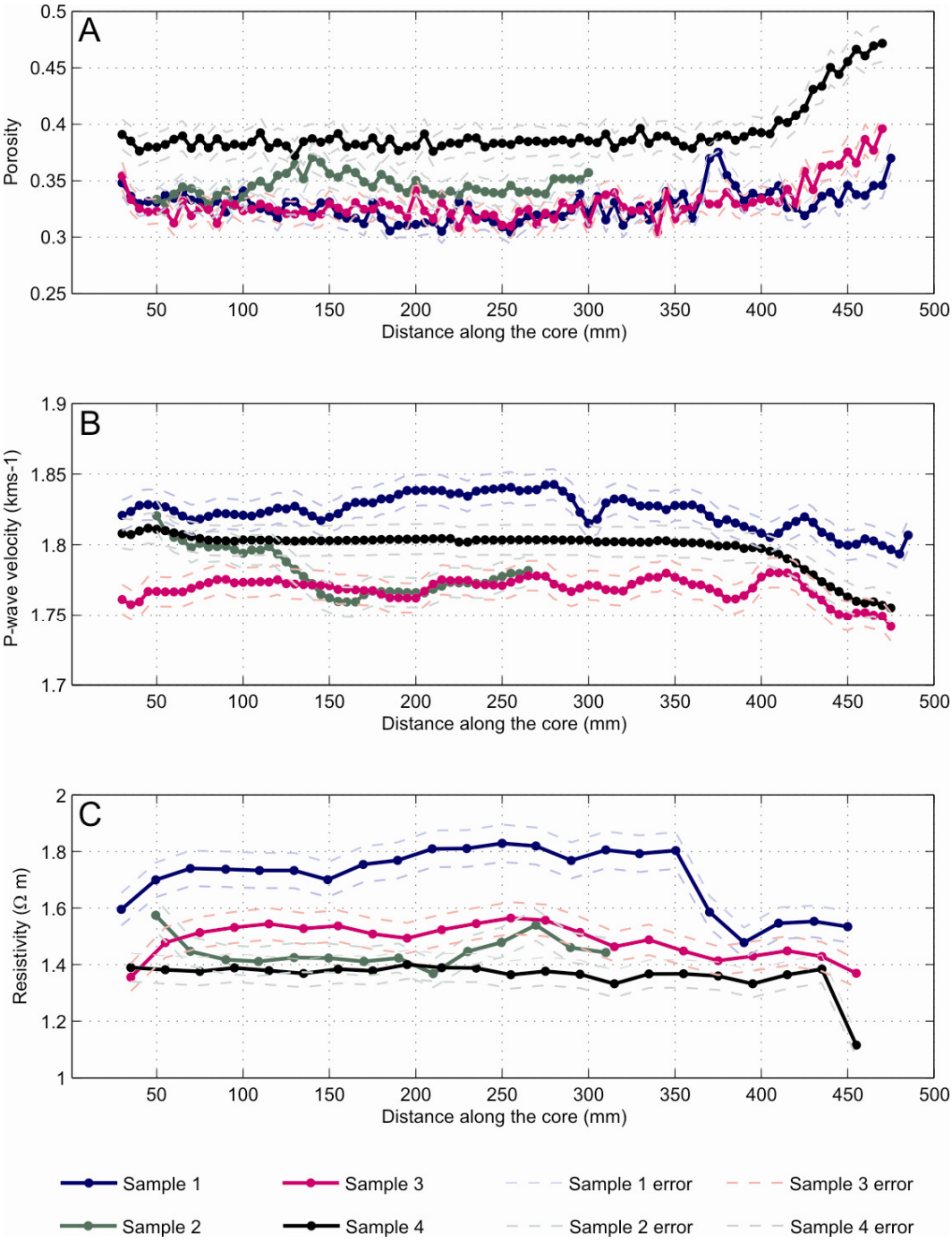

Figure 5.9 Mean physical properties measurements along the sediment cores. (A) Porosity as a volume fraction of the total, (B) P-wave velocity and (C) Resistivity. The base of the samples is at 0mm and the top of the sample is towards 500mm.

Another noticeable feature of the porosity plots is that porosity increases towards the end of each core. This is the top part of the core where the sediment was the last to form. This increase in porosity may indicate that the packing was looser here that at the base due to the shorter fall distance.

Resin core

A second method was used to see how homogeneous a sample was using this method of sample preparation. An extra core sample was made up in the same way as the previous ones. This sample was then dried and impregnated with blue resin. two thin sections were made from the resin sample, one across the core and one along the length of the core. These thin sections were then digitally scanned (Figure 5.10(A)).

The colour image was converted into black and white using a given threshold, the grains come up white and the fluid black. The image was then subdivided into smaller squares and the number of black pixels in each square was counted and divided by the total number of pixels to give porosity in each section. The image was then recompiled (Figure 5.10 B) to show the variation in porosity across the sample.

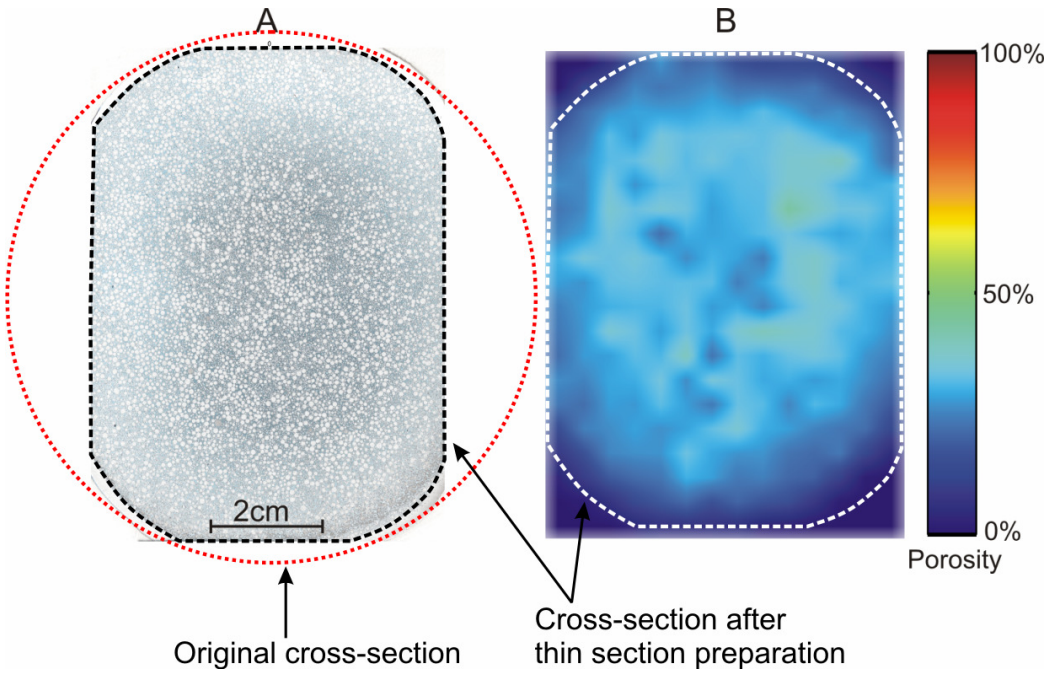

Figure 5.10 (A) crosS-section of resin sample (grain size 1000-450µm and 250-150 µm). (B) Change in porosity of the resin cross section. The Red dotted line indicated the original shape and size of the cross section from the sediment core sample before the thin section was made. The dashed line indicates the edge of the sediment on the thin section slide. It is smaller than the original cross section due to the size and shape of the thin section glass slides, on which the sediment is mounted.

Unfortunately, the colour histogram of the original thin section image (Figure 5.11) showed no obvious point at which to set the threshold between black and white. Also if the blue, green and red channels are compared (Figure 5.11), and despite the resin being coloured blue the red channel appears to be spread better (although less intense). Therefore it may be better to use this channel to determine the threshold.

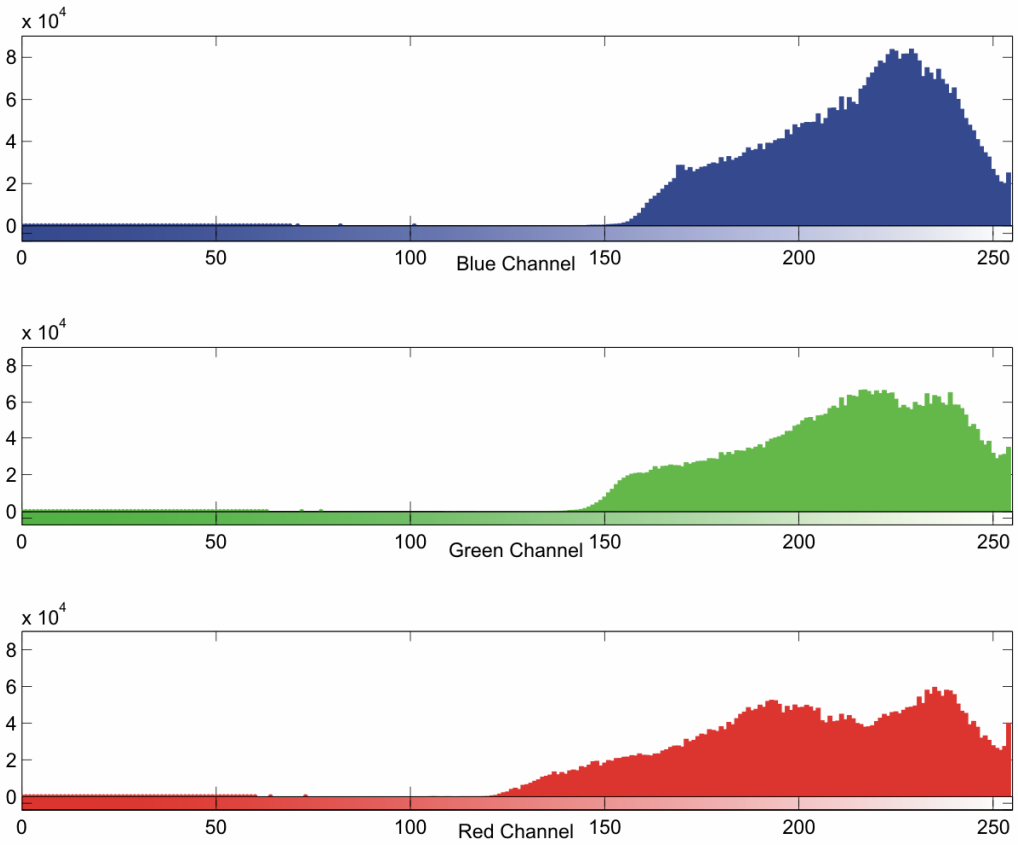

Figure 5.11 Histograms of the blue, green and red channels of the thin section image.

The problems of picking an appropriate threshold is due to the internal refraction of light in the thin sections causing the colour contrast difference between the grain and resin to be low. Therefore absolute porosities cannot be determined. Despite this, the images produced can still be used to estimate the homogeneity of the samples. Figure 5.10 (B) was created using the red channel with a threshold of 180 (colour ranges from 0 to 255). Around the edge of the sample there are lower porosities than towards the centre. This is due to the thin section being slightly thinner at the edge than in the middle. It can also be seen that there are a few spots of low porosity in the centre of the thin section. This

indicates that there is some small scale heterogeneity across the samples with a approximate length scale of 0.5 cm.

P-wave velocity measurements

Figure 5.9B shows the variation of the P-wave velocity along the samples. The P-wave velocity varies more smoothly than the porosity. This is probably because the P-wave velocity is an average velocity over a 2 cm thick slice through the core, which is determined by the transducer beam diameter, whereas the porosity is only measured over a 0.5 cm wide area. The porosity measurements therefore are able to pick out smaller scale heterogeneities along the core than the P-wave velocity measurements. The P-wave velocity and porosity do however correlate well together. High porosities along the samples are reflected in the velocity measurements as low velocities (Figure 5.12).

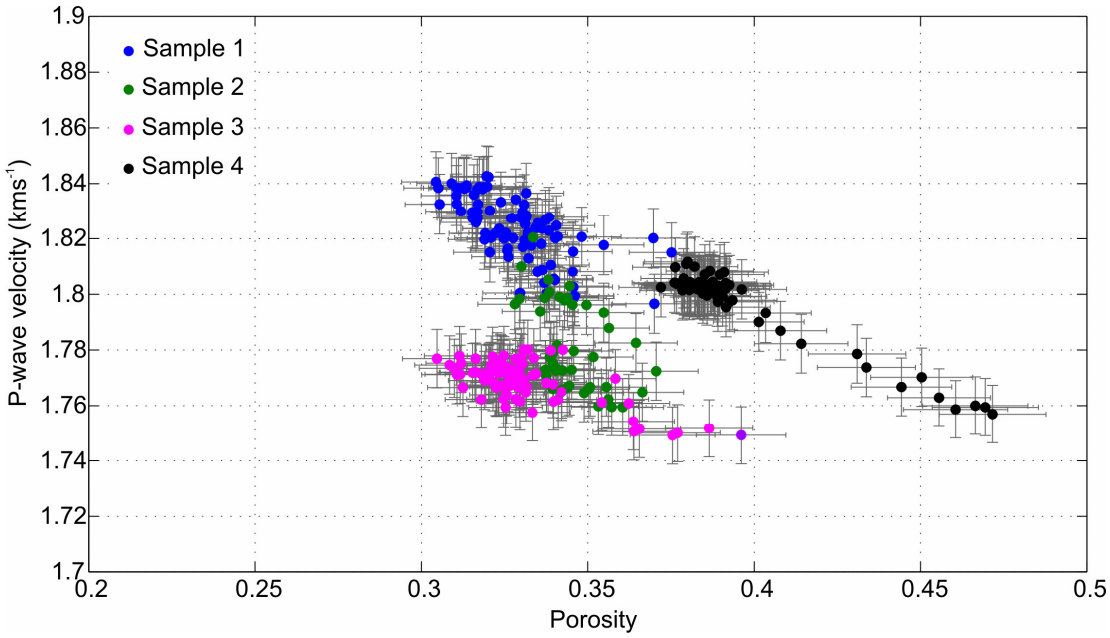

Figure 5.12 P-wave velocity verse porosity for all samples.

Resistivity measurements

Assuming that the current is distributed evenly through the crosS-section of the sediment filled tube, the potential difference (V_{pd}) can be converted into resistivity (ρ) using the following equation.

$$\rho = \frac{V_{pd} \times A}{D \times I}, \tag{5.4}$$

where D is the distance between the electrodes and A is the crosS-sectional area of the sediment cell (~32.5cm^2) and I is the current.

Figure 5.9C shows the resistivity changes along the core. Comparing these to the porosity measurements show that as the porosity increases the resistivity decreases (Figure 5.13). Errors for the resistivity were calculated as combination of the error of the voltmeters, current source (which were calibrated against resistors of 10, 50, 250, 1000 Ωm) and the error in the distance between the electrodes. Absolute errors are approximately 3.6%. When the velocity measurements and the resistivity measurements are compared (Figure 5.14) it is seen that as velocity increases so does the resistivity.

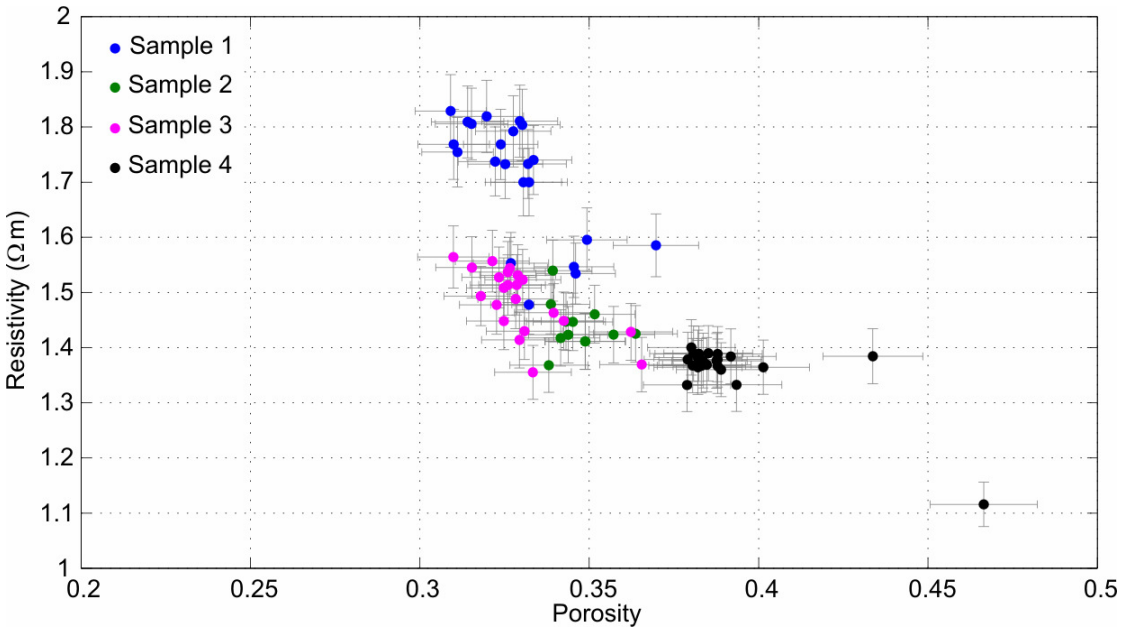

Figure 5.13 Resistivity verse porosity for all samples.

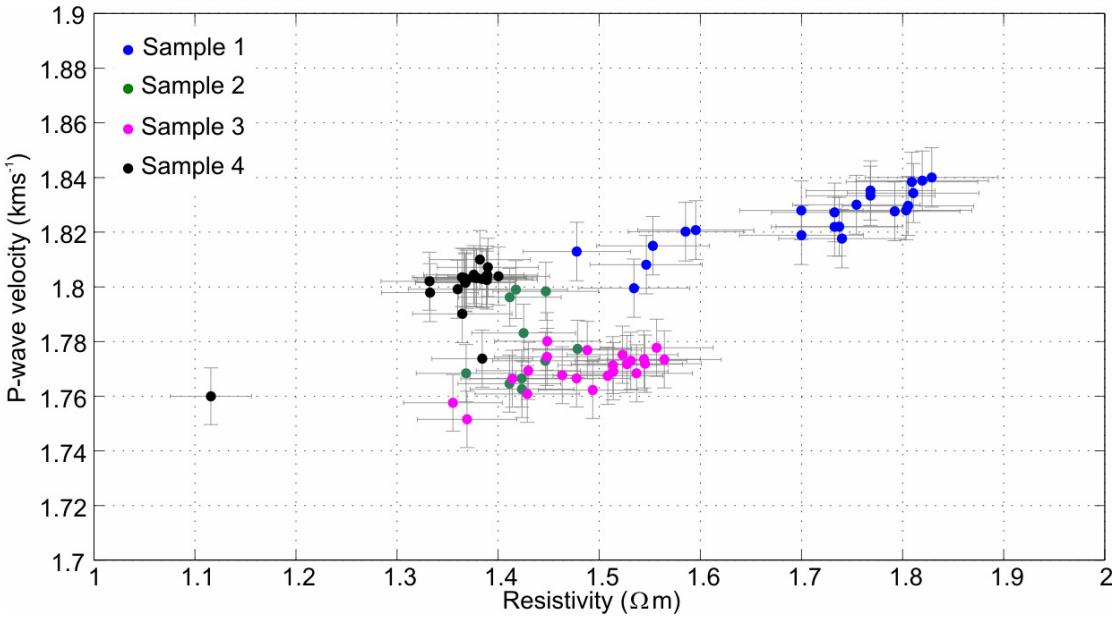

Figure 5.14 Resistivity versus P-wave velocity for all samples.

5.2.5 Conclusion

Four sediment cells composed of glass beads and brine were made successfully. These samples contained only 2 constituents of which the bulk properties were known. The measured porosity of these samples ranged from 30-47% (with an error of ±3.4%). P-wave velocities were measured every 0.5cm along the core with errors of ±0.59%. Resistivity measurements were made every 2cm along the core at 5°C (error is ±3.6%). The range of porosity, P-wave velocity and resistivity are sufficiently wide enough to test the 2 phase models in Chapters 3 and 4 and will be discussed in Chapter 6.

5.3 Three Phase Experiments

5.3.1 Introduction and Aim

To test the three phase models a method is needed to make measurements on hydrate bearing sediments. The method used in Section 5.2 for two phase sediments is inappropriate, because a confining pressure cannot be placed on the system which is needed to make hydrate at temperatures above the ice point. As mentioned earlier no equipment was already available to make hydrate in sediments and measure the physical properties of the hydrate bearing sediments. However there was a high pressure rig which had been previously designed and used to measure the ultrasonic properties of reservoir

rocks under a confining pressure. This rig was adapted during the course of this work to create hydrate in the sediment samples by adding a cooling jacket. An electrical setup, which included a ring of electrodes around the sediment sample, also had to be designed and added to allow resistivity and velocity to be measured simultaneously.

5.3.2 Pressure rig

An adapted Wykeham Farrance high pressure rig (Figure 5.15) was used to make velocity and resistivity measurements on rock samples under high pressure. The sample and ultrasonic setup were placed within the rig. A rubber sleeve kept the sample isolated from the surrounding hydraulic oil, which was used to apply confining pressure to the sample. A ram was used to apply a uni-axial confining stress to the top and base of the sample assembly. Hydraulic oil was used to actuate the ram in such a way that the uni-axial stress was equal to the pressure of the oil surrounding the pulse echo assembly. Hence the confining stress on the sample was hydrostatic (equal in all directions). Pore pressure is controlled via a water inlet at the base of the sample (Figure 5.16).

Figure 5.15 Wykeham Farrance high pressure rig with cooling jacket.

The rig was originally developed to be used to measure velocity and attenuation of rock samples under simulated effective pressures up to 60MPa. Hence, its pressure rating was more than adequate for seabed hydrate studies that require pressures only up to 20MPa. However it had no temperature control, so it was adapted by J. Sothcott for this laboratory work to include a temperature control jacket. This allowed the rig's temperature to be dropped to 4°C so that the sediment samples could be placed within the hydrate stability zone (Figure 1.4). The water inlet was also adapted to switch between gas and water to allow both the methane and brine to be added into the sample via the same port. The rig was further adapted in include a ring of 12 electrodes so that resistivity of the samples could be measured. Figure 5.16 shows a schematic diagram of the adapted rig.

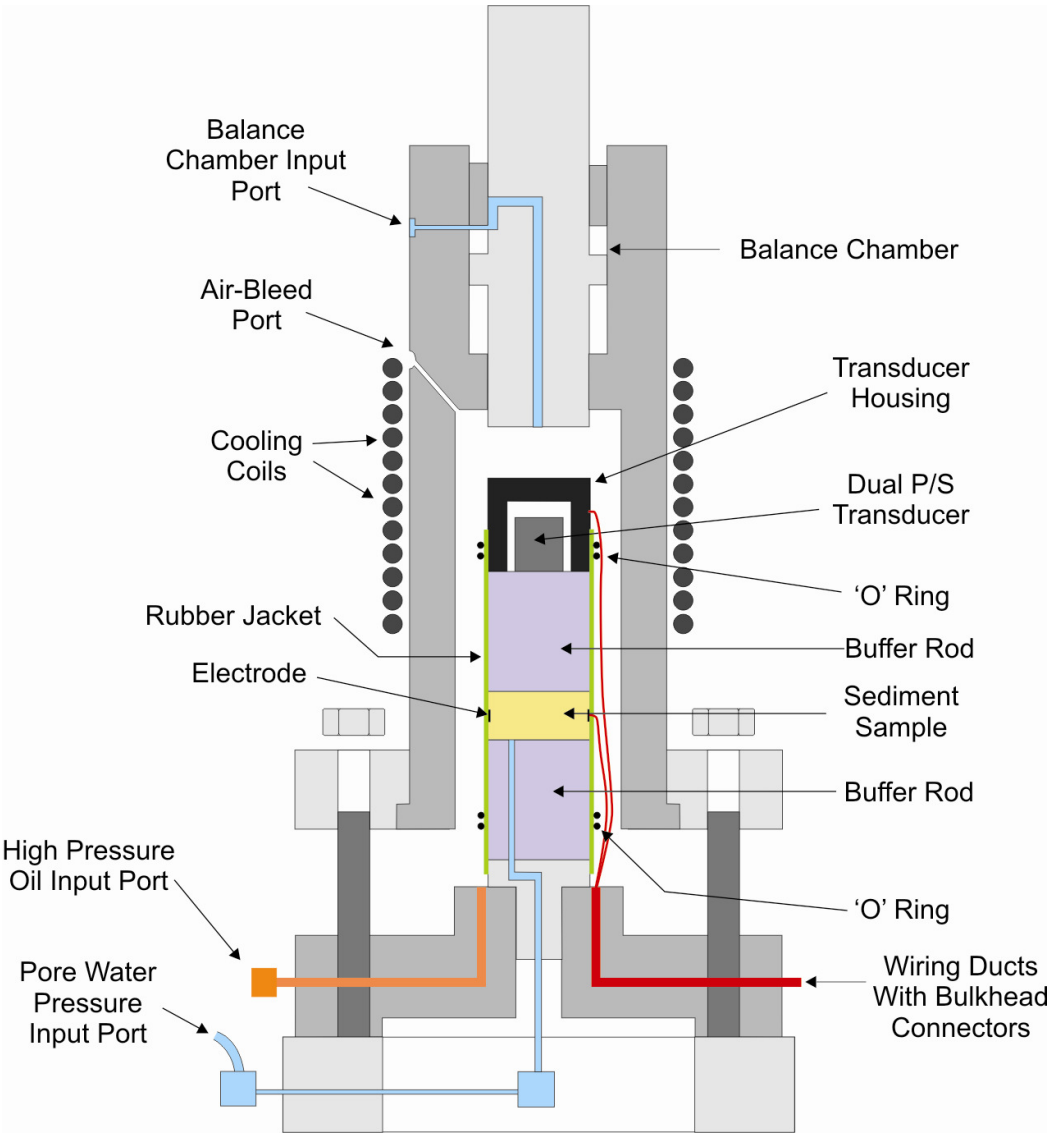

Figure 5.16 Schematic diagram of the adapted Wykeham Farrance Pressure Rig.

Reflection system

P- and S-wave velocity were measured using a reflection technique based on the method of Winkler & Plona (1982) (Figure 5.17). A rock sample was sandwiched between two Perspex buffer rods. The type of buffer rod was chosen such that it had a different density from the sediment and therefore an acoustic impedance contrast between the two. An ultrasonic pulse was coupled into the top buffer rod from a piezo-electric transducer. The pulse is partly reflected back from the top of the rock sample and from the base of the sample (Figure 5.17). The velocity of the sample is calculated from the time difference between the two arrivals and the thickness of the sample. The length of the buffer rods are chosen so that no other reflections, such as from the base of the lower buffer rod, interfere with the arrivals from the sediment. The length of the top buffer rod (i.e. the buffer rod connected to the transducer) was 4cm and the length of the bottom buffer rod was 5cm. The transducer was a combined P- and S-wave piezoelectric broadband transducer with a 2.54 cm diameter and nominal frequency of 1 MHz. Using a dual P/S-wave transducer is very useful for this type of experiment as it allows both P- and S-wave measurements to be made on the same sample without having to dismantle the rig to change the transducer. Hydrate takes some considerable time to form and stabilize in the rig (~1 week, Section 5.3.7) so being able to make both measurements at the same time saves a lot of time. The transducer is surrounded by a steel housing to protect it from the high pressure applied to the sample assembly. The ultrasonic pulse was generated using one of two generators. The Arenberg generator produces a single frequency sine wave tone burst whereas the Avetech produces a broadband pulse.

An advantage of the pulse-echo system is that it allows very accurate velocity measurements to be made on the sample (±0.3%). The disadvantage with the system is that it requires a solid rock sample rather than loose unconsolidated sediment although a weakly cemented sediment is permissible. The velocity models in Chapter 3 were developed for unconsolidated sediments and this must be taken into account when comparing the models and the data. This comparison will be presented in Chapter 6.

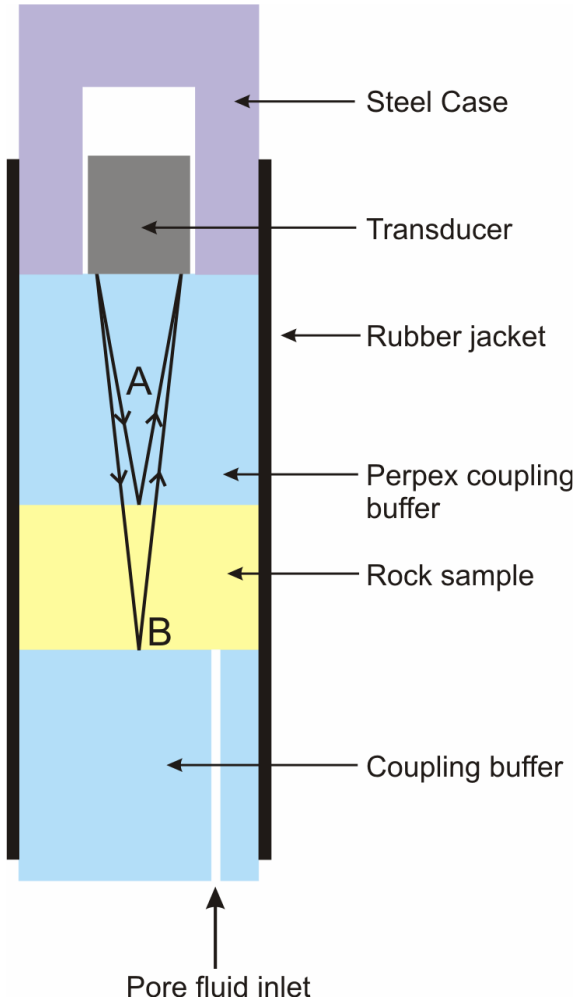

Figure 5.17 Reflection system (adapted from Winkler & Plona, 1982)

Electrical setup

The pulse-echo system was modified to allow electrical resistivity measurements. The electrical measurement required a 4-point setup rather than a 2-point setup in order to obtain the true potential difference. The electrodes at which the voltage is measured must not draw any current. Using such a setup means that any small scale heterogeneities in the rock at the point at which the current is introduced will not cause large error in the voltage because voltage is not measured at this point. Also the contact resistance between the rock material and the electrodes does not matter because no current is being drawn through those electrodes. To meet these design requirements the electrical system comprised 12 electrodes positioned in a ring at equal spacings around the circumference of the rock sample (Figure 5.18). This was achieved by incorporating electrodes into the rubber sleeve surrounding the sample. A current produced from an external current source can be passed

between any pair of electrodes and the voltage can be measured at any other pair of electrodes. Although any electrode configuration can be used, in practice the current was always passed across opposites pairs of electrodes and the voltage was measured at adjacent electrodes as shown in Figure 5.18. In case of sample heterogeneity this electrode configuration was rotated around so that the resistance could be measured in different orientations. The current was passed through a total of 6 different electrode pairs and resistance was measured 24 times around the sample at each measurement time.

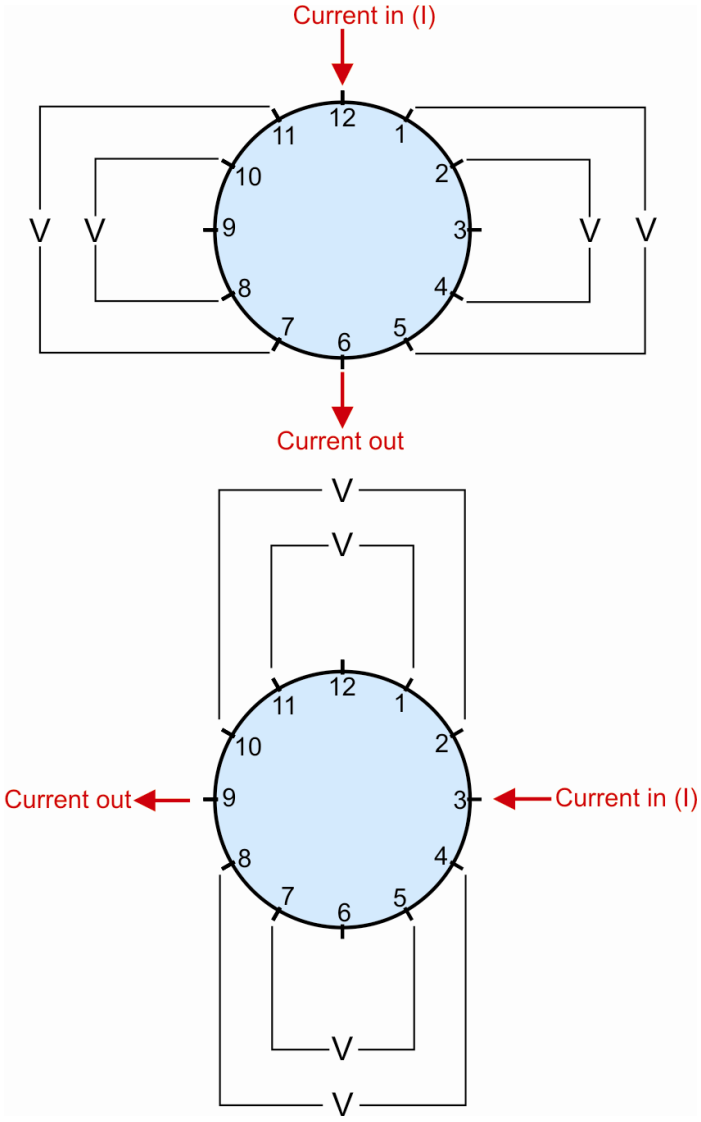

Figure 5.18 Electrode configuration of the resistivity measurement system. The voltage, *V*, is measured between adjacent electrode pairs while the current, *I*, is kept constant.

The cylindrical shape of the samples makes the theoretical calculation of resistivity complicated. Therefore, to simplify the problem an empirical geometric factor was determined to relate resistance to resistivity. A brine cell was set up identical in size and shape to the solid sediment samples (Figure 5.19). The electrodes were positioned around the cell in the same configuration as in the pressure rig. The cell was washed with distilled water and then filled with brine of a known salinity and sealed. The brine was composed of distilled water and salt (NaCl). The brine was allowed to equilibrate to room temperature (in a temperature controlled room) so that all measurements were made under the same temperature conditions (~19^{o}C). The resistance was then measured across the same electrodes as the sediment samples in the rig. The brine measurements were made using a Terrameter which calculates the resistance automatically with a current of 0.2 mAmps. The Terrameter was calibrated using a series of resistors and is correct to ±0.5%. The measurements were then repeated using different brine concentrations. The results are shown in Table 5.3.

Figure 5.19 Electrical brine cell used to calculate the geometric factors for the sediment samples. The inside of the cell has the same dimensions of the sediment samples.

The resistivities of the brines were then calculated using a water bath and a Wenner array (Figure 5.20):

$$\rho = 2\pi D \frac{V_{pd}}{I}, \qquad (5.5)$$

where *D* is the distance between the electrodes. This equation assumes that the water bath is large enough to be considered a uniform half space.

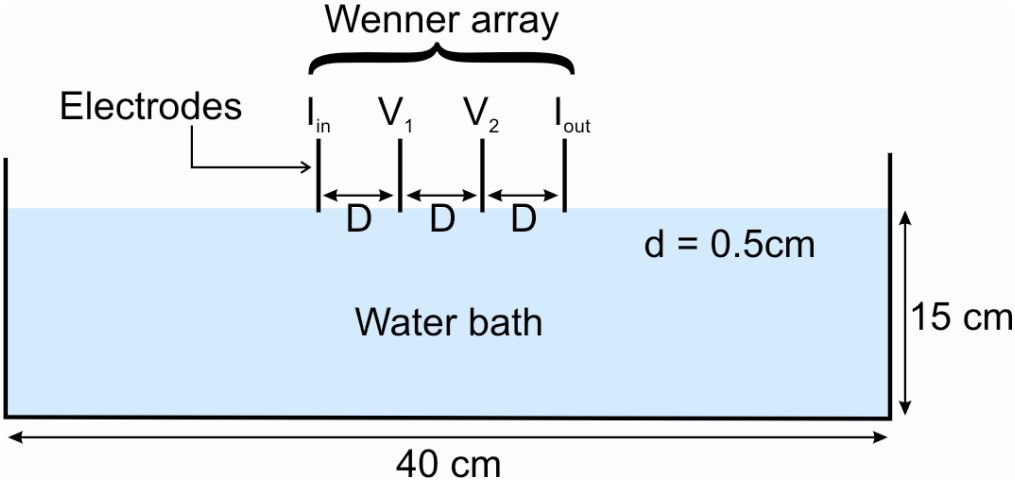

Figure 5.20 Schematic diagram of the water bath and Wenner array.

The geometric factors for closely and widely spaced electrodes were then determined by crosS-plotting the known resistivity for each brine concentration with the measured resistance for the electrode pairs in the brine cell (Figure 5.21).

Sample number	Salt content per litre of water (g)	Resistance of narrow spaced electrodes (mΩ)	Resistance of wide spaced electrodes (mΩ)	Resistivity calculated from the Wenner array (Ωm)
1	20	5.78 ± 0.03	14.15 ± 0.07	0.385 ± 0.002
2	8	13.19 ± 0.07	32.35 ± 0.16	0.825 ± 0.004
4	6	17.43 ± 0.09	42.95 ± 0.21	1.079 ± 0.005
5	4	26.45 ± 0.13	65.50 ± 0.33	1.497 ± 0.007
6	2	49.85 ± 0.25	123.18 ± 0.62	2.922 ± 0.015
7	1	95.43 ± 0.47	234.50 ± 1.17	5.515 ± 0.028

Table 5.3 Sample numbers, salt content, resistance of the brine samples in the resistivity cell (between two sets of electrodes) and resistivity calculated from the Wenner array setup. Values given for the resistance are averaged over orientations around the cell as seen in Figure 5.21.

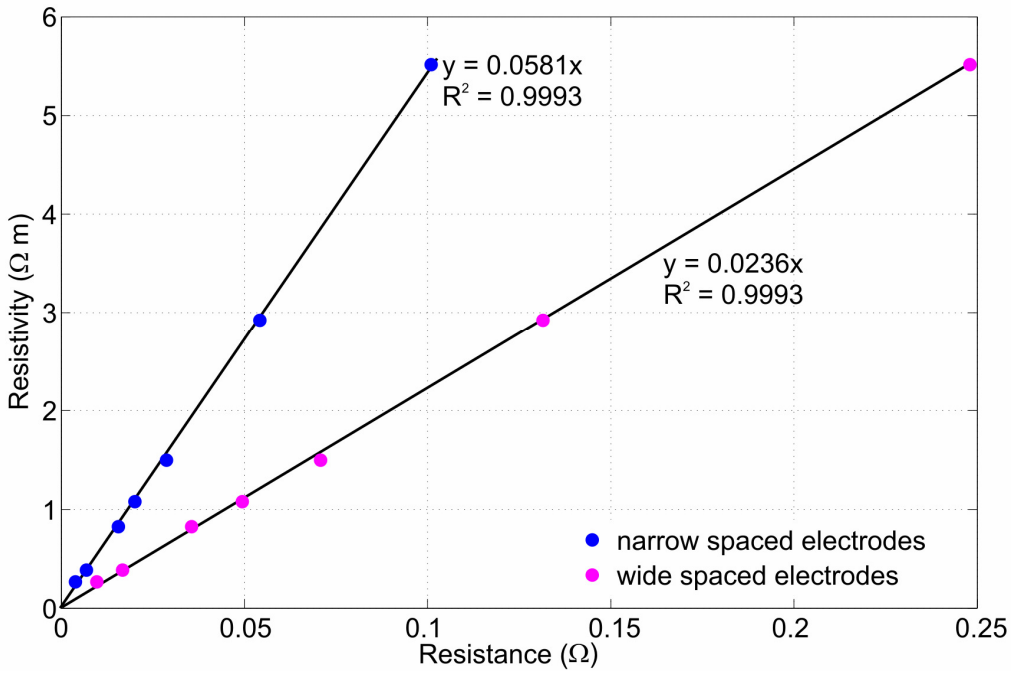

Figure 5.21 Plot of the resistance calculated from the brine cell plotted against the resistivity of the brine calculated from the Wenner array (R^2 is the coefficient of determination).

Figure 5.21 shows a linear trend between the resistance of the brine cell samples and the resistivity of the brine as determined from the Wenner array. The trends have been constrained to pass through the origin. Both the narrow and the wide spaced electrodes have a coefficient of determination (R^2) value of 0.9993. R^2 is the square of the correlation coefficient and is essentially a way to gauge how well the measurements fit a linear trend. R^2 ranges between 0 and 1, $R^2 = 1$ indicates a perfect linear trend while $R^2 = 0$ indicates no correlation between measurments. R^2 values from both the wide and narrow spaced electrodes are high indicating that the relationship between the resistance from the brine cell and the brine resistivity is linear and very well correlated. From this trend a numerical factor can be used to determine the resistivity of a sample from the resistance of the cell. For the narrow spaced electrodes

$$\rho = 58.075 R_n ; \tag{5.6}$$

and for the wide spaced electrodes:

$$\rho = 23.597 R_w . \tag{5.7}$$

5.3.3 Sediment preparation

Cylindrical shaped samples of cemented sediment were needed for the pulse-echo rig as opposed to loose sediment. This was because the accuracy of the pulse-echo method relies on having perfectly flat and parallel sample faces. This is only possible to obtain with lithified or cemented sediments (i.e. rocks). Because the results from these samples would be compared to the effective medium models the composition of the samples had to be known. Hence, initial experiments were conducted using a synthetic glass bead sample. The artificial sediment samples were composed of glass beads held together by a small amount of resin and saturated brine. The idea was to use as little resin as possible to achieve a cemented glass bead sample that could be ground to the required tolerance for the pulse-echo system, but at the same time approximate to a grain pack with high porosity.

The resin was composed of 50g of araldite resin mixed with 16.5g hardener and 30g of acetone. The acetone was added to reduce the viscosity of the resin. A mass of 260g of glass beads was mixed into the resin. Once the sample was mixed, it was then de-aired using a vacuum pump to remove as much air as possible (Figure 5.22).

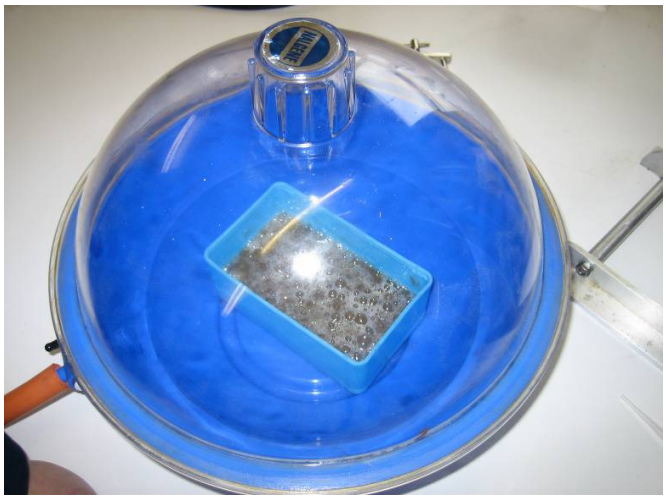

Figure 5.22 Sediment and resin mixture being de-aired in a vacuum chamber.

A piece of gauze was attached to one of the open ends of a metal cylinder, which had a diameter of ~6cm. It was in turn fitted to a sieve with a piece of filter paper between the two. The sieve was fixed to a vacuum flask which was attached to a vacuum pump (Figure 5.3). The de-aired bead/resin mixture was poured into the metal cylinder and a vacuum was then applied drawing most of the resin out of the mixture. The gauze and filter paper

prevented the glass beads from falling out of the cylinder. When no more resin could be removed the vacuum was removed and the cylinder was placed in an oven at 50°C to set. This took approximately 6 hours.

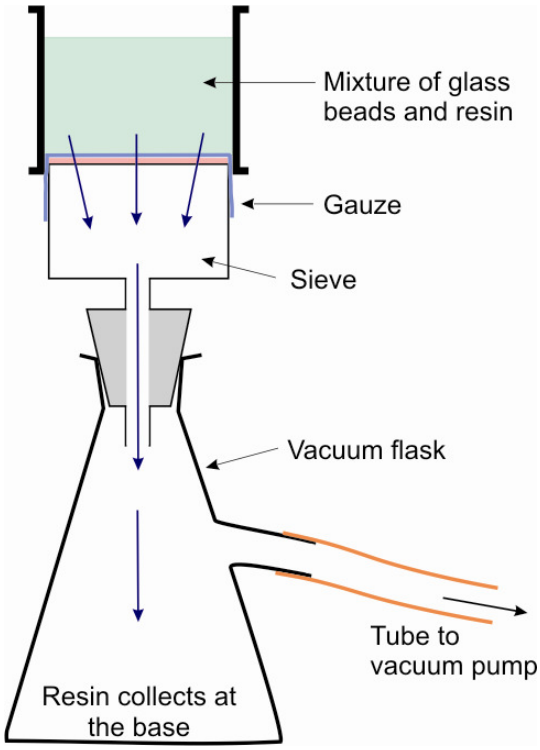

Figure 5.23 Setup for removing the resin from the sediment sample.

Figure 5.24 shows a Scanning Electron Microscope (SEM) picture of the final sediment sample. It shows that very little of the resin remains and that what is left is found at the grain contacts only.

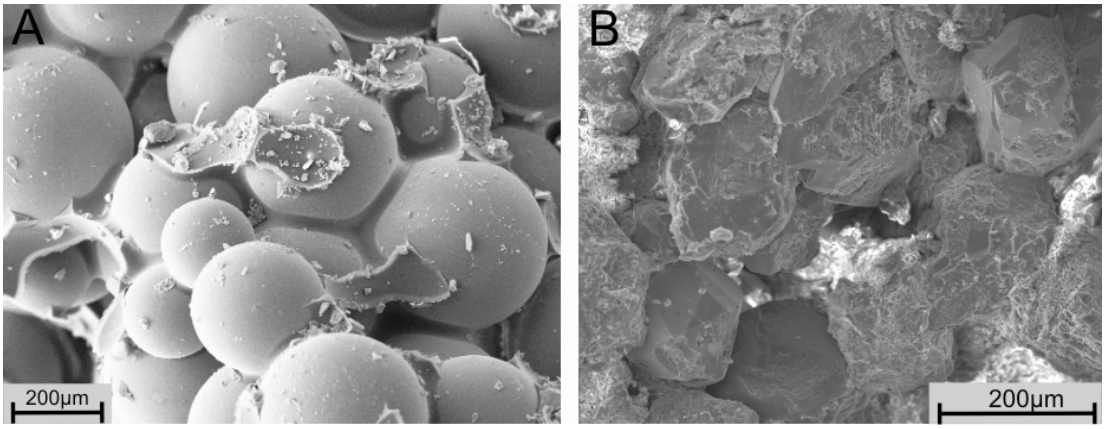

Figure 5.24 SEM photos of resin and glass bead mixture (A) and Berea Sandstone (B).

Once the sediment had set it was cut into shape using a diamond core bit. The samples were cut into 2 cm long cylinders with a radius of 2.5cm

Figure 5.25 Pictures of the sediment sample being cut.

The samples were then ground down so they are exactly 2cm thick (see Figure 5.26). This gave the surface of the samples a smooth finish and ensured that the top and the base of the samples were flat and parallel. The sample was measured at 7 different points to ensure that it was the same thickness within the required tolerance ±5μm. The average of these 7 thicknesses was used to give the mean sample length in the velocity calculations.

Figure 5.26 Synthetic sediment samples being ground down so that the sides of the samples were flat and parallel.

Porosity was determined by weighing the samples when oven dry and then fully saturating the samples with water and re-weighing them.

	Dry parameters	Water saturated parameters
Thickness 1 (mm)	19.931	-
Thickness 2 (mm)	19.934	-
Thickness 3 (mm)	19.94	-
Thickness 4 (mm)	19.94	-
Thickness 5 (mm)	19.935	-
Thickness 6 (mm)	19.926	-
Thickness 7 (mm)	19.932	-
Average Thickness (cm)	1.9934	-
Mass (g)	68.39	74.97
Diameter (cm)	4.961	-
Density (gcm^{-3})	1.775	1.946
Volume (cm^3)	38.5	38.53
Porosity (%)	17.08	

Table 5.4 Measurements made to calculate the porosity of the glass bead sample.

It was soon discovered that during the hydrate formation procedure (Section 5.2.4) the synthetic glass bead sample would not allow an even distribution of gas in the pore spaces due to its low capillary pressures. To solve this problem, a real rock sample was used with a finer grain size and higher capillary pressure. A piece of Berea sandstone was cut, ground and measured in the same way as the glass bead sample was. The sample of Berea sandstone is composed of quartz (68.1%), feldspar (22.3%), calcite (2.2%) and clay (7.5%) and has a porosity of 23.7% (Assefa *et al*., 1998). The Berea sandstone is not as close a representation of an idealised sphere pack as the glass bead sample due to the natural grain shapes and cementation, however the grains are rounded and have an aspect ratio approaching one (Figure 5.24), also the porosity of the rock is higher compared to the glass bead sample.

5.3.4 Hydrate formation procedure

The sediment samples were placed in the rig dry. Air was then removed by placing a vacuum on the sample for several minutes. Methane was then injected into the sample. It is important to ensure that only methane and no other impurities were present in the sample

for two principal reasons. Firstly, the hydrate saturation calculations (described later in this section), which are dependent on the volume of hydrate in the sample, would be incorrect. Second, air trapped in the sample would not turn into hydrate. It would therefore alter the physical properties of the sample. Once this has been done more methane or/and brine can be added to the sample depending on the requirements of each individual run.

The methane pressure was dependent on the amount of hydrate that needed to be formed (discussed later in this section). The temperature of the sample at this point was room temperature (~20^{o}C). Brine of a known salinity was then added via the same inlet port to approximately 15MPa. Because the temperature is approximately 20^{o}C the sample is still well outside of the hydrate stability zone (Figure 5.27). The sample was then left for a period of 2-3 days to allow the methane to redistribute itself around the sample. The temperature was then dropped to approximately 4^{o}C, well within the methane hydrate stability zone. Methane hydrate was left to form, which took several days depending on the amount of methane gas in the sample. Figure 5.27 shows this hydrate formation procedure on a pressure temperature plot of the methane hydrate stability curve.

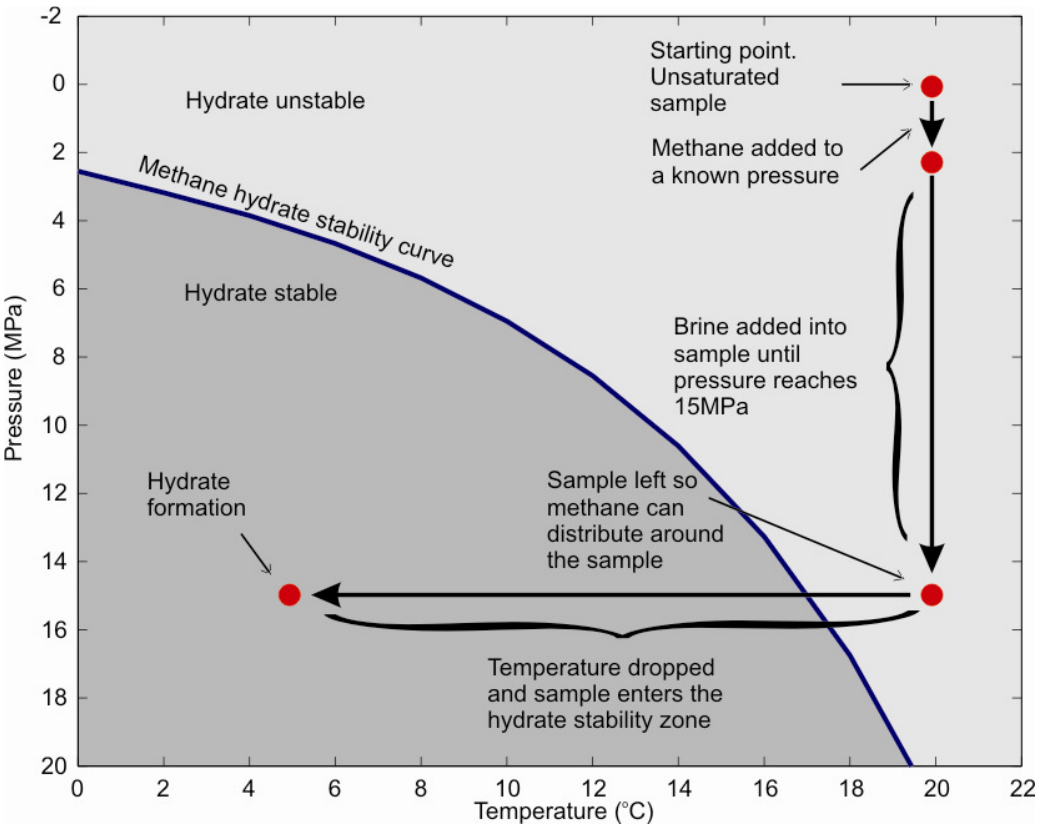

Figure 5.27 Hydrate formation procedure represented on a pressure and temperature plot of hydrate stability.

It is important to know how much hydrate was formed within the samples as this will affect the physical properties of the samples. Hydrate saturations were measured by controlling the amount of gas that was added to the sediment sample. This was achieved by calculating the gas pressure needed for the desired gas hydrate saturation. Gas pressures were calculated using Van der Waal's Real gas law (Tipler, 1999). The Ideal gas law cannot be used because the high pressures involved at the desired high gas hydrate saturations leads to large errors. Van der Waals gas law is given as:

$$\left[p + a_m \left(\frac{mol}{V_m} \right)^2 \right] \left(V_m - mol \cdot b_m \right) = mol \cdot UT \,, \tag{5.8}$$

where p is pressure, mol is the number of moles of gas, V_m is the volume that the methane occupies, a_m is the correction for the intermolecular forces, b_m is the volume occupied by one mole of molecules, U is the universal gas law constant (= 8.32 $J.mol^{-1}.K^{-1}$) and T is temperature in degrees Kelvin. The number of moles is calculated by:

$$mol = \frac{V_m S_h \chi_h}{m_h} \,, \tag{5.9}$$

where S_h is the hydrate saturation, χ_h is the density of structure I methane hydrate assuming that 100% of the cages are filled with methane, and m_h is the mass of one mole of methane gas hydrate at STP. The mass of one mole of methane hydrate can be calculated from the chemical formula of structure I methane hydrate, $8(CH_4) \cdot 48(H_2O)$. Replacing mol in equation 5.8 with equation 5.9 and solving for p gives:

$$p = \frac{S_h \chi_h UT}{1 - S_h \chi_h b_m} - a_m \left(\frac{S_h \chi_h}{m_h} \right)^2 \,, \tag{5.10}$$

All the V_m terms cancel out, therefore the final pressure calculated is independent of the sample size and is only dependent on the hydrate saturation and temperature. The constants used in equations 5.7 – 5.9 are given in Table 5.5.

Constants	Symbol	Value	Units
Density of methane at STP	χ_m	0.711	kg/m^3
Density of Structure I methane hydrate	χ_h	910	kg/m^3
Mass of 1 mole of hydrate at STP	m_h	0.120	kg
Mass of 1 mole of methane at STP	m_m	0.0160	kg
Universal gas law constant	U	8.32	$J.mol^{-1}.K^{-1}$
Volume of 1 mole at STP (Ideal gas)	V_m	0.0224	m^3
Mass of 1 mole of methane at STP	m_m	16.0	kg
Methane (Real Gas) Van der Waals Coefficient a	a_m	0.228	$(m^3)^2$. Pa. mol^{-2}
Methane (Real Gas) Van der Waals Coefficient b	b_m	4.28×10^{-5}	$m^{3.}mol^{-1}$
Water (Real Gas) Van der Waals Coefficient a	a_w	0.554	$(m^3)^2$. Pa. mol^{-2}
Water (Real Gas) Van der Waals Coefficient b	b_w	3.05×10^{-5}	$m^{3.}mol^{-1}$
Solubility of methane in water at 5 ^oC expressed as $mLCH_4$ at STP dissolved in 1mL H_20	S_{ol}	0.0497	$m^3(CH_4)/1.m^3(H_2O)$

Table 5.5 Constants used to calculate pressure for different hydrate saturations using the Van der Waals equation (Sloan, 1998; Marion & Hornyak, 1982; Kehiaian, 1990). Values are given to 3 s.f.

The previous calculations assumed that none of the methane dissolves into the water, however methane is slightly soluble in water so the effect of solubility was checked. To do this the number of moles of methane gas required to form hydrate was corrected to take into account the number of moles that dissolved into the pore fluids. This can be done using the following equations:

$$mol_c = \frac{P_h\left(V_{mp} + V_d\right)}{UT_h}; \tag{5.11}$$

$$V_{mp} = \frac{molUT_h}{P_h}, \tag{5.12}$$

$$V_f = \frac{PS_{ol}T_h\left(V_m - V_{mp}\right)}{T_o P_h}, \tag{5.13}$$

where mol_c is the corrected number of moles required to form a given hydrate saturation when the solubility of methane in taken into account. V_{mp} is the volume of free methane in the pore space just before hydrate forms. V_f is the volume of methane dissolved in the pore fluid just before hydrate forms. Both V_{mp} and V_f are dependent on temperature and pressure. T_h and T_o are the temperatures at which hydrate forms and 0°C in degrees Kevin respectively. P_h is the pressure at which hydrate forms and S_{ol} is the solubility of methane in water at STP. The value mol_c can then replace mol in equation 5.9 to determine the gas pressure required to form a given hydrate saturation.

Table 5.6 gives uncorrected and corrected pressure values for different hydrate saturations. It is assumed that hydrate formation starts to occur at 5°C and 15MPa. The difference between the uncorrected and corrected pressure values is very low and can be neglected.

The assumptions include that there is no leaking gas from the rig, all of the gas turns into hydrate and 100% of the cages within the crystal lattice of the hydrate are filled with methane.

Hydrate saturation	**Pressure (MPa)**	
	Uncorrected for solubility	**Corrected for solubility**
0.1	1.784	1.789
0.2	3.438	3.441
0.3	4.975	4.978
0.4	6.413	6.415
0.5	7.770	7.772
0.6	9.069	9.070
0.7	10.336	10.337
0.8	11.601	11.601
0.9	12.901	12.901
1.0	14.279	14.279

Table 5.6 Methane gas pressures needed to form the desired hydrate saturations when uncorrected and corrected for methane solubility.

It was assumed that once the gas and brine have been added to the system that the gas will distribute itself evenly throughout the pore structure due to capillary forces. If the capillary forces are large enough the gas will move to the largest pores. During the course of these experiments it was determined that the gas only partially distributed itself and tended to pool in one area. This was probably due to the large pores in the glass bead samples. In the real rock samples the distribution tended to be better although not completely uniform. This distribution issue is easily seen in the results from the electrical resistivity measurements (see section 5.3.7).

Another complication was the brine salinity concentration. Salt is known to depress the hydrate stability phase boundary as shown in Figure 5.28. Ideally, distilled water should be used to make hydrate. However, because we wish to measure the effect of hydrate on the resistivity of a medium we need to be able to transmit an electrical current through the sample. Distilled water has a very high resistivity therefore salt was added to reduce the resistivity. Figure 5.28 shows the difference between the hydrate stabilities for distilled water and brine with approximately the same amount of salt as sea water. It also shows the point at which the samples were left to form hydrate. The temperature and pressure of the sample is well within both the distilled water and the brine methane stability zones. Therefore the brine concentration would not effect the formation of the hydrate at salinities between 0 and 3.5 salt weight %. The final brine solution was composed of 8g of NaCl per litre of distilled water was chosen because it was well within hydrate stability while the brine was saline enough to allow a current to pass through the sample.

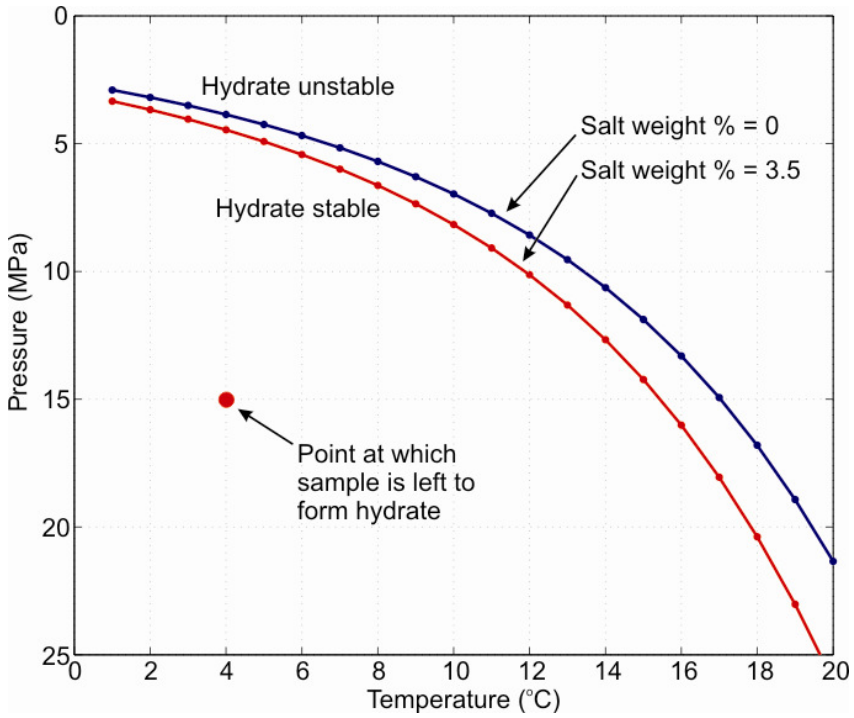

Figure 5.28 Methane hydrate stability phase boundary with and with salt (NaCl). Temperature and Pressure values are calculated from Sloan (1998). The point at which the samples were left to form hydrate is included for comparison with the different methane hydrate stabilities.

5.3.5 Ultrasonic velocity measurements

Both P- and S-wave velocity were measured at 12 hour intervals on each sample run from the point when the sample entered the hydrate stability zone until it stabilized. Figure 5.29 and Figure 5.30 shows the 1st and 2nd arrivals from the Arenberg and Avtech pulse generators. The Arenberg produces a single frequency pulse whereas the Avtech produces a broadband pulse. To reduce the signal to noise ratio, 1000 signals were averaged for each travel time measurements. The Arenberg generator was used to measure the travel time between the 3rd positive cycle from the 1st arrival and the 3rd negative cycle from the 2nd arrival. Velocity was calculated from the thickness of the sample and the time it takes the ultrasonic pulse to travel through the sample. The travel time was measured using an oscilloscope.

$$Vel = \frac{2d}{\Delta T} \tag{5.14}$$

where Vel is the P- or S- wave velocity, d is the thickness of the sample between the two parallel faces and ΔT is the travel time between the 1st and 2nd reflections.

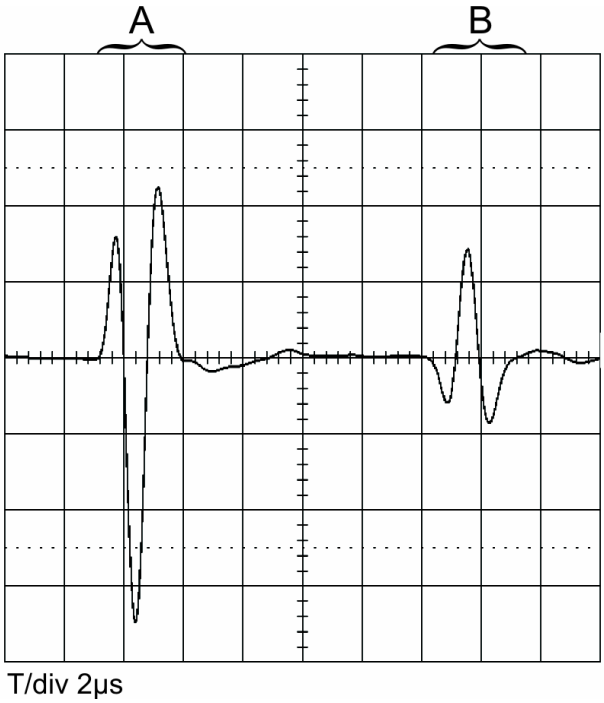

Figure 5.29 Broadband frequency waveform produced from the Avtect pulse generator, (A) the reflection from the top of the sample and (B) the reflection from base of the sample.

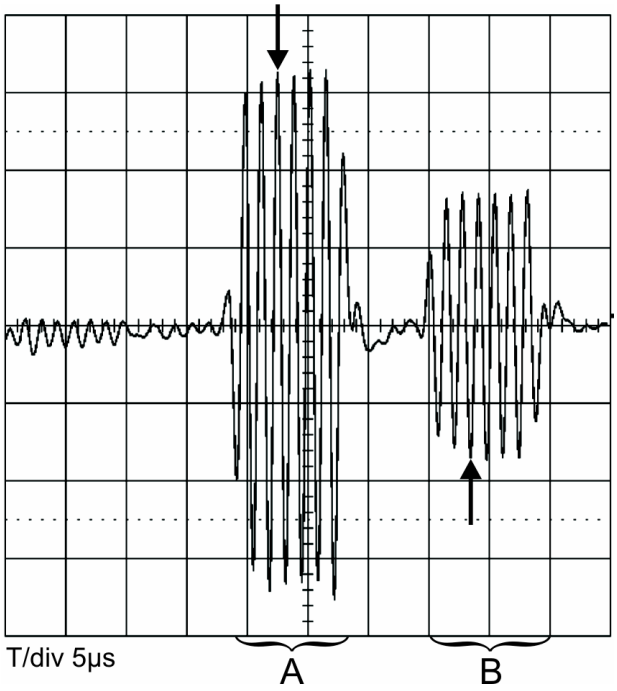

Figure 5.30 Single frequency waveform produced from the Arenberg pulse generator, (A) the reflection from the top of the sample and (B) the reflection from base of the sample. The time delay between the two wave reflections is measured between the arrows.

McCann & Sothcott (1992) demonstrate that the velocity errors using the pulse echo rig are ± 0.3%. Errors are caused by sample swelling, compression of the sample, the faces of the sample not being flat or parallel, diffraction and side wall reflections. Measurements were made using both the Arenberg and the Avtech however velocity results from the Arenberg are more precise than the Avtech (McCann & Sothcott, 1992), therefore the velocity results presented later in this chapter are those measured used the Arenberg.

5.3.6 Electrical resistivity measurements

At the start of the experiment the resistance was measured by hand using the setup in Figure 5.18. A current of 1-2mA was used throughout the experiment. At this small current level the voltage was measurable without any electro-chemical effects occurring at the electrodes. The resistance was measured as the system cooled and hydrate formed until the resistance had stabilized for a period of time. The final resistance of the system was then measured. Hydrate growth and the resistance stabilization took some time to occur and was dependent on the amount of hydrate growing in the sample. During the course of the laboratory work a switching box was developed to measure the voltage of the sample automatically. It was set to record the voltage of the sample at 1 hour intervals for 5 seconds with a sampling rate of 4 kHz. Figure 5.31(A) shows an example of the raw data. It can be seen that voltage takes up to 0.25 sec to stabilize therefore during the processing of the data the first 0.25 seconds were removed. Figure 5.31 (B) shows part of the voltage waveform. To remove the noise from the raw data a Butterworth band pass filter was applied. The final voltage from the sample is the amplitude of the waveform which was determined by applying a Fast Fourier Transform (FFT) to the filtered data (Figure 5.31 C).

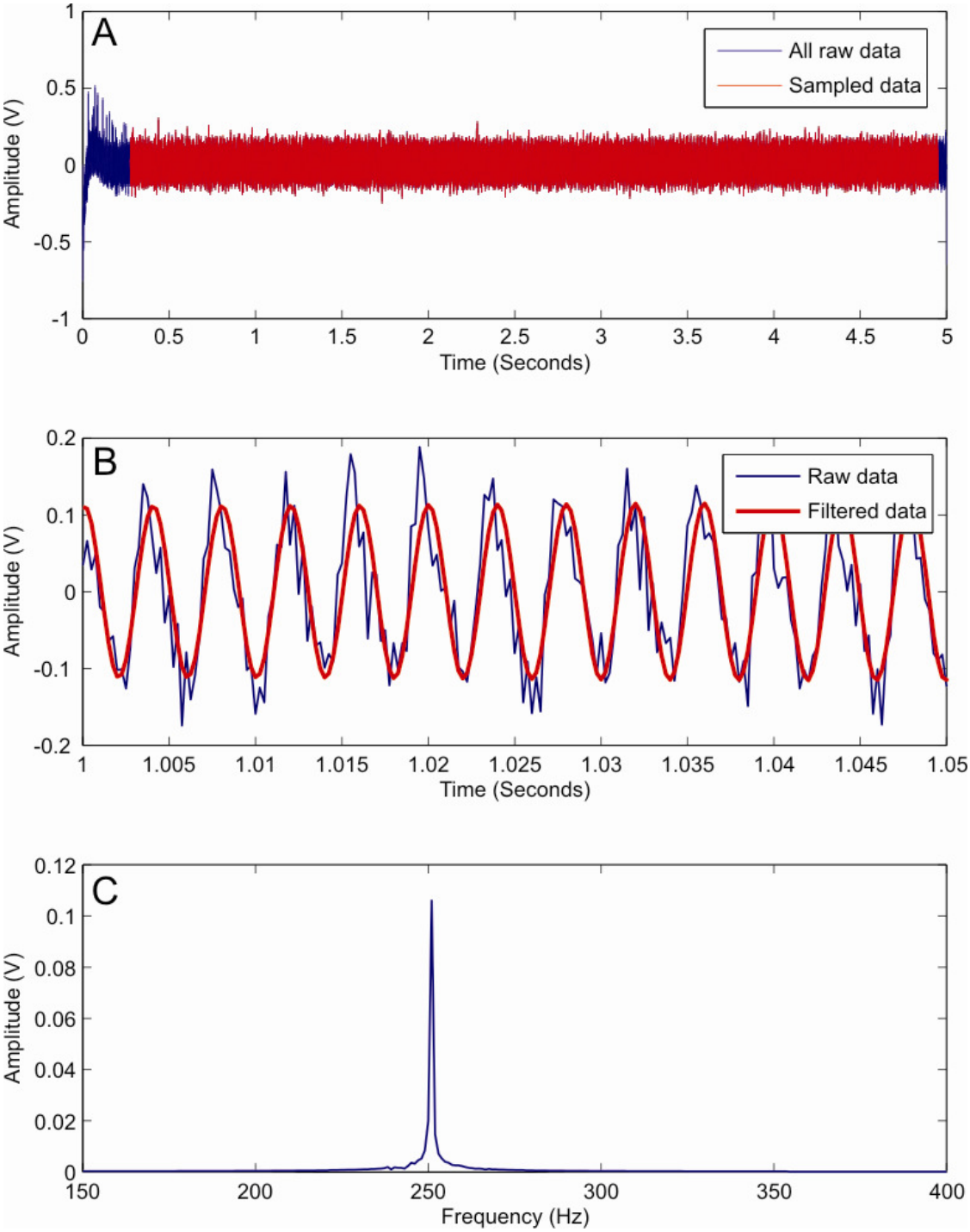

Figure 5.31 (A) An example of the original raw electrical data. The data coloured in red was used to calculate the resistivity of the sample. (B) Part of the electrical raw data waveform (blue) with the Butterworth filtered data superimposed on top. (C) Amplitude versus frequency calculated using an FFT from the filtered data.

5.3.7 Results

In total four runs were successfully completely using this setup where both velocity and resistivity data was measured. Two runs were achieved using the glass bead sample where hydrate was formed at 10% and 30% pore space saturation. Due to problems with the distribution of the hydrate throughout that sample it was decided to try and use a real rock sample, Berea Sandstone. It was expected that the Berea Sandstone would allow the hydrate to distribute more evenly because it had smaller pores than the glass bead sample and therefore higher capillary forces. Two runs were accomplished using the Berea sandstone sample with 20% and 0% hydrate.

Ultrasonic results

Figure 5.32 and Figure 5.33 show examples of the P- and S-wave velocities measured versus time for the glass bead sample with 30% target hydrate saturation. The rest of the velocity measurements for the other runs are shown in Appendix D. It can be seen that both P-wave and S-wave velocities increase with time as the free methane gas is converted to hydrate. As hydrate forms, the free gas bubbles shrink and are replaced with hydrate and brine causing both P- and S-wave velocity to increase. Once the velocity measurements have stabilized it was assumed that all of the methane had been converted to hydrate. The length of time this took was dependent on the amount of hydrate being formed in the samples. All of the methane had been converted to hydrate after 150 hours when the sample was filled with 10% hydrate, whereas when it was saturated with 30% hydrate, it took at least 300 hours. Hydrate formation was much fastest when formed in the Berea sandstone (30 hours). This was probably due to the methane distributing more evenly though the sample allowing a larger surface area around the gas for the hydrate to form compared to the glass bead sample.

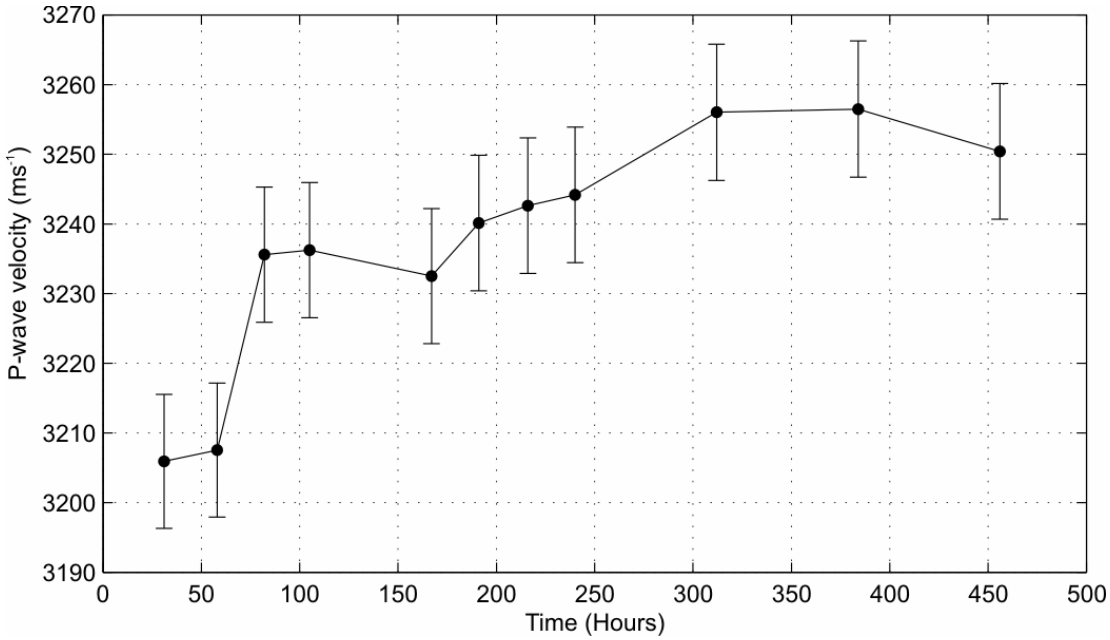

Figure 5.32 An example of P-wave velocity measurements versus time measured using the pulse echo rig on the glass bead sediment example. Measurements start from the point the sample is put into the hydrate stability zone and shows an increase in velocity as hydrate forms. Gas hydrate saturation target was 30%.

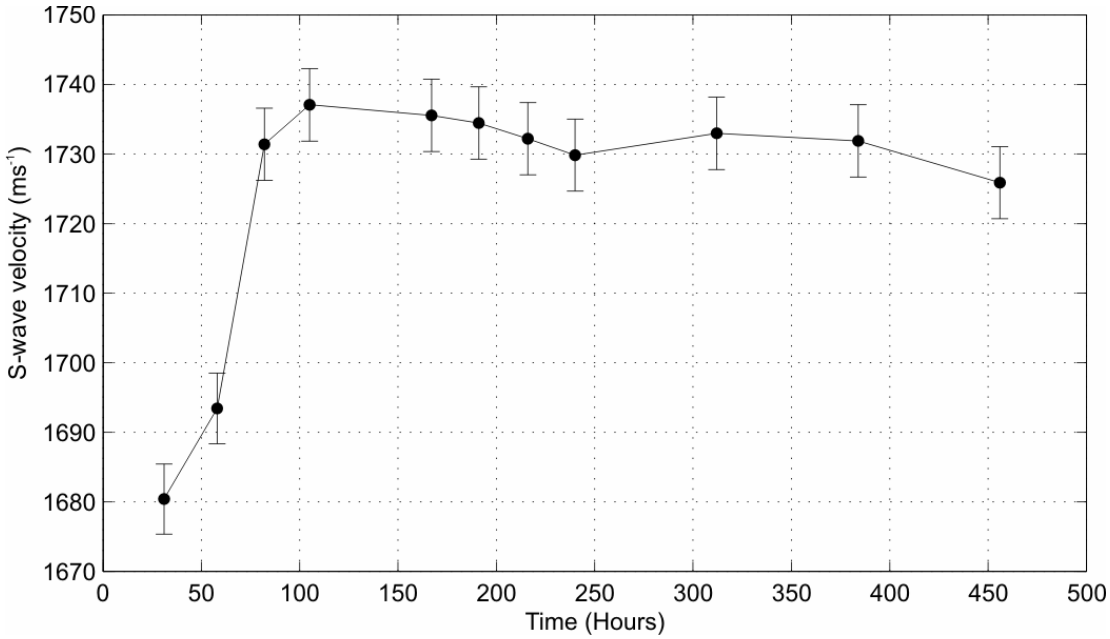

Figure 5.33 An example of S-wave velocity measurements versus time measured using the pulse echo rig on the glass bead sediment example. Measurements start from the point the sample is put into the hydrate stability zone and shows an increase in velocity as hydrate forms. Gas hydrate saturation target was 30%.

The final P- wave and S-wave velocities, given in Table 5.7 are averages of velocity measurements once the samples had stabilized. The P-wave velocities from the glass bead sample show little difference between the two different hydrate contents although the 30% hydrate saturation final P-wave velocities are slightly higher than the 10% hydrate saturation velocities. The S-wave final velocity of the 30% hydrate sample is slightly lower than the 10% hydrate sample. This may be caused by the increase in brine salinity due to the formation of hydrate leading to higher brine densities. If the density of the brine increases but the shear modulus remains the same the overall velocity will be less. Both the P- and S-wave velocities increase as the hydrate content increases in the Berea sandstone samples.

	Sample type	**P-wave Velocity ($mS\text{-}^{1}$)**	**S-wave Velocity ($mS\text{-}^{1}$)**	**Hydrate Saturation (%)**
Run 1	Glass bead	3250 ±10	1770 ±5	10
Run 2	Glass bead	3254 ±10	1730 ±5	30
Run 3	Berea Sandstone	3787 ±11	2278 ±7	20
Run 4	Berea Sandstone	3711 ±11	2263 ±7	0

Table 5.7 Final P- and S-wave velocity averages of each of the runs when hydrate had formed and the velocities had stabilized. Velocities are rounded to the nearest 1 $mS\text{-}^{1}$.

Electrical results

Figure 5.34 shows an example of the change in resistivity versus time from the point that the sample was put into the hydrate stability zone. The figure shows the resistivities from only one current electrode configuration where the current is passed between electrodes 4 and 10 and the voltage is measured at the adjacent pairs. There are six configurations in total for each sample. The other electrode configurations and those for the other runs are given in Appendix D. Figure 5.34 shows that the resistivity increases with time. This is due partly to decrease in the sediment temperature. However Figure 5.6 shows a ~50% increase in resistivity caused by a temperature change from 20^{o}C to 4^{o}C (approximately the same as the temperature change during hydrate formation) in the two phase experiment. The resistivity increase observed during hydrate formation in the rig is ~100% indicating that possible effects other than temperature are contributing the increase.

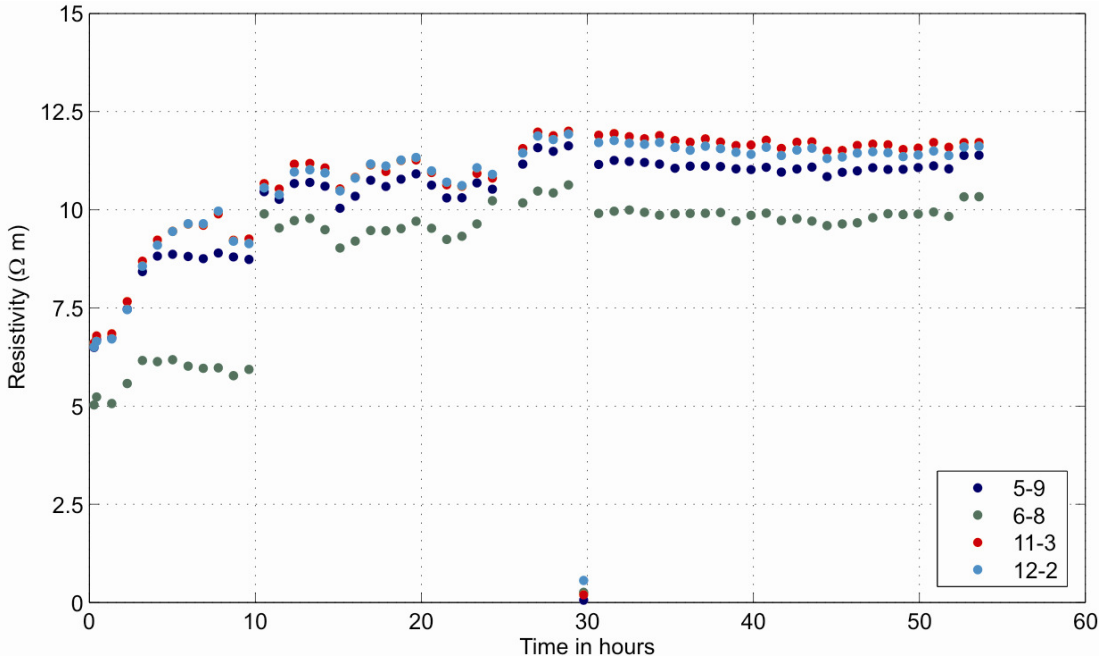

Figure 5.34 An example of resistivity measurements versus time measured using the ring of electrodes on the Berea Sandstone sediment example. The current was passed through electrodes 4 and 10 and resistance was measured across electrodes 5 & 9, 6 & 8, 11 & 3 and 12 & 2. Measurements start from the point the sample is put into the hydrate stability zone and shows an increase in resistivity as hydrate forms. Target gas hydrate saturation was 20%.

As with the velocity measurements the final resistivity of each sample was calculated from the average of the resistivities once the resistivity measurements has stabilized and are given in Table 5.8. The stabilization times are shorter for the Berea sandstone samples than the glass bead samples. This is because the surface area of the methane gas prior to hydrate formation is larger due to the improved distribution of gas.

Resistivity of the samples tends to increase with time as the hydrate formed in the samples. This is partly because hydrate replaces some of the conductive fluids and possibly it also blocks some of the pores. The rest of the resistivity change was cause by the drop in temperature which in turn causes the resistivity of all the constituents to increase. The drop in resistivity due to the above reasons is counteracted by the decrease in resistivity of the brine as the salinity of the brine increases due to the expulsion of the salt from the hydrate. No quantitative interpretation of the measurement variations was attempted during the

formation of hydrate as only the final P- and S-wave velocities and resistivity values are required for comparison with the theoretical models developed in Chapters 3 and 4. A comparison of the laboratory data and the models is presented in Chapter 6.

	Sample type	Electrical Resistivity (Ωm)	Standard Deviation	Hydrate Saturation (%)
Run 1	Glass bead	24.92 ±0.314	1.693	10
Run 2	Glass bead	16.04 ±0.288	0.436	30
Run 3	Berea Sandstone	15.28 ±0.389	14.61	20
Run 4	Berea Sandstone	14.61 ±0.372	10.06	0

Table 5.8 Final resistivities averages of each of the runs when hydrate had formed and the resistivities had stabilized. Resistivites are given to 2 d.p.

Stacked Resistivity Pseudo-Section

Ideally the resistivity calculated from each electrode pair should be the same. This would mean that the samples are homogenous. However the resistivities obtained from the samples electrode pairs were not all the same in each of the runs. This indicated that the samples were not homogeneous. To determine where the high and low resistivities were in the samples, some simple resistivity pseudo sections were made.

Each pair of current electrodes was analysed separately. It was assumed that the resistivity was constant between each pair of voltage electrodes (i.e. the electrodes where the voltages are measured). It is also assumed that the resistivity varies linearly between pairs of electrodes. From these two assumptions an array of resistivities can be created to represent the resistivity distribution of the sample. This is repeated for each set of current electrodes. In total 6 arrays should be produced. Each of the arrays is then orientated to match their relative positions to the sample and then added together and divided by 6. This produces an image of where any anomaly is situated within the sample (Figure 5.35). It should be stressed that this is in no way a true tomography and that it cannot be used to determine the actual resistivities at different points around the sample. It is however a useful quick method to determine approximately where there are resistivity anomalies.

Figure 5.35 shows data from Run 2 prior to hydrate formation (i.e. free gas is still present in the sample). The top six images are the six arrays orientated into the correct position. The bottom figure shows the six arrays after the addition. Red represents high resistivities and blue are low resistivities. The red colour, near electrodes 12 and 1, indicates where approximately the gas (which is resistive) was within the sample.

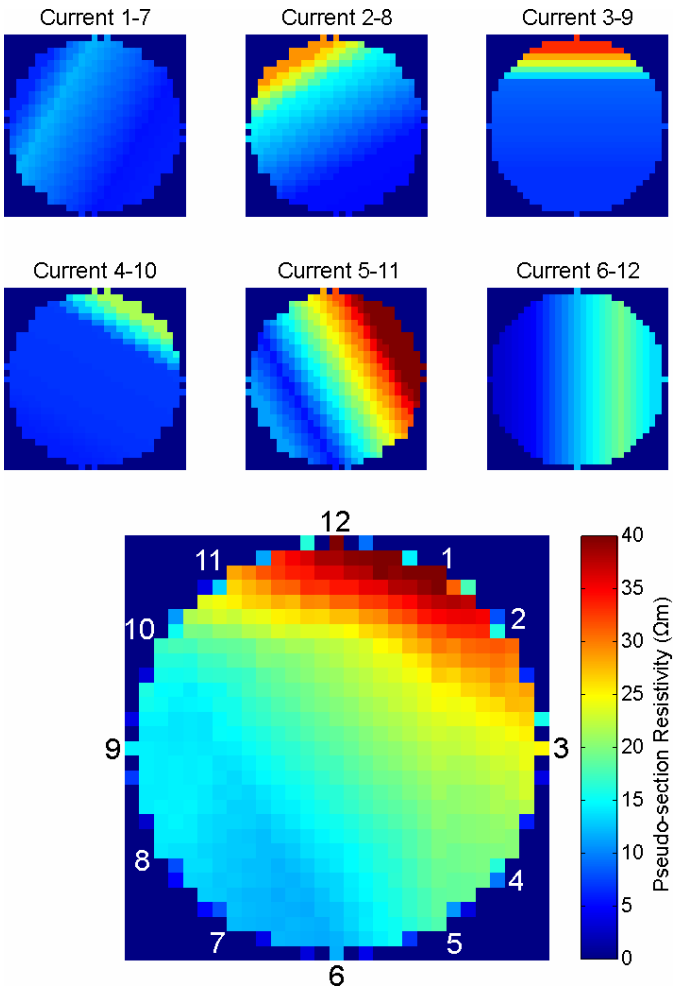

Figure 5.35 Pseudo-tomography of the glass bead sample before it was put into the GHSZ showing areas of high (red) and low (blue) resistivity through the sample.

Figure 5.36 shows two stacked sections from run 2 at two different times. The first section is taken from time = 80 hours before hydrate formation started. It shows high resistivity in one corner of the sample. In this run a gas bubble was believed to be present in the sample causing the high resistivities. The second section is taken from Time = 700 hours after hydrate formation has occurred. The section shows a more even distribution of resistivity. The resistivities appear lower in this section than the previous. This will be due

to the increase in conductivity of the conducting pore fluids due to the expulsion of salt from the hydrate. Also hydrate saturation is lower than the gas saturation and the difference in volume will be filled with conduction pore fluids. There are some small scale changes in resistivity in the second of the stacked plots which are hard to see. There is a slight increase in resistivity in the second plot in the areas of the sample which had high resistivity before hydrate formation. This indicates that more hydrate formed in the area of the gas bubble than away from it.

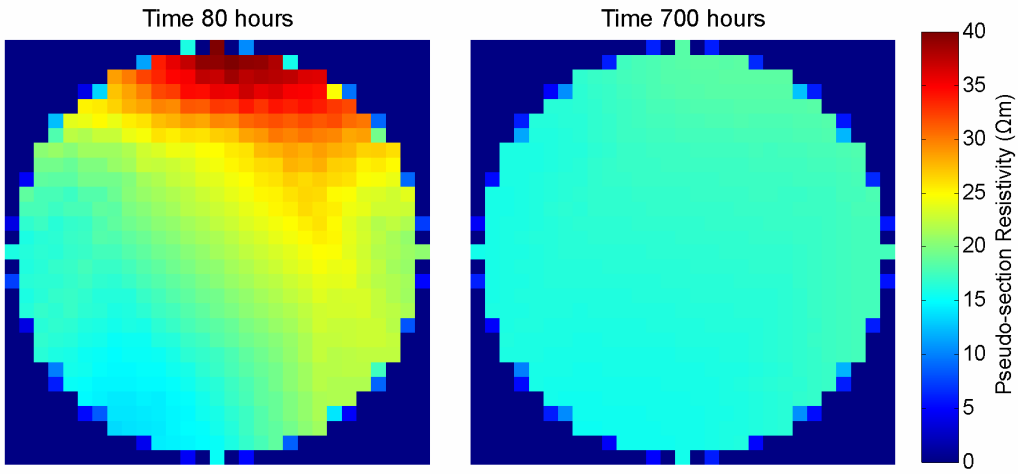

Figure 5.36 Stacked Resistivity Pseudo-sections of run 2 before hydrate formation (Time 80 hours) and after hydrate formation (Time 700 hours).

5.3.8 Imaging hydrate

Although the physical properties did change when the rig samples were placed into the hydrate stability zone, it is useful to visually confirm that hydrate did form under the same temperature and pressure conditions and to determine the hydrate morphology. To do this a small pressure cell with a window was built (Figure 5.37). Within the pressure cell there was a small space (2 mm in diameter) into which a glass cover slip was placed. Glued to the cover slip were a single layer of glass beads. Water and methane gas could be pumped into the space via a small inlet tube.

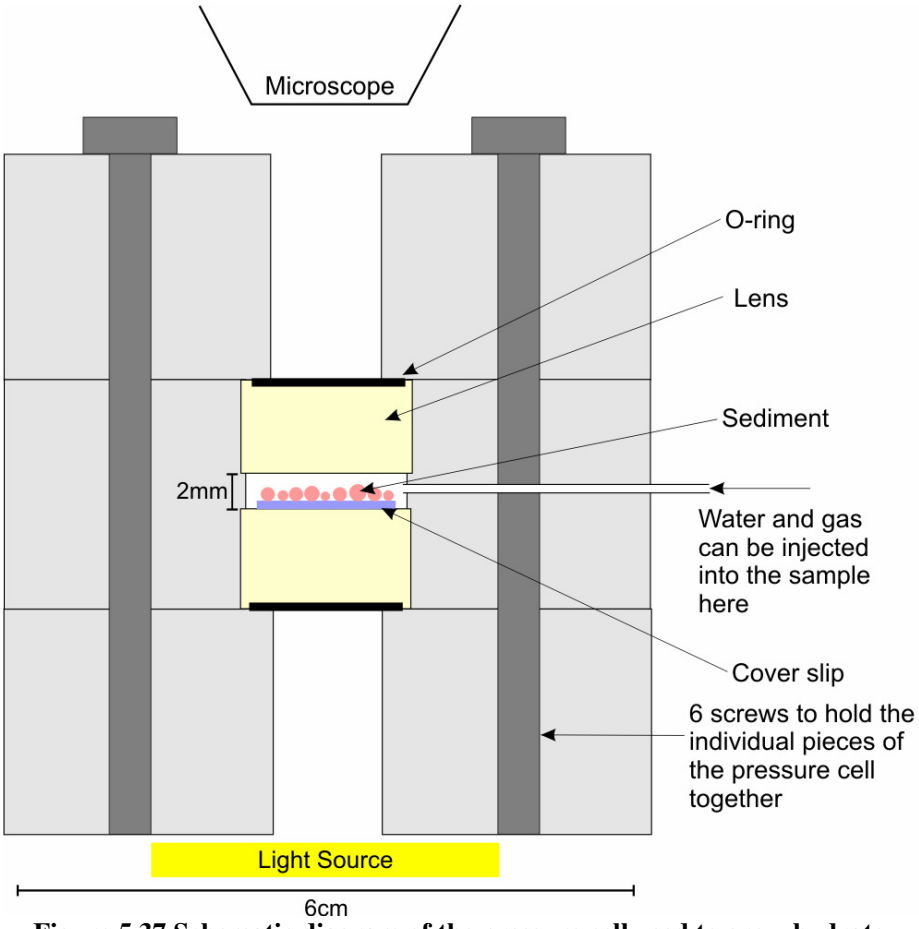

Figure 5.37 Schematic diagram of the pressure cell used to grow hydrate.

To create hydrate in the cell methane gas was pumped into the sample to a known pressure. Distilled water then was added to a pressure that was still outside of the hydrate stability zone at room temperature (~10MPa). A photo of the glass beads was then taken using a microscope and transmitted light from beneath the pressure cell (Figure 5.38). The pressure cell was then placed into a fridge to cool to ~4^{o}C. At these temperature and pressure conditions the sample was now within the hydrate stability zone. The sample was left there to form hydrate for 4 days. Any hydrate formed using this technique was formed from free methane gas in the same manner as hydrate was formed in the pressure rig. After 4 days the pressure cell was removed from the fridge and a second photo was taken. The pressure cell has enough thermal inertia to prevent the cell temperature to increase while the photo was being taken. Therefore hydrate did not dissociate while the photos were being taken.

Figure 5.38 shows photo of the glass beads before the sample was placed in the stability zone and after the sample had been left in the hydrate zone for 4 days. It shows that hydrate does form under similar pressure and temperature conditions as the rig samples. The hydrate appears in the photo to be both coating the grains and filling the pore space.

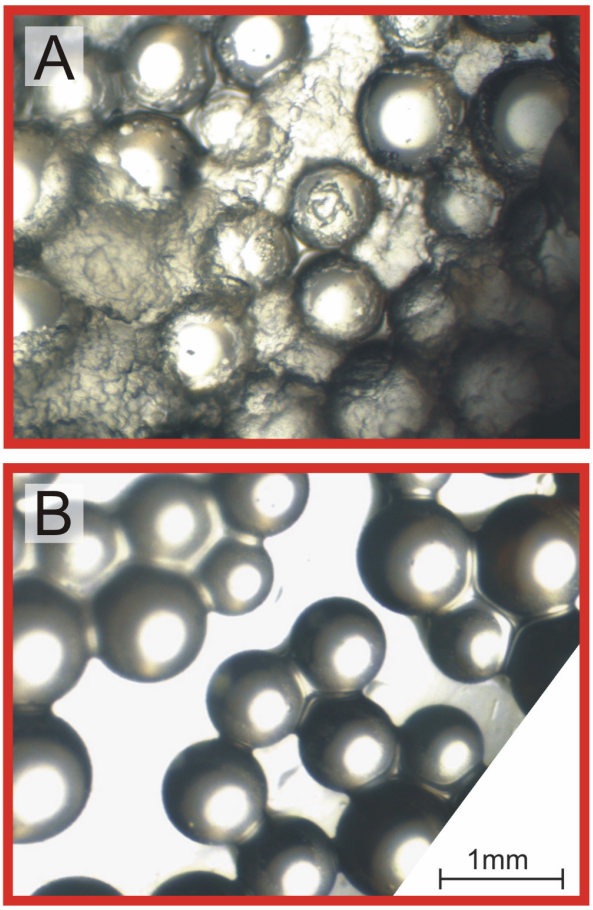

Figure 5.38 Microscope photos of glass beads in the "see-through" pressure cell. (A) Photo after the sample was left in the hydrate stability zone for 4 days. (B) Photo of before the sample was put into the hydrate stability zone.

5.3.9 Discussion and Conclusion

Hydrate was successfully formed from free gas and brine in the pressure rig at 15MPa and 4°C. Hydrate was formed by injecting the samples with methane and then brine. The pressure was then increased and the temperature dropped so that the samples were within the hydrate stability zone. This allows the final samples to be water saturated as opposed to gas saturated. Water saturated samples were needed to allow resistivity measurements to

be made. Hydrate formation was confirmed visually using a "see-through" cell at the same temperature and pressure conditions. Hydrate saturation was controlled by measuring the amount of methane gas injected into the samples and assuming that all the methane was converted into hydrate using an excess water method.

One major problem experienced during this work was the distribution of the methane gas and therefore the hydrate in the sediment samples. The first sediment sample was composed of glass beads and resin. This type of sample was used so that the results could easily by compared to the effective medium models the grains were of uniform shape (spherical). It was assumed that capillary forces would allow the hydrate to distribute evenly through the glass bead sample. However it was obvious that this was not the case when analysing the resistivity data. The problem with distribution was partially solved by using a real sediment rock sample, Berea sandstone. The pores in the Berea sandstone are smaller and therefore the capillary forces are greater allowing the gas to distribute more evenly. Berea also has a small amount of clay.

It was assumed that all the hydrate had formed once the physical properties had stopped changing after it had been put into the hydrate stability zone. This took up to 300 hours depending on the target hydrate saturation. At the beginning of each run the sample was left with the methane and the brine sealed in at pressure (15MPa) for a minimum of a week to allow the gas to distribute around the sample. Because of this each run could take up to a month, limiting the total number of runs that could be achieved.

The seismic velocity was successfully measured at approximately 12 hour intervals on each of the sample runs using the pulse-echo system. Velocity was determined from the difference in the travel times between the reflection from the top and the base of the samples and the thickness of the sample. In runs 1-3 the seismic velocity increased as hydrate was formed.

The electrical resistance of the samples were successfully measured using a ring of 12 electrodes around the samples. Current was passed between opposite electrodes and the voltage was measured at pairs of electrodes either side of the current electrodes. Determination of the resistivity of the samples was complicated by the shape of the samples. A simple approach was taken to convert the resistance to resistivity using an

empirical geometric factor. The geometric factor was established by measuring the resistance of different salinity brines using a calibration cell with the same shape as the sediment samples and comparing them with the resistivities of the brines. It was determined that the resistance varied linearly with resistivity. The resistivity of the samples increases as hydrate formation occurs. This is due to the drop in temperatures and the formation of resistive hydrate. These effects are however counteracted by the decrease in resistivity of the pore fluids caused by the expulsion of salt from the hydrate. This effect will be discussed further in Chapter 6.

An advantage of the resistivity ring was that the resistivity could be measured at many different points around the sediment samples. If the sample was homogenous the resistivity at each point would be the same. If the resistivity varied across the sample the resistivities measured at different point would be different. This was seen in each of the runs and indicated that the methane gas had not distributed evenly. Simple pseudo-tomograms were used to determine areas of high resistivity. The resistivity measurements were therefore able to show more detail than the velocity measurements which are unable to show the uneven distribution of the hydrate and methane gas, but were a bulk average of the whole sample given the beam width of the ultrasound.

Chapter 6. Comparison of Effective Medium Models with Experimental Data and Joint Interpretation Method

In this chapter both the two-phase and three-phase models will be compared to the experimental data collected from the artificial sediments as discussed in Chapter 5. This comparison allows us to see whether these theoretical effective medium models are able to predict the velocities and resistivities of non-hydrate and hydrate bearing sediments. After this the chapter introduces a method for jointly interpreting co-located seismic and resistivity data for two-phase medium (i.e. solid sediment grains and pore fluids) and tests the method against the two-phase data. In this case two variables can be determined, the aspect ratio of the sediment grains and the porosity. The three-phase joint case is then developed for both non-load bearing and load bearing hydrate models. In this case either hydrate saturations and porosity or hydrate saturations and aspect ratio can be solved.

6.1 Comparison of experimental data with the two-phase effective medium models

6.1.1 Seismic Velocity Comparison

Figure 6.1 shows a comparison of several effective medium models with laboratory data. P-wave velocity measurements were made on two-phase artificial sediments where the physical properties of the constituents were known. The sediments were composed of sand sized glass beads and brine. Appendix A gives the physical property values for each of the constituents needed to calculate the effective media. The effective medium P-wave velocities (V_p) were calculated from the effective bulk and shear moduli using,

$$V_p = \sqrt{\frac{\kappa + 4/3\,\mu}{\chi}}, \qquad (6.1)$$

where κ is the bulk modulus, μ shear modulus and χ is the bulk density of the effective medium.

It can be seen in Figure 6.1 that the effective medium models cover a wide spread of P-wave velocities. When the models are compared to the laboratory data only a couple of the models come close to the experimental data values. It is understandable that models

such as the Hill's average and the HS upper bound over predicted the values substantially because these were not designed for media that resemble sediments. Table 6.1 gives the root mean square (RMS) misfit of the velocity difference between the laboratory data and each of the models in Figure 6.1 when compared to the laboratory measurements. From these it can be seen that the SCA/DEM (with a 0.6 critical porosity) and the HS lower bound give the best predictions of the effective P-wave velocity.

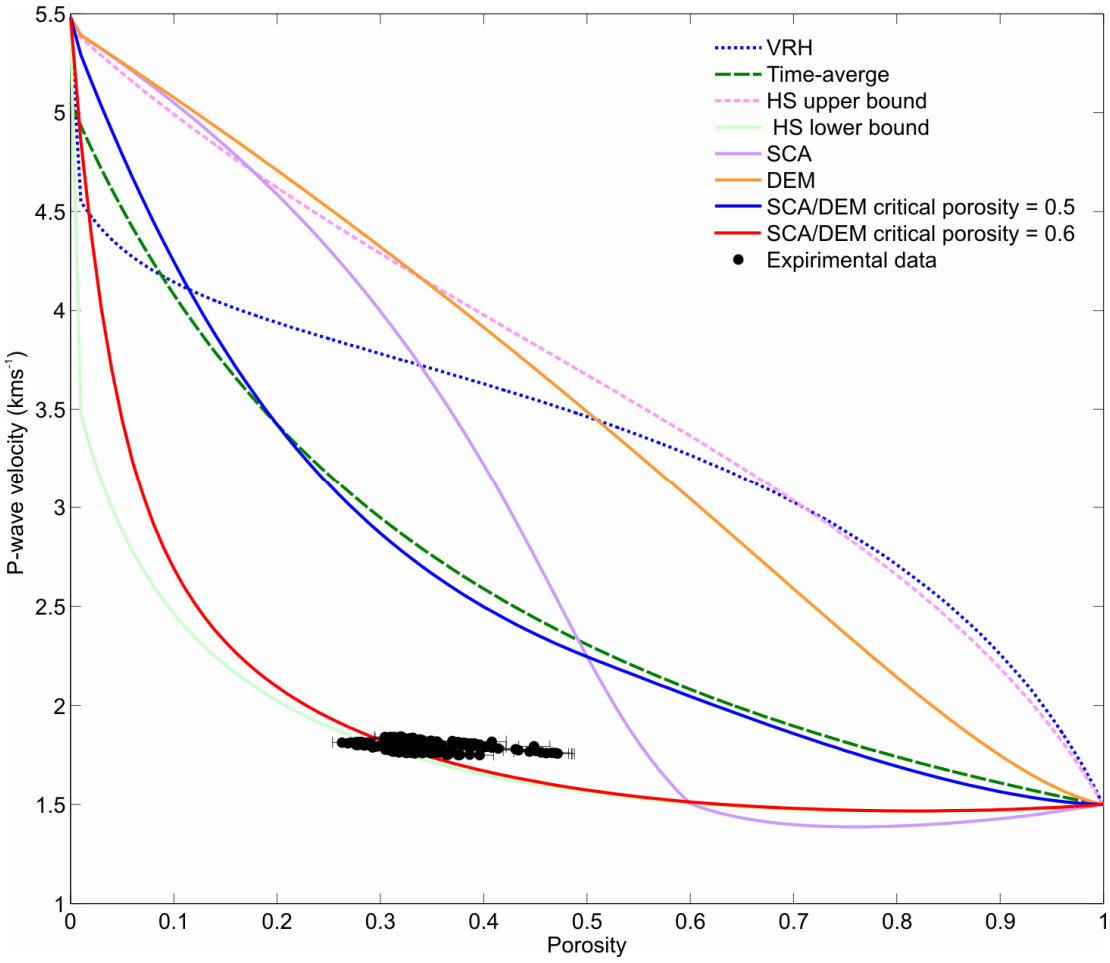

Figure 6.1 Comparison of the P-wave velocities computed from a range of seismic effective medium models and P-wave laboratory data. P-wave velocity errors for the experimental data are not shown because they are smaller than the markers used in the plot. The velocity errors are 0.59% and the porosity errors are 3.4%.

Figure 6.1 also shows a comparison between the SCA/DEM model with a critical porosity of 0.5 (used by Sheng 1990, 1991; Hornby *et al* 1994; Jakobsen *et al*., 2000) and 0.6 (the value calculated using the method in chapter 3.4.1). It shows that when the critical porosity is 0.6 there is a better fit with the laboratory data.

Model	Vp RMS misfit (kmS^{-1})
Hill's average	1.918
Willie Time average equation	0.994
HS upper bound	2.355
HS lower bound	0.088
SCA	1.887
DEM	2.350
SCA/DEM ($\varphi_c = 0.5$)	0.908
SCA/DEM ($\varphi_c = 0.6$)	0.072

Table 6.1 Root mean square (RMS) of the velocity values for each of the models when compared to laboratory measurements on artificial sediments (Chapter 5).

It should be noted that none of the models predict the slope of the data particularly well. This may be because the sediment pore geometry changes with porosity systematically and the rate of this change may not be matched by any of the theories. The corner in the HS curve at 0.01 porosity (Figure 6.1) is a visual artefact of the sample interval of 0.01 and the curve would be smoothed if the interval were reduced.

6.1.2 Electrical Resistivity Comparison

Figure 6.2 shows the comparison between the laboratory data and Archie's equations (with various *m* and *t* coefficients), the HS conductive bound and the Geometric Path-length Effective Resistivity model which was developed in Chapter 4. The experimental data comes from laboratory measurements made on artificial sediments composed of brine and glass beads. The resistivity of the fluid used in the laboratory samples was 0.36 ±0.01 Ωm. Both the HS conductive bound and the Geometric Path-length Effective Resistivity models predict the resistivities well. Three of the four Archie's curves do not go through any of the resistivity data points. The *m* and *t* coefficients used to calculate one of the Archie's curves are both equal to 1.0. These are the values that are generally used when modelling straight cylindrical pore channels (Herrick *et al.,* 1994). The other two Archie's curves are created using *m* and *t* coefficients recommended in the Schlumberger log interpretation charts for soft sediments (Schlumberger, 1977). The fourth Archie's curve is calculated using *m* and *t* coefficients of 1.25 and 1. These values are generally used to calculate the resistivity of unconsolidated sands and spherical glass beads (Archie 1942, Wyllie et al., 1953, Atkins *et al*., 1961; Jackson *et al*., 1978). This curve fits the data better than any of the other

Archie's models but not as well as the Geometric Path-length Effective Resistivity model. If the coefficients were further adjusted a better fit between the laboratory data and the Archie's model could be achieved.

As with the velocity models the resistivity RMS misfit was calculated between the resistivity models and the laboratory data (Table 6.2). The Geometric Path-length Effective Resistivity model has the lowest RMS and therefore is an improvement on the HS conductive bound. It can also predict the resistivities well without empirical constants which Archie's equations require.

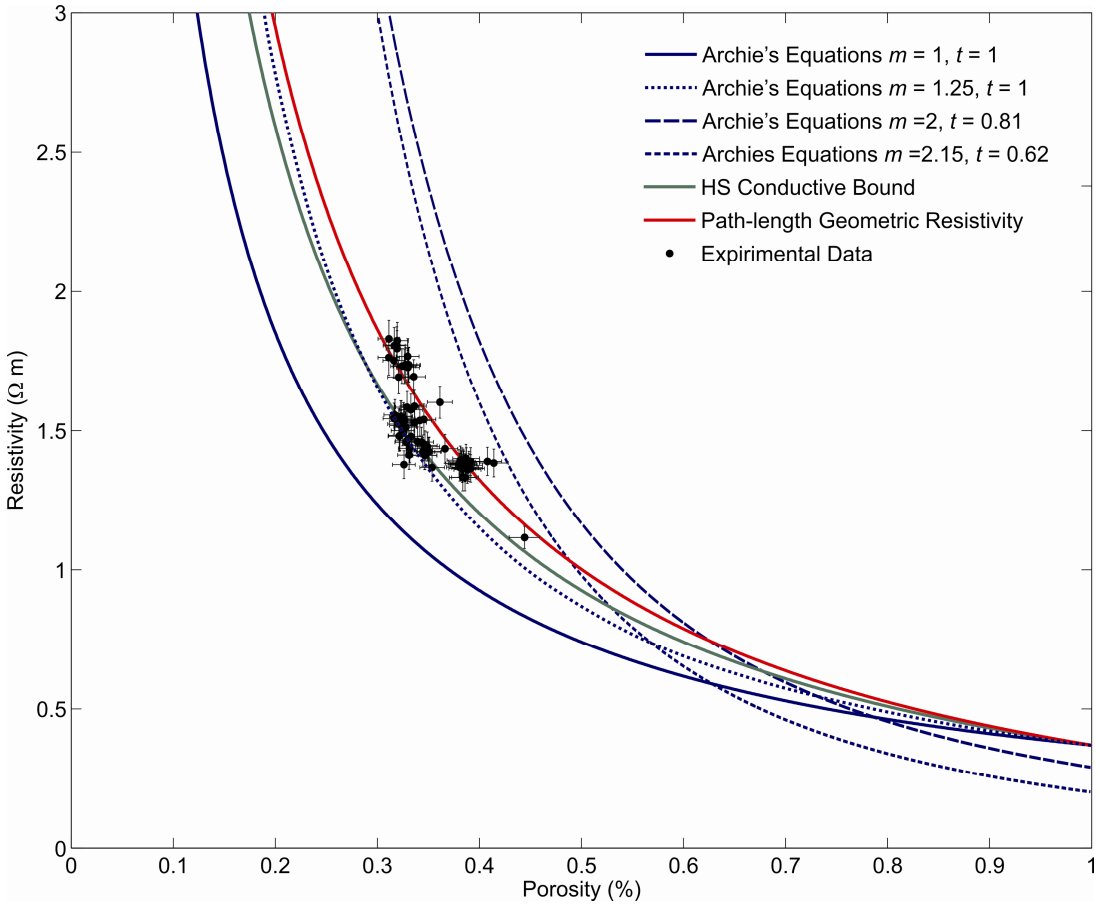

Figure 6.2 The comparison of the resistivity experimental data and Archie's equations, the HS Conductive Bound and the Geometric Path-length Effective Resistivity models.

Model	Resistivity RMS misfit (Ωm)
Archie's equations (where $m = 1$, $t = 1$)	0.451
Archie's equations (where $m = 1.25$, $t = 1$)	0.183
Archie's equations (where $m = 2.15$, $t = 0.62$)	0.765
Archie's equations (where $m = 2$, $t = 0.81$)	1.007
HS conductive bound	0.134
Geometric Path-length Effective Resistivity	0.123

Table 6.2 RMS misfit values for each of the electrical models when compared to the laboratory resistivity measurements on artificial sediments.

6.2 Comparison of experimental data with the three-phase effective medium models

Having compared two-phase models to the laboratory data and established that they are able to predict the velocity and resistivities of sediments as well as or better than other effective medium models we can move on to the more complex three-phase comparisons. In this section the three-phase data measured in the pressure rig will be compared to the three-phase effective medium models.

6.2.1 Seismic Velocity Comparison

Figure 6.3 shows the comparison between the P- and S- wave velocities measured in the pressure rig and the SCA/DEM effective medium model velocities for each of the 4 successful runs. Run1 and Run 2 were made using the artificial cemented glass bead sample and contained 10% and 30% gas hydrate saturation respectively. Run 3 and Run 4 were made using the Berea sandstone and contained 20% and 0% gas hydrate saturation respectively. In each of the plots the velocities calculated from the effective medium model have a fixed porosity and vary with hydrate saturation. They show that when a critical porosity of 0.6 is used, the SCA/DEM model seriously under-predicts the measured P- and S-wave velocities in all of the runs. This is in contrast to the two-phase case when the SCA/DEM method determines the velocities extremely well. There are several possibilities why this may occur. The first is that the SCA/DEM model does not cope well with adding a hydrate phase. This however can be dismissed because a run was completed in the rig where no hydrate was formed (Figure 6.3) and the under prediction still occurs.

A second possibility was that the hydrate was load bearing. Figure 6.3 shows the non-load bearing effective medium models. If the hydrate was modelled as load bearing the effective velocities would be higher. Figure 6.4 shows an example comparison of the laboratory data and the load bearing model for Run 2. It shows that the SCA/DEM model over-predicts the velocities.

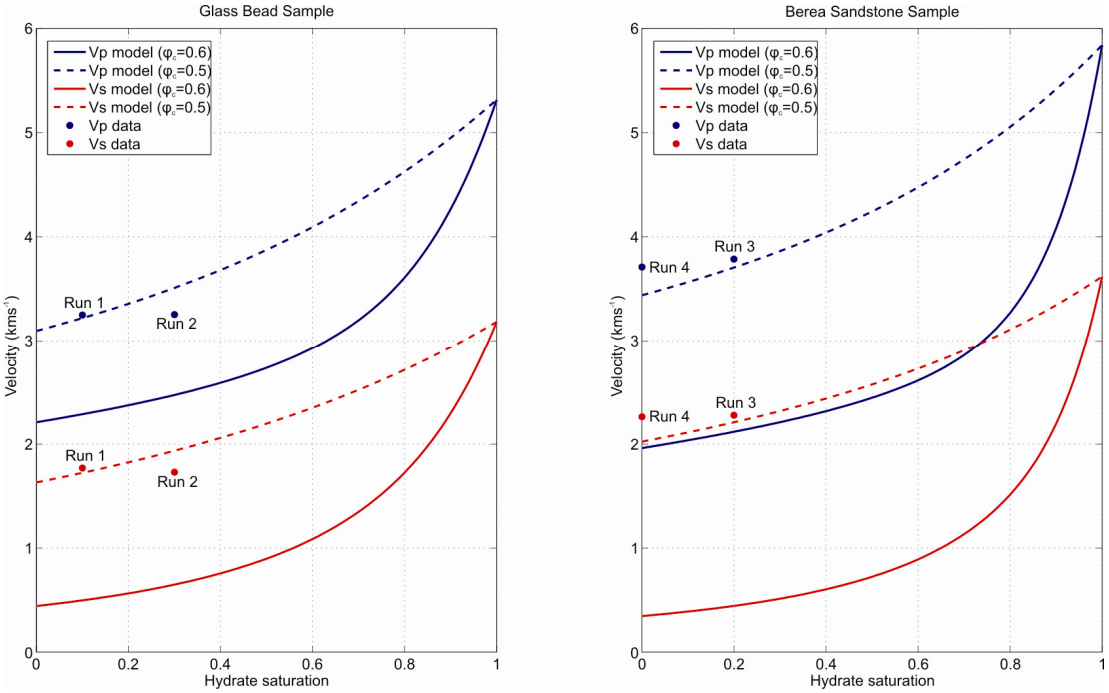

Figure 6.3 Comparison of the measured P- and S-wave velocity with the SCA/DEM non-load bearing hydrate effective medium models with a critical porosity of 0.6 and 0.5 using results collected from the glass bead and Berea sandstone samples. The plots show the changes in velocity as hydrate saturation changes. Porosity is fixed at 17% for the glass bead sample and 23% for the Berea Sandstone sample. Velocity and hydrate saturation errors are smaller than the plot markers. However it should be noted that hydrate distribution was uneven in the samples.

Another possible reason for the high experimental velocities is that the sediment used in the rig was cemented together. This cementation causes the sediment to be much stiffer and in consequence the velocities are much higher than for uncemented sediment. The SCA/DEM model with a critical porosity of 0.6 works well for uncemented material (Figure 6.1) but not for cemented sediments (Figure 6.3). Sheng's (1990) original SCA/DEM model was designed for sandstones using a critical porosity of 0.5. The three-phase laboratory data was therefore also compared to the SCA/DEM model using a critical porosity of 0.5 (Figure 6.3). The comparison shows that using a critical porosity of 0.5

gives a much better fit than 0.6. Therefore the data suggests that a critical porosity of 0.5 should be used for cemented sediments and a critical porosity of 0.6 should be used for uncemented sediments.

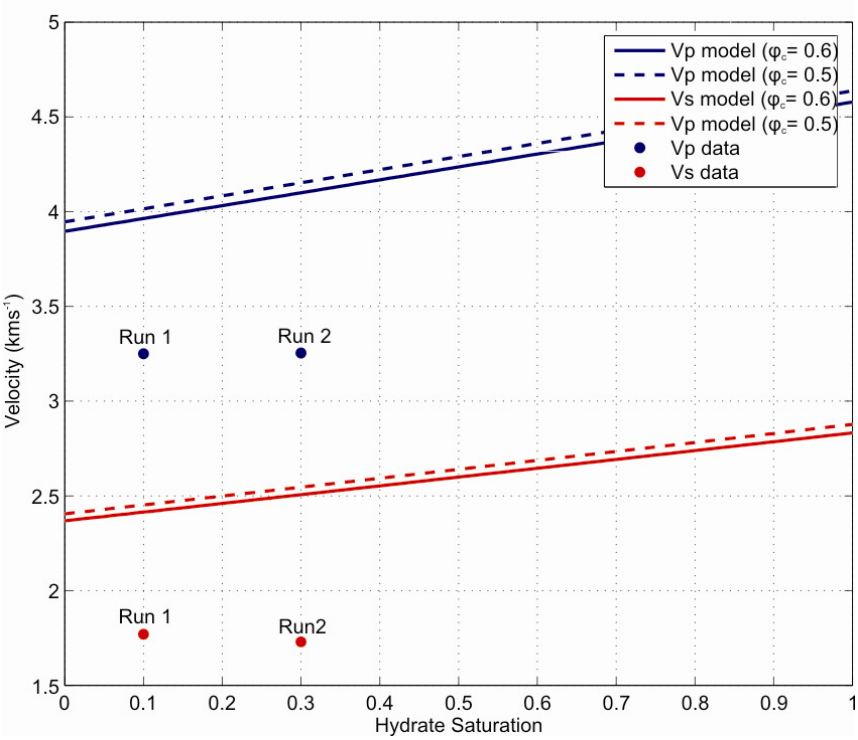

Figure 6.4 Comparison of laboratory measured P- and S-wave velocities and the SCA/DEM model velocities with a critical porosity of 0.6 and 0.5 for Run 2. The porosity is fixed at 17% to calculate the velocities.

6.2.2 Electrical Resistivity Comparison

Before comparing the resistivity models to the experimental data the pore fluid resistivities must be calculated. Although the salinity of the initial brine is known it changes as the hydrate forms in the sediment. Hydrate forms from pure water and expels salt causing the brine to become more saline. Correcting for pore fluid resistivity was achieved by calculating the amount of water used to form the hydrate and the weight of the salt expelled from that water for a given sample fluid volume (V). The method is as follows:

Volume of hydrate (V_h)

$$V_h = VS_h \tag{6.2}$$

Volume of water in the sample after hydrate has formed (V_w)

$$V_w = V(1 - S_h) \tag{6.3}$$

Mass of hydrate

$$W_h = V_h \chi_h , \tag{6.4}$$

where χ_h is the density of hydrate.

Mass of water contained in the hydrate is given by

$$W_{wh} = \varsigma W_h , \tag{6.5}$$

where ς is the weight fraction of water in the hydrate. For Structure I hydrate, R can be calculated from the atomic weights of the molecules and has a value of 0.866 assuming all the clathrate cages are filled with methane.

Mass of salt expelled from the hydrate

$$W_{SE} = S_b W_{wh} \tag{6.6}$$

where S_b is the weight of salt in 1 kg of water before hydrate formation.

Mass of water remaining in the sample after hydrate formation

$$W_w = V_w \chi_w \tag{6.7}$$

where χ_w is the density of the water.

Mass of salt in the water before the salt has been expelled from the hydrate

$$W_{sw} = W_w S_b \tag{6.8}$$

Total mass of salt in the water after hydrate formation

$$W_{TS} = W_{sw} + W_{SE} \tag{6.9}$$

Mass of salt (kg) in one litre of water after hydrate formation

$$S = \frac{W_{TS}}{W_w} \tag{6.10}$$

By re-arranging the equations 6.2-6.10 the number of grams of salt per litre of water is given by:

$$S = S_b \left[1 + \frac{R S_h \chi_h}{\chi_w (1 - S_h)} \right] \tag{6.11}$$

S is fairly insensitive to the values of R. Once the amount of salt has been calculated the resistivity of the pore waters can be calculated using Fofonoff's (1985) equations which calculate the resistivity of a fluid based on the salinity of the brine and its temperature. Table 6.3 gives the corrected resistivity of the brine fluid for each of the runs.

Initial salt contents (g/litre)	Corrected salt contents (g/litre)	Gas Hydrate Saturation (%)	Temperature (^{o}C)	Resistivity (Ωm)	Run number
8	8	0	4	1.183	4
8	8.69	10	4	1.095	1
8	9.56	20	4	1.003	3
8	10.67	30	4	0.961	2

Table 6.3 Pore water resistivity calculated from the temperature and the corrected salt contents using Fofonoff (1985) equations.

Figure 6.5 shows the difference in the model resistivities for a given porosity when the fluid resistivity is corrected and hydrate saturation is varied. It can be seen the curve for the uncorrected resistivities is much steeper than for the corrected resistivities. This is because the pore fluid resistivities decrease as salt is expelled from the hydrate. It also shows that these corrections are far more important at higher hydrate saturations that at lower ones. The shallow curve of the corrected resistivity model may also explain why there was only a small change in the resistivity between Runs 3 and 4.

Figure 6.5 also shows comparisons of the resistivity data collected from the pressure rig with the Geometric Path-length Effective Resistivity model for the pore floating hydrate growth model. The pore blocking model is not shown because in each case it seriously over-predicts the laboratory resistivities by several orders of magnitude. From this we can assume that the hydrate is not pore blocking. When comparing the pore floating hydrate models to the laboratory data the models do go through the resistivity data points for Runs 2-4. There is however a large range of resistivities from the laboratory data. This is due to the uneven distribution of hydrate in the samples and possibly due to uneven porosity in the sediment samples. The porosity measurements are calculated from the wet and dry weights of the samples and are therefore an average of the whole sample and local variation may occur. This would explain some of the resistivities range in Run 4 where no hydrate was formed. However because the high resistivities were always measured when electrode 1 was in use, it is possible that this electrode was in some way damaged or corroded.

Comparing the models to the mean measured resistivity it can be seen that the Run 2 mean is very close to the model predictions. This is not the case in Run 3 and 4 due to some high outliers among the measurements skewing the results. Therefore the median value for each data set was also calculated and it can be seen that the median values are close to the model predictions.

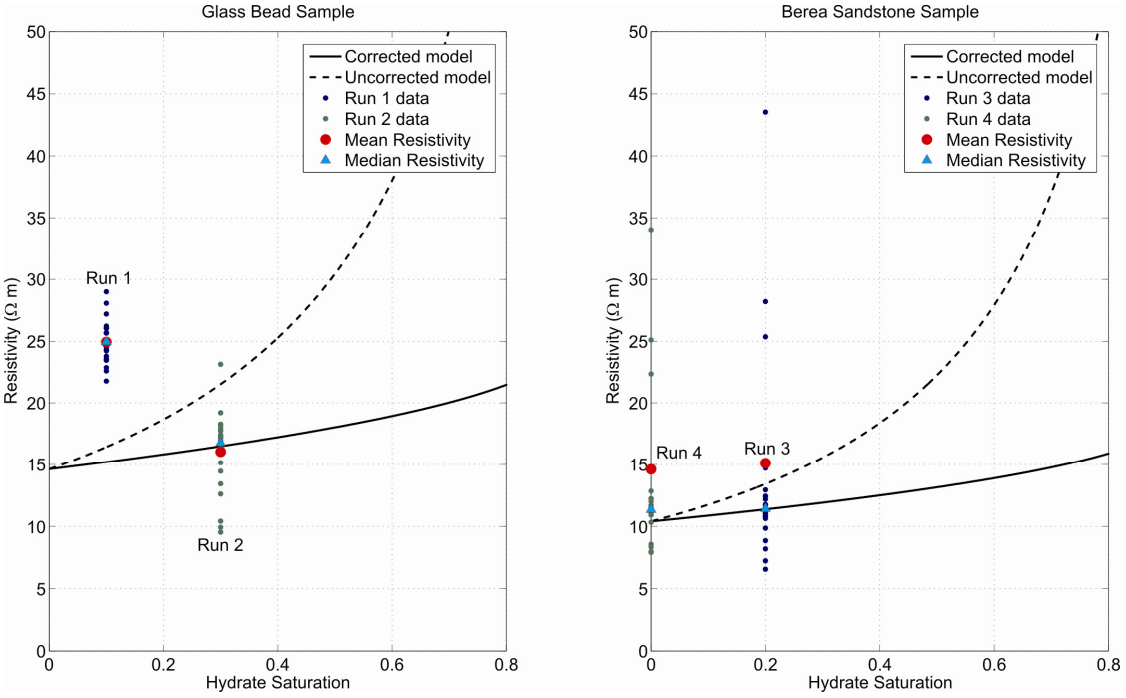

Figure 6.5 Comparison of the 3-phase resistivity laboratory data with a corrected and uncorrected Geometric Path-length Effective Resistivity three-phase model. The resistivity model is corrected for hydrate saturation which affects the pore water resistivity. The porosity in each of the models is fixed at the sample porosity and varies with hydrate saturation. The glass bead sample has a porosity of 0.17 and the Berea sandstone sample has a porosity of 0.23.

The resistivities from Run 1 (Figure 6.5) are much higher than the model predictions and the resistivities from the other runs. It is possible that the hydrate was partially pore blocking in this case causing higher resistivities. This is however unlikely because the hydrate was formed in the same way as for Runs 2-4. No explanation can be given for the high resistivities in Run1 apart from some unaccounted for experimental error. It should be remembered that this was the first ever run using this newly developed resistivity setup and resistivities were still being measured by hand at this point.

6.3 Joint Interpretation Method

Having developed seismic and electrical models which are both purely physical (i.e. have no empirical constants) and compare reasonably well to sediments we are now able to jointly analyse data from material where there are co-located seismic and electrical results. Data sets where this would be useful would include data collected from seismic and electromagnetic surveys where both of these macroscopic physical properties of the sediments are measured. Unless core samples are collected or wells are drilled and logged the porosity and microstructure of the sediments are unknown. The electrical and seismic models developed can help to determine those properties and when jointly interpreted reduce the errors. The section starts by explaining the joint model for the two-phase case and then develops it for the three-phase case.

6.3.1 Two-Phase Joint Interpretation Method

The two-phase joint interpretation allows two variables, porosity and aspect ratio, to be determined using both the seismic and electrical models. These variables are common to both the seismic and the electrical effective medium model. Changing either of the variables will cause both the effective resistivity and the effective velocity to alter. The joint method will take co-located resistivity and velocity data and solve for porosity and aspect ratio, which cannot be done using the seismic or electrical model alone. The joint interpretation starts by determining all the possible porosities and aspect ratios that will match the observed velocity data value and then it repeats this for the resistivity data value. This is achieved using an interval decimating method.

Each effective medium model is run for a given aspect ratio and at a range of porosities ranging from 0 to 1 at intervals of 0.1. The porosity values that give the nearest velocity or resistivity values above and below the experimental value are then determined. The forward model is then run again for porosity values between the two previous values at smaller intervals. The process is repeated until the porosity values are found for the given velocity or resistivity value to the nearest 10 mS^{-1} or 0.01 Ωm. This approach is thought to be accurate enough because the possible porosity error this causes is far smaller than errors usually associated with velocity and resistivity data. The whole process is then repeated for the next aspect ratio. Aspect ratio values start at 1 and decrease to 0.01 at intervals of 0.01. The 2-Phase seismic model that was used is the combined SCA/DEM

model described in Chapter 3. Appendix B gives the full equations needed to calculate P- and S-wave velocity.

Figure 6.6 (A) shows the range of velocities that can be produced by altering the aspect ratio and the porosity. Figure 6.6 (B) shows the aspect ratios and porosities calculated using the above method for a given velocity. It can be seen that as the aspect ratio changes the porosity only varies to a small degree, ~3% when a critical porosity of 0.6 is used. When the critical porosity is lower the range of aspect ratios is greater.

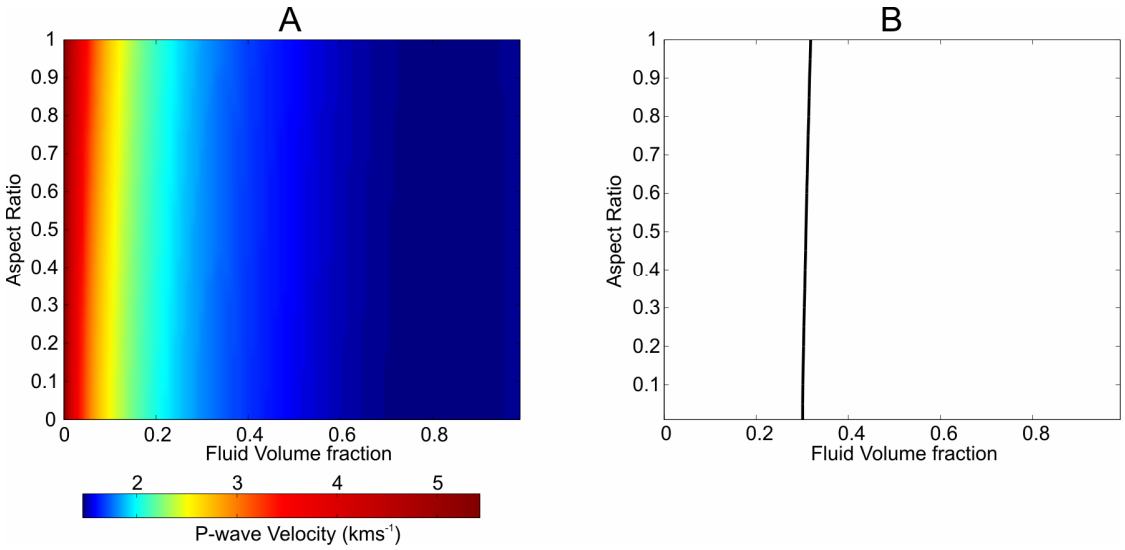

Figure 6.6 (A) Velocity of a two-phase effective medium with aligned grains as a function of fluid volume fraction and aspect ratio calculated using the SCA/DEM model with a critical porosity of 0.6. (B) Two-phase example result showing all the possible fluid volume fractions and aspect ratios that will give a predetermined velocity of 1.8 mS-^{1}.

The two-phase electrical forward model was described in Chapter 4. Figure 6.7(A) shows an example of the resistivities that the model predicts as a function of fluid volume fraction and aspect ratio. Figure 6.7(B) shows an example of the range of fluid volume fractions and aspect ratios that satisfy for a single resistivity. As with the velocity model the result from the resistivity model is non-unique.

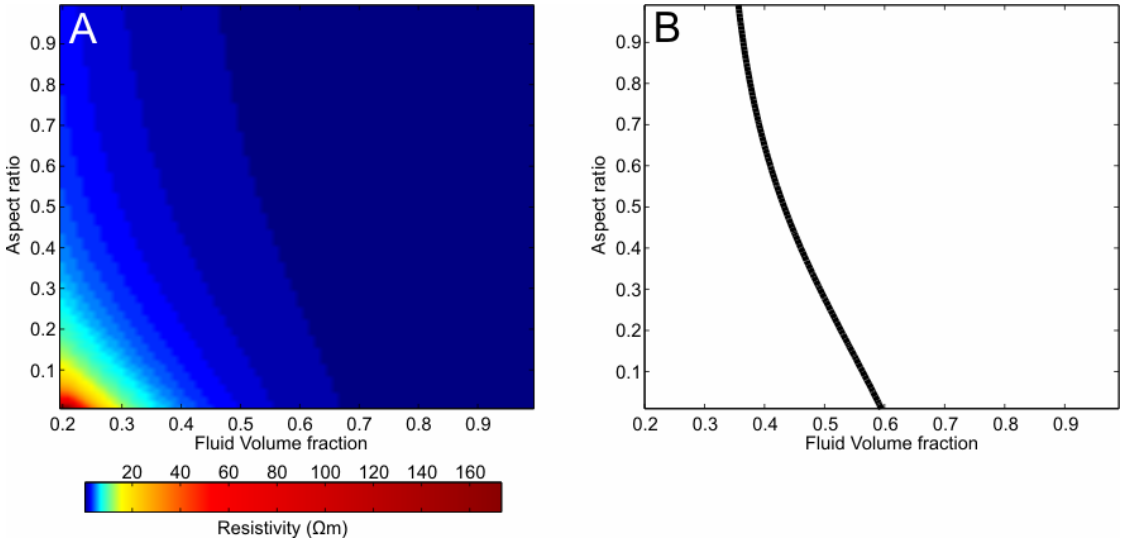

Figure 6.7 (A) Resistivity of a two-phase effective medium with fully aligned oblate grains as a function of fluid volume fraction and aspect ratio when resistivity is calculated in the resistive direction. (B) Two-phase result showing all the possible porosities and aspect ratios that will give a predetermined resistivity of 1.5 Ωm.

It can be seen in Figure 6.6 and Figure 6.7 that the solution for a given value of resistivity and velocity is non-unique with respect to porosity and aspect ratio. However if both solutions are plotted together in the same graph it can be seen that the plots intersect. This intersection point is the point at which both the velocity and resistivity models are satisfied. These are the values that we take to be the actual aspect ratio and porosity for these particular co-located values. Figure 6.8 shows an example of this joint method of interpretation for co-located resistivity and velocity measurements of one of the two-phase sediment cores measured earlier. The grains have an aspect ratio of one. In this example both the velocity and resistivity models have been calculated so that the grains are fully aligned producing two results. The resistivity and the velocity lines only intersect in one of the plots, Figure 6.8 (A) but in both plots the velocity and the resistivity curves both almost intersect at an aspect ratio of 1 as they should.

Figure 6.9 shows an example of this joint interpretation along the length of sample 1 from the two phase experiment described in Chapter 5. The sample was composed of glass beads with an aspect ratio of one and brine. P-wave velocity, resistivity and porosity measurements were made along the length of the sample. The resistivity data (Figure 6.9 B) were re-sampled to match the sample locations for velocity data (Figure 6.9 A) using a spline fit. The porosities were then determined using the joint interpretation method for co-located values (Figure 6.9 C). These were then compared to the porosity values that were

measured using the core logger. The predicted porosities are in agreement with the measured porosities to an RMS misfit of 0.011. This is well within the errors of the measured porosities. Figure 6.9 (C) shows the calculated aspect ratio. The actual aspect ratio of the glass beads is one although no error information is provided from the glass bead manufactures. Thin sections of the beads (Chapter 5) do show some variation in the aspect ratio of the beads which may account for the difference between the actual and calculated aspect ratios. The aspect ratio RMS misfit between the actual and calculated aspect ratio is 0.08.

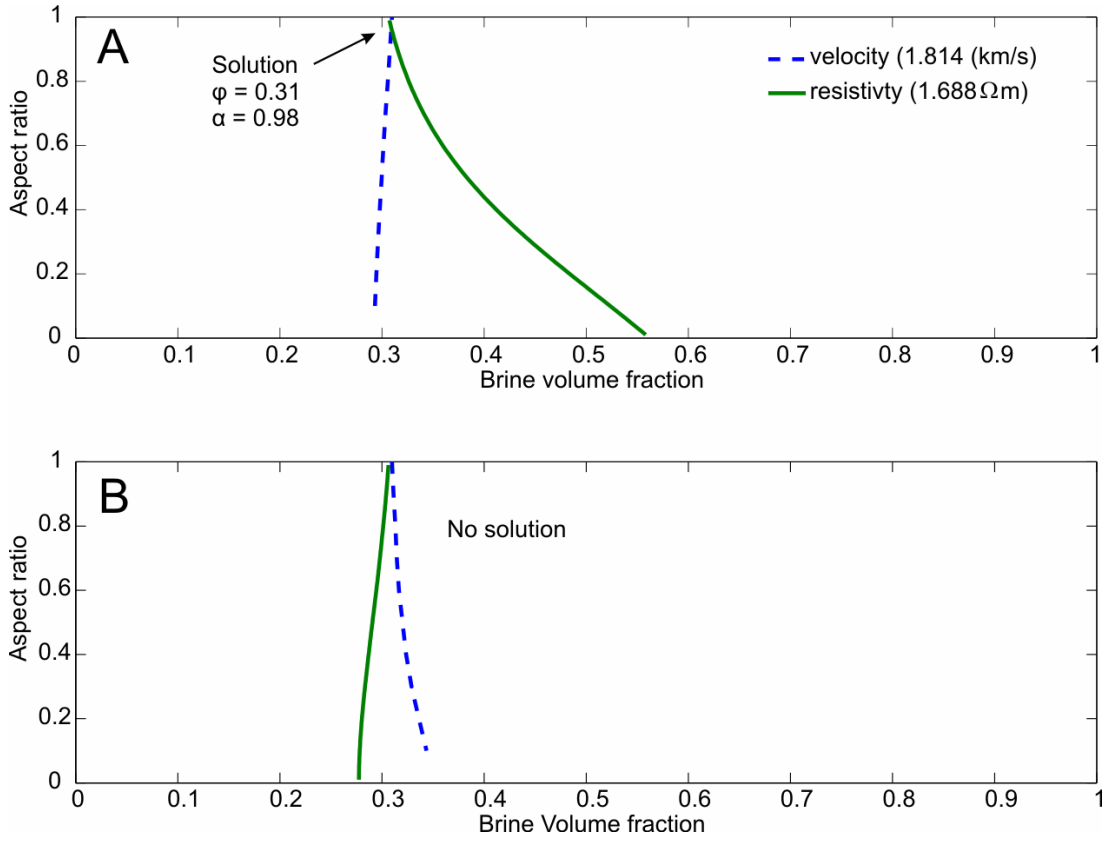

Figure 6.8 Two phase velocity and resistivity results for co-located laboratory data points measured on artificial sediment composed of spheroidal glass beads and brine. (A) Inversion calculated for grains aligned in the most resistive direction. (B) Inversion calculated for grains aligned in the least resistive direction.

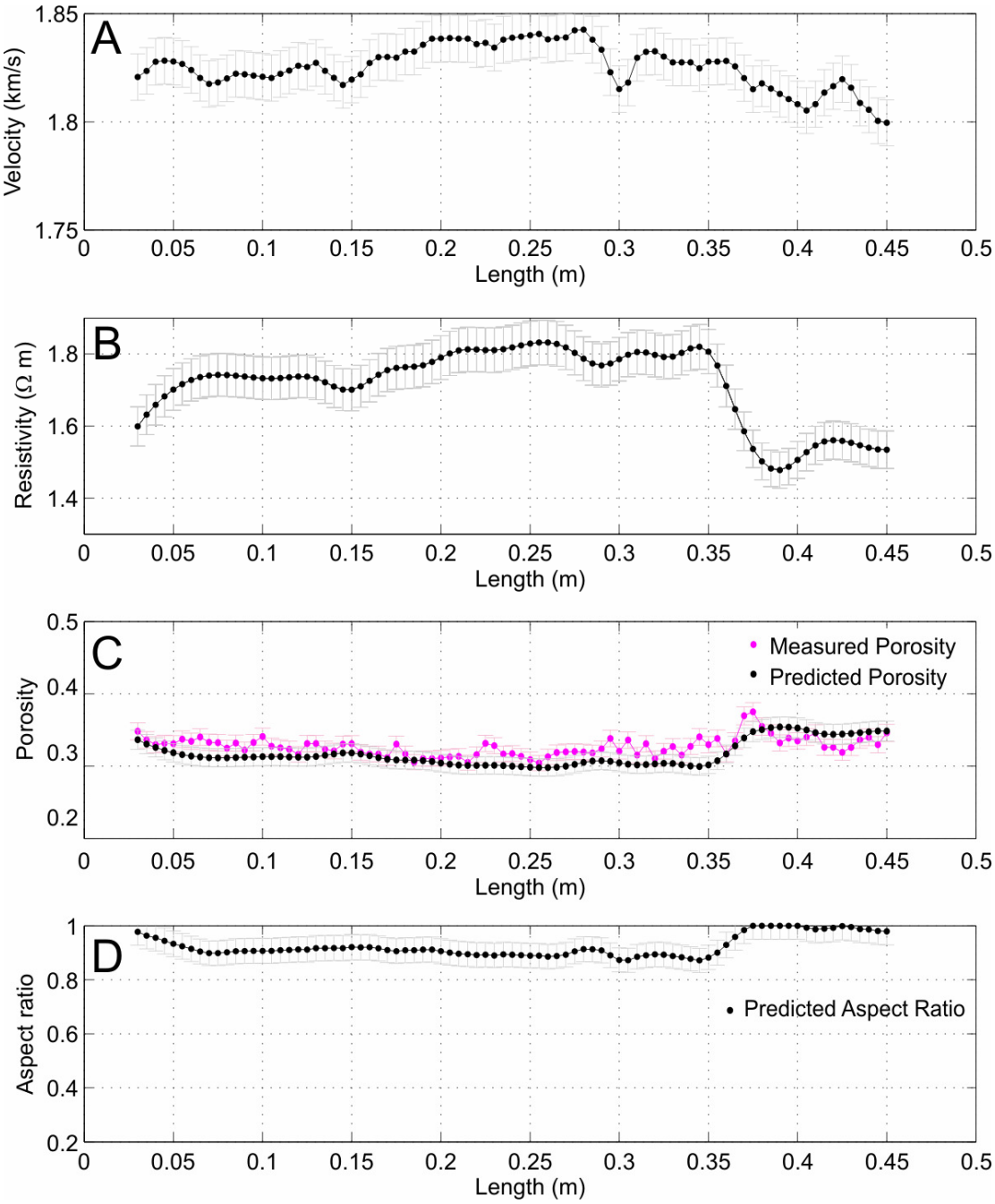

Figure 6.9 Examples of the two-phase joint method of interpretation along the length of sample 1. (A) Velocity. (B) Re-sampled resistivity. (C) Measured and predicted porosity calculated from the resistivity and the velocity using the joint interpretation method. (D) Predicted aspect ratio; the actual aspect ratio of the glass beads is one.

6.3.2 Three-Phase Joint Interpretation Method

In the case of the three-phase model there are now three variables: aspect ratio, hydrate saturation and porosity, which are common to both the seismic and electrical effective

medium models. However we can only solve for two variables therefore one of the variables must be fixed before the forward inversion can be run. In the following examples the aspect ratio value has been fixed, although any of the other variables can just as easily be the fixed variable. The three-phase joint interpretation is performed in the same manner as the two-phase interpretation. Hydrate saturation replaces aspect ratio if solving hydrate saturation and porosity. If the joint method is solving for hydrate saturation and aspect ratio, hydrate saturation replaces porosity.

When performing the joint interpretation the resistivity model which complements the velocity model should be used. Therefore when running the inversion for the seismic non-load bearing hydrate model, the pore floating hydrate resistivity model must also be used. Figure 6.10 (A) shows an example of the non load bearing hydrate forward model for P-wave velocity assuming that the aspect ratio is fixed at one. The black line picks out the contour where the velocity is that of the sought after value. Figure 6.10(B) shows a similar example but here the load bearing model has been used. In both cases the results are non-unique.

Figure 6.11 (A) shows all the possible resistivities that can be calculated by the pore floating hydrate effective medium model as the porosity and the hydrate saturations are altered. Again the black line picks out all the possible hydrate saturations and porosities that will give a particular resistivity. Figure 6.11 (B) shows a similar example for the pore blocking hydrate resistivity model. In both cases there are a range of hydrate saturations and porosities that will satisfy a given resistivity.

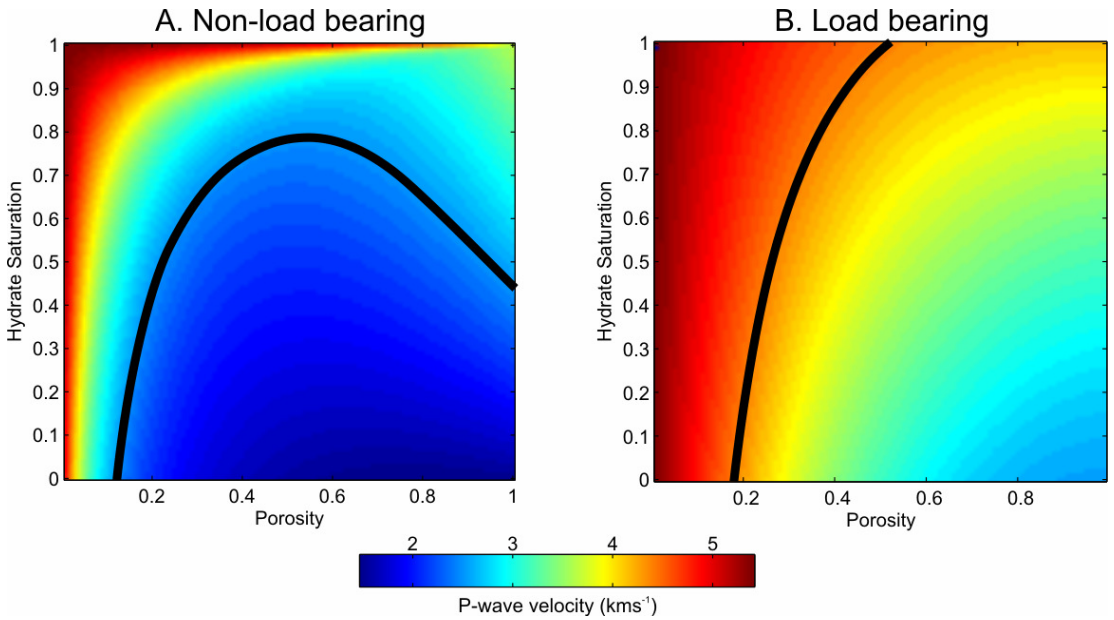

Figure 6.10 (A) P-wave velocity of a non-load bearing effective medium calculated using the SCA/DEM method and a fixed aspect ratio of one. The black line shows the hydrate saturations and porosities that satisfy a given P-wave velocity of 2.5 kmS-^{1}. (B) P-wave velocity of a load bearing effective medium calculated using the SCA/DEM method and a fixed aspect ratio of one. The black line shows the hydrate saturations and porosities that satisfy a given P-wave velocity of 4.5 kmS-^{1}.

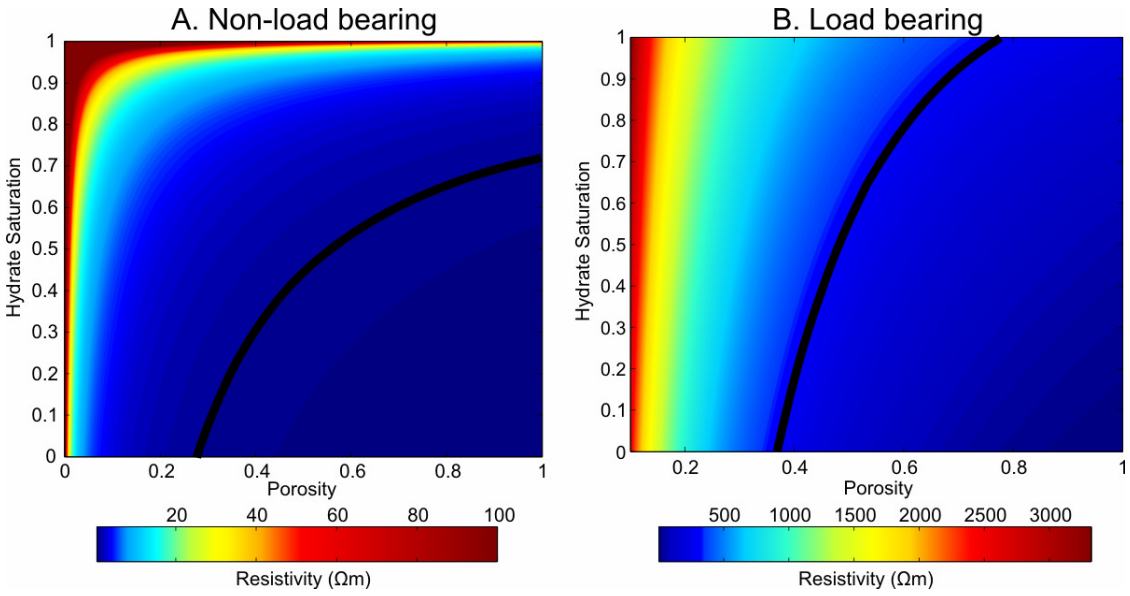

Figure 6.11(A) Resistivity of a non-load bearing effective medium calculated using the Geometric Path-length Effective Resistivity and a fixed aspect ratio of one. Black line represents all the hydrate saturations and porosities that satisfy a resistivity of 2 Ωm (B) Resistivity of a load bearing effective medium calculated using the Geometric Path-length Effective Resistivity method and a fixed aspect ratio of one. Black line represents all the hydrate saturations and porosities that satisfy a resistivity of 300 Ωm.

Joint Interpretation

The method for determining the final hydrate saturation and porosity is similar to the two-phase system. The curves produced from the separate inversions for both the velocity and the resistivity are plotted together. The intersection of the two curves is again taken as the point which satisfies both the velocity and resistivity models. Figure 6.12 shows an example of this for both the non-loading bearing hydrate medium (hydrate floats in the pore spaces) and the load bearing hydrate medium (hydrate blocks the pores).

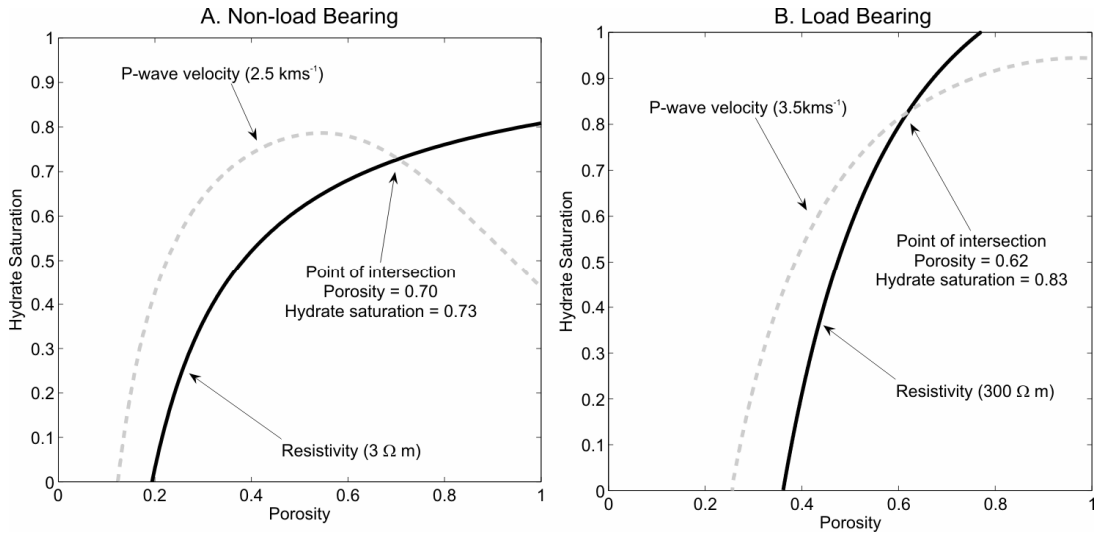

Figure 6.12 Joint interpretation of velocity and resistivity data for non-load bearing hydrate (A) and load bearing hydrate (B).

As mentioned earlier any of the 3 variables can be fixed and the joint method then searches for the others. Figure 6.13 shows an example of the joint interpretation when porosity is fixed rather than aspect ratio. This would be more appropriate when analysing bore hole logging data when independent porosity information is often available.

Another way to determine the unique S_h and φ or S_h and α for a given set of geophysical data is to use the method of Greer (2001). However Greer's method must be adapted to account for the significantly lower resistivities found in sediments compared to cracked crystalline rocks. Greer's method is used to determine the porosity and aspect ratio of an effective medium which has only two components. This is achieved by determining all the resistivities and velocities of an effective medium at every porosity and aspect ratio. A residual is determined between each of the calculated resistivities and velocity and the fixed resistivity and velocity. This residual is then normalised using the maximum and

minimum resistivities and velocities. The normalised residuals of the resistivity and velocity are then added together. The results can be plotted using a contour plot and the point where the global minimum appears indicates the porosity and aspect ratio of medium.

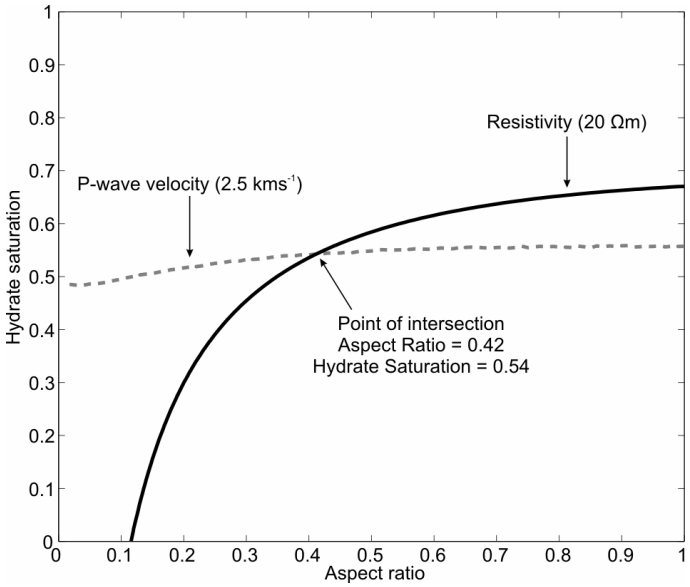

Figure 6.13 P-wave velocity and resistivity results for co-located velocity (2.5 kmS-^{1}) and resistivity (20 Ωm) for a three-phase medium with non-load bearing hydrate where the porosity is fixed (21%).

To perform this method for this work some adjustments must be made. Instead of porosity and aspect ratio, porosity and hydrate saturation or hydrate saturation and aspect ratio are determined. Normalizing the residuals using the maximum and minimum resistivities causes problems when dealing with sediment resistivity values. The normal resistivity of a sediment with or without hydrate is relatively small when compared to the maximum resistivities determined by the effective medium model. Therefore when the resistivity residual are normalized the values become very small. When these are added to the velocity residuals they have virtually no impact on the plot of the normalized residuals and all that is seen are the velocity residuals. Therefore to remove this problem both the resistivity and the velocity residuals can be scaled by the fixed resistivity and velocity value. Once this is done the results can be plotted and both the velocity and resistivity contribute to the shape of the plot and the position of the global minimum. Two examples of this can be seen in Figure 6.14. These figures used the same data and models as Figure 6.12A and Figure 6.13 and have the results from those figures superimposed on top. It can be seen that both methods produce the same final result.

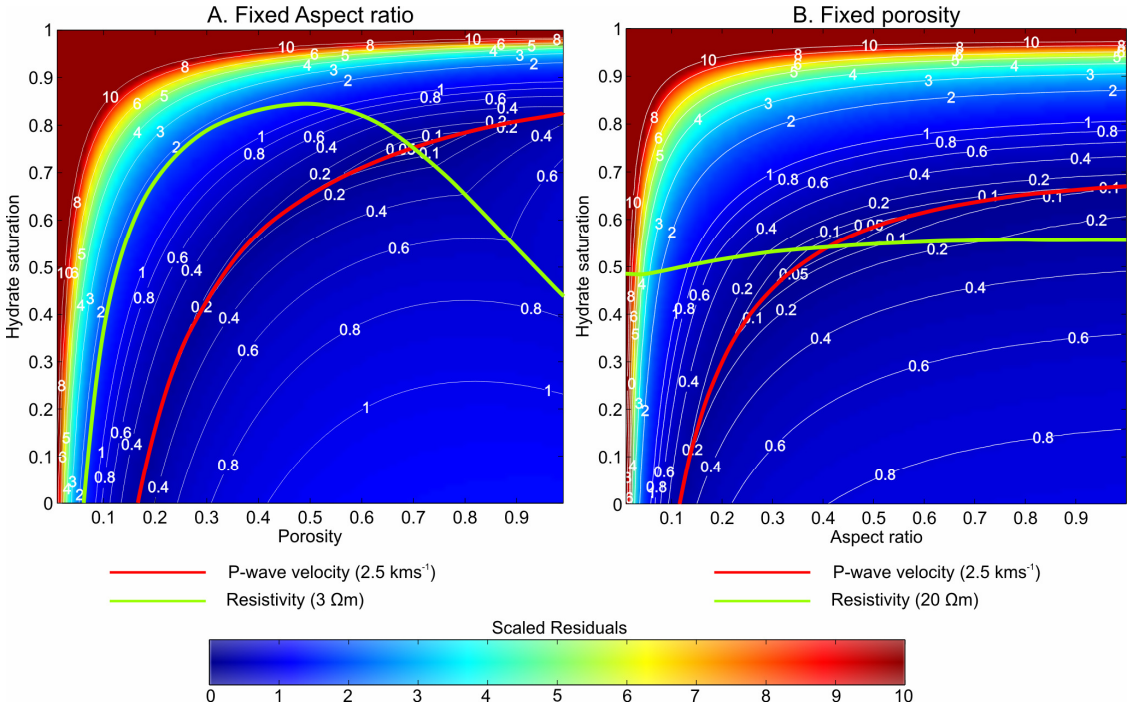

Figure 6.14 Contour plots of joint residuals adapted from Greer's (2001) method and the Joint interpretation method (developed in this chapter) superimposed on top. Plot A uses the same data and models as Figure 6.12 and Plot B uses the same data as Figure 6.13.

The advantage with the adapted Greer method is that an idea of the sensitivity of the final results can be determined from the plots. The disadvantage with the Greer method is that the effective medium must be calculated at all hydrate saturations and porosities or all hydrate saturations and aspect ratios. This can take a long time. The joint interpretation method developed in this chapter is quicker because the effective medium velocity and resistivity need not be calculated as many times. The time the Greer method takes to determine a result becomes more of a problem if we wish to reduce the misfit between the predicted and the fixed resistivity and velocity measurements. The plots in Figure 6.14 were created using a 100x100 matrix. This means that the final results are to the nearest 1% porosity and 1% hydrate saturation (assuming aspect ratio is fixed). If a more precise result is needed, for example 0.1%, a 1000x1000 matrix would need to be determined. To achieve a more precise result using the Interval Decimating method (described in section 6.3.1), only one extra iteration is needed. This illustrates why the number of times the effective medium velocity or resistivity has to be calculated is so much smaller, and therefore why the method is quicker.

The results in this Chapter and in Chapter 7 are determined using the joint interpretation method described above; but the sensitivity of the results can be checked using the adapted Greer (2001) method.

Comparison with data

Figure 6.15 shows two examples of the method of joint interpretation using the three-phase data collected in the laboratory. It shows an example using P-wave velocities and resistivity data from Run 3 using the non-load bearing models. Because the velocity model using a critical porosity of 0.6 severely under predicted the measured velocities, the critical porosity was set at 0.5 for this example. The figure shows examples of the joint interpretation when the aspect ratio is fixed and when the porosity is fixed. In both cases the joint method come to within 5% of the measured hydrate saturation of 20%. Due to the shape of the curves in Figure 6.15 (A) at these values, any small error in the resistivity or velocity could lead to large errors in the predicted hydrate saturations values. In Figure 6.15 (B) small errors in the co-located data points may lead to large errors in the aspect ratios. This can also be seen in Figure 6.16 where the Greer method can be used to look at the sensitivity of the results. The contours around the global minimum in this figure are far more elongated than those in Figure 6.14. This indicates that a small error in the resistivity will cause large errors in the hydrate saturation result.

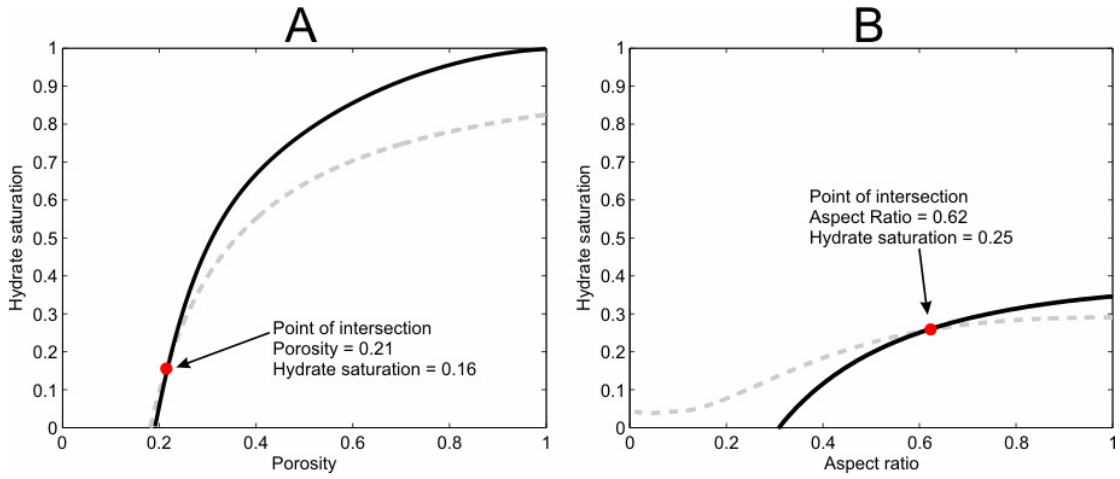

Figure 6.15 Joint model predictions for Run 3 using the non-load bearing forward models. A critical porosity of 0.5 is used for the forward velocity model. (A) The joint method solves for porosity and hydrate saturation, while aspect ratio is fixed at 1. (B) The joint method solves for aspect ratio and hydrate saturation, while porosity is fixed at 0.23.

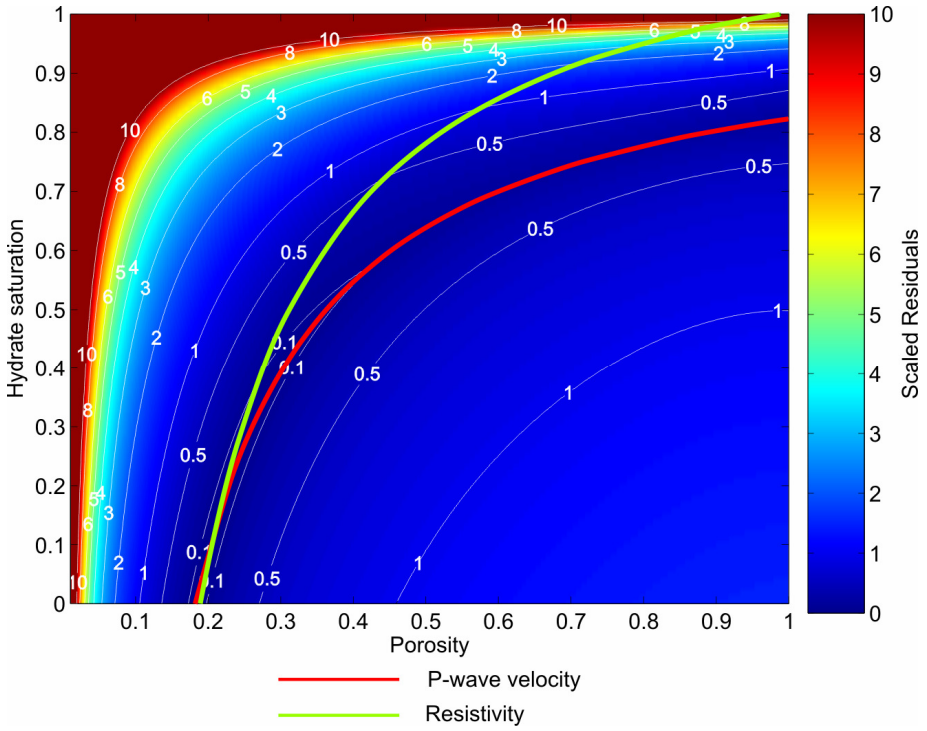

Figure 6.16 Greer 2001 interpretation method of Run 3 data. Data and models used to create this plot are the same as Figure 6.15 A.

This problem appears not to be so apparent when the porosity of the sediment is higher. Figure 6.17 shows the joint inversion for two co-located data points from site 1326 on IODP leg 311. The porosity at this location, obtained from the porosity log, was 0.65. The model assumes that the sediment is composed of clay and the resistivity of the pore fluids is 0.3 Ωm. In Figure 6.17 (A) the aspect ratio has been fixed at 0.1 and in Figure 6.17 (B) the porosity has been fixed at 0.65. In both cases the angle between the curves is much greater. This means that small errors in the resistivity and velocity measurements do not transfer to large errors in the hydrate saturation and aspect ratio results. In both plots similar hydrate saturations are determined. When the aspect ratio is fixed a porosity of 0.63 is obtained which compares well to the measured porosity of 0.65. The hydrate saturation calculated using Archie's method given in Collett *et al.* (2005) for this data set is 0.14. This compares well to the joint interpretation hydrate saturations of 0.10 and 0.11. However they are both dependent on the same resistivity data set. It should also be mentioned that the 0.3 aspect ratio determined in Figure 6.17 may actually be lower if a different grain alignment is used.

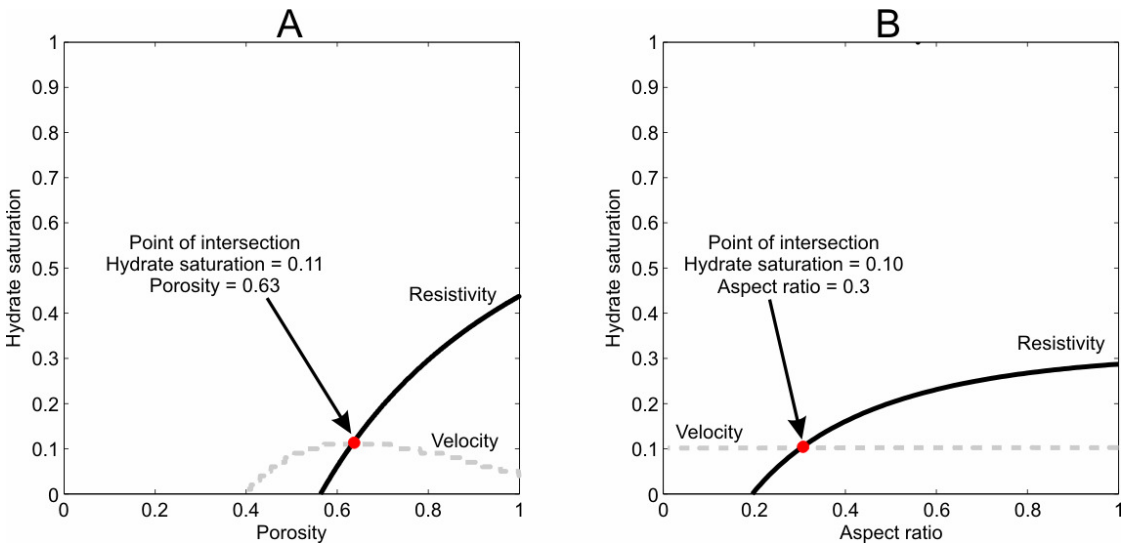

Figure 6.17 Joint interpretation of IODP site 1326 resistivity (0.86 Ωm) and velocity (1.61 kmS-^{1}) data. (A) Aspect ratio is fixed at 0.1. (B) Porosity is fixed at 0.65.

If the two curves do not intersect then there is no hydrate saturation or porosity which will satisfy both the resistivity and the velocity. Assuming that the measurements of resistivity and velocity are correct then another explanation for the lack of intersection must be sought.

When calculating the resistivities and the velocities in the forward model, prior knowledge of the resistivities and velocities of the individual components that make up the composite medium are required. If one of these values is wrong, then it may account for the lack of intersection. Figure 6.18 shows a hypothetical situation where there is no intersection between the resistivity and velocity curves for co-located measurements of a non-load bearing medium composed of hydrate, glass bead and brine with a resistivity of 0.35 Ωm. By altering the resistivity of the brine to 0.5 Ωm and recalculating the resistivity curve we now see that the curves intersect and the hydrate saturation and porosity can be calculated. The method therefore may allow problems with the prior assumptions to be identified.

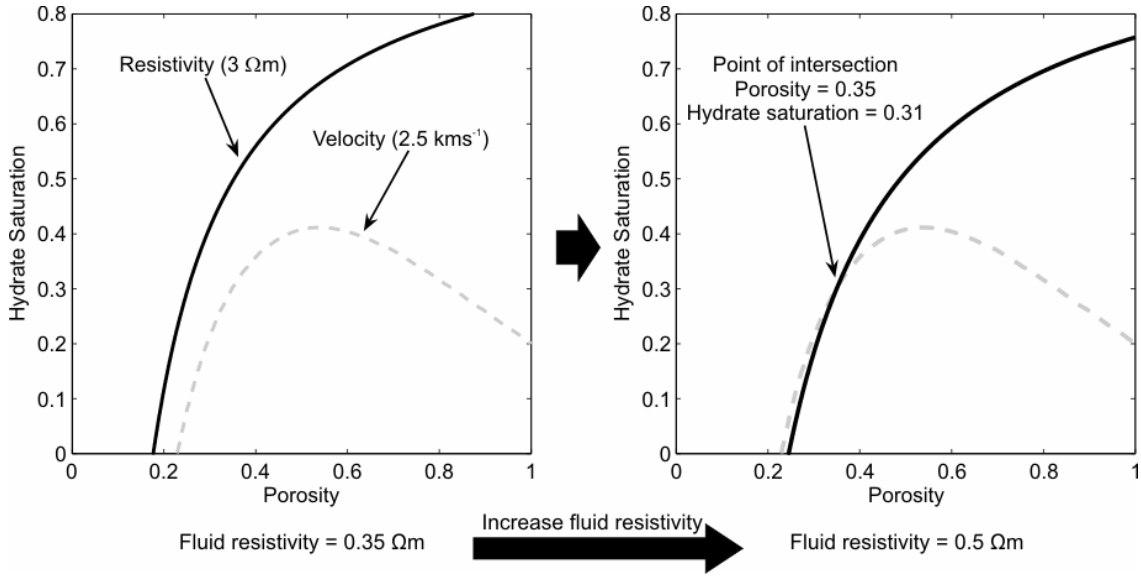

Figure 6.18 Hydrate saturation and porosity values of a non-load bearing three-phase medium composed of glass beads, hydrate and brine for a co-located resistivity value of 3Ωm and velocity value of 2.5 kmS-^{1}. Left - no intersection of the resistivity and velocity curve for a brine resistivity of 0.35 Ωm. Right – brine resistivity is increased to 0.5 Ωm causing the resistivity curve to move allowing the velocity and resistivity curves to intersect.

An alternative method would be to change the model type used to calculate the hydrate saturation and porosity values. Figure 6.19 shows another hypothetical situation of co-located measurements of a three-phase composite. In the first case the resistivity and velocity curves are calculated assuming that the gas hydrate was non-load bearing. It can be seen for a resistivity of 300 Ωm and a velocity of 3 kmS-^{1} that the curves do not intersect. However the velocity and resistivity curves were re-calculated assuming that the hydrate is load bearing, and in this case then both the curves move and intersect. It is possible that not only the hydrate saturation and the porosity values can be calculated but the nature of the hydrate morphology can also be determined in some cases.

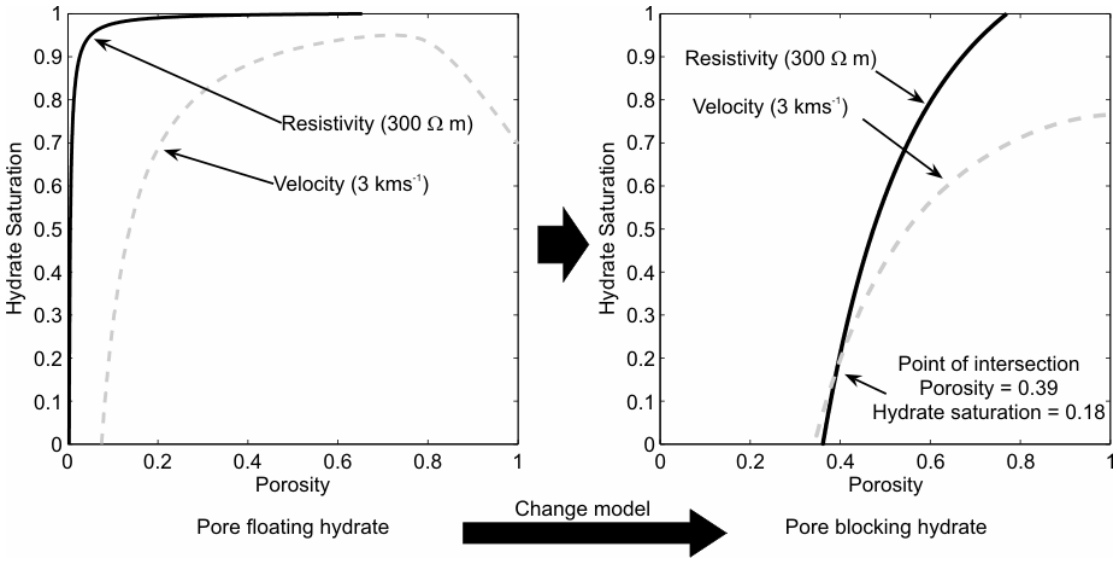

Figure 6.19 Hydrate saturation and porosity values calculated for a three-phase medium composed of hydrate, glass beads and brine for co-located measurements of resistivity (300 Ωm) and velocity (3 kmS-^{1}). Left - non-load bearing hydrate model with no intersection of the resistivity and velocity curves. Right – Load bearing hydrate model causing both the resistivity and velocity curves to move and allowing intersection of the curves.

6.3.3 Conclusions

The two-phase velocity model with the critical porosity determined at the point at which shear stress is lost (φ_c = 0.6) shows a good fit to the experimental data for an unconsolidated sediment. The model appears to the fit experimental data better than many other common effective medium models including the HS lower bound and the SCA/DEM model when the critical porosity is 0.5. However when comparing the model to data obtained from consolidated sandstone a critical porosity of 0.5 fits the data better. These results suggest that when predicting the velocities from an unconsolidated sediment a critical porosity of 0.6 should be used whereas a critical porosity of 0.5 should be used for a consolidated sandstone.

The three-phase seismic model does not fit the three-phase experimental data well when a critical porosity of 0.6 is used for either the load-bearing or the non-load bearing hydrate models. When a critical porosity of 0.5 is used the non-load bearing seismic model predicts the experimental data well. Therefore the Jakobsen *et al*. (2000) method of adding hydrate into the model does appear to be successful. However the laboratory experiments

yielded very few data points with which to test the model, due to the time taken to form hydrate in the samples.

The two-phase Geometric Path-Length Effective Resistivity model predict the resistivities from the two-phase experimental data well and produces a better fit than the HS conductive bound and Archie's law with *m* and *t* coefficients for soft formations or for loose glass bead samples, though these coefficients could be altered to produce a better fit for Archie's law.

The electrical three-phase pore blocking model over-predicts the experimental data, indicating the hydrate in the samples is not pore blocking. The non-load bearing model passes through the electrical data points, indicting that the three-phase model works, although there is a wide spread of resistivities from the samples due to the uneven distribution of the hydrate in the samples and possible uneven porosities.

A method has been developed for jointly interpreting velocity and resistivity data for both two- and three-phase media. For a two-phase medium separate inversions are used to determine all the aspect ratio and porosity values that will give a certain velocity or resistivity value. The points at which the velocity and the resistivity curves intersect give the aspect ratio and porosity value that satisfies both velocity and resistivity. When dealing with a medium which also contains hydrate there are three variables. One of the variables has to be fixed and then the inversion process is repeated. The variable that is fixed should be based on the prior data available.

There are a number of assumptions associated with using this method to determine the porosity, aspect ratio and hydrate saturation.

- The physical properties of the constituents that make up the sediment are known. Elastic moduli of material such as quartz and water are well known, however the elastic moduli of clay are not and may lead to errors. In experimental measurements of sediment in the laboratory the resistivity of the conducting pore fluids is easy to determine. However in the field there may be little information about the resistivity of the pore fluid. The resistivity of the pore fluids is the major control on the final resistivity of the effective medium, and inaccurate values may lead to large errors in the final results.
- The shape of the inclusions must be idealized to ellipsoids in both the electrical and seismic models.

- The degree of grain alignment is assumed to either be fully aligned or completely random.
- In the three-phase models the hydrate is assumed to be either fully interconnected or totally isolated.

Chapter 7. Case study: IODP Exp. 311 Cascadia Gas Hydrates

In this chapter the electrical and seismic effective medium models, developed in Chapters 3 and 4, will be applied to well log data collected offshore Vancouver Island in hydrate bearing sediments. The joint interpretation method (Chapter 6) will also be applied to co-located seismic velocity and electrical resistivity measurements, where available, to determine the hydrate saturations. This will also test whether the joint interpretation method can provide more information about the sediments than the individual effective medium models.

7.1 Introduction

Integrated Ocean Drilling Program (IODP) Expedition 311 took place in September–October 2005. The area under investigation was the accretionary prism of the Cascadia Subduction zone off the coast of Vancouver Island (Figure 7.1). The accretionary prism is the result of the Juan de Fuca plate subducting under the North American plate. This location is well known for the widespread abundance of gas hydrates in the continental margin sediments and has been the subject of numerous geophysical studies (Chapman *et al.,* 2002; Hyndman & Spence 1992; Hobro *et al.,* 2005; Riedel *et al.,* 2002; Westbrook *et al.,* 1994; Yuan & Edwards, 1996).

The principal objective of the expedition was to constrain geological models for the formation of gas hydrates in subduction zone accretionary prisms. This objective required high-quality data on the vertical and regional concentrations and distributions of gas hydrates within the accretionary prism. To this end four sites (U1325, U1326, U1327 and U1329) were drilled and cored along a transect perpendicular to the margin (Figure 7.1). These sites represented four different stages in the evolution of the gas hydrate stability zone. A fifth site (U1328) was drilled at an active cold vent near site U1327. Sites U1327 and U1328 are situated near ODP site 889 which was drilled during ODP Leg 146. Figure 7.2 shows the positions of the four sites in the transect on a seismic profile (MCS line 89-

08, Riedel *et al.*, 2006) of the area. The author participated in this expedition as a physical properties specialist.

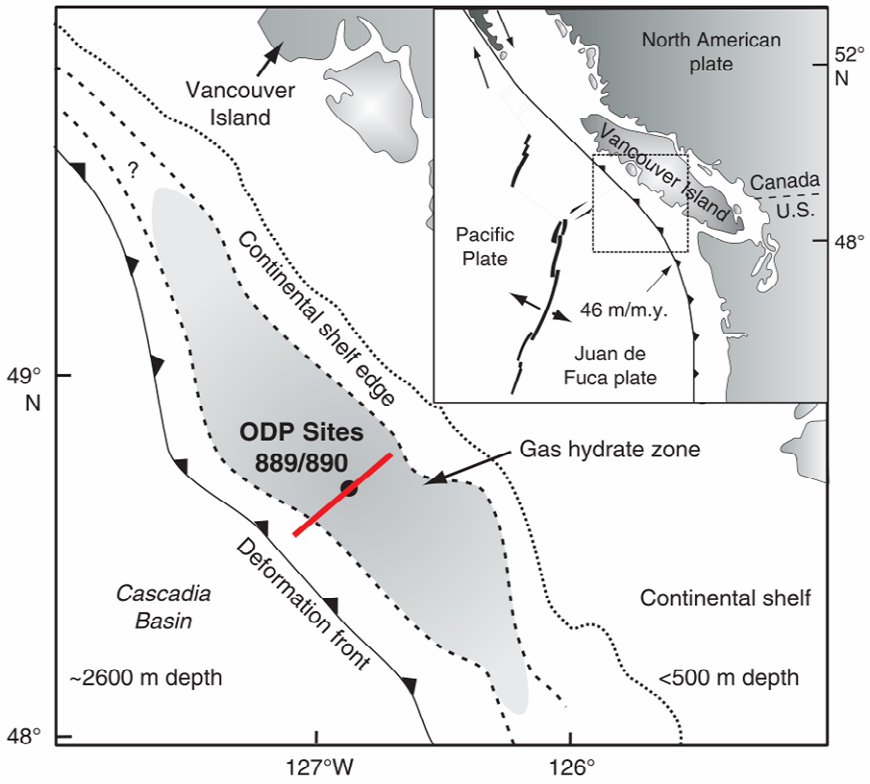

Figure 7.1 General location of IODP Expedition 311 drilling transect (red line) near the previous ODP Sites 889/890 off the coast of Vancouver Island. A bottom-simulating reflector is present on ~50% of the mid-continental slope (shaded area) (after Riedel, *et al.*, 2006)

At each site logging while drilling (LWD), coring and wireline logging took place, apart from site U1329 where wireline logging was not accomplished. In general 4-5 boreholes were drilled at each site labeled A-E. The first borehole drilled at each site (Borehole A) was solely dedicated to LWD measurements. These measurements included resistivity, porosity, natural gamma ray and density. Boreholes B-E were used for sediment coring and then wireline logging. The cored sediments were subject to a suite of shipboard measurements. These included core temperature measurements using IR images immediately after core retrieval, physical properties measurements, sediment lithology descriptions, interstitial water (IW) geochemistry analyses and void gas geochemistry. The physical properties measurements included non-contact and contact resistivity, velocity, shear strength and moisture and density (MAD) analysis where wet and dry density and porosity can be measured. Wireline logging measurements, which often took place in the same bore hole as the coring, included resistivity, porosity and P- and S-wave velocity.

The boreholes within each site were located approximately 20m from each other. Table 7.1 gives a summary of which measurements were made in each borehole at each site.

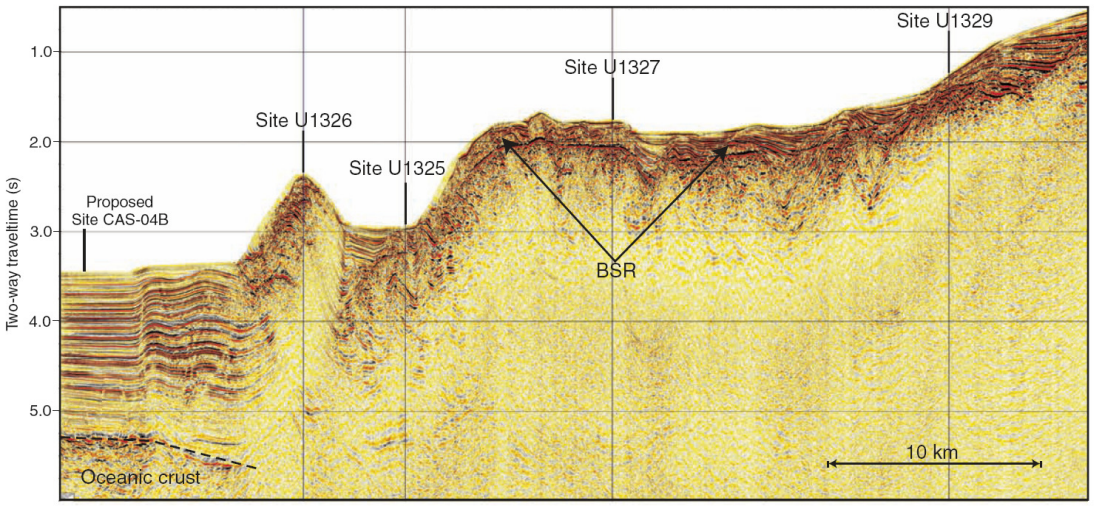

Figure 7.2 Overview of Seismic line MCS line 89-08 across the northern Cascadia margin. The Position of the four transect sites cored and logged are shown. Site U1328 is two miles southeast of Site U1327 (after Riedel *et al.*, 2006).

A gas hydrate related BSR occurs over a ~30km wide band parallel to the coast (Figure 7.1). The largest amount of gas hydrate is predicted to occur just above the BSR (Hyndman & Davis, 1992, Buffett & Archer 2004). This model also predicts that hydrate concentrations should be at their greatest toward the centre of the accretionary prism and disappear towards the edges. At Cascadia the BSR has been interpreted to be approximately 200-300m below the seafloor (Riedel *et al.,* 2006). Previous predictions of gas hydrate saturation of the pore space range from few percent up to 35% (Yuan *et al.*, 1996, 1999; Hyndman *et al.*, 1999, 2001; Hobro *et al.,* 2005; Riedel *et al.*, 2005). It was hoped that the new data from Expedition 311 would allow the saturation values to be better constrained. A more complete summary of the expedition along with methods used and preliminary results is given in the Proceedings of the Integrated Ocean Drilling Program, Volume 311 (Riedel *et al.,* 2006). The aim of this chapter is to estimate the gas hydrate saturations from the down hole logging data, in combination with chlorinity and physical property data.

Hole	Wire line Logging				LWD			Core recovery (mbsf)
	γ	φ	V_p and V_s	ρ	γ	φ	ρ	
U1325A	-	-	-	-	Y	Y	Y	-
U1325B	-	-	-	-	-	-	-	0-206
U1325C	Y	-	Y	Y	-	-	-	188-294
U1326A	-	-	-	-	Y	Y	Y	-
U1326B	-	-	-	-	-	-	-	0-1.5
U1326C	-	-	-	-	-	-	-	0-85
U1326D	Y	-	Y	Y	-	-	-	78-271
U1327A	-	-	-	-	Y	Y	Y	-
U1327B	-	-	-	-	-	-	-	0-10
U1327C	-	-	-	-	-	-	-	0-266
U1327D	Y	Y	-	Y	-	-	-	0-247*
U1327E	Y	-	Y	Y	-	-	-	0-129*
U1328A	-	-	-	-	Y	Y	Y	-
U1328B	-	-	-	-	-	-	-	0-47
U1328C	Y	Y	Y	Y	-	-	-	56-293
U1328D	-	-	-	-	-	-	-	0-15
U1328E	-	-	-	-	-	-	-	0-234*
U1329A	-	-	-	-	Y	Y	Y	-
U1329B	-	-	-	-	-	-	-	0-10
U1329C	-	-	-	-	-	-	-	0-188
U1329D	-	-	-	-	-	-	-	200-210
U1329E	-	-	-	-	-	-	-	0-126*

Table 7.1 Summary of wireline logging, LWD and core recovery at each borehole at each site. * indicates sections of borehole where non-continuous coring took place.

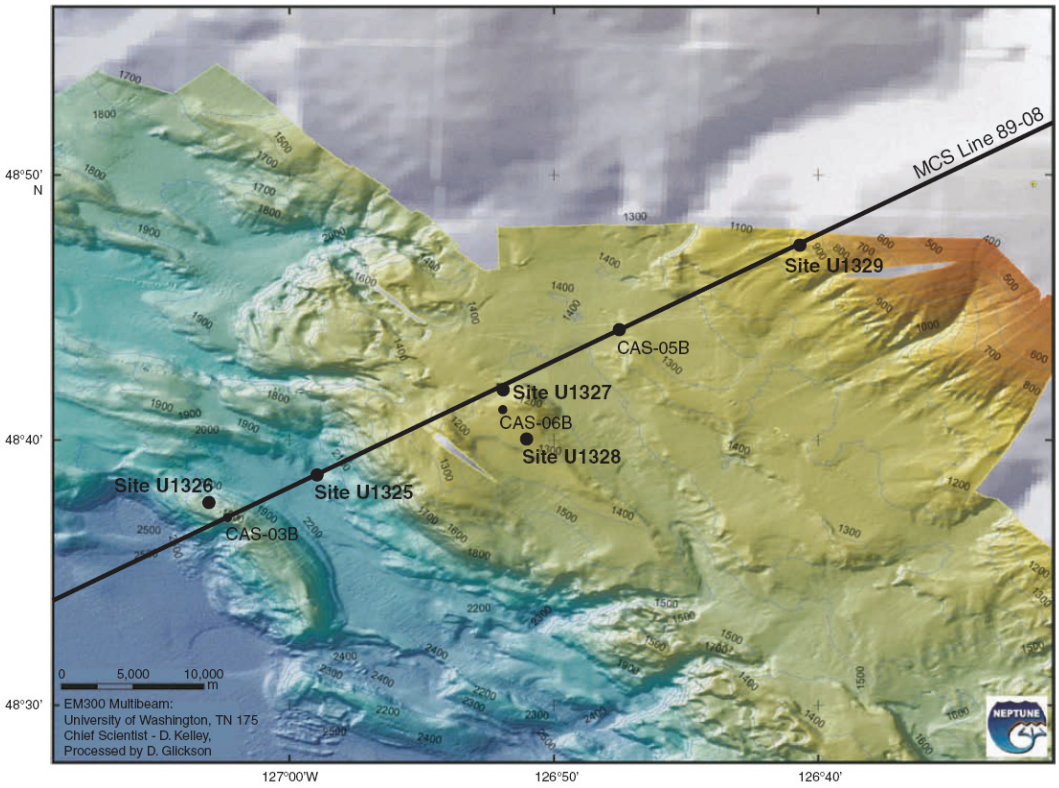

Figure 7.3 Multibeam bathymetry map along the transect across the accretionary prism offshore Vancouver Island indicating the position of each of the sites from IODP expedition 311 (after Riedel *et al*., 2006).

7.2 Hydrate saturation from resistivity logs

7.2.1 Resistivity and porosity logs

LWD and physical property measurements such as resistivity, porosity and density, were recorded at all five sites. LWD resistivity was recorded using the GeoVISION tool which provides electrical resistivity measurements of the formation and electrical images of the borehole. The tool uses two transmitter coils and a number of electrodes to obtain the Bit resistivity (RBIT), the Ring resistivity (RING) and the Button resistivity at three depths of investigation, shallow (BSAV), medium (BMAV) and deep (BDAV).

LWD porosity was measured in two ways. Neutron porosity is measured by emitting fast neutrons from a radioactive source. These are then slowed down in collisions before being captured by nuclei in the formation at which point a gamma ray is emitted. Hydrogen is the predominant molecule which causes this slowing down effect. A detector measures the gamma rays to determine the porosity. Because gas hydrate has

approximately the same concentration of hydrogen atoms as water the porosity tool does not distinguish between hydrate and water in the pore space.

Porosity can also be determined from the density log. Density is determined using a gamma ray source and detector which measures the number of Compton scattering collisions (similar to that of the MSCL used in Chapter 5). The change in gamma ray energy is related to the formation density. Porosity can then be determined from the following equation,

$$\varphi = \frac{(\chi_g - \chi_b)}{(\chi_g - \chi_w)}, \tag{7.1}$$

where χ_w is the water density, χ_g is the grain density, χ_b is the bulk density and φ is the porosity. A value of 1.03 g/cm^3 was used for the water density. Grain density was determined by taking a mean of the grain density measurements on the sediment cores which were drilled at each site (Riedel *et al*., 2006). Values for the average grain density at each site are given in Table 7.2. Moisture and Density (MAD) techniques (described in Riedel *et al.,* 2006) are a set of measurements made by measuring the wet and dry mass of discrete samples (~ 1cm^3 in size) at approximately 0.5m intervals along the length of the retrieved sediment cores. The measurements allow independent values from the logging of porosity and bulk density to be determined. Figure 7.4 shows a comparison of the MAD porosity, LWD density porosity and LWD neutron porosity. The density porosity log and the neutron log show the same pattern down the borehole but the neutron porosity values are consistently higher than the density porosity values. This is because the neutron tool also picks up bound water in the clay which is not part of the pore fluids. Figure 7.4 also shows two plots of MAD porosity versus density porosity (B) and neutron porosity (C) and compares them to the ideal fit. In Figure 7.4 (B) the ideal fit line goes through the middle of the cloud of data points and in Figure 7.4 (C) the cloud of data points appears offset against the ideal fit line. This indicates that the density porosity is a better fit to the MAD porosity. RMS misfits between the MAD porosities and the density and neutron derived porosities were also calculated. The density derived porosity has a 5.9% RMS misfit and the neutron porosity has an 8.2% misfit. This also indicates that the density derived porosities show a better fit to the MAD porosities compared to the neutron derived porosities. Therefore the porosity calculated from the density logs will be used to calculate the hydrate saturations in the following sections.

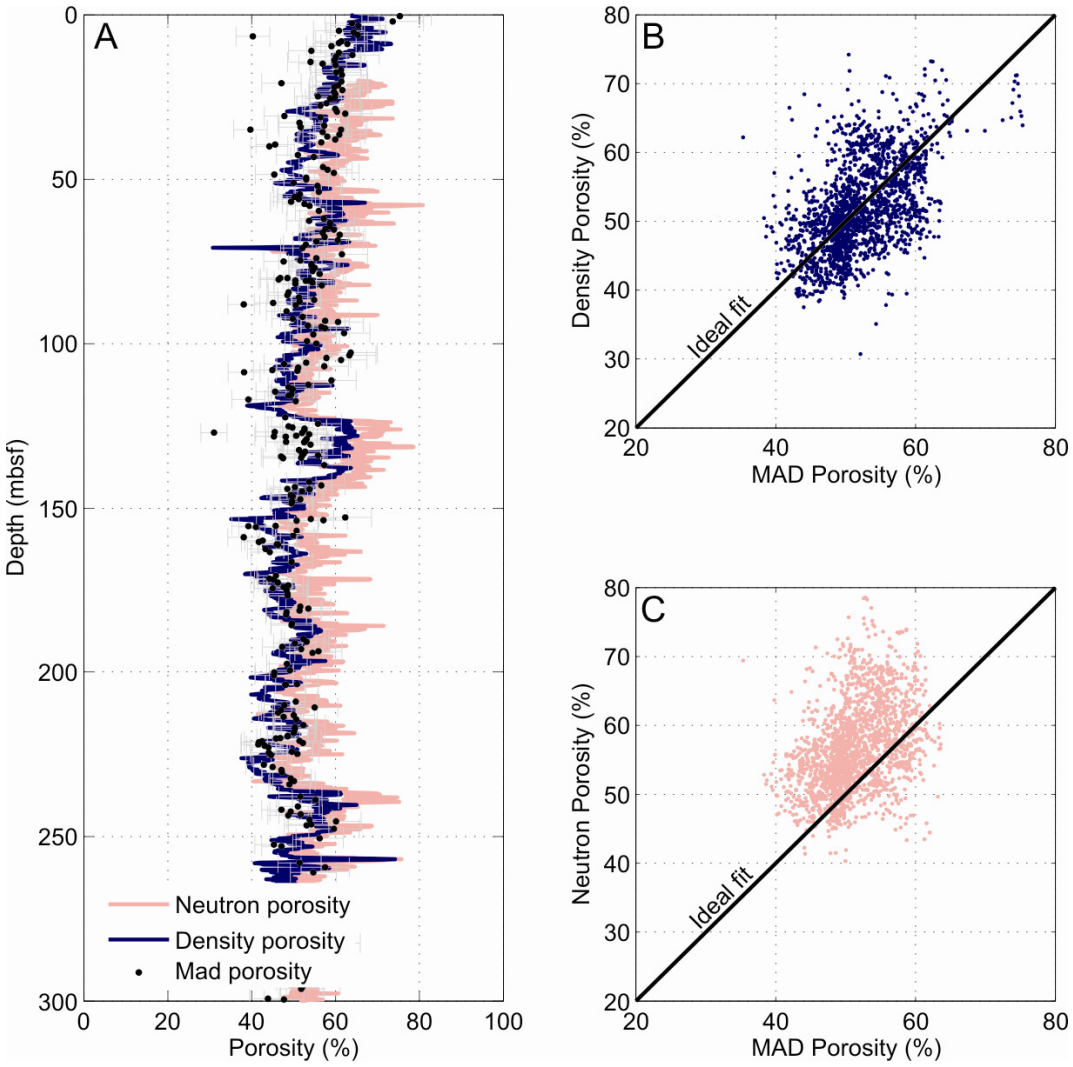

Figure 7.4. (A) Comparison of the density derived porosity, neutron derived porosity from the LWD logs and the MAD porosities from the sediments cores for site U1327. (B) Comparison between the Density derived porosity and the Mad Porosity with the Ideal fit. (C) Comparison between the Neutron derived porosity and the Mad Porosity with the Ideal fit.

7.2.2 Hydrate saturation (using Archie's equations)

Calculating the hydrate content of sediments is most frequently done using Archie's law. It is therefore useful to calculate the Archie derived saturations to compare with the Geometric Path-Length Effective Resistivity model derived values. The Archie's method used here is the one utilized by Collett & Ladd (2000). Gas hydrate saturation is calculated using the following equations:

$$S_w = \left(\frac{t\rho_w}{\varphi^m \rho_B} \right)^{1/n}, \tag{7.2}$$

$$S_h = 1 - S_w, \tag{7.3}$$

where S_w is the water saturation, t and m are the Archie's coefficients of tortuosity and cementation respectively. φ is the porosity, n is the saturation coefficient, ρ_w is the resistivity of the pore fluid and ρ_B is the formation resistivity (i.e. the resistivity obtained from the logs). ρ_w is calculated from the salinity of the interstitial waters (IW), which was measured in cores at 15m intervals, and downhole formation temperature measurements, using the equations of Fofonoff (1985). t, m and n values used in the following calculations are those given by Riedel *et al.* (2006). t is given a value of 1 because this gives a resistivity equal to that of pore fluid water resistivity when the porosity is 100%. m was estimated from,

$$m_{est} = -\log(F) \Big/ \log(\varphi), \tag{7.4}$$

where,

$$F = \left(\rho_B \Big/ \rho_w \right). \tag{7.5}$$

This is calculated along the entire log and m is then estimated from the base line. m was given values that range from 2.4 to 2.6 (Table 7.2). A saturation coefficient of n = 2 was also used. It should be noted that these values were used for a quick shipboard analysis of the resistivity data to determine water saturation of the sediments. A more in depth study of the Archie's parameters by Chen (2006) indicates that more realistic Archie's parameters of t = 1.41, m = 1.76 and n = 1.94 could be used, although these values do change depending on which porosity log is used.

Figure 7.5 shows the formation resistivity log, pore water resistivity, porosity and hydrate saturation (calculated using Archie's method) profiles for Site U1327. A thick layer (from 120m 145m depth) of high hydrate concentrations appears which corresponds to the area of high resistivity (between 5 and 10 Ωm) in the resistivity log.

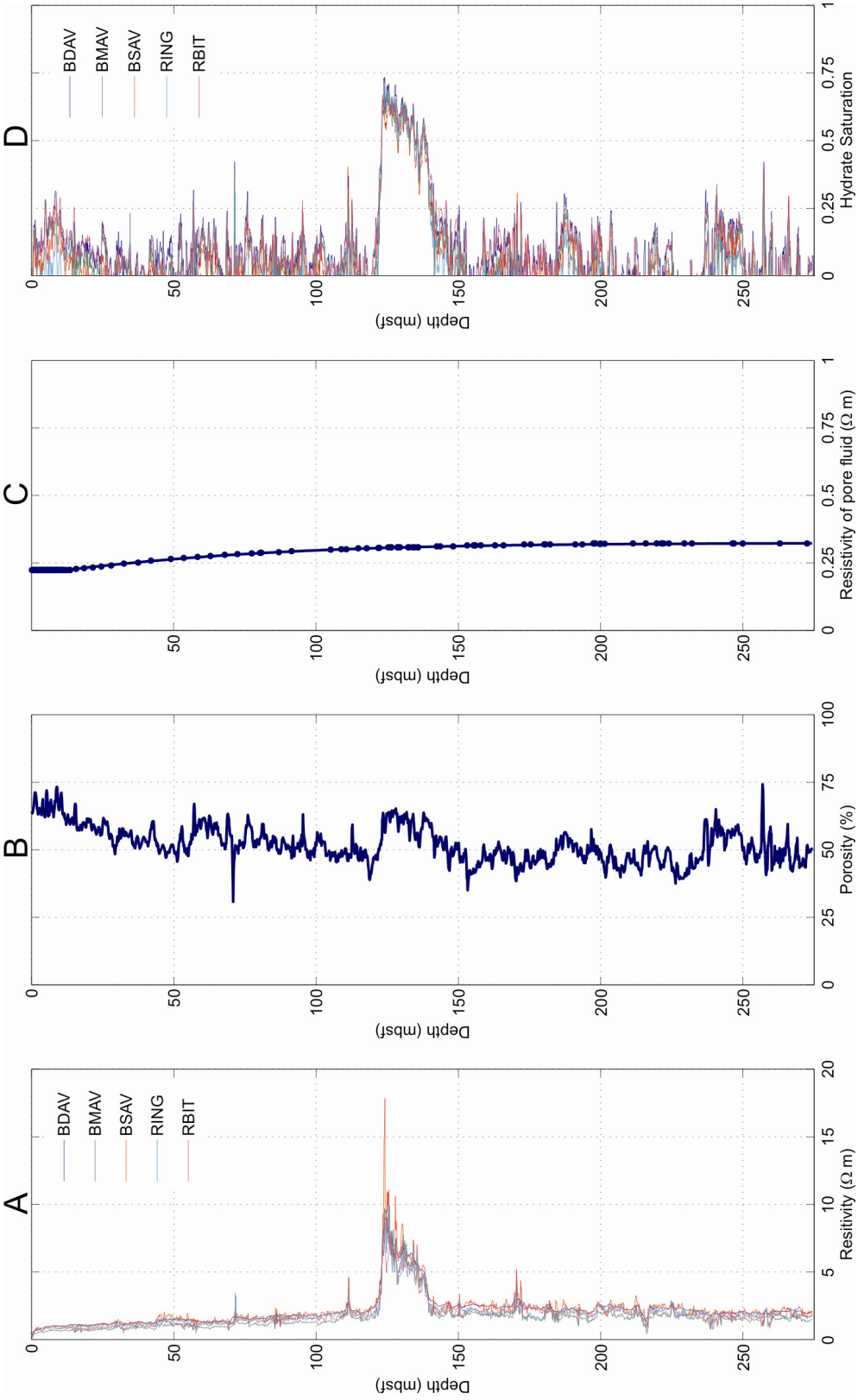

Figure 7.5(A) Resistivity from the LWD. (B) Density log porosity. (C) Resistivity of the pore fluid calculated from the chorinity data, from the IW samples and temperatures (D) Hydrate saturations of the pore space calculated from Archie's equation for site U1327.

	U1325	U1326	U1327	U1328	U1329
m	2.5	2.5	2.4	2.6	2.5
n	2	2	2	2	2
t	1	1	1	1	1
Grain density (g/cm^3)	2.75	2.76	2.75	2.76	2.73

Table 7.2 Cementation (*m*), saturation coefficient (*n*) and tortuosity (*t*) coefficients used in the Archie's calculations for each site and grain density values used in the calculations of porosity from density.

7.2.3 Hydrate Saturation using the Geometric Path-Length Effective Resistivity Method

Hydrate saturations were calculated using the Geometric Path-Length Non-Pore-Blocking Effective Resistivity model ($\rho_{GPLnon\text{-}block}$) as opposed to the Pore Blocking model ($\rho_{GPLblock}$). Resistivities calculated using the Pore Blocking method are far too high when compared to the formation resistivities measured in the logs.

To use the Geometric Path-Length Non-Pore-Blocking Effective Resistivity method an aspect ratio must be used within the equations. However in continental margin sediments the average aspect ratio is near impossible to determine and the alignment of the grains is also problematic. To determine a sensible aspect ratio and geometric factor we first look at the resistivity log and determine depths where hydrate is not believed to be present. Hydrate is unlikely to be present below the BSR or where resistivity has not increased above background levels. Figure 7.6A shows potential depth intervals without hydrate on the resistivity log for site U1327. An aspect ratio is then determined so that the resistivity gives a hydrate saturation of zero for these areas. This aspect ratio and corresponding geometric factor can then be applied to the whole log. Figure 7.6 D-F shows predicted hydrate saturations using different possible aspect ratios and geometric factors. Figure 7.6 D shows an aspect ratio that is too high and gives high hydrate saturations throughout the sediment column even at depths where hydrate cannot be present. Figure 7.6 F shows the hydrate saturations when too low an aspect ratio is used leading to an underestimation the hydrate content. Figure 7.6 E shows the results when the aspect ratio is adjusted so that zero hydrate saturation is predicted for the background resistivity leaving an interval of increased hydrate saturation which corresponds to the resistivity increase on the resistivity log.

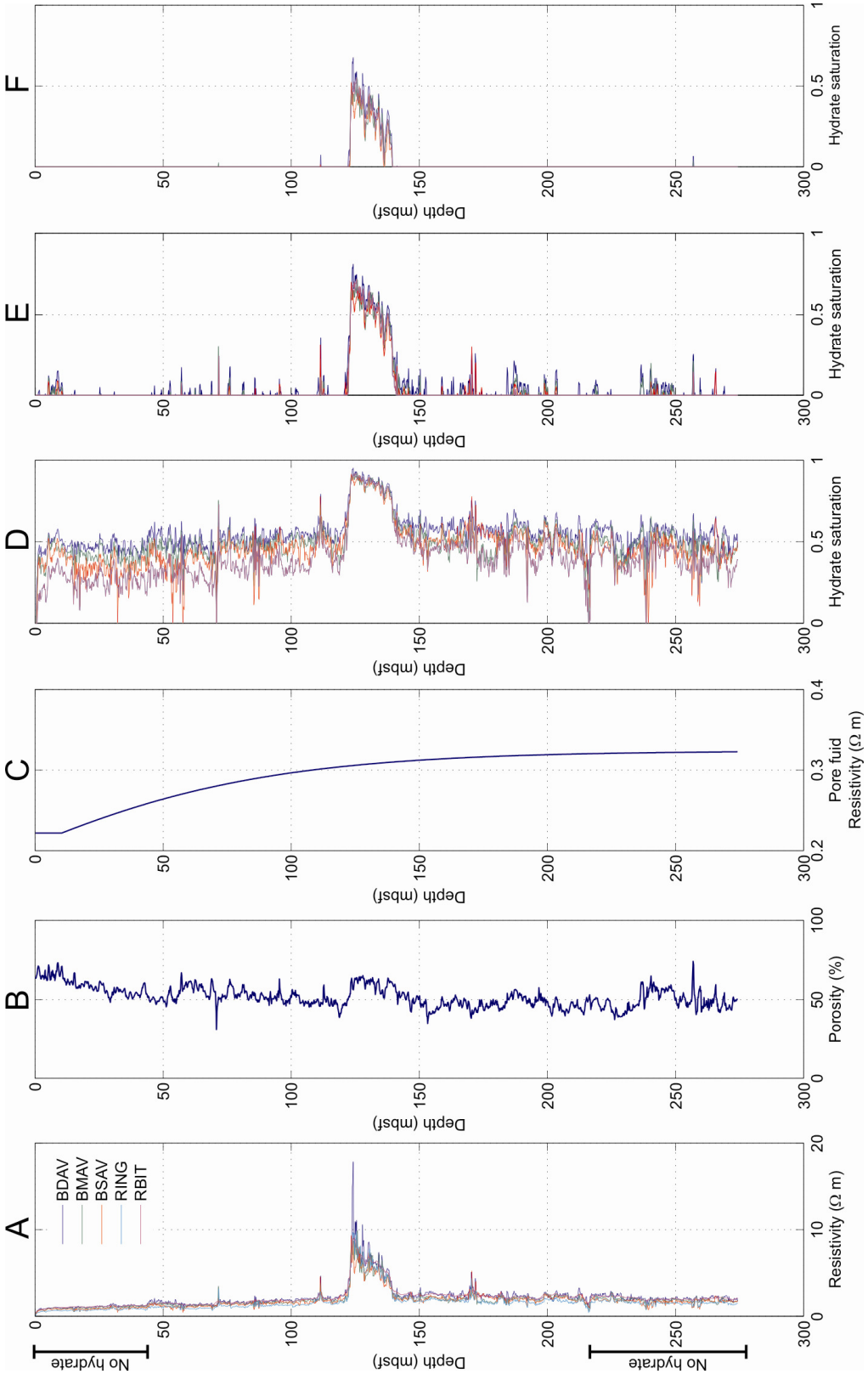

Figure 7.6 Logging and gas hydrate saturations (calculated from the geometric path-length effective resistivity method) for site U1327. (A) LWD resistivity logs (B) Density porosity log (C) Resistivity of the pore fluid (D) Gas hydrate saturation calculated using a geometric factor of 1.17 and aspect ratio of 1 (E) Gas hydrate saturation calculated using a geometric factor of 6.9 and aspect ratio of 0.1 (F) Gas hydrate saturation calculated using a geometric factor of 13.6 and an aspect ratio of 0.05.

No values could be obtained from the literature for the resistivity of clay. This is presumably because of the difficulty in measuring the resistivity of such small grains. Therefore quartz resistivity (10^{17} Ωm) was used for the grain resistivity. As mentioned earlier (Chapter 4) the grain resistivity has little effect on the bulk resistivity of the sediment which is primarily controlled by porosity and pore fluid resistivity.

It is assumed that all the changes in resistivity are caused by changes in the pore water resistivity and porosity (which are both known), and in the unknown hydrate saturation. Using this method grain aspect ratios of 0.1-0.2 are needed. These are plausible values for the grains because the mineralogy is primarily clay and clay generally has low grain aspect ratios (Chapter 3).

Comparison of Archie's and the Geometric methods

Figure 7.7 shows a comparison of Archie's and the Geometric Path-Length Non-Pore-Blocking Effective Resistivity method for Site U1327. Both methods clearly show a thick hydrate layer between 120m and 150m depth. The maximum gas hydrate saturation of this layer calculated by either method is approximately 65%. Each of the methods show some background hydrate saturation throughout the length of the logs although the Archie derived saturations are in general slightly higher. Both methods also show some hydrate below the predicted BSR.

7.3 Hydrate Saturation from velocity logs

To use the SCA/DEM method to solve for hydrate saturation the porosity, individual moduli of the components, aspect ratio and critical porosity must be given values. Whether to use a load-bearing or non load-bearing model must also be determined. The porosity values can be obtained from the LWD density logs in the same way as in Section 7.2.1. The bulk and shear moduli of hydrate and brine are well constrained and are given in Appendix A. The composition of the grains in the matrix is important when determining the hydrate saturation from the seismic velocities. Hobro *et al*. (2005) use a sediment grain composition of 35% clay, 20% quartz and 45% feldspar to determine hydrate saturations. Chen (2006) and Reidel *et al*., (2001) use a much higher clay fraction of 85% with the rest of the sediment being composed of quartz. Clay has much lower bulk and shear moduli than either feldspar or quartz (Appendix A). Using a predominantly clay mineralology to

model the sediment will produce lower velocities and consequently hydrate saturation estimates will be higher than if a predominantly quartz and feldspar mineralogy is used. Therefore it is important to obtain the correct sediment composition to prevent incorrect results. Figure 7.8 shows a lithographic log of the sediment composition obtained from smear slides and confirmed by XRD (Reidel *et al.,* 2006) at each site. The smear slide data indicates that the sediments at all of the sites are predominantly clay (~80%) with smaller amounts of quartz, feldspar and biogenic opal. Therefore to determine the hydrate saturations at each of the sites a predominantly clay composition will be used. The exact mineral percentage values of the sediments used at each site is given in Table 7.3. The bulk and shear moduli of clay are very hard to measure due to the small size of the grains. Clay bulk modulus values between 20 GPa and 50 GPa have been reported (Vanorio *et al*., 2003). A bulk modulus of 20.9 GPa and a shear modulus of 6.9 GPa have commonly been used to interpret seismic velocity data (Chand *et al*., 2006; Lee, 2004; Carcione & Gei, 2004) and will be used here.

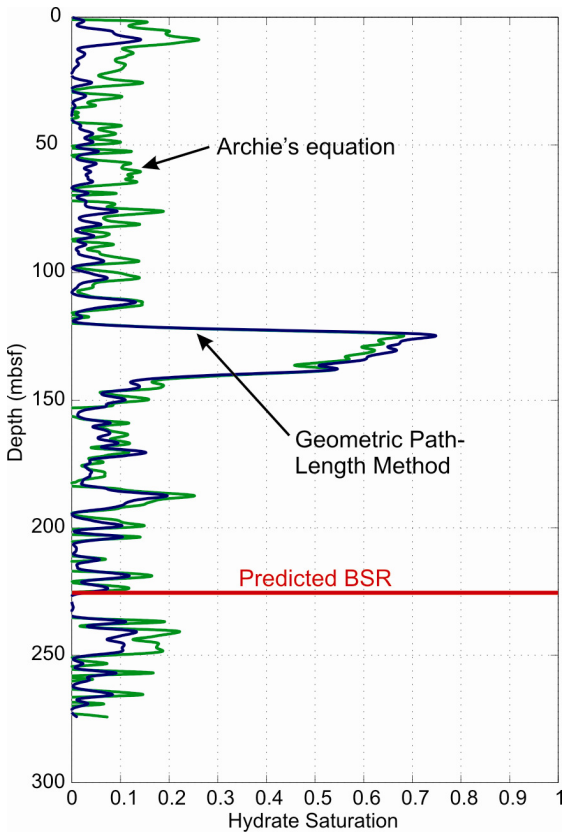

Figure 7.7 Comparison of Archie's and Geometric Path-Length derived gas hydrate saturations for site U1327 using the RBIT Resistivity log.

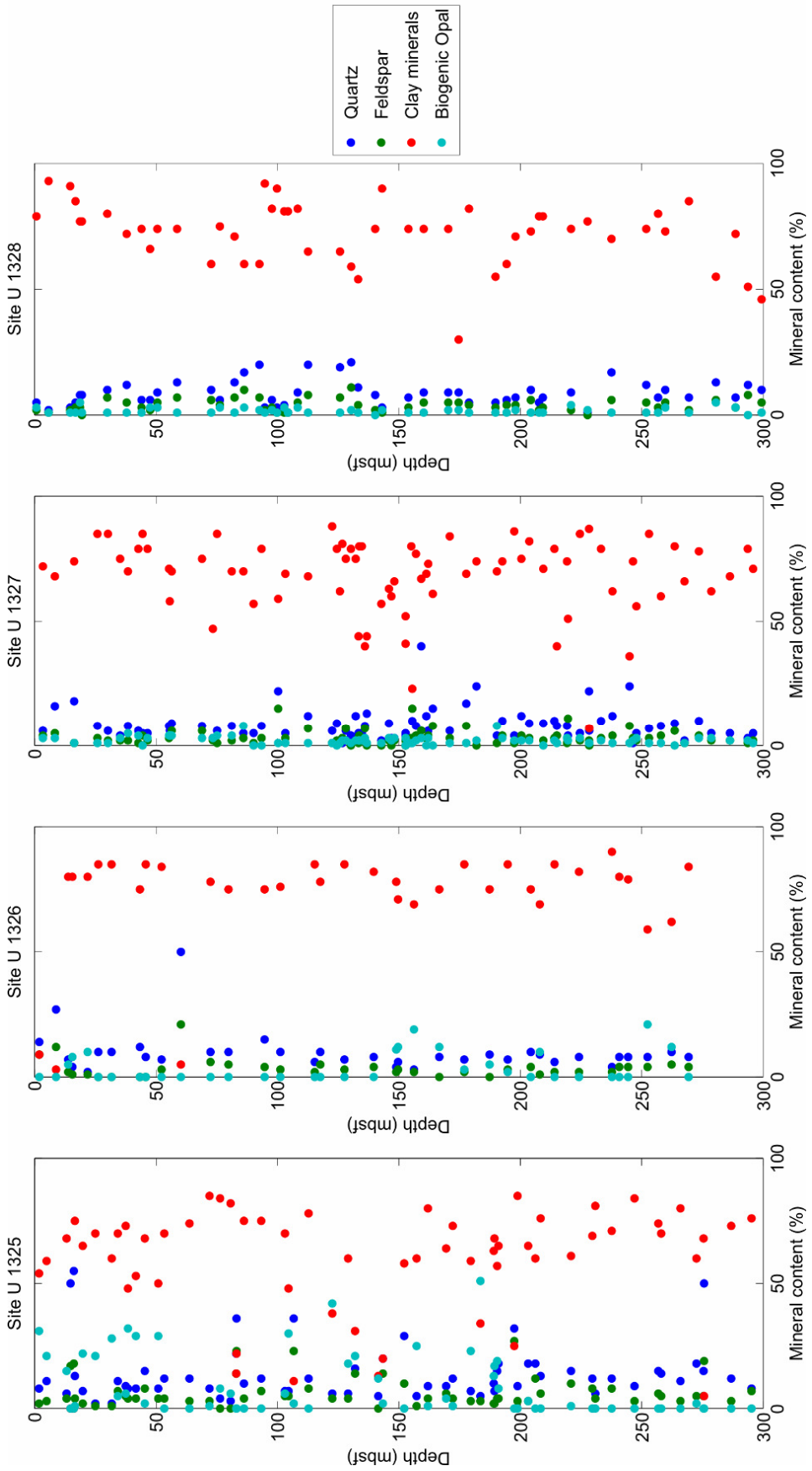

Figure 7.8 Dominant grain composition at sites U1325-U1329 determined from petrophysical smear slides and XRD analysis (Riedel *et al.*, 2006).

Site	Quartz	Feldspar	Clay Minerals	Biogenic Opal
U1325	15	5	70	10
U1326	15	5	80	0
U1327	11	5	84	0
U1328	10	5	85	0

Table 7.3 Grain composition percentages used to model the seismic properties sediment at each site.

Figure 7.9 shows that the aspect ratio is far more important when the critical porosity is lower than when it is higher. For a high critical porosity (φ_c = 0.6) velocity does not change a great deal with aspect ratio. A lower critical porosity (φ_c = 0.5) shows a greater dependence on the aspect ratio. A critical porosity of 0.5 appears to be too low and produces velocities that are too high when compared to experimental data as discussed in Chapter 6. Therefore to start a φ_c of 0.6 will be used to interpret the velocity data.

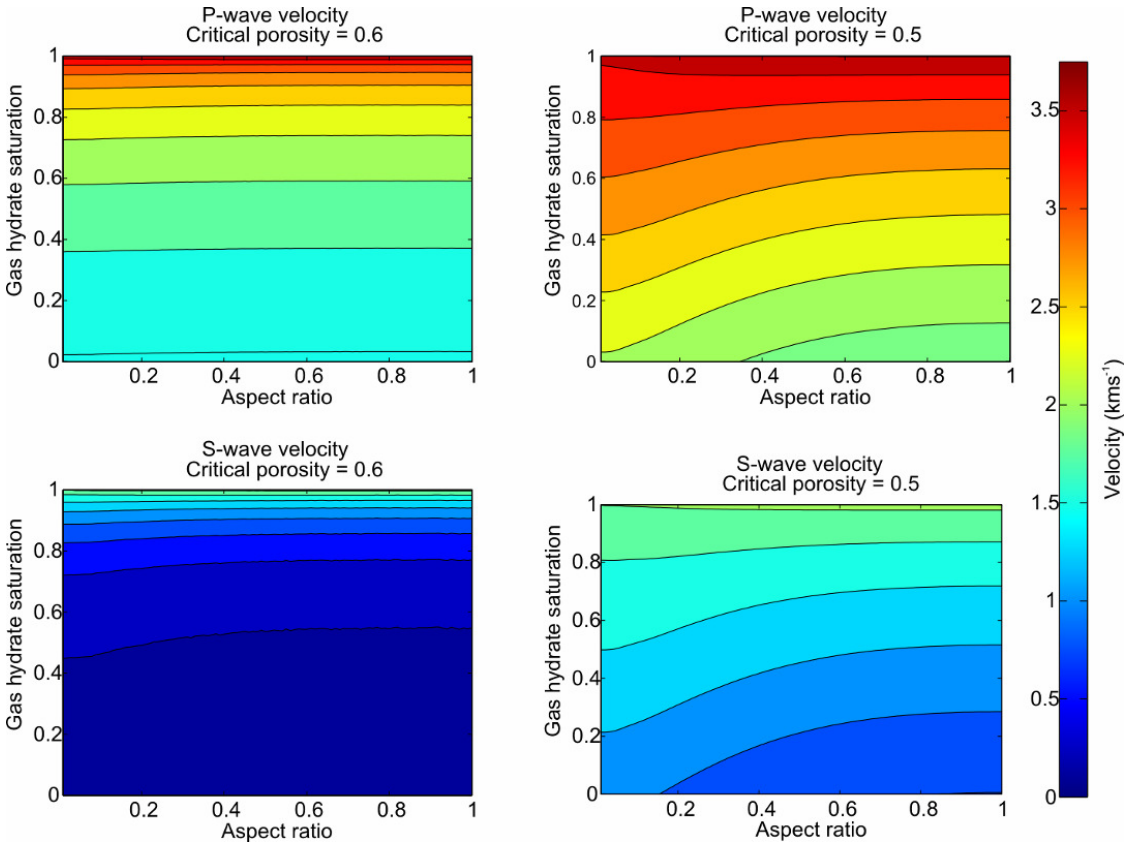

Figure 7.9 The effect of the aspect ratio on predicted seismic velocities for a three phase medium calculated for critical porosities of 0.6 and 0.5.

Starting with a non-load-bearing model with φ_c = 0.6, an aspect ratio matching the resistivity logged derived aspect ratios, the velocities were converted into hydrate content for site U1327. The hydrate saturations from the S-wave log were considerably higher than the P-wave derived ones. There are several possible reasons for this. The critical porosity, the aspect ratio and/or the model type (load bearing or non-load bearing) may be incorrect. To determine a more suitable critical porosity and aspect ratio the mean P- and S-wave velocity and porosity was determined for areas of the log where no hydrate is present. All the possible critical porosities and aspect ratios that can be used to calculate these velocities can then be determined and plotted (Figure 7.10). Ideally these lines would cross, however for this site they did not. Only critical porosities of 0.57-0.59 appear to be useable for the data set. Therefore a critical porosity of 0.58 was used, with an aspect ratio of 0.1. The aspect ratio of 0.1 was chosen because it matched the aspect ratio value derived from the resistivity analysis (Section 7.2.3). The φ_c of 0.58 was chosen because this matched the corresponding aspect ratio of 0.1 in Figure 7.10.

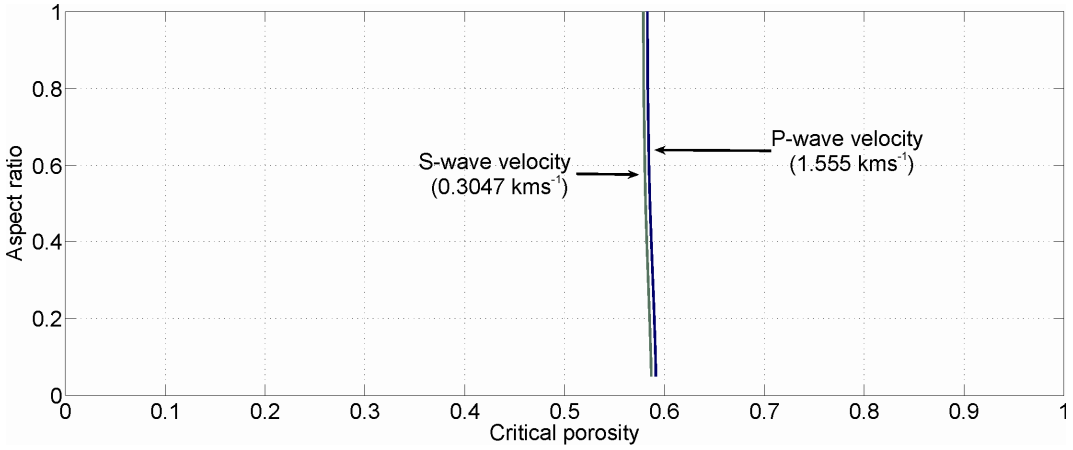

Figure 7.10 Possible Aspect ratios and critical porosities that can be used in a non-load bearing SCA/DEM model for a porosity of 55%.

Figure 7.11 shows the velocity logs and the inferred gas hydrate saturations for site U1327. It can be seen that the S-wave derived saturations are still higher than the P-wave ones although the effect is not so pronounced. The S-wave derived hydrate saturation is very sensitive to velocity changes: only a small change in velocity will cause a large change in predicted gas hydrate content. If we assume that the gas hydrate is load bearing and determine the hydrate saturation the values become much less sensitive to S-wave

velocity changes. However if this is done then the SCA/DEM model predicts effective velocities that are much higher than those measured in the sediments. Therefore all the gas hydrate saturations were predicted assuming that the hydrate was non-load bearing.

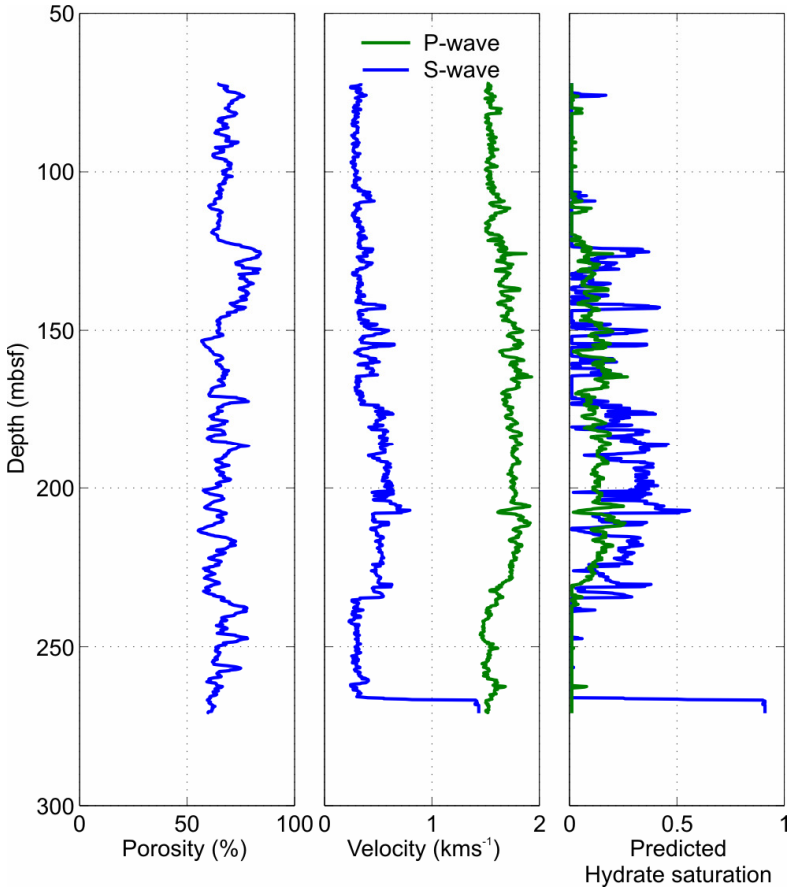

Figure 7.11 Porosity (LWD) and velocity logs (Wireline) for site 1327. Hydrate saturation as calculated from the SCA/DEM model for a non-load bearing system (blue line is P-wave derived values, and the green line is the S-wave derived values).

7.4 Gas Hydrate Saturations

Each of the methods described above has been applied to the resistivity and velocity logs at each site. Figure 7.12-Figure 7.14 show the changes in hydrate saturation with depth at each site using the LWD resistivity logs, the wireline resistivity logs, the wireline velocity logs and the density derived porosities from the LWD logs along with the geometric path-length effective resistivity model and the SCA/DEM velocity model. The plots for each site appear in order along the transect rather than the order in which they were drilled.

7.4.1 Hydrate saturations in the transect

Figure 7.12 and Figure 7.13 show the LWD and wireline resistivity derived hydrate saturations across the margin transect (sites U1326, U1325, U1327 and U1329). Wireline resistivity measurements are made after the borehole has been drilled unlike the LWD measurements. Therefore the time delay and/or the disturbance to the sediments may cause some discrepancy between the two logging measurements.

At site U1326 both the wireline and the LWD logs record the maximum hydrate saturation at 90m below the sea floor, well above the predicted BSR. At this point the predicted hydrate saturation is approximately 90%. This observation is contrary to the predictions of numerical models such as that of Hyndman and Davis (1992) and of Buffett & Archer (2004) of maximum hydrate saturation just above the BSR. Throughout the rest of the sediment column the mean hydrate saturation is 9%. Maximum hydrate saturation occurs much lower in the sediment column at site U1325. It occurs between 190 m and 230 m depth and is just above the BSR. Maximum hydrate saturation occurs at site U1327 in a very distinctive band between 120 and 140 m depth (Figure 7.12). Hydrate saturations calculated from the LWD resistivities indicate that the saturations are approximately 70% in this area. The very high hydrate saturation is not seen to the same extent in the wireline logging calculations where hydrate saturations of approximately 20% are inferred.

Hydrate saturations appear to steadily increase with depth at site U1329A. Saturation of 40% is observed at a depth of 200 m which is well below the predicted BSR depth of 129 m. In fact at all of the site's hydrate is inferred to be present below the BSR. The BSR depth is well constrained in this area and is unlikely to be incorrect to more than 10 m therefore another explanation must be sought. A possibility is that free gas is present in the sediments below the BSR. Free gas also causes the resistivity of the sediments to increase. The Geometric Path-Length model assumes that the changes in resistivity are due solely to the presence of hydrate but free gas would have a similar effect. Sonic log studies of data obtained during ODP Leg 146 indicate that some free gas must be present beneath the BSR in the region of site U1327 and U1328. MacKay *et al*. (1994) estimate free gas concentrations of 1-5% to account for the low velocities observed below the BSR.

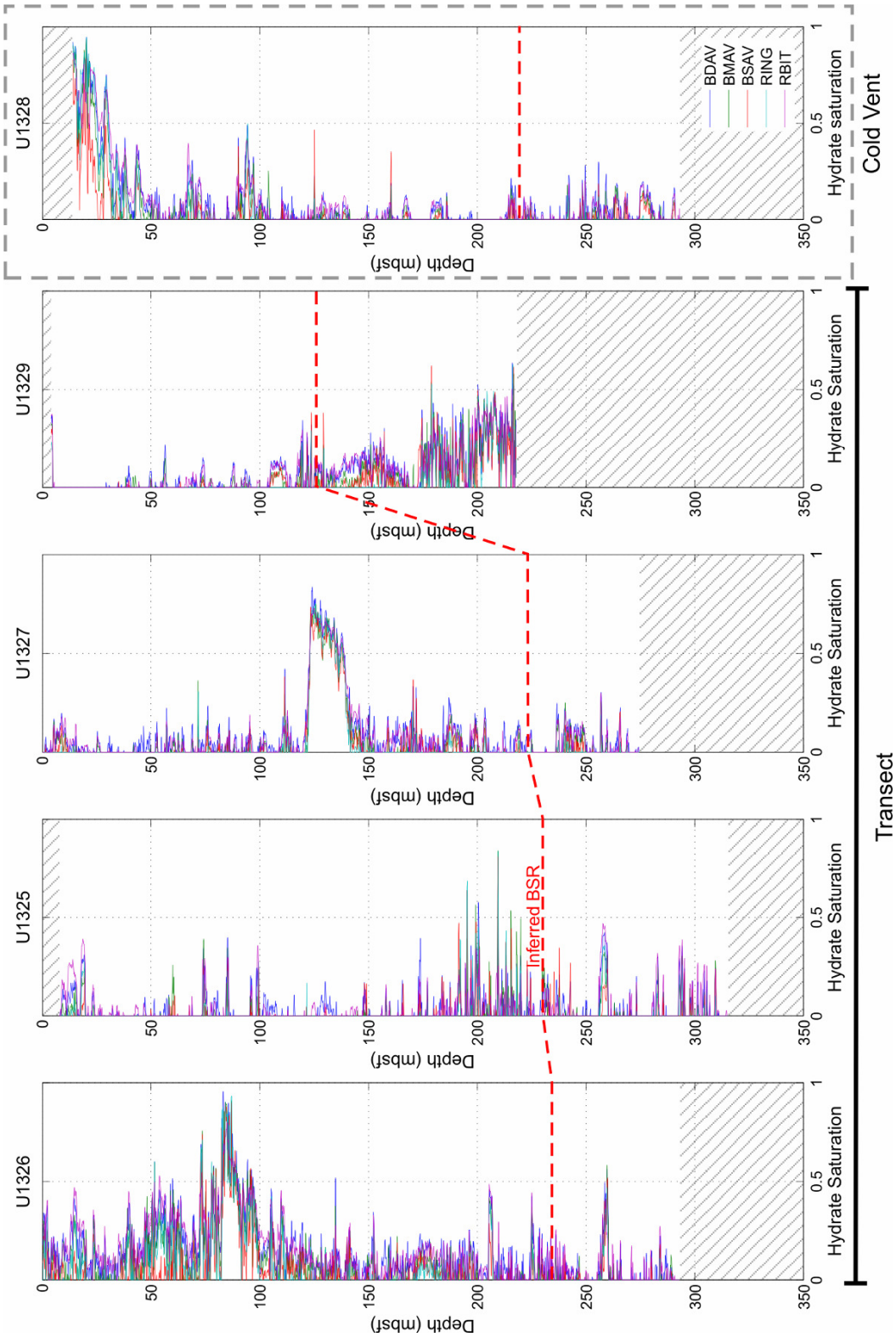

Figure 7.12. Gas hydrate saturations derived from the LWD resistivity logs and the LWD density derived porosity log for all sites. Gas hydrate is assumed to be pore floating. BSRs are inferred from seismic velocity data (Reidel et al., 2006). Dashed areas in the plots represent depths where no velocity data was collected.

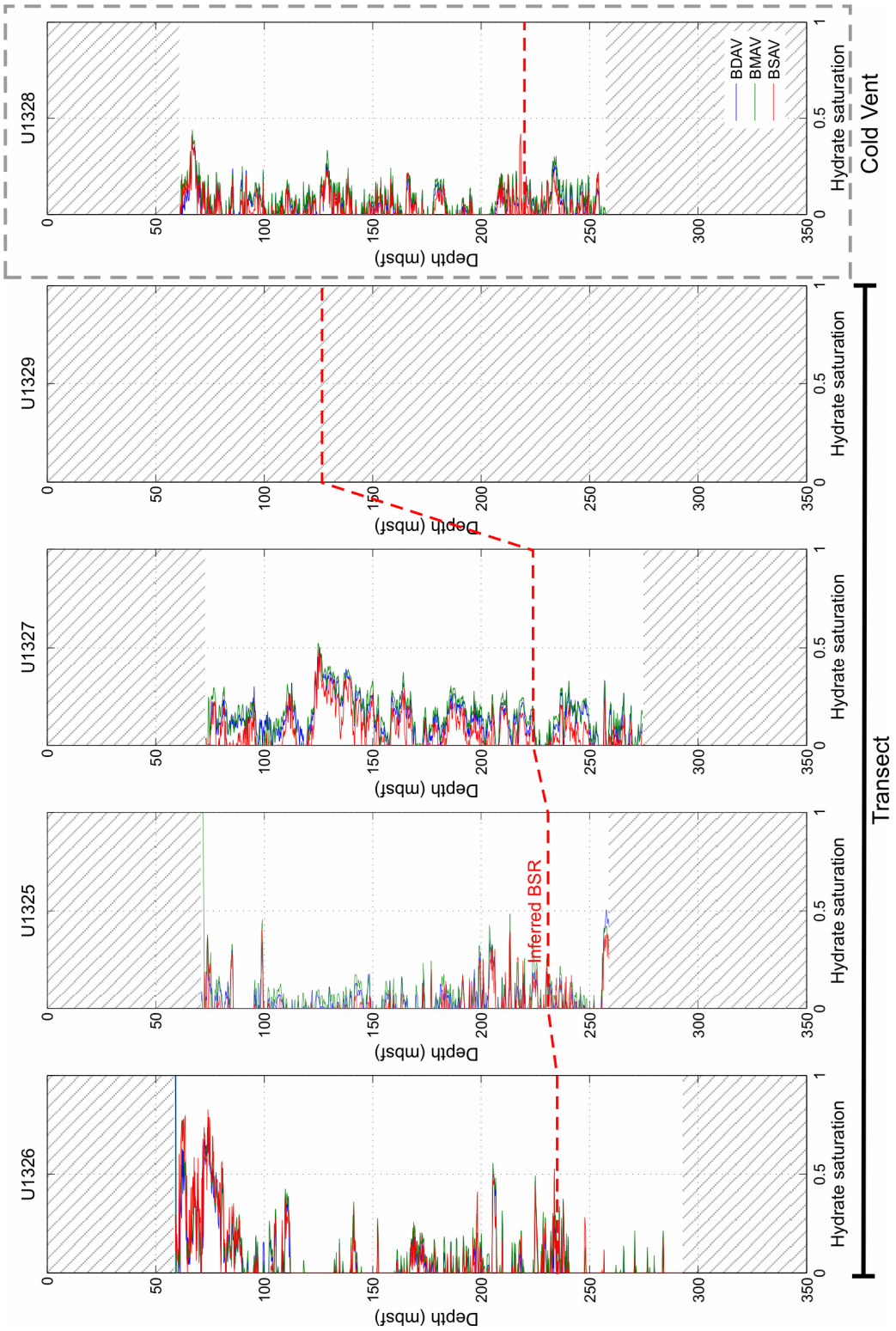

Figure 7.13 Gas hydrate saturations derived from the Wireline resistivity logs and the LWD density derived porosity log for sites U1326, U1325, U1327 and U1328. Gas hydrate was assumed to be floating in the pores. Dashed areas in the plots represent depths where no velocity data was collected.

Figure 7.14 shows velocity derived gas hydrate calculations for each of the sites across the transect. There is unfortunately no velocity data available for site U1329. The hydrate saturations were calculated using both the load bearing and the non load-bearing velocity models. When the hydrate was assumed to be load bearing the hydrate saturation predictions indicated that there was no hydrate present in any of the logs. From this we can infer that the hydrate is non-load bearing.

Hydrate saturations appear to be very laterally discontinuous across the transect. Even within the same site, different boreholes show very different hydrate saturations. Site U1327 is a prime example. The LWD resistivities show a thick zone of high hydrate saturation which does not appear on the velocity or the resistivity wireline logs. The LWD logging always was measured in a separate borehole to the wireline logs. These boreholes were generally about 20m apart indicating a high degree of heterogeneity in the sediments. The prediction that the maximum hydrate saturations should occur just above the BSR does not seem to be the common case along this transect. Maximum hydrate concentrations occur higher in the sediment column at most of the sites.

Downhole logging data from a previous expedition (ODP leg 146, sites 889/890) in the same area has been used to determine the gas hydrate saturations. Saturations may reach up to 30% of the pore space in a region 100m above the BSR (Hyndman *et al.*, 2001; 1999; Spence *et al.*, 2000). Other estimates have put the hydrate concentrations at 20-35% (Yuan *et al.*, 1996, 1999). If such concentrations exist then they are far higher than other margins studied (Riedel *et al.*, 2005). Blake Ridge saturations are thought to be less than 10% (Paull *et al.*, 1996) and Hydrate Ridge they are thought to be less than 5% (Trehu *et al.*, 2004). Ussler & Paull (2001) estimated much lower hydrate saturations from the chorinity data from Leg 146. Gas hydrate saturations have recently been recalculated from the Leg 146 logging data and the chorinity data by Riedel *et al.* (2005) indicating hydrate values of 5-10%. Using a three-dimensional topographic seismic study Hobro *et al.* (2005) estimate an even lower mean hydrate saturation of 2% with a maximum hydrate saturation of 15%. Yuan & Edwards (2000) used EM methods to determine hydrate saturations near ODP site 889A (near IODP sites U1327 and U1328). They estimate that the hydrate saturation is 17-36% 100m above the BSR. Data from Leg 311 using the above methods indicate that the hydrate saturations vary from a few percent to a maximum of 60% of the pore space in some very localized areas. Seismic methods put the average hydrate

saturation at 2-19% across all the sites. Electrical methods estimates for the average hydrate saturations ranges from 2-11% across all of the sites. Results from the analysis in this chapter indicate that hydrate saturations on the Cascadia margin are towards the lower end of the range of reported hydrate saturations.

Chen (2006) uses the same data set as used in this thesis and estimates mean gas hydrate saturation of 5-15% at depths between 20-100m using Archie's equations. Mean hydrate saturations calculated used the Geometric Path-Length method at the same depth interval vary between 4-20% across all sites. This indicates that the Geometric Path-length method produces very similar hydrate saturations values to the Archie's equation derived values. Both sets of results indicate that hydrate saturation may be slightly lower than previously thought. Chen (2006) also derives hydrate saturations using velocity data collected from the same expedition and Helgerud's (2001) rock physics model (described in Chapter 2.3.2). Chen (2006) estimates mean hydrate saturation at site U1326 between 185-240 mbsf to be 30% whereas the SCA/DEM model puts the hydrate saturation at 27% in the same depth interval. Similarly at site U1327 between 150 and 225 mbsf Chen (2006) puts the mean hydrate saturation value at 22% whereas the SCA/DEM method estimates a mean hydrate saturation of 14%. The hydrate saturations calculated using the adapted SCA/DEM model are slightly lower than the Chen (2006) derived values.

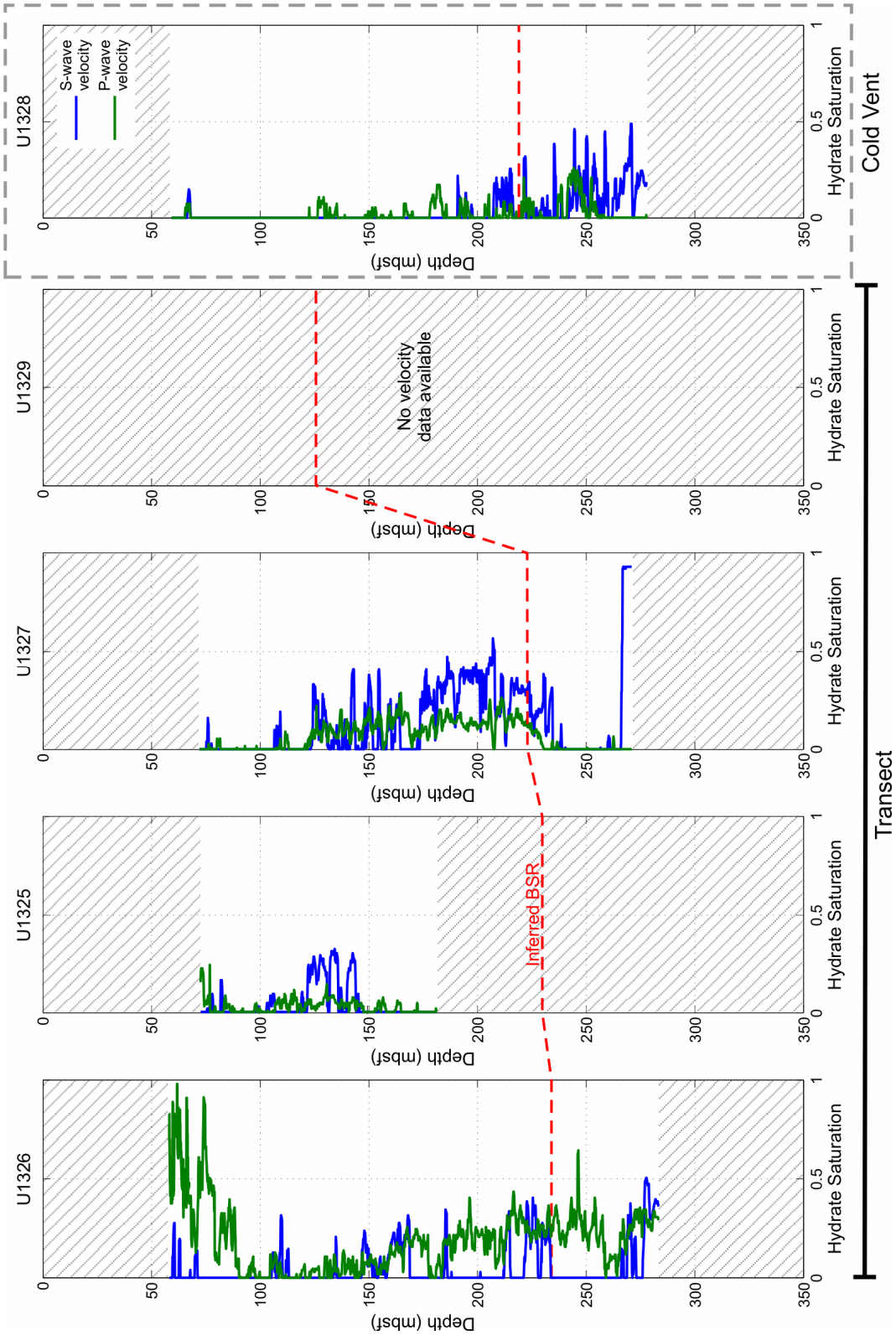

Figure 7.14. Gas hydrate saturations calculated from the P- and S-wave velocity logs at sites U1325, U1326, U1327 and U1328. The gas hydrate saturations are calculated assuming that the hydrate is non-load bearing. Dashed areas in the plots represent depths where no velocity data was collected.

7.4.2 Hydrate saturation at the cold vent site (U1328)

For completeness data from site U1328 were also analyzed. Site U1328 was drilled at a cold vent off the transect line. It has been identified as a cold vent by vertical seismic blanking and is associated with near-surface faults (Riedel, 2001; Wood *et al.,* 2000). The area has also been extensively cored (Novosel *et al.,* 2002; 2005). These cores sampled massive gas charged hydrates. However due to the stiff hydrate preventing further penetration of the sediments the thickness of the massive hydrate cap could not be established (Novosel *et al.,* 2005). This area has also been the subject of EM studies which indicate high resistivities at the vent site (Yuan & Edwards *et al.,* 2000; Schwalenberg *et al.,* 2005). As a result gas hydrate was expected to be concentrated in the top few metres as a cap over the sediments. Hydrate saturation calculated here from the resistivity LWD log is approximately 40% at the surface and decreases with depth until it disappears completely by 50m below the sea floor (Figure 7.12). Two smaller zones where hydrate is present are located at 68 and 94m. Hydrate saturation here is less than 10%. Comparing the wireline resistivity derived hydrates saturations (Figure 7.13) to those from the LWD shows a similar overall pattern. The wire line log misses the top 55m of the sediment column which is why the high hydrate saturations are not observed on the wireline log. Both the wireline and the LWD logs show small hydrate layers at different depths throughout the log. This is probably due to the heterogeneity of the area. The velocity data (Figure 7.14) indicates that there is very little hydrate along the entire length of the log. However the velocity log also misses the top 55m of the sediment column.

7.5 Joint interpretation of wireline logging data.

If the resistivity and the velocity derived hydrate saturations are compared to each other, it can be seen that they do not always match. While the lateral discontinuity of the hydrate may explain this difference between different boreholes it does not explain differences within the same borehole. The best example of this is seen in Site U1326, 130 m below the sea floor and deeper, where the hydrate saturations calculated from the velocity wireline logging data are much higher than the resistivity derived values. The joint interpretation method, developed and tested in Chapter 6, may help to explain why this occurs.

To utilize the joint interpretation method the velocity and resistivity measurement must be located in the same area. Because of the heterogeneity of the sediment between different boreholes, as discussed earlier, only the wireline logging measurements were

analyzed using the joint interpretation method. Wireline resistivity and wireline velocity were measured at the same borehole where as the LWD measurements were obtained from a different borehole. The same physical properties of the effective medium components are used for the joint interpretation as were used in the separate velocity and resistivity analyses.

Figure 7.15 shows an example of the joint interpretation method for a single set of co-located velocity and resistivity data points from site U1326 at 285 m depth. At this depth the gas hydrate saturation predictions from the individual velocity and resistivity models are completely different (Figure 7.12, Figure 7.13, Figure 7.14). Figure 7.15 shows why this occurs. The aspect ratio at this site was set to be 0.15. At this aspect ratio the velocity model predicts a gas hydrate saturation of 0.25. The resistivity model indicates that at an aspect ratio of 0.15 no hydrate is contained in the sediments. However if the aspect ratio is permitted to vary (as is allowed in the joint interpretation method), there is an aspect ratio and hydrate saturation which satisfies both the velocity and resistivity data. In this example the hydrate saturation is slightly higher than the velocity predicted aspect ratio and much higher than the resistivity predicted values. The aspect ratio at which both the velocity and the resistivity is satisfied is much higher that the aspect ratio that was used in the individual models. Changes in effective grain aspect ratio could therefore explain the difference in the hydrate saturations predicted using the individual electrical and seismic effective medium models. Correcting for such changes enables a better estimate of the hydrate saturation to be obtained and also provides information regarding the microstructure of the sediments.

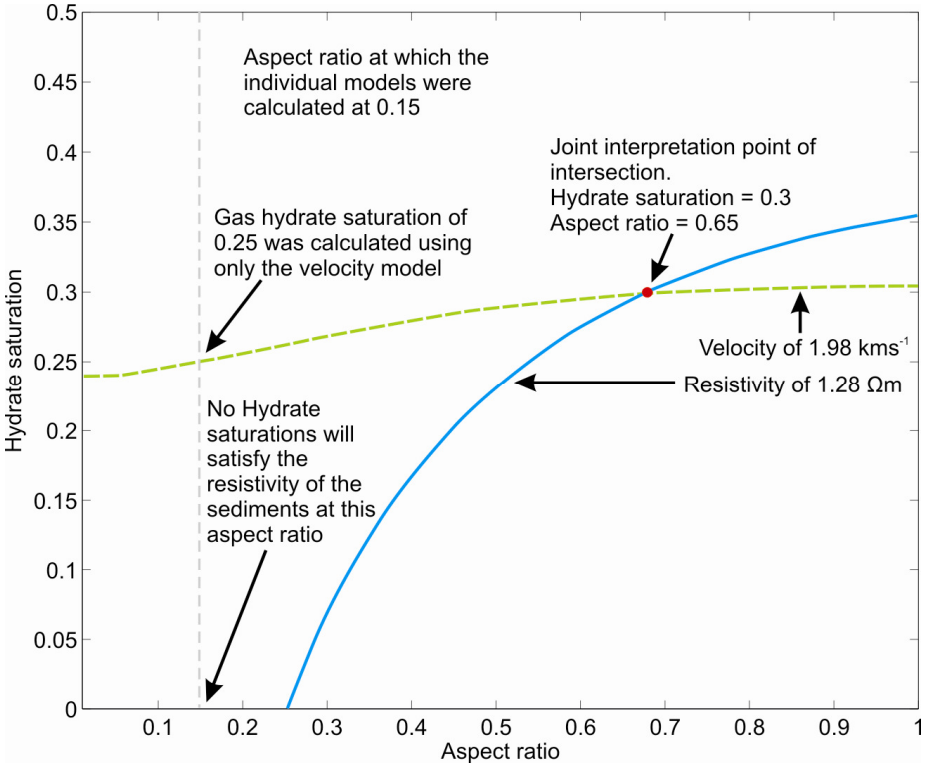

Figure 7.15. Joint interpretation of co-located velocity (1.98 kmS-^{1}, green line) and resistivity (1.28 Ωm, blue line) data from Site U1326 at 285 m below the sea floor (porosity = 0.39). Plot also shows the hydrate saturations that were calculated using only the velocity and resistivity models which give completely different results.

Figure 7.17 shows porosity, velocity and resistivity data collected at Site U1326. It also shows the hydrate saturation and aspect ratio values determined using the joint interpretation. The red markers in these plots show the values determined where the joint interpretation converges on a single value. The blue markers indicate where the resistivity and velocity do not converge on a single hydrate saturation or aspect ratio value. At these points some of the other assumptions (such as φ, φ_c, ρ_w, ρ_g, component moduli etc.) must be incorrect. The blue markers on the aspect ratio plot are positioned at an aspect ratio of zero. The joint interpretation method cannot determine the aspect ratio of the sediments when no hydrate is present. The markers are placed at zero simply to indicate where in the log the joint interpretation cannot determine an aspect ratio value and not that the aspect ratio of the grains is zero (as this is impossible). If the aspect ratios are compared to the clay content plot in Figure 7.17 it can be seen that at a depth of ~60m below the seafloor the clay content drops to almost zero as the predicted aspect ratio increases to almost one. Clays have low aspect ratios whereas sands and silts tend to have higher aspect ratios. This indicates that the joint interpretation method may be picking out a thick sand and silt layer

within the clays. Unfortunately at the only other place where the predicted aspect ratios approach a value of one, ~290 m below the sea floor, there is no clay content information.

Hydrate saturations predicted by the joint interpretation method also appear to be higher in areas where the grain aspect ratio is high. This observation indicates that hydrates in this area preferentially form in coarse grain sediment such as sands. This matches shipboard observations where gas hydrate was mainly concentrated in sand and silt layers (Figure 7.16).

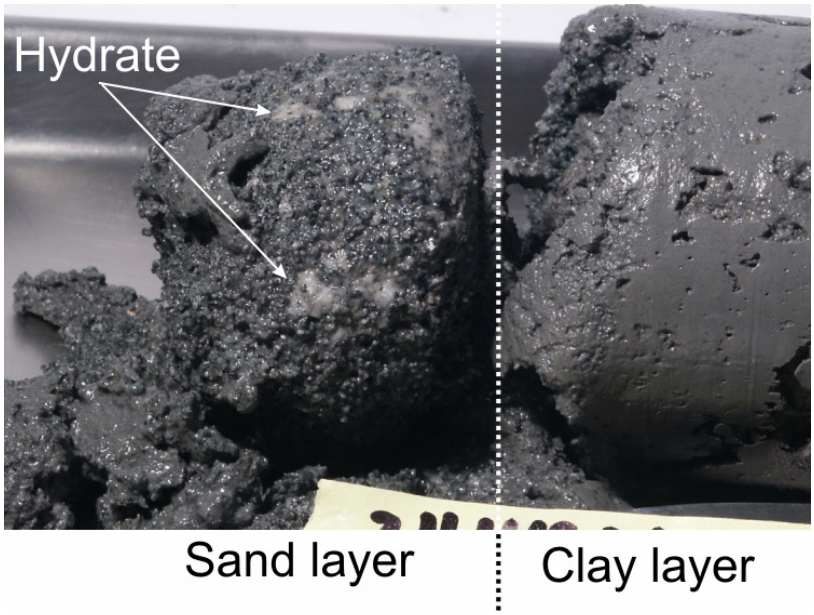

Figure 7.16 Gas hydrate bearing sand layer next to hydrate free clay layer (photo taken during Exp. 311 by expedition scientists).

Figure 7.17 to Figure 7.20 show the joint interpretation results for each of the sites, as well as the porosity, velocity and resistivity data that were used to determine them. Only one site has high gas hydrate saturations, site U1326 (Figure 7.17). At this site gas hydrate starts off high, ~90%, and then drops to zero at 100 mbsf before slowly increasing with depth to approximately 40%. This is fairly consistent with IR data collected on the core samples (Riedel *et al.*, 2006). IR images have been used to determine whether sediment cores contain hydrate before they are cut open (see Chapter 1 for explanation). The IR images show only small localized cold spots until a depth of 155 m whereupon the sediment temperature drops for the rest of the cores. Site U1325 (Figure 7.18) shows little to no hydrate present in any of the sediments measured. However there are only velocity measurements from a depth of ~70-180m. IR images from this site indicate that hydrate is

primarily located in the top 20 m. There are a few localized cold spots from 140m depth. At site U1327 (Figure 7.19) no hydrate is observed until a depth of 120m. It is then permanently present until a depth of ~230m. Mean hydrate saturation in this depth interval is ~11%. Little to no hydrate is observed in the sediments at site U1328 (Figure 7.18) from the joint interpretation. This is consistent with the IR images, however hydrate samples were retrieved from this site. IR images and LWD resistivities indicate that hydrate is predominantly present in the top 30-40m of the sediment column. This area is missed by the wireline logging. The mean hydrate saturations for all the sites are given in Table 7.4.

Aspect ratios at all the sites apart from site U1326 ranges from 0.05 to 0.3 and the mean aspect ratio is ~0.17. This is lower than at site U1326 where the mean aspect ratio was 0.24. Site U1326 also shows more variation of grain aspect ratio than the others.

	Geometric /Path- length Electrical model		**SCA/DEM Seismic model**		**Joint Interpretation**
	Resistivity LWD	**Resistivity Wireline**	***Vp* Wireline**	***Vs* Wireline**	***Vp* Wireline**
Site U1325	0.02	0.04	0.02	0.02	0.03
Site U1326	0.09	0.07	0.19	0.06	0.14
Site U1327	0.06	0.11	0.07	0.11	0.05
Site U1328	0.06	0.06	0.03	0.07	0.03
Site U1329	0.06	-	-	-	-

Table 7.4. Mean gas hydrate saturations throughout the logged sedimentary columns at each of the sites. Gas hydrate saturations were calculated from the logging data using the Geometric Path-Length Effective Resistivity model, the SCA/DEM model and the joint interpretation method. It should be noted that the length of the logs were often different at the same site.

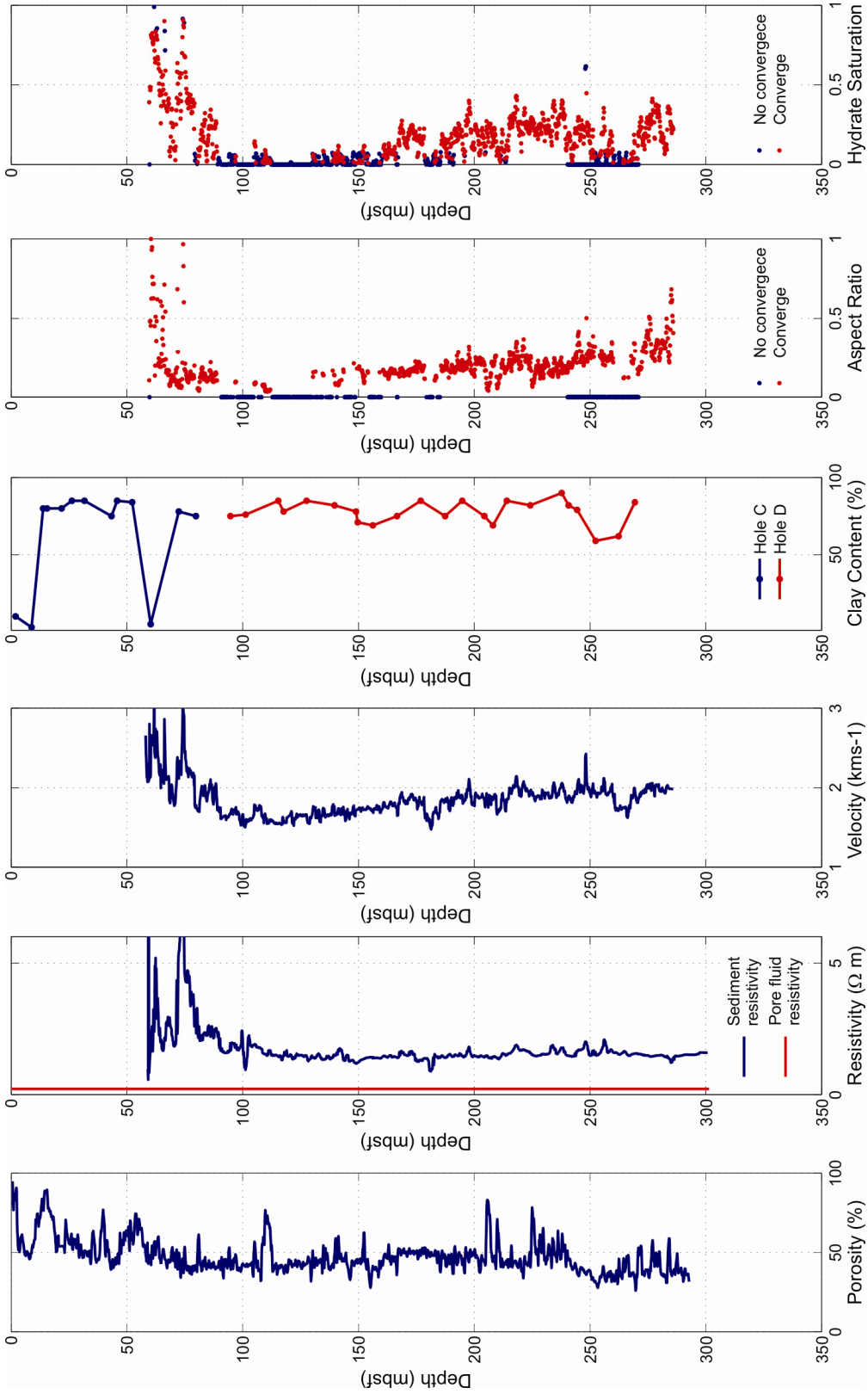

Figure 7.17. Porosity, velocity and resistivity logs from site U1326. Clay content with depth obtained from the sediment core at site U1326. Aspect ratio and gas hydrate saturations predicted using the joint interpretation method. Red dots indicate that the joint interpretation method was able to converge on a single value of hydrate saturations and aspect ratio.

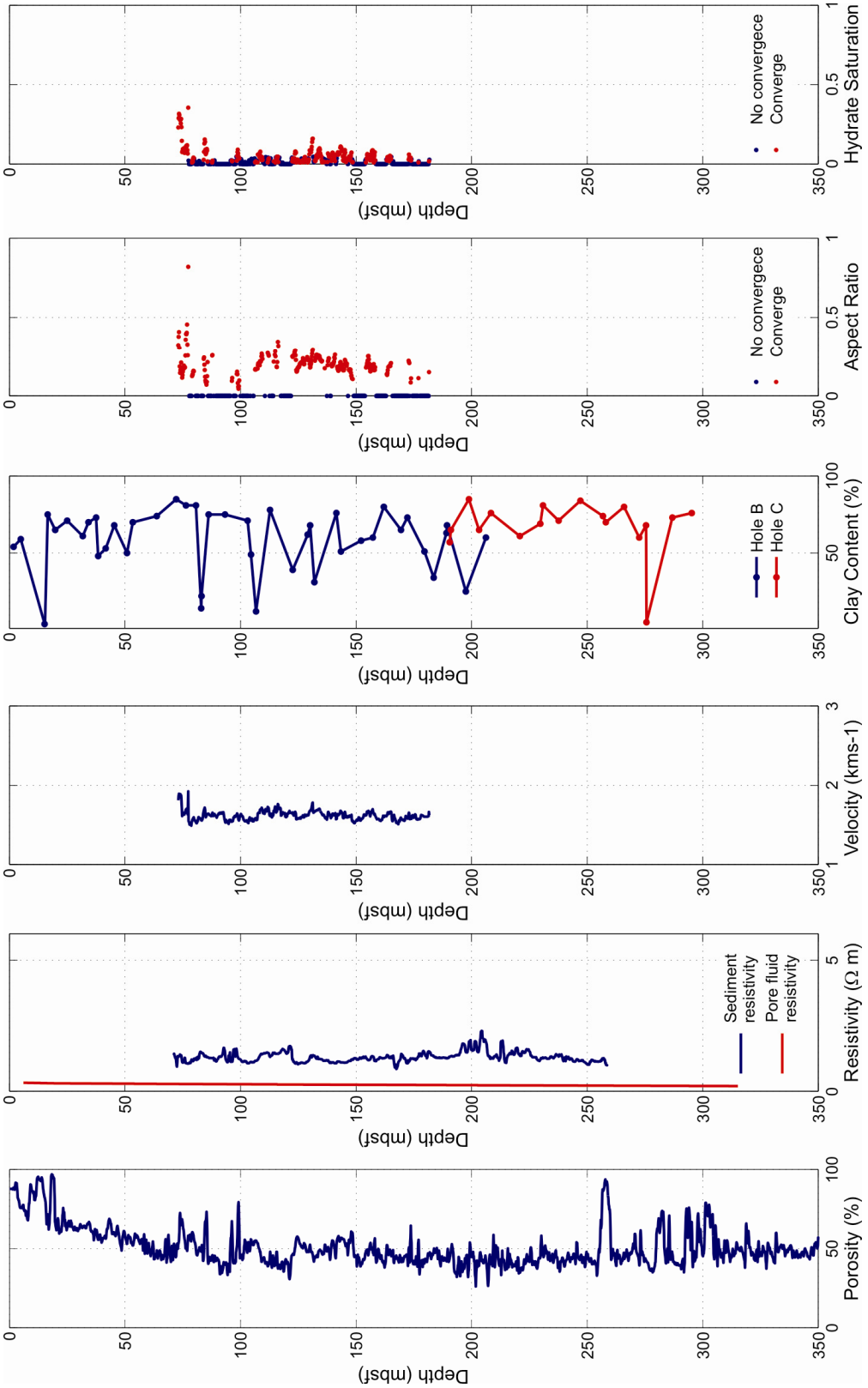

Figure 7.18. Porosity, velocity and resistivity logs from site U1325. Clay content with depth obtained from the sediment core at site U1325. Aspect ratio and gas hydrate saturations predicted using the joint interpretation method. Red dots indicate that the joint interpretation method was able to converge on a single value of hydrate saturations and aspect ratio.

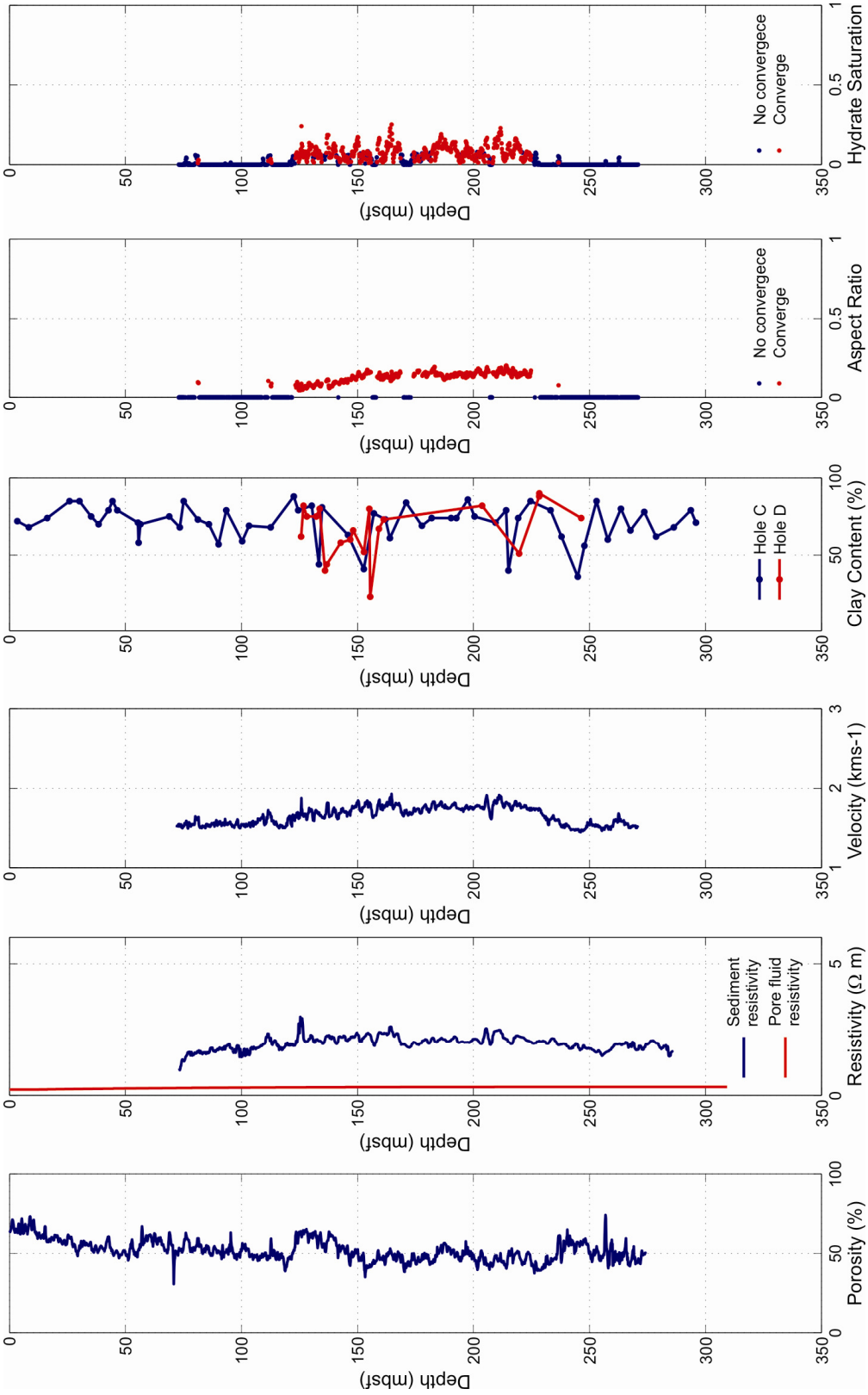

Figure 7.19. Porosity, velocity and resistivity logs from site U1327. Clay content with depth obtained from the sediment core at site U1325. Aspect ratio and gas hydrate saturations predicted using the joint interpretation method. Red dots indicate that the joint interpretation method was able to converge on a single value of hydrate saturations and aspect ratio.

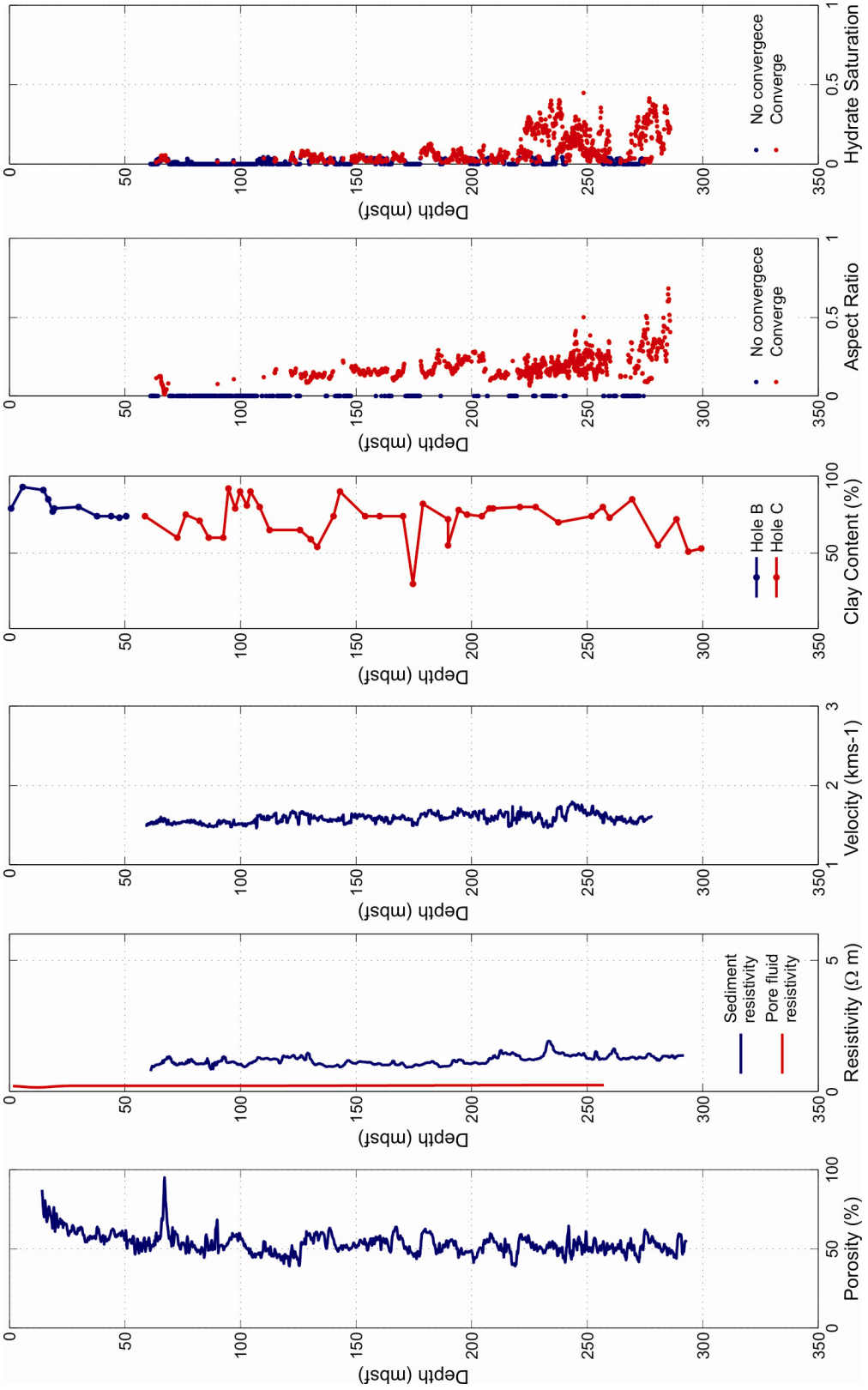

Figure 7.20. Porosity, velocity and resistivity logs from site U1328. Clay content with depth obtained from the sediment core at site U1325. Aspect ratio and gas hydrate saturations predicted using the joint interpretation method. Red dots indicate that the joint interpretation method was able to converge on a single value of hydrate saturations and aspect ratio.

7.6 Conclusion

The Geometric Path-Length Effective Resistivity and the SCA/DEM effective medium models developed in Chapters 3 and 4 were used to determine gas hydrate saturations in the sediments from measurements collected during Expedition 311. The seismic velocity and electrical resistivity models produced similar results for all but one of the sites. At site U1326 the gas hydrate saturations determined from the velocity were higher than those determined from the resistivity. The joint interpretation method was able to determine a possible reason why this occurs. The joint interpretation indicates that the aspect ratio that was used in the individual resistivity and velocity models was too low, and higher aspect ratios needed to be used. The actual aspect ratio of the sediments is unknown and therefore must be estimated when using the individual electrical and seismic effective medium models. The aspect ratio was determined initially using the LWD resistivity logs by choosing an aspect ratio which would predict a hydrate saturation of zero in sediments believed to contain no hydrate. The joint interpretation method allows this problem to be removed.

Non-load bearing gas hydrate is present at each of the sites. Apart from site U1325 the hydrate does not appear to be concentrated just above the BSR as suggested by Hyndman & Davis (1992). At all the sites the hydrate appears to be present in sediments below the inferred BSR. However this may be due to incorrect velocities being used to calculate the BSR depth. Gas hydrate saturation was low (2-9%) at all sites apart from Site U1326 where a mean gas hydrate saturation of 14% was calculated. Aspect ratio predictions determined using the joint interpretation method were approximately 0.17 apart from at site U1328 where higher aspect ratios were observed. Hydrate calculations for the cold vent site were similar to those determined by Riedel *et al.,* (2005) although peak hydrate saturation in the very top sediments were calculated to be approximately 80%.

A number of assumptions and compromises had to be made to determine the gas hydrate saturations. Assumptions had to be made about the physical properties of the sediments. The sediments were assumed to be composed predominantly of clay and are assumed to be the same along the entire length of the log. The electrical and seismic physical properties of clay are not well constrained. The pore water resistivity was not directly measured and was determined from the pore water chorinity and downhole temperature measurements. It is also assumed that the hydrate is disseminated throughout

the pore structure, i.e. it is non-load bearing and does not block any of the pores. This is probably correct at low gas hydrate saturations but as the saturation increases may not hold true. Also hydrate nodules were retrieved during the drilling process and these are not accounted for in the models. Another problem was the porosity of the sediments. The porosities used for all the calculations were obtained from the LWD because they matched the MAD values closely. However there appears to be a large degree of heterogeneity in the sediments between holes at the same site. Therefore the porosities used may not be correct.

Chapter 8. Conclusions

This chapter starts by listing the principal achievements made during the course of this work. It then adds some more general thoughts about the work achieved and the problems encountered.

8.1 Principal Achievements

- Altering the critical porosity of the combined SCA/DEM model such that it is able to determine the seismic properties of un-cemented sediment. This altered SCA/DEM model compared well with laboratory data.
- Development of the Electrical model
    - Development of a two-phase electrical model in which no empirical constants are required, and which is compatible (i.e. has the same type of input parameters) with the seismic models used in this thesis.
    - Development of the HS conductive bound estimates to include a geometric factor which is grain size independent and allows different grain shapes to be investigated. This ability to change the grain shape is important because it allows both sands and clays to be modelled by changing the aspect ratio of the grain. It is also important because by aligning the grains with aspect ratios below 1, electrical anisotropy can be investigated.
    - Development of at set of 3-phase electrical models which allow both pore blocking hydrate and non-pore blocking hydrate morphologies to be modelled. These 3-phase models are consistent with the load bearing and non-load bearing seismic models.
- Laboratory work
    - Collection of a good two-phase experimental data set in which the individual constituents of the sediment are known and the resistivity, velocity and porosity measurements are co-located.
    - Development of a new method in which methane hydrate can be grown in sediment in the laboratory with known hydrate saturation.
    - Collection of co-located resistivity and velocity measurements on hydrate bearing sediments.

- Development of a joint seismic and electrical interpretation method for both non-hydrate and hydrate bearing sediments. This method allows two variables (porosity/hydrate saturation/aspect ratio) to be determined from the two non-unique effective medium models.
- Predictions of hydrate saturations using both the separate seismic and electrical effective medium models, as well as with the joint interpretation method.
- An explanation for hydrate saturation discrepancies between separate electrical and seismic derived values at IODP site U1326 using the joint interpretation method.
- Demonstration that the joint interpretation method can help to detect sand bodies (grains with aspect ratios of ~1) in a sediment column composed predominantly of clay (grains of aspect ratios << 1).

8.2 Effective medium models

The original aim of this work was to develop a joint seismic and electrical model to investigate hydrate bearing sediments and how they relate to geophysical field measurements. It proved not to be possible to form a general model for hydrate in sediment because of the various possible morphologies in which hydrate forms. Instead two models have been produced: one to model hydrate as a completely isolated material in the pore spaces, and one to model hydrate as part of the grain frame where it is totally interconnected. This was achieved by adapting existing seismic velocity effective medium models and developing compatible electrical effective medium models. In essence, the new models are end members and give either maximum or minimum velocity or resistivity for a given hydrate saturation. There is no general consensus on the morphology of hydrate in sediments although it probably depends on the conditions under which the hydrate forms. Therefore it cannot currently be predicted which model should be used for a specific sediment example. Comparisons between the model predictions and both experimental and geophysical logging data indicate that hydrate forms in the pore space, but hydrate saturation in these sediments was generally low. As hydrate saturation increases, at some point the hydrate will start to become load bearing either when the pore spaces are completely filled with hydrate or at lower hydrate saturation if isolated pore fluid drops are formed. Therefore an intermediate model between the two end members would be desirable but difficult without a detailed investigation of hydrate morphology and growth which is outside of the scope of this thesis. Such a development has already been started

for seismic models (Chand *et al*., 2006) but not for electrical models. Anisotropy due to grain shape can also be accounted for using both the seismic and the electrical models. Such an effect can often be important for analysing continental margin sediments.

In order to apply either the seismic velocity model or the electrical resistivity model some knowledge about the properties of the sediment to be modelled is required. Porosity has a very significant effect on both the resistivity and the seismic velocity of a sediment and must be known in order to determine the hydrate saturation. The mineralogical composition of a sediment also needs to be known in order to model the sediments although its effect on the electrical modelling is not as profound as it is for seismic velocity. This is because the current dominantly travels through the pore fluids, so the resistivity of the grains makes only a small contribution the effective resistivity. It follows that the resistivity of the pore fluid is very important when modelling the effective resistivity of a sediment. Trying to determine hydrate saturation in sediment without knowing some or any of these properties would lead to large uncertainties in the result.

Neither the electrical nor the seismic models account for the effects of pressure or cementation of the sediment grains (excluding hydrate cementation). While cementation will probably not have a large effect on the electrical resistivity of a sediment unless its presence causes pores to become isolated, it would have a significant effect on the seismic velocities by stiffening the sediment and therefore increasing the effective moduli. The effect of grain cementation could be accounted for by treating the cement in a similar manner as the hydrate in the load bearing model where hydrate is effectively a cement. In this thesis cementation is effectively accounted for by altering the critical porosity of the effective medium.

8.3 Validation of the individual electrical and seismic effective medium models

Both the hydrate bearing and the non-hydrate bearing models were validated using laboratory data. For the non hydrate bearing (two-phase) models the individual resistivity and seismic velocity model predictions compare closely with laboratory data. The comparison between the hydrate bearing (three-phase) laboratory measurements and the three-phase effective medium models proved complicated for two principal reasons: (1) The hydrate in the laboratory samples was not evenly distributed and therefore it was not known whether the velocity was constant along the path travelled by the acoustic pulse used to measure velocity, leading to a possible inaccuracy in the results. The uneven

distribution also meant that a large range of resistivities was measured from each sample depending on where in the sample the measurements took place. This result leads to the problem of which electrical resistivity measurement of the large range recorded to test the model with or whether to use a mean resistivity. In the end the median resistivity value was used because the mean resistivity was skewed by very high resistivity outlier measurements. (2) The pressure rig in which the hydrates were formed required solid sediment samples while the modified seismic effective medium model is designed for unconsolidated sediment. Therefore the three-phase seismic laboratory measurements were tested using the original effective medium model developed by Jakobsen *et al.* (2000) although useful results were still obtained. The cementation of the grains does not affect the path length of an electrical current through the sample and the geometric path-length model could be tested using the laboratory data set. The problem of uneven hydrate distribution was partially solved by using tighter sediment samples in which the grains are smaller and therefore so are the pore spaces. This results in higher capillary forces which allows the methane gas to more evenly distribute prior to hydrate formation. However, although an improvement was observed the hydrate was still not evenly distributed. The problem may be solved either by obtaining even tighter sediment samples, using a rig with multiple inlet ports, or by forming hydrate from dissolved gas. These technological challenges are outside the scope of this work

8.4 Joint interpretation

The electrical resistivity and the seismic velocity models developed in this thesis individually cannot uniquely calculate the porosity and aspect ratio for a two-phase system that will match a given seismic velocity or electrical resistivity measurement. For example, when trying to determine porosity from a resistivity measurement a range of values will be determined if the aspect ratio of the grains is unknown. The joint interpretation is achieved by independently calculating all the possible values for the two variables that match the measured resistivity and velocity; the final variable values are those that satisfy both the measured resistivity and the velocity values. The three-phase joint interpretation method, while identical to the two-phase method, does require one parameter to be assumed. One of the three variables (aspect ratio, porosity or hydrate saturation) must be fixed as the joint interpretation method can only solve for two. By developing a joint interpretation method

we are able to improve estimates of porosity, sediment microstructure and/or gas hydrate saturation from co-located resistivity and velocity data points.

The joint method was tested using two-phase and three-phase experimental data and logging measurements from the Cascadia margin. Using two-phase data the joint method improved the estimates of porosity and grain aspect ratio. The joint method did require good information regarding the sediment composition and the pore fluid resistivity, although these parameters did not need to be known any better than for any other method or model attempting to determine porosity and/or grain aspect ratios from resistivity and velocity data. When using the three-phase version of the joint interpretation method for sediments on the Cascadia margin, it was decided that the porosity was the variable to be fixed because this value was available from another source (i.e. a porosity well log). Complications arose when attempting to validate the joint interpretation method with the three-phase experimental data. These problems were the same as those faced when validating the individual models, i.e. the uneven distribution of hydrate and cemented grains. However, using the same solutions as employed during the individual model validation, the joint method was able to determine porosity, hydrate saturation and/or grain aspect ratio.

A significant advantage of using laboratory data rather than field geophysical data is the co-location of resistivity and seismic velocity measurements. The joint interpretation method makes the fundamental assumption that seismic velocity and resistivity are measured through the same volume of sediment. This situation is far easier to control in the laboratory environment than in the field. When the joint interpretation was applied to logging data from the Cascadia margin it could only be applied to velocity and resistivity data measured in the same borehole (wireline resistivity and velocity) despite possibly better quality resistivity data (LWD resistivity) being available in another borehole at the same site. The LWD data were used successfully with the Geometric Path-Length Effective resistivity model and an assumed grain aspect ratio. If the intention is to use the joint interpretation method to interpret other data sets, great care must be taken to ensure that the velocity and resistivity data are co-located, especially in areas when there is rapid change in lithology, gas hydrate saturation and pore fluid properties through the sediment column.

8.5 Gas hydrate saturations on the Cascadia margin

The aim of the Cascadia margin case study was not just to test the effective medium models and the joint interpretation method, but also to determine gas hydrate saturations on this margin. In order to apply the models, assumptions had to be made about the composition of the sediments, physical properties of the individual components in the sediment, and the aspect ratio of the grains. These assumptions were guided by lithology, physical property, and chemical measurements made during IODP Expedition 311. The model results for hydrate saturation calculated from the logged velocity and resistivity were generally similar to the values calculated from Archie's equations (Riedel *et al.,* 2006) using the resistivity data alone. There was however a major discrepancy between the gas hydrate saturations derived from velocity and resistivity at one drill site (U1326). When the joint interpretation method was applied to this site, by allowing both the gas hydrate saturation and the aspect ratio of the sediment to vary it was established that the aspect ratio of the grains may be higher than at the other sites. This difference could not have been determined using Archie's equation and shows a significant advantage of the joint method. In general the hydrate saturations determined using the methods developed in this thesis tend toward the lower end of estimates reported in the literature in this geographical area. The hydrate saturation results produced in this thesis are probably a better indication of the hydrate saturations in the Cascadia sediments due to a variety of reasons: (1) Because the sediments were cored, the sediment mineralogy and the pore fluid chemistry are established at each site without the need to make any assumptions. (2) Most of the previous studies in this area use remote sensing methods to determine velocity and resistivity, thus providing poorer data than direct measurements. Another problem with determining hydrate saturation from remote sensing methods is that porosity, one of the major controls on resistivity and velocity in sediment, is not directly measured and must either be estimated or extrapolated from a nearby borehole or outcrop leading to increased error. (3) All previous surveys have determined hydrate saturation from velocity and resistivity data separately, while in this work the hydrate saturation is jointly interpreted from velocity and resistivity data. More information is therefore available regarding the sediments and, although this information makes the data more complicated to interpret, the results are better constrained.

Appendix A

Seismic properties table

Mineral	Bulk Modulus (GPa)	Shear Modulus (GPa)	Density (gcm^{-3})	C11	C33	C44	C66	C13
Clay	20.9	6.85	2.58	30.0	30.0	6.85	6.85	16.3
Water	2.32	0	1	2.32	2.32	0	0	2.32
Quartz	36.6	45	2.65	96.6	96.6	45.0	45.0	6.60
Calcite	76.8	32	2.71	119	119	32.0	32.0	55.5
Feldspar	75.5	25.6	2.7	110	110	25.6	25.6	58.5
Opal	36	18	2.09	60	60	18	18	24
Hydrate	7.7	3.2	0.90	12.0	12.0	3.20	3.20	5.57
Brine	2.29	0	1.02	2.29	2.29	0	0	2.29
Glass beads (Balotini)	34.16	29.6	2.5	73.63	76.63	29.6	29.6	14.42

After Mavko *et al.* (1998) and Birch (1966)

Appendix B

Effective Medium Models

2-phase Effective medium models

Seismic

SCA at φ_c:

$$C_{sca} = \frac{\varphi_c C_f Q_f + (1-\varphi_c) C_g Q_g}{\varphi_c Q_f + (1-\varphi_c) Q_g} \tag{B.1}$$

At φ_c:

$$C_{sca} = C_{dem} \tag{B.2}$$

DEM for other other φ:

If $\varphi > \varphi_c$

$$dC_{dem} = d\beta_f (C_f - C_{dem}) Q_f - d\beta_g (C_g - C_{dem}) Q_g \tag{B.3}$$

If $\varphi < \varphi_c$

$$dC_{dem} = d\beta_g (C_g - C_{dem}) Q_g - d\beta_f (C_f - C_{dem}) Q_f \tag{B.4}$$

To calculate velocity:

$$V_p(0^\circ) = \sqrt{\frac{C_{11}}{\chi}} \tag{B.5}$$

$$V_p(90^\circ) = \sqrt{\frac{C_{33}}{\chi}} \tag{B.6}$$

$$V_s(0^\circ) = \sqrt{\frac{C_{44}}{\chi}} \tag{B.7}$$

$$V_s(90^\circ) = \sqrt{\frac{C_{11} - C_{12}}{2\chi}} \tag{B.8}$$

When the effective medium is isotropic $V_p(0^o) = V_p(90^o)$ and $V_s(0^o) = V_s(90^o)$

Electrical

$$\rho_{geo} = \left[\frac{1}{G\rho_f} + (1-\beta)\left(\frac{\rho_f G \rho_s}{\rho_f G - \rho_s} + \frac{G\beta\rho_f}{3} \right)^{-1} \right]^{-1}, \tag{B.9}$$

$$\rho_{HS,conductive} = \left[\frac{1}{\rho_f} + (1-\beta)\left(\frac{\rho_f \rho_s}{\rho_f - \rho_s} + \frac{\beta\rho_f}{3} \right)^{-1} \right]^{-1}, \tag{B.10}$$

$$F_{grain} = \frac{3l_{2ave}(1-\beta)}{4r}, \tag{B.11}$$

$$\rho_{GPL} = \left(\frac{(1-F_{grain})}{\rho_{HS,conductive}} + \frac{F_{grain}}{\rho_{geo}} \right)^{-1}. \tag{B.12}$$

G and l_{2ave} values are given in Appendix C.

3-Phase non-load bearing effective medium models

Seismic

The three-phase forward model is run using the same equations, equations B.1-B.8, as the two-phase forward model to a given porosity. The DEM method is then used to add hydrate replacing only the fluid:

If β_h>0 $$dC_{dem} = d\beta_h (C_h - C_{dem}) Q_h - d\beta_f (C_f - C_{dem}) Q_f \tag{B.13}$$

Electrical

$$\beta_m = (S_h \varphi) + (1-\varphi) \tag{B.14}$$

$$\rho_m = \frac{1}{\beta_G + \beta_H}(\beta_G \rho_G + \beta_H \rho_H) \tag{B.15}$$

$$\rho_{geo} = \left[\frac{1}{G\rho_f} + \beta_m \left(\frac{\rho_f G \rho_m}{\rho_f G - \rho_m} + \frac{G\beta\rho_f}{3} \right)^{-1} \right]^{-1}, \tag{B.16}$$

$$\rho_{HS,conductive} = \left[\frac{1}{\rho_f} + \beta_m \left(\frac{\rho_f \rho_m}{\rho_f - \rho_m} + \frac{\beta\rho_f}{3} \right)^{-1} \right]^{-1}, \tag{B.17}$$

$$F_{grain} = \frac{3l_{2ave}\beta_m}{4r}, \tag{B.18}$$

$$\rho_{GPL,non-block} = \left(\frac{(1-F_{grain})}{\rho_{HS,conductive}} + \frac{F_{grain}}{\rho_{geo}} \right)^{-1}. \tag{B.19}$$

3-Phase load bearing effective medium models

Seismic

SCA at $\beta_h = 0.6$:

$$C_{sca} = \frac{\varphi_c C_h Q_h + (1-\varphi_c) C_g Q_g}{\varphi_c Q_h + (1-\varphi_c) Q_g} \tag{B.20}$$

At $\beta_h = 0.6$:

$$C_{sca} = C_{dem} \tag{B.21}$$

DEM for other β_h:

If $\beta_h > 0.6$

$$dC_{dem} = d\beta_h (C_h - C_{dem}) Q_h - d\beta_g (C_g - C_{dem}) Q_g \tag{B.22}$$

If $\beta_h < 0.6$

$$dC_{dem} = d\beta_g (C_g - C_{dem}) Q_g - d\beta_h (C_h - C_{dem}) Q_h \tag{B.23}$$

Use DEM to add fluid replacing only the hydrate.

If $\beta_f > 0$

$$dC_{dem} = d\beta_f (C_f - C_{dem}) Q_f - d\beta_h (C_h - C_{dem}) Q_h \tag{B.24}$$

Electrical

$$\beta_{H1} = \left(\frac{\varphi S_H}{\varphi S_H + \beta_G} \right) \tag{B.25}$$

$$\rho_{geo} = \left[\frac{1}{G\rho_H} + (1-\beta_{H1}) \left(\frac{\rho_H G \rho_s}{\rho_H G - \rho_s} + \frac{G\beta_{H1}\rho_H}{3} \right)^{-1} \right]^{-1}, \tag{B.26}$$

$$\rho_{HS,conductive} = \left[\frac{1}{\rho_H} + (1-\beta_{H1}) \left(\frac{\rho_H \rho_s}{\rho_H - \rho_s} + \frac{\beta\rho_H}{3} \right)^{-1} \right]^{-1}, \tag{B.27}$$

$$F_{grain} = \frac{3 l_{2ave} (1-\beta_{H1})}{4r}, \tag{B.28}$$

$$\rho_{GPL} = \left(\frac{(1-F_{grain})}{\rho_{HS,conductive}} + \frac{F_{grain}}{\rho_{geo}} \right)^{-1}. \tag{B.29}$$

$$\rho_{GPL,block} = \left[\frac{1}{\rho_{GPL}} + \beta \left(\frac{\rho_{GPL}\rho_f}{\rho_{GPL} - \rho_f} + \frac{(1-\beta)\rho_{GPL}}{3} \right)^{-1} \right]^{-1} \tag{B.30}$$

Appendix C

Geometric factors (G) and Vertical path lengths (l_2) calculated by Equation 4.16 for different grain aspect ratios needed to calculate the Geometric Path Length effective resistivities described in Chapter 4. The Geometric factors and Vertical path lengths are all given to 3 significant figures.

Oblate grain (most resistive)

Aspect Ratio (α)	Geometric Factor (G)	Vertical length (l_2)
0.01	67.9	0.0170
0.1	6.90	0.169
0.2	3.57	0.337
0.3	2.50	0.502
0.4	1.98	0.660
0.5	1.68	0.812
0.6	1.49	0.954
0.7	1.37	1.08
0.8	1.28	1.19
0.9	1.22	1.28
1.0	1.18	1.33

Oblate grain (least resistive)

Aspect Ratio (α)	Geometric Factor (G)	Vertical length (l_2)
0.01	1.00	1.33
0.1	1.00	1.331
0.2	1.02	1.33
0.3	1.03	1.33

0.4	1.05	1.33
0.5	1.08	1.33
0.6	1.10	1.33
0.7	1.12	1.33
0.8	1.14	1.33
0.9	1.16	1.33
1.0	1.18	1.33

Prolate grain (most resistive)

Aspect Ratio (α)	Geometric Factor (G)	Vertical length (l_2)
0.01	1.27	0.0133
0.1	1.27	0.133
0.2	1.27	0.267
0.3	1.26	0.400
0.4	1.25	0.533
0.5	1.24	0.667
0.6	1.23	0.800
0.7	1.22	0.933
0.8	1.21	1.07
0.9	1.19	1.12
1.0	1.18	1.32

Prolate grain (least resistive)

Aspect Ratio (α)	Geometric Factor (G)	Vertical length (l_2)
0.01	1.00	1.33
0.1	1.00	1.33
0.2	1.01	1.33

0.3	1.024	1.33
0.4	1.04	1.33
0.5	1.05	1.33
0.6	1.07	1.33
0.7	1.10	1.33
0.8	1.126	1.33
0.9	1.15	1.33
1.0	1.18	1.33

Appendix D

Velocity and resistivity data measured in the hydrate pressure rig for Runs 1-4.

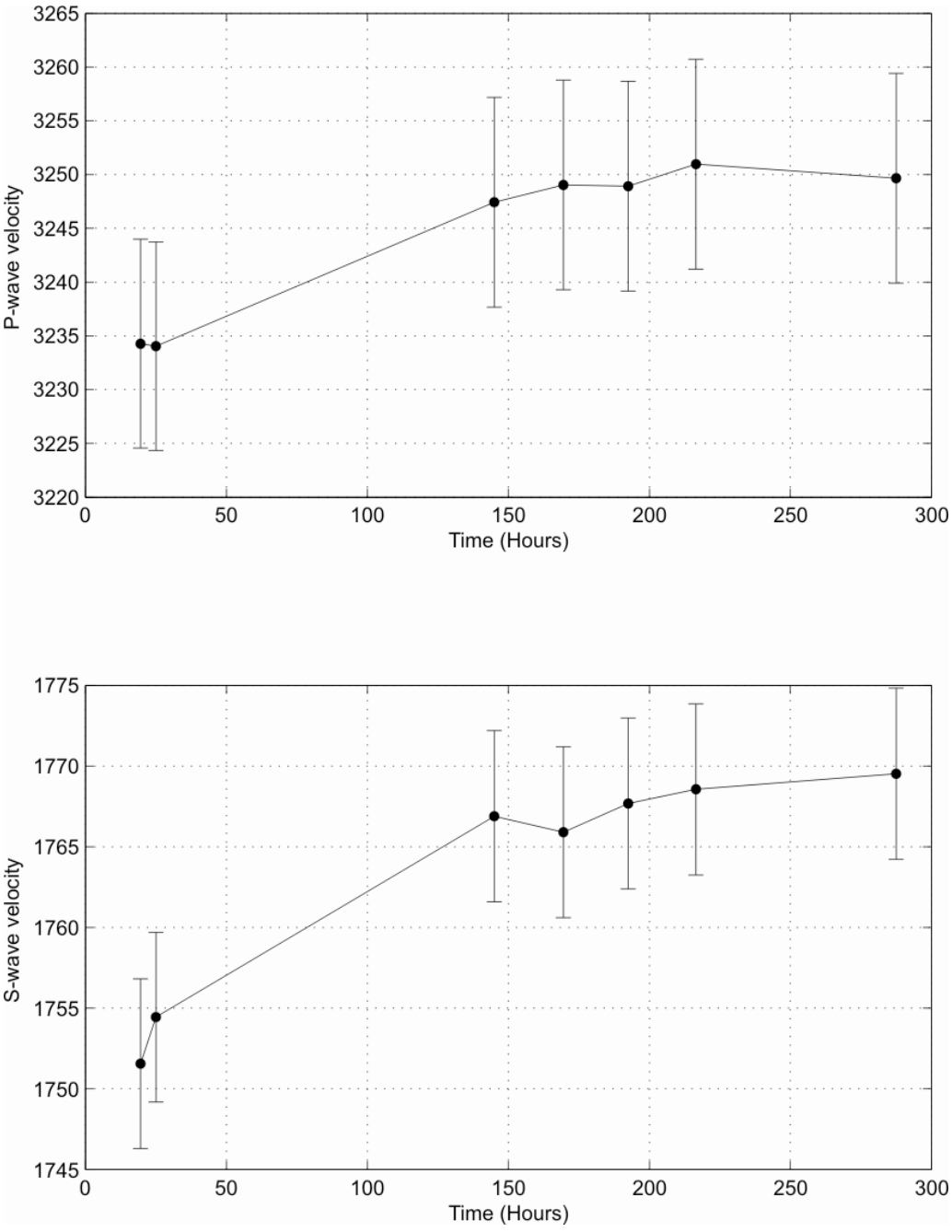

Figure D-8.1 P-wave (top) and S-wave (bottom) velocity of the glass bead sediment sample with a target hydrate saturation of 10% versus time (Run1). Velocities were recorded from the point the sample was put into the hydrate stability zone.

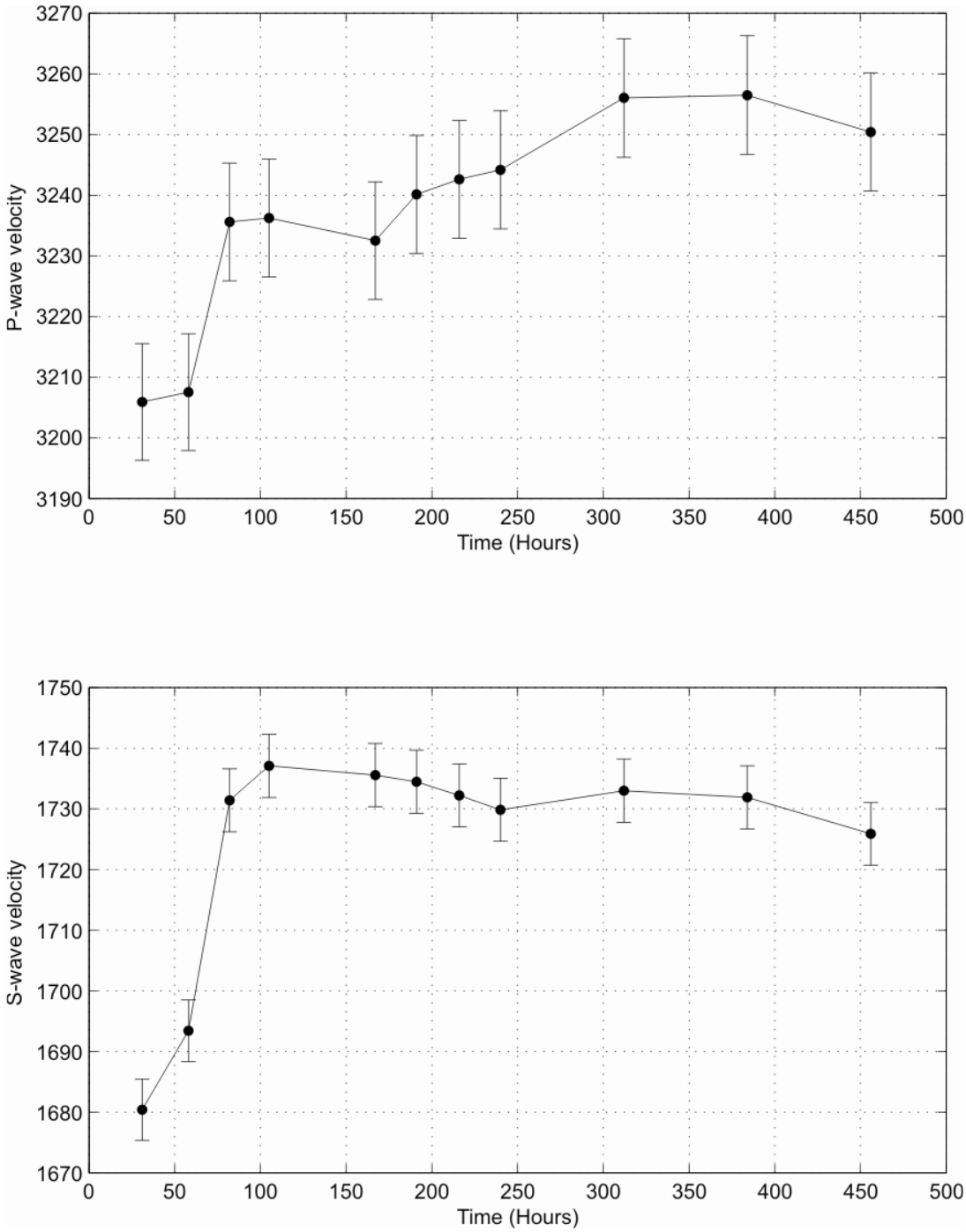

Figure D-8.2. P-wave (top) and S-wave (bottom) velocity of the glass bead sediment sample with a target hydrate saturation of 30% versus time (Run 2). Velocities were recorded from the point the sample was put into the hydrate stability zone.

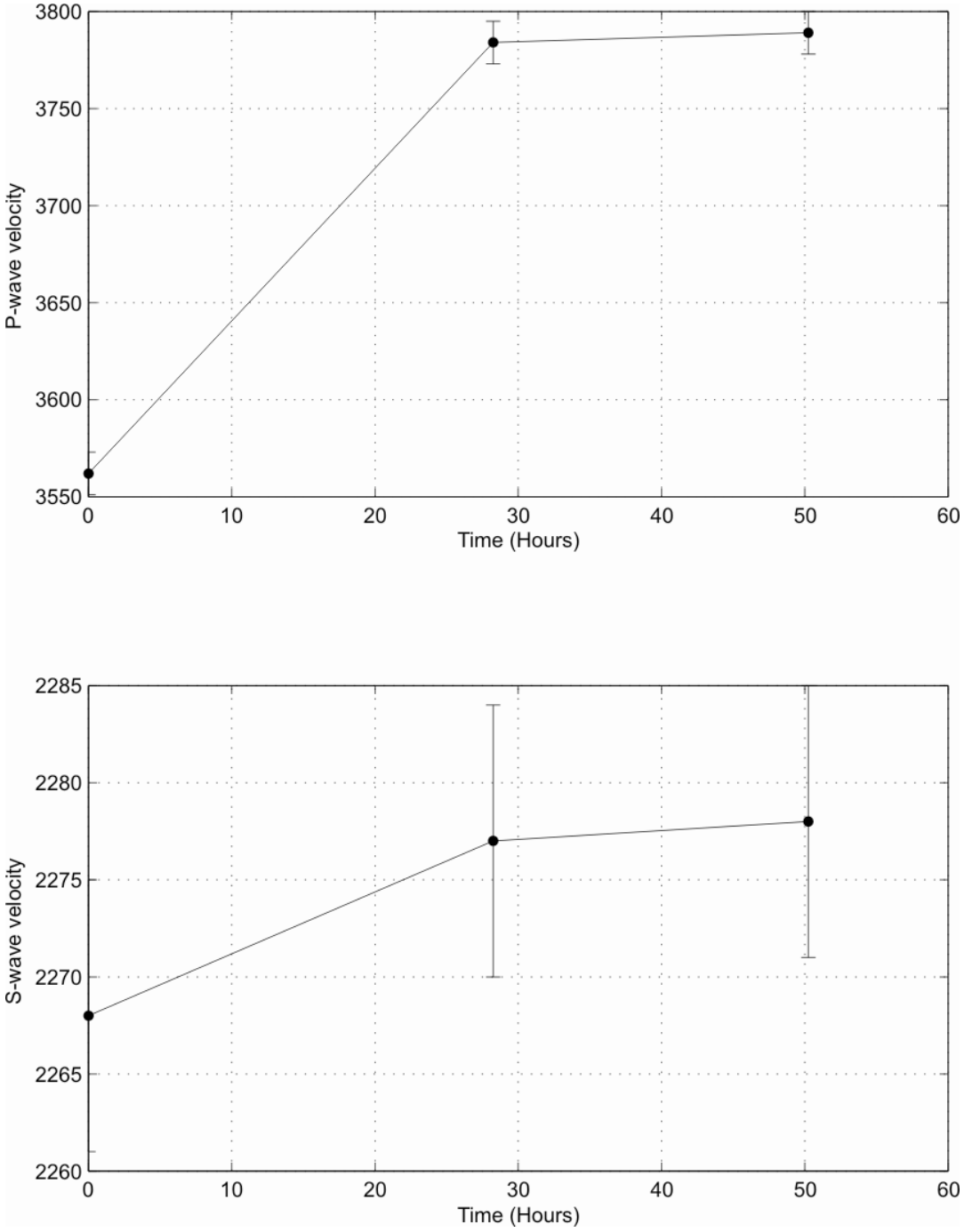

Figure D-8.3 P-wave (top) and S-wave (bottom) velocity of the Berea Sandstone sample with a target hydrate saturation of 20% versus time (Run 3). Velocities were recorded from the point the sample was put into the hydrate stability zone.

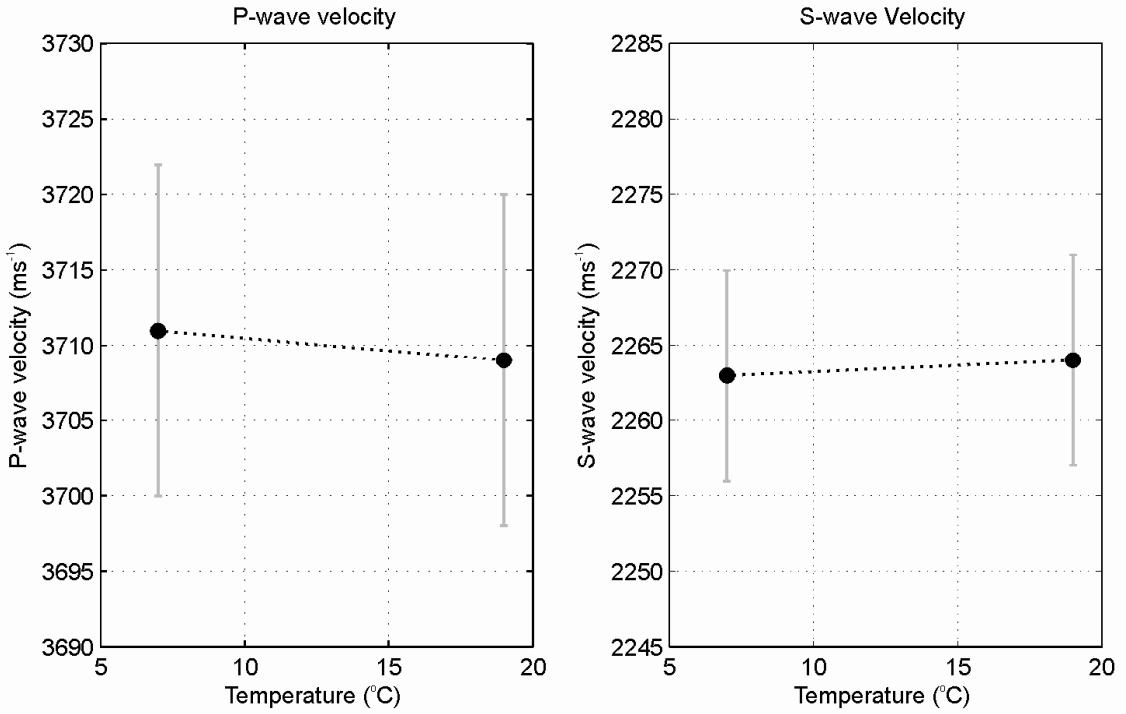

Figure D-8.4 P-wave (left) and S-wave (right) velocity of the Berea Sandstone sample with a target hydrate saturation of 0% versus time (Run 4).

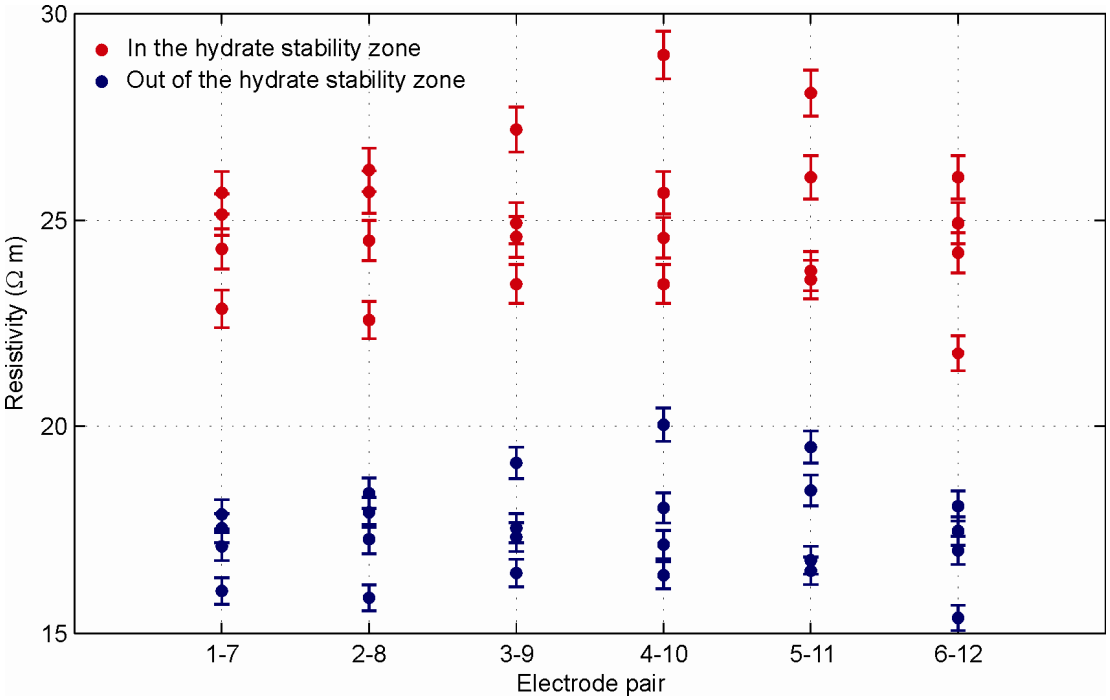

Figure D-8.5 Resistivity measured around the glass bead sediment sample before (blue) and after the sample was placed in the hydrate stability zone. The samples was 10% hydrate saturated (Run 1).

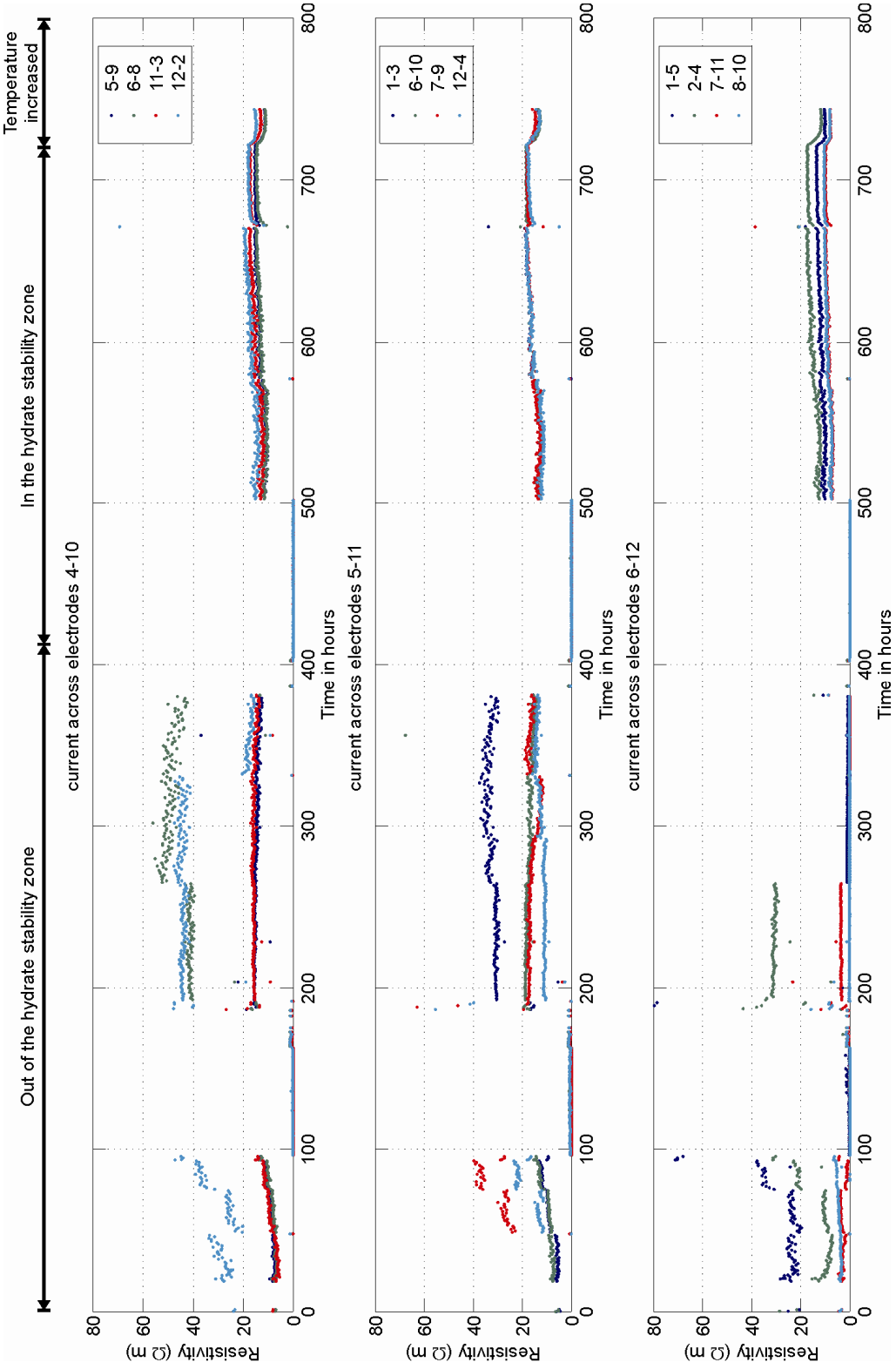

Figure D-8.6 Resistivity measurements of the glass bead sample with 30% hydrate saturation versus time (Run 2). Resistivities were recorded from the point the sample was put inside the pressure rig. Current is pass through electrodes 1-7, 2-8 and 3-9.

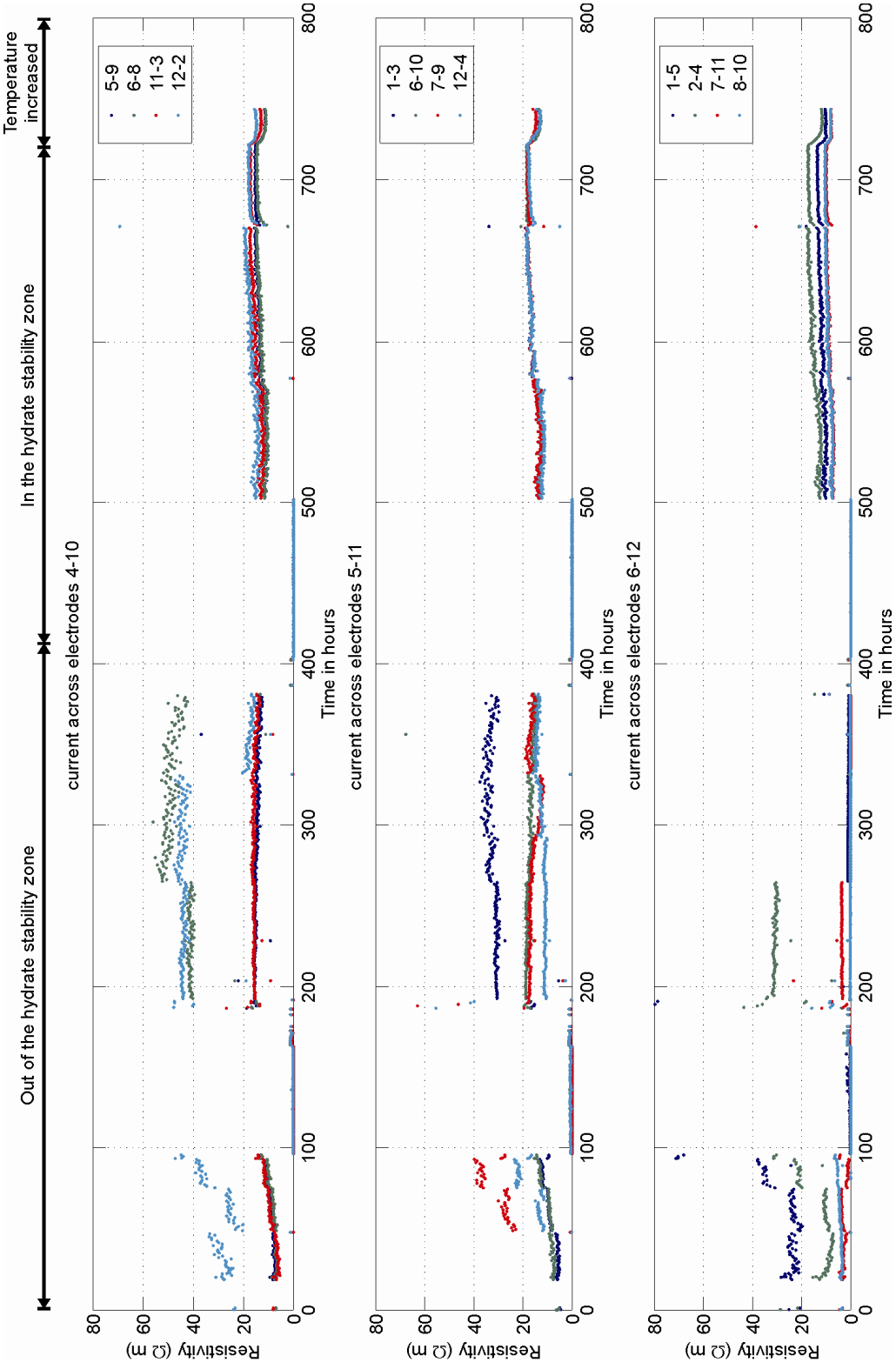

Figure D-8.7. Resistivity measurements of the glass bead sample with 30% hydrate saturation versus time (Run1). Resistivities were recorded from the point the sample was put inside the pressure rig. Current is pass through electrodes 4-10, 5-11 and 6-12.

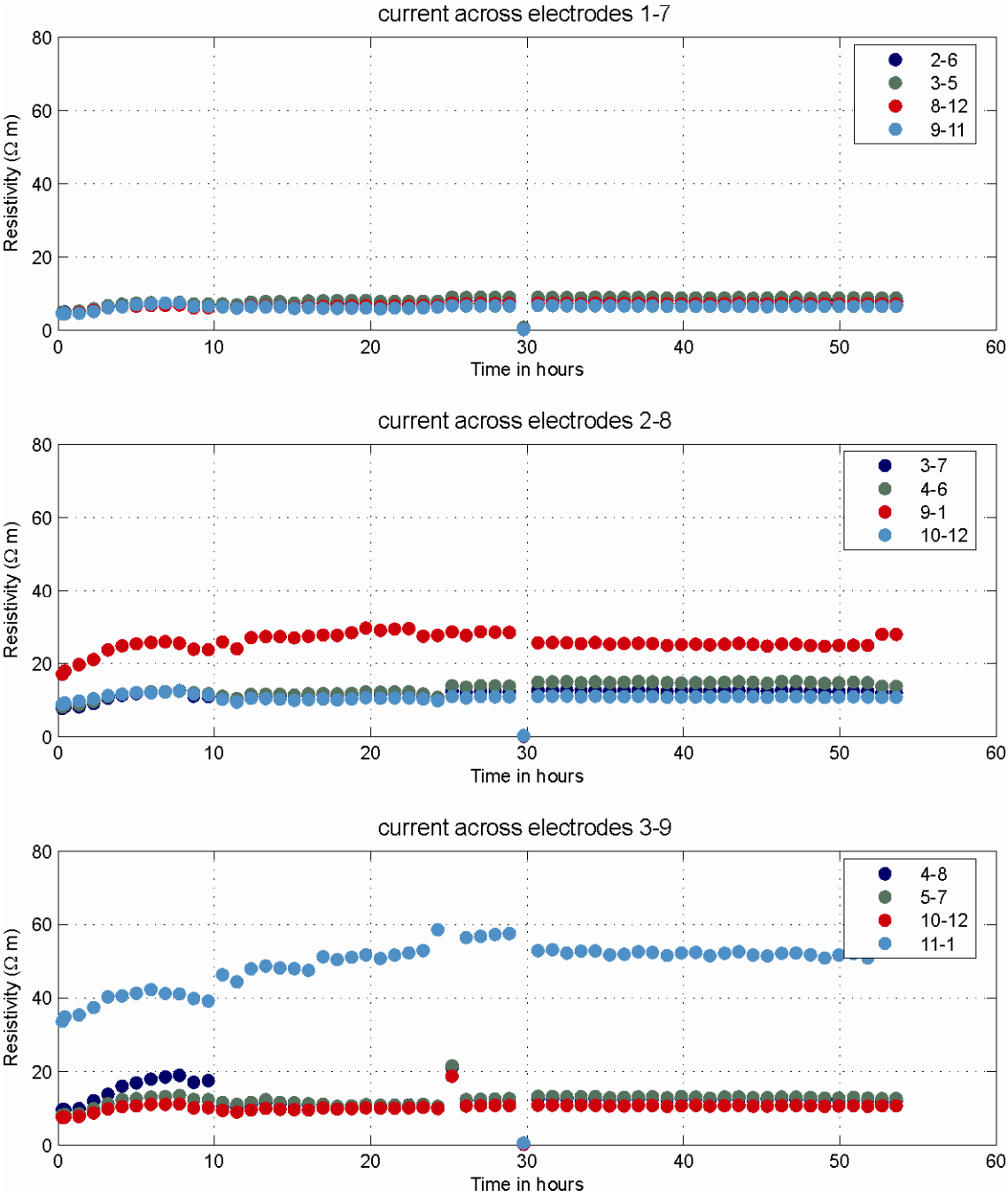

Figure D-8.8 Resistivity measurements of the Berea Sandstone sample with 20% target hydrate saturation versus time (Run 3). Resistivities were recorded from the point the sample was pushed into the hydrate stability zone. Current is pass through electrodes 1-7, 2-8 and 3-9.

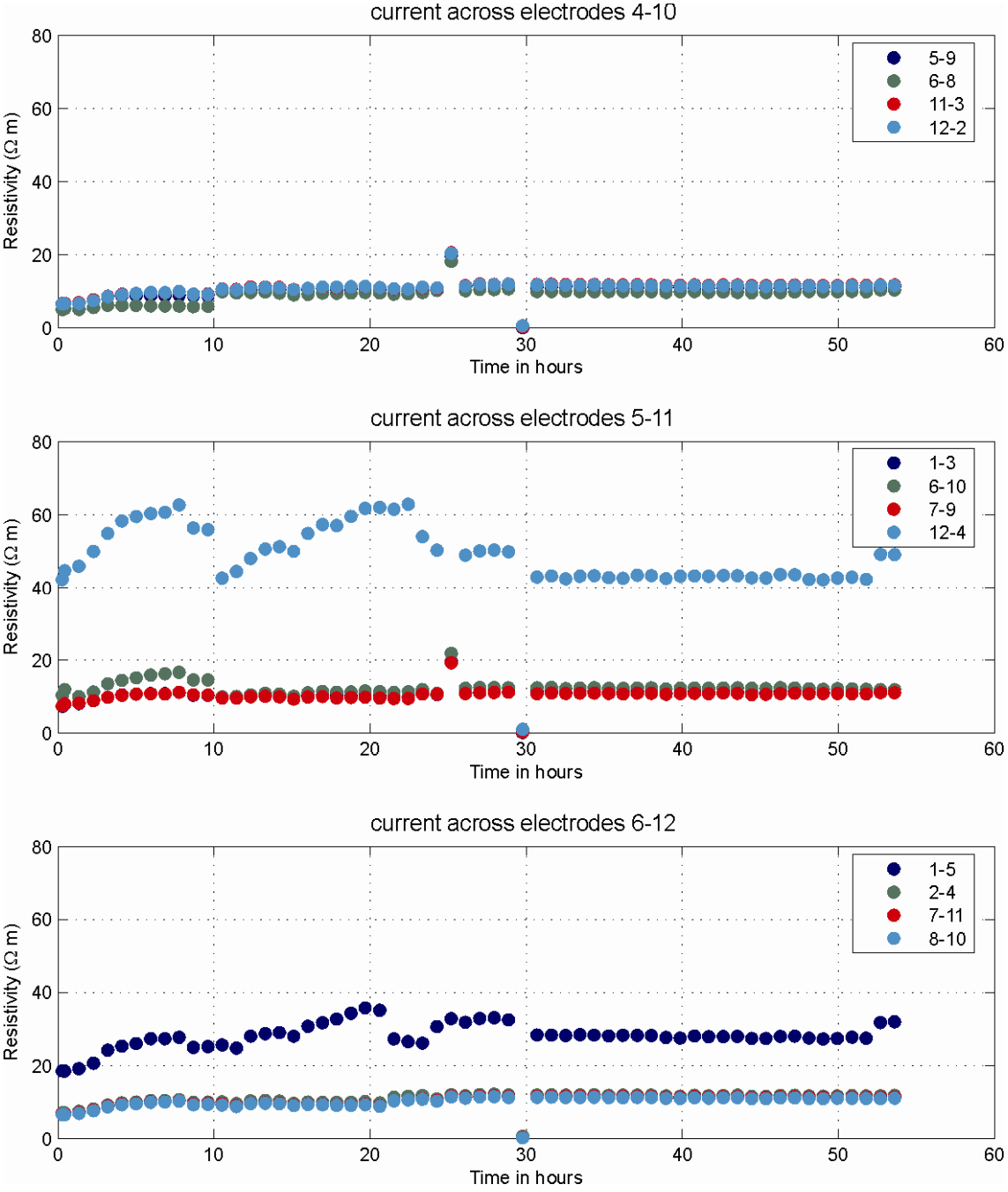

Figure D-8.9 Resistivity measurements of the Berea Sandstone sample with 20% target hydrate saturation versus time (Run 3). Resistivities were recorded from the point the sample was pushed into the hydrate stability zone. Current is pass through electrodes 4-10, 5-11 and 6-12.

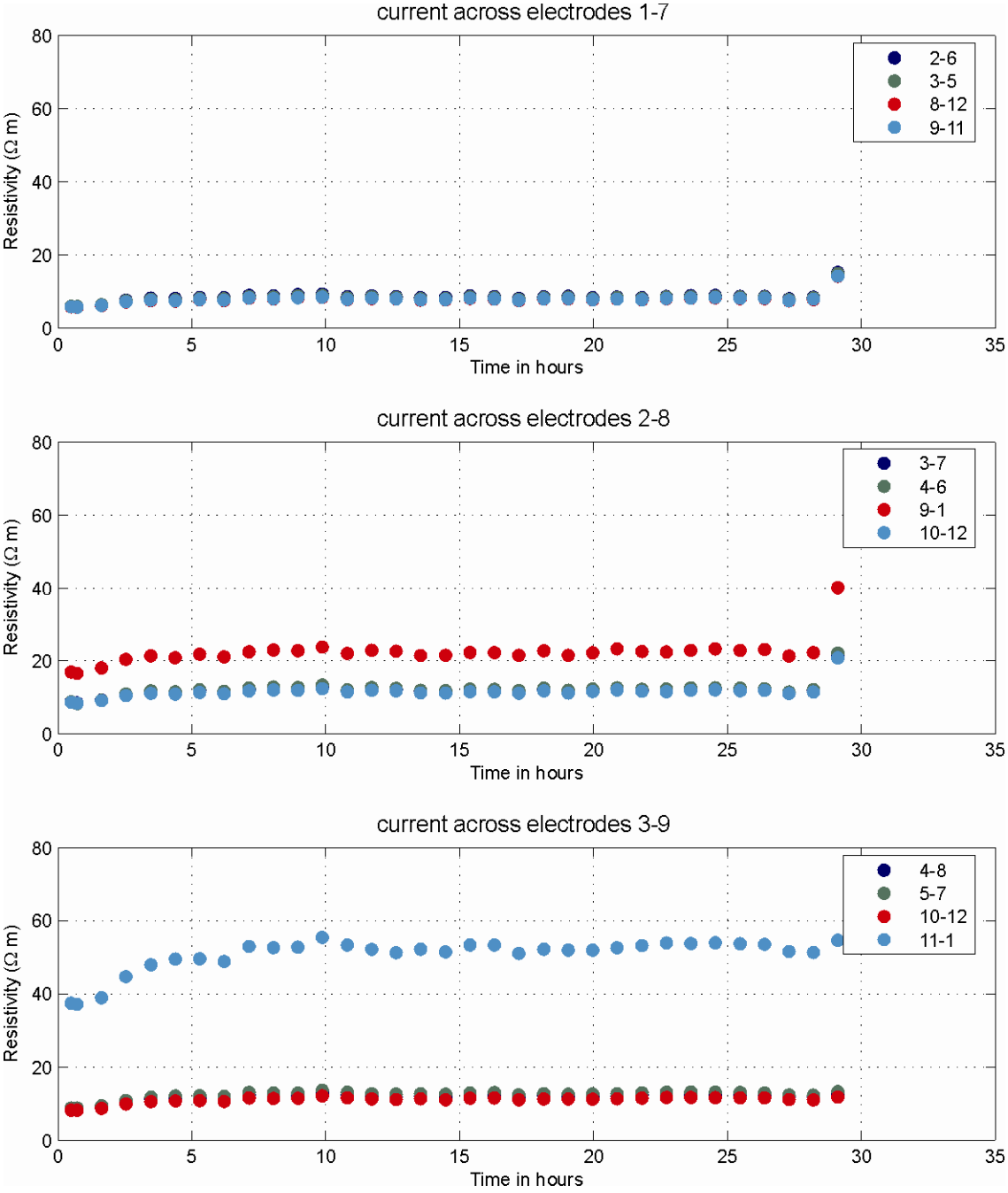

Figure D-8.10 Resistivity measurements of the Berea Sandstone sample with 0% hydrate saturation (brine saturated) versus time (Run 4). Resistivities were recorded from the point the sample was pushed into the hydrate stability zone. No hydrate forms in this sample because no methane was added to the sample. Current is pass through electrodes 1-7, 2-8 and 3-9.

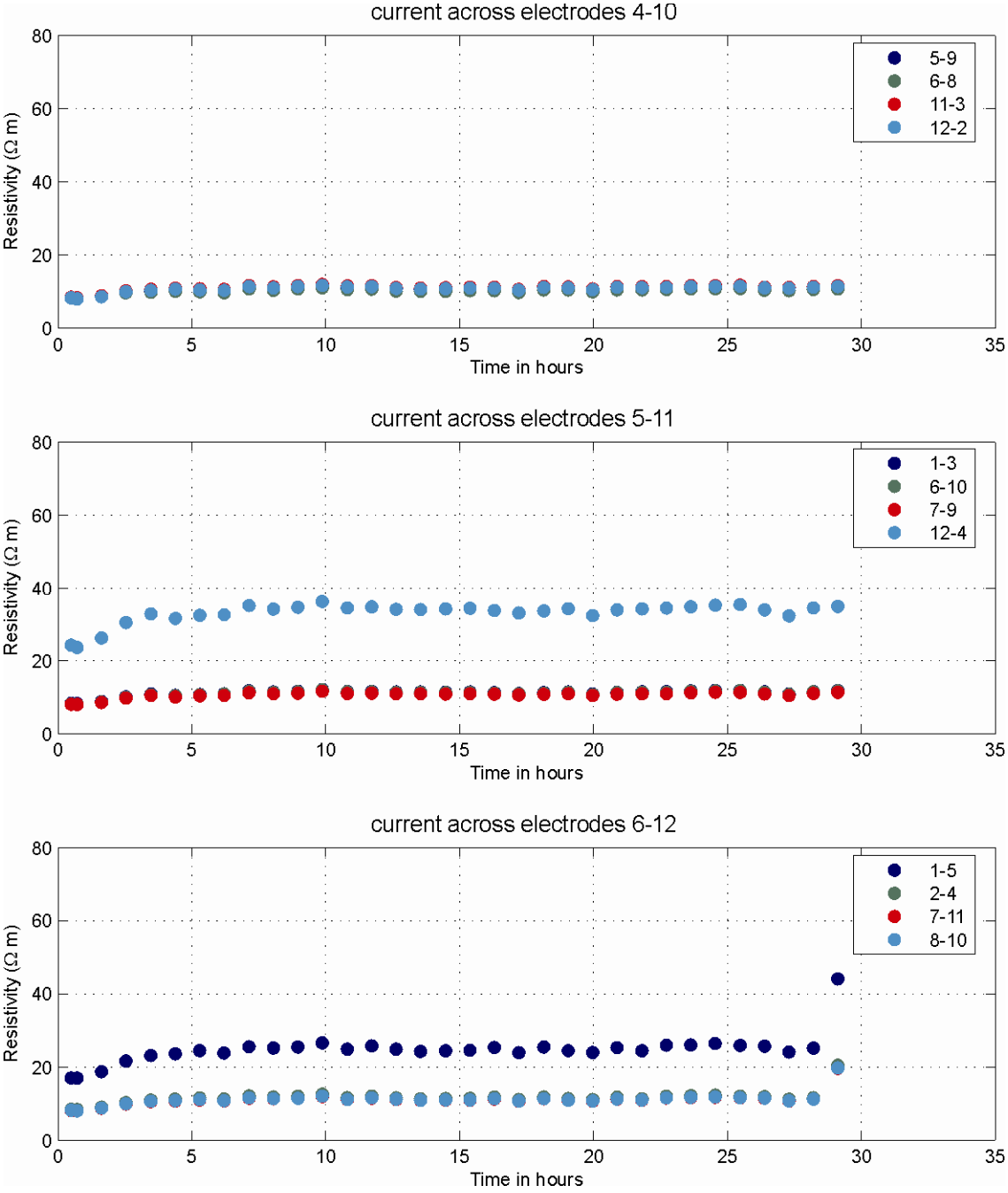

Figure D-8.11 Resistivity measurements of the Berea Sandstone sample with 0% hydrate saturation (brine saturated) versus time (Run 4). Resistivities were recorded from the point the sample was pushed into the hydrate stability zone. No hydrate forms in this sample because no methane was added to the sample. Current is pass through electrodes 4-10, 5-11 and 6-12.

Current electrodes	Voltage electrodes	Resistivity (Ωm)		
		Glass beads 30% Hydrate (Run 2)	Berea Sandstone 20% Hydrate (Run 3)	Berea Sandstone 0% Hydrate (Run 4)
1-7.	2-6.	12.62	8.20	8.57
1-7.	3-5.	17.40	8.86	8.34
1-7.	8-12.	16.17	7.24	7.92
1-7.	9-11.	9.54	6.56	7.99
2-8.	3-7.	16.75	12.44	12.01
2-8.	4-6.	17.34	14.71	12.24
2-8.	9-1.	18.16	25.35	22.34
2-8.	10-12.	16.29	10.85	11.57
3-9.	4-8.	16.91	12.42	12.24
3-9.	5-7.	16.09	12.95	12.85
3-9.	10-12.	19.20	10.64	11.40
3-9.	11-1.	23.13	52.39	52.74
4-10.	5-9.	15.14	11.07	10.92
4-10.	6-8.	14.46	9.86	10.33
4-10.	11-3.	17.17	11.67	11.23
4-10.	12-2.	17.74	11.48	10.99
5-11.	1-3.	18.28	11.09	11.42
5-11.	6-10.	16.18	12.19	11.31
5-11.	7-9.	17.93	10.80	10.92
5-11.	12-4.	17.41	43.53	34.04
6-12.	1-5.	13.44	28.20	25.10
6-12.	2-4.	17.17	11.76	11.70
6-12.	7-11.	9.93	11.35	11.18
6-12.	8-10.	10.42	11.07	11.25

Table D-1. Mean resistivity values for each electrode pair when hydrate has formed in the sample and resistivity has stabilized for runs 2-4.

References

Anstey, N.A., 1991. Velocity in thin section. *First Break*, **9**, 449–457.

Archie, G.E., 1942, The electrical resistivity log as an aid in determining some reservoir characteristics, *Transactions of the American Institute of Mining Engineers*, **146**, 54-62.

Atkins, E.R. & Smith, G.H., 1961, The significance of particle shape in formation factor porosity relationships, *Journal of Petroleum Technology*, **13**, 285-291.

Assefa, S., Sothcott, J., McCann, C., Astin, T.R., Gunn, D.A., Jones, L.D., McCann, D.M., Culshaw, M.G., Pearce, J. & Hards, V., 1998, Seismic Properties of seafloor sediments and rock: Part 1, *University of Reading*.

Bassiouni, Z., 1994, Theory, Measurement, and Interpretation of Well Logs, *Society of Petroleum Engineers, Richardson, Texas,*

Berg, C.R., 1995, A simple, effective-medium model for water saturation in porous rocks, *Geophysics*, **60**, 1070-1080.

Berge, L.I., Jacobsen, K.A., & Solstad, A. 1999, Measured acoustic wave velocities of R11 (CCL3F) hydrate samples with and without sand as a function of hydrate concentration, *Journal of Geophysical Research*, **104**, 15,415– 15,424.

Berryman, J., 1980, Long-wavelength propagation in composite elastic media I. Spherical inclusions. *Journal of the Acoustical Society of America*. **68**, 1809-1819.

Berryman, J., 1980, Long-wavelength propagation in composite elastic media II. Ellipsoidal inclusions. *Journal of the Acoustical Society of America*. **68**, 1820-1831.

Berryman, J., 1992., Single-scattering approximations for coefficients in Biot's equations of poroelasticity, *Journal of the Acoustical Society of America*., 91, 551-571.

Berryman, J., 1995, Mixture theories for rock properties, In Ahrens, T.J., (eds) A Handbook of Physical Constants, *American Geophysical Union, Washington, D.C.,* 205-228.

Best, A.I. & Gunn, D.E., 1999, Calibration of marine sediment core logger for quantitative acoustic impedance studies. *Marine Geology*. **160**, 137-146

Biot, M.A., 1956, Theory of propagation of elastic waves in a fluid-saturated porous solid I. Low-frequency range & II. Higher frequency range, *Journal of Acoustical Society of America*. **28**, 168-191.

Biot, M.A., 1962, Mechanics of deformation and acoustic propagation in porous media, *Journal of Applied Physics*, **33**, 1483-1496.

Birch, F., 1966, Compressibility; Elastic Constants, In Clark, S. P., (eds) Handbook of Physical Constants., *The Geological Society of America*.

Blangy, J.P., Strandeness, S., Moos, D., & Nur, A., 1993. Ultrasonic velocities in sandS-revisited, *Geophysics,* **58**, 344–356.

Brooks, J.M., Kennicutt, M.C., III, Fay, R.R., Mcdonald, T.J. & Sassen, R. 1984. Thermogenic gas hydrates in the Gulf of Mexico, *Science,* **225** 409-411.

Bruggeman, D.A.G., 1935, Berechnung verschiedener physikalischer konstanten von heterogenen Substanzen, *Ann. Physik*, **24**, 636-664.

Budiansky, B. & O'Connell, R.J., 1976, Elastic moduli of a cracked solid, *International Journal of Solid Structures*., **12**, 81-97.

Buffett, B.A., & Zatsepina, O.Y., 2000, Formation of gas hydrate from dissolved gas in natural porous media, *Marine Geology,* **164**, 69– 77.

Buffett, B., & Archer D., 2004, Global inventory of methane clathrate: sensitivity to changes in the deep ocean, *Earth and Planetary Science Letters,* **227** 185–199.

Bugge, T., Befring, S., Belderson, R.H., Eidvin, T., Jansen, E., Kenyon, N.H., Holtedahl, H., & Sejrup, H.-P., 1987. A giant three-stage submarine slide off Norway. *Geo-Marine Letters*, **7**, 191-198.

Bünz, S., & Mienert, J., 2004, Acoustic imaging of gas hydrate and free gas at the Storegga Slide, *Journal of Geophysical Research,* **109,** B04102.

Bussian A.E., 1983, Electrical conductance is a porous medium, *Geophysics*, **48**, 1258-1268.

Carcione, J.M. & Gei, D., 2004, Gas hydrate concentration estimated from P- and S-wave velocities at the Mallik 2L-38 research well, Mackenzie Delta, Canada, *Journal of Applied Geophysics,* **56**, 73–78.

Carcione, J.M. & Tinivella, U., 2000, Bottom simulating reflectors: seismic velocities and AVO effects, *Geophysics,* **65**, 54–67.

Carcione, J.M., Gei, D., Rossi, G., & Madrussani, G., 2005, Estimation of gaS-hydrate concentration and free-gas saturation at the Norwegian-Svalbard continental margin, *Geophysical Prospecting,* **53**, 803–810.

Chand, S. & Minshull, T.A., 2003, The effects of gas hydrate on sediment physical properties and fluid flow: Seismic Constraints, *Geofluids,* **3**, 275-289.

Chand, S., Minshull, T.A., Gei, D. & Carcione, H.M., 2004, Elastic velocity models for gaS-hydrate-bearing sediments – a comparison, *Geophysical Journal International*, **159**, 573-590.

Chand, S., Minshull, T.A., Priest, J.A., Best, A.I., Clayton, C.R.I. & Waite, W.F., 2006, An effective medium inversion algorithm for gas hydrate quantification and its application to laboratory and borehole measurements of gas hydrate-bearing sediments, *Geophysical Journal International*, **166,** 543–552.

Chapman, N.R., Gettrust, J.F., Walia, R., Hannay, D., Spence, G.D., Wood, W.T., & Hyndman, R.D., 2002., High-resolution, deeP-towed, multichannel seismic survey of deeP-sea gas hydrates off western Canada, *Geophysics*, **67**, 1038-1047.

Chen, M-A. P., 2006, Northern Cascadia Marine Gas Hydrate: Constraints from Resistivity, Velocity, and AVO, MSc Thesis, *University of Victoria.*

Clavier C., Coates G. & Dumanoir J. 1984. Theoretical and experimental bases for the dual-water model for interpretation of shaly sands. *Society of Petroleum Engineers Journal*, **4**, 153–168.

Cleary, C., Chen, I-W., & Lee, S-M. 1980, Self consistent techniques for heterogeneous media. *Journal of Engineering, Mechanics Division*, **106**, 861-887 American Society of Civil Engineers

Clennell, M.B., Hovland, M., Booth, J.S., Henry, P. & Winters, W.J., 1999, Formation of natural gas hydrates in marine sediments 1. Conceptual model of gas hydrate growth conditioned by host sediment properties. *Journal of Geophysical Research* **104,** 22,985-23,003.

Collett, T.S. 2000. Natural gas hydrate as a potential energy resource, In M.D. Max, (eds.), Natural Gas Hydrate in Oceanic and Permafrost Environments, *Kluwer Academic Publications.*

Collett, T.S., & Ladd, J., 2000, Detection of gas hydrate with downhole logs and assessment of gas hydrate concentrations (saturations) and gas volumes on the Blake Ridge with electrical resistivity data, *Proceedings of the Ocean Drilling Program, Scientific Results*, **164,** 179-191.

Collett, T.S., 1998, Well log evaluation of gas hydrate saturation. Transactions of the Society of Professional Well Log Analysts, *Thirty-Ninth Annual Logging Symposium, Paper MM. Washington, DC: Library of Congress.*

Constable, S.C., & Weiss, C.J., 2006, Mapping thin resistors and hydrocarbons with marine EM methods: Insights from 1D modeling: *Geophysics*, **71**, G43–G51.

Cresswell, A., Barton, M.E. & Brown, R., 1999, Determining the Maximum Density of Sands by Pluviation, *Geotechnical Testing Journal,* **22(4),** 324-328.

Darcy, H., 1856, Dètermination des lois d'ècoulement de l'eau à travers le sable, Les Fontaines Publiques de la Ville de Dijon, *Victor Dalmont,Paris*, 590–594.

Dickens, G.R., Schroeder, D., Hinrichs, K.-U., & Leg 201 Scientific Party, 2003. The pressure core sampler (PCS) on Ocean Drilling Program Leg 201: general operations and gas release. (In) D'Hondt, S.L., Jørgensen, B.B., Miller, D.J., *et al*., *Proceedings of the ODP, Initial Reports,* **201**, 1–22.

Dillon, W.P., & Max, M.D., 2000, Oceanic gas hydrate, In Max, M.D. (ed.), 2000 Natural Gas Hydrate in Oceanic and Permafrost Environments, *Kluwer Academic Publishers*, 61-76.

Dvorkin, J. & Nur, A., 1996. Elasticity of high-porosity sandstones: theory for two North Sea data sets, *Geophysics,* **61,** 1363–1370.

Dvorkin, J., & Nur A. 1998, Time-average equation revisited, *Geophysics*, **63**, 460– 464.

Dvorkin, J., Helgerud, M.B., Waite, W.F., Kirby, S.H., & Nur, A. 2000 Introduction to physical properties and elasticity models. In Max M.D., (ed.), Natural Gas Hydrate In Oceanic and Permafrost Environments, *Kluwer, Dordrecht, Netherlands*, 245–260.

Dvorkin, J., Helgrud, M.B., Waite, W.F., Kirby, S.H., & Nur, A., 2000, Oceanic gas hydrate, In Max, M.D. (ed), 2000 Natural Gas Hydrate in Oceanic and Permafrost Environments, *Kluwer Academic Publishers*, 245-260.

Dvorkin, J., Nur, A., & Yin, H., 1994, Effective properties of cemented granular material. *Mechanics of Materials*, **31,** 461–469.

Dvorkin, J., Prasad, M., Sakai, A., & Lavoie, D., 1999, Elasticity of marine sediments: rock physics modeling, *Geophysical Research Letters*, **26**, 1781–1784.

Ecker, C., Dvorkin, J. & Nur, A., 1998, Sediments with gas hydrates; internal structure from seismic AVO, *Geophysics,* **63**, 1659-1669.

Edwards, R.N., 1997, On the resource evaluation of marine gas hydrate deposits using sea-floor transcient electric dipole-dipole methods, *Geophysics,* **62**, 63–74.

Eidesmo, T., Ellingsrud, S., MacGregor, L.M., Constable, S., Sinha, M.C., Johansen, S., Kong, F.N. & Westerdahl, H., 2002, Sea bed logging (SBL), a new method for remote and direct identification of hydrocarbonfilled layers in deepwater areas, *First Break*, **20**, 144– 152.

Ellingsrud, S., Sinha, M.C., Constable, S., MacGregor, L.M., Eidesmo, T. & Johansen, S., 2002, Remote sensing of hydrocarbon layers by Sea Bed Logging (SBL): results from a cruise offshore Angola,. *The Leading Edge*, **21**, 972 – 982.

Englezos, P., Kalogerakis, N., Dholabhai, P.D., & Bishnoi, P.R., 1987, Kinetics of formation of methane and ethane gas hydrate, *Chemical Engineering Science*, **42**, 2647– 2658.

Eshelby, J.D., 1957, The determination of the elastic field of an ellipsoidal inclusion and relation problem, *Proceedings of the Royal Society, London,* **A241**, 376-396

Evans, H.B., 1965, GRAPE – A device for continuous determination of material density and porosity, *Society of professional well log analysts, logging 6th annual symposium. Dallas, Texas, Transaction 2,* B1-B25

Evans, R.L.; Constable, S.C.; Sinha, M.C., Cox, C.S. & Unsworth, M.J., 1991, Upper crustal resistivity structure of the Easy Pacific rise near 13°N, *Geophysical Research Letters*, **18**(10), 1917-1920

Fofonoff, N.P., 1985, Physical properties of seawater: a new salinity scale and of state for seawater, *Journal of Geophysical Research*, **90**, 3332-3342.

Gassmann, F., 1951, Uber die elastizitat poroser medien, *Veirteljahrsschrift der Naturforschenden Gesellschaft*, **96**, 1-23.

Gei, D., & Carcione, J.M., 2003, Acoustic properties of sediments saturated with gas hydrate, free gas, and water, *Geophysical Prospecting,* **51**, 141–157.

Ginsburg, G., Soloviev, V., Matveeva, T. & Andreeva, I., 2000, Sediment grain size control on gas hydrate presence, sites 994, 995, and 997, *Proceedings of the. ODP Scientific Results,* **164**, 237– 245,

Ginsburg, G.D., Guseynov, R.A., Dadashev, A.A., Ivanova, G.A., Kazantsev, S.A,. Soloviev, V.A., Telepnev, E.V., Askery-Nasirov, R.Ye., Yesikov, A.D., Mal'tseva, V.I., Mashirov, Yu.G. & Shabayeva, I.Yu., 1992, Gas hydrates of the Southern Caspian, *International Geology Review,* **34**, 765-782.

Goldberg, D., 1997, The role of downhole measurements in marine geology and geophysics, *Review of Geophysics*, **35 (3),** 315-342.

Goldberg, D., Collett. T.S., & Hyndman, R.D., 2000, Ground truth: in-situ properties of hydrate, In Max, M.D., (ed.), Natural Gas Hydrate in Oceanic and Permafrost Environments, *Kluwer Academic Publishers, The Netherlands*, 295-310.

Greer, A.A., 2001, Joint Interpretation of seismic and electromagnetic results, investigating zero age oceanic crust., *PhD thesis. University of Cambridge.*

Greer, A.A., Sinha, M.C., & MacGregor, L.M., 2002, Joint effective medium modelling for co-incident seismic and electromagnetic data, and its application to studies of porosity structure at Mid-Ocean Ridge crests, *LITHOS Science Report,* **4,** 103-120

Gubernatis, J.E. & Krumhansl, J.A., 1975, Macroscopic engineering properties of polycrystalline materials: Elastic properties, *Journal of Applied Physics*, **46**, 1875-1883.

Gunn, D.E. & Best, A.I., 1998., A new automated non-destructive system for high resolution multi-sensor core logging of open sediment cores., *Geo-marine Letters,* **18**, 70-77.

Haacke, R. & Westbrook, G.K., 2006, A fast, robust method for detecting and characterising azimuthal anisotropy with marine PS converted waves, and its application to the west Svalbard continental slope, *Geophysical Journal International.* **167(3),** 1402-1412.

Hanai, T., 1960, Theory of the dielectric dispersion due to the interfacial polarization and its application to emulsion, *Kolloid Z,* **171,** 23–31.

Hanai, T., 1961, Dielectric theory on the interfacial polarization for two-phase mixtures *Bulletin of the Institute for Chemical Research*, **39**, 341-368.

Handa, Y.P., 1986, Composition, enthalpies of dissociation and heat capacities in the range 85 to 270K for clathrate hydrates of methane, methane and propane and the enthalpy of iso-butane hydrate, as determined by a heat-flow calorimeter, *Journal of Chemical Thermodynamics*, **18**, 915–921.

Haq, B., 1998, Natural gas hydrates: Searching for the long-term climatic and slope stability records, in Gas Hydrates: Relevance to World Margin Stability and Climate Change, In Henriet J.-P. & Meinert J., (eds.) *Geological Society, Special Publication,* **137**, 303–318.

Hashin, Z. & Shtrikman, S., 1963, A variational approach to the theory of elastic behaviour of multi-phase materials, *Journal of the Mechanics and Physics of the solids*, **11**, 127-140

Hashin, Z. & Shtrikman, S., 1962, A variational approach to the theory of the effective magnetic permeability of multiphase materials, *Journal of Applied. Physics,* **33**, 3125–3131.

Helgerud, M.B., 2001. Wave speeds in gas hydrate and sediments containing gas hydrate: a laboratory and modeling study, Ph.D. thesis, *Stanford University*.

Helgerud, M.B., Dvorkin, J., Nur, A., Sakai, A. & Collett, T.S., 1999. Elastic wave velocity in marine sediments with gas hydrates: Effective medium modelling, G*eophysical Research Letters,* **26,** 2021–2024.

Henry, P., Thomas, M. & Clennell, M.B. 1999, Formation of natural gas hydrates in marine sediments 2. Thermodynamic calculations of stability conditions in porous sediments. *Journal of Geophysical Research,* **104,** 23,005-23,022.

Herrick, D.C. & Kennedy, W.D., 1994, Electrical efficiency: a pore geometric-theory for interpreting the electrical properties of reservoir rocks, *Geophysics,* **59(6),** 918 -927.

Hertz, H., 1881, Über die Berührung fester elastischer Körper, *J. Reine Angew. Math.* **92**, 156–171.

Hill, R., 1952, Elastic properties of reinforced solids some theoretical principles, *Proceedings of the Physical Society of London A,* **65,** 349–354.

Hill, R., 1965, A self consistent mechanics of composite materials, *Journal of the Mechanics and Physics of the solids,* **13**, 213-222

Hobro, J.W.D., Minshull, T.A., Singh, S.C. & Chand, S., 2005, A three-dimensional seismic tomography study of the gas hydrate stability zone, offshore Vancouver Island, 2005., *Journal of Geophysical Research*, **110**, B09102,

Holbrook, W.S., 2001, Seismic studies of the Blake Ridge: implications for hydrate distribution, methane expulsion, and free gas dynamics, In: Paull, C.K., & Dillon, W.P., (eds.), *Natural Gas Hydrates, Geophysical Monograph* **124**, Am. Geophys. Un., Washington, D.C., 235-256.

Holbrook, W.S., Hoskins, H., Wood, W.T., Stephen, R.A., Lizarralde, D. & Leg 164 Science Party, 1996, Methane hydrate and free gas on the Blake Ridge from vertical seismic profiling, *Science*, **273**, 1840-1843.

Holland, M., Schultheiss, P., Roberts, J., Druce, M., IODP Expedition 311 Shipboard Scientific Party & NGHP Expedition 1 Shipboard Scientific Party, 2006, Gas Hydrate-Sediment Morphologies Revealed by Pressure Core Analysis, *Eos Trans. AGU, **87***(**52**)**,** Fall Meet. Suppl., Abstract OS33B-1689.

Hornby, B.E., Schwartz, L.M. & Hudson, J.A., 1994. Anisotropic effective-medium modelling of the elastic properties of shales*, Geophysics*, **59**, 1570-1581.

Hyndman, R.D. & Spence, G.D., 1992, A seismic study of methane hydrate bottom simulating reflectors, *Journal of Geophysical Research,* **97**, 6683-6698.

Hyndman, R.D., Spence, G.D., Chapman, N.R., Riedel, M., & Edwards, R.N., 2001, Geophysical Studies of Marine Gas Hydrate in Northern Cascadia, In C.K. Paull & W.P. Dillon, (eds.), Natural gas hydrates: occurrence, distribution, detection, *American Geophysical Union Monographs,* **124**, 273-295.

Hyndman, R.D., Yuan, T. & Moran, K., 1999, The concentration of deep sea gas hydrates from downhole electrical resistivity logs and laboratory data, *Earth and Planetary Science Letters*, **172,** 167-177.

Hyndman, R.D. & Davies E.E., 1992, A Mechanism for the formation of methane hydrate and sea-floor Bottom simulating reflectors by vertical fluid expulsion. Journal of Geophysical Research-Solid Earth 97, 7025-7041.

Jackson, P,D., Tayor-Smith. D. & Stanford, P.N., 1978, Resistivity-porosity-particle shape relationships for marine sands. *Geophysics*, **43**, 1250-1268.

Jakobsen, M., Hudson, J.A., Minshull, T.A. & Singh, S.C., 2000, Elastic properties of hydrate-bearing sediments using effective medium theory, *Journal of Geophysical Research.*, **105**, 561-577.

Jeffrey, G.A. & McMullan, R.K., 1967, The clathrate hydrates, *Progress in Inorganic. Chemistry.*, **8**, 43–108.

Kearey, P., Brooks, K. & Hill, I., 2002, An Introduction to Geophysical Exploration, *Blackwell Science Ltd.*

Kehiaian, H.V., 1990, Virial coefficients of selected gases, In Lide, D.R., (ed) Handbook of chemistry and physics 71st edition, *The chemical rubber publishing company*, 6-47.

Kleinberg, R.L., Flaum, C., Griffin, D.D., Brewer, P.G., Malby, G.E., Peltzer, E.T. & Yesinowski, J.P., 2003, Deep sea NMR: Methane hydrate growth habit in porous media and its relationship to hydraulic permeability, deposit accumulation, and submarine slope stability, *Journal of Geophysical Research*, **108,** 2508

Kolbuszewski, J.J., 1948, An Experimental Study of the maximum and Minimum Porosities of Sands, *Proceedings of the Second International Conference on Soil Mechanics and Foundation Engineering,* **1**, 158-169.

Korringa, J., 1973, Theory of elastic constants of heterogeneous media, *Journal of Mathematical Physics,* **14**, 509-513.

Krajew, A.P., 1957, Grundlagen der Geoelektrik. *VEB Verlag Technik, Berlin*, 358.

Kumar, D., Sen, M.K., Bangs, N.L., Wang, C., & Pecher, I., 2006, Seismic anisotropy at Hydrate Ridge: *Geophysics Research Letters*, **33,** L01306.

Kunerth, D.C., Weinberg, D.M., Rector, J.W., Scott, C.L. & Johnson, J.T., 2001, Acoustic laboratory measurement during the formation of a THF-hydrate in unconsolidated porous media, *Journal of Seismic Exploration*, **9**, 337– 354.

Kuster, G.T. & Toksoz, M.N., 1974, Velocity and attenuation of seismic waves in two-phase media: part I. Theoretical formulations, *Geophysics*, **39**, 587-606.

Kvenvolden K.A., Lorenson T.D., 2001, The global occurrence of natural gas hydrate, In Paull C.K., Dillon W.P., (eds.), Natural Gas Hydrates Occurrence, Distribution, and Detection, *Geophysical Monographs,* **124**, 3– 8.

Kvenvolden, K.A., 1998, A primer on the geological occurrence of gas hydrates, in Gas Hydrates: Relevance to World Margin Stability and Climate Change, In J.-P. Henriet & J. Meinert, (eds.), *Geological Society of London Special Publication*., **137**, 9 –30.

Kvenvolden, K.A., 1995, A review of the geochemistry of methane in natural gas hydrate, *Organic Geochemistry,* **23**, 997–1008.

LeBlanc, C., Louden, K., & Mosher, D., 2007, Gas hydrates off eastern Canada: Velocity models from wide-angle seismic profiles on the Scotian slope, *Marine and Petroleum Geology*.,24, 321-335.

Leclaire, P.H., Cohen-Ténoudji, F. & Aguirre-Puente, J., 1994, Extension of Biot's theory of wave propagation to frozen porous media, *Journal of the Acoustical Society of America.* **96**, 3753–3768.

Lederhos, J.P., Mehta, A.P., Nyberg, G.B., Warn, KJ., & Sloan, E.D., 1992, Structure H clathrate hydrate equilibria of methane and adamantane. *American Institute of Chemical Engineers Journal*, **38**, 1045-1048.

Lee, M.W., Hutchinson D.R., Dillon W.P., Miller J.J., Agena, W.F. & Swift, B.A., 1993, Method of estimating the amount of in situ gas hydrates sediments, *Marine and Petroleum Geology*, **10,** 493-506.

Lee, M.W., Hutchinson, D.R., Collet, T.S. & Dillon, W.P., 1996, Seismic velocities for hydrate-bearing sediments using weighted equation. *Journal Geophysical Research*, **101**, 20347-20358.

Lu, H., Seo, Y., Lee, J., Moudrakovski, I., Ripmeester, J.A., Chapman, N.R., Coffin, R.B., Gardner, G. & Pohlman, J., 2007, Complex gas hydrate from the Cascadia margin. *Nature*, **445,** 303-306.

MacGregor, L.M. & Sinha M.C., 2000, Use of marine controlled source electromagnetic sounding for sub-basalt exploration, *Geophysical Prospecting*, **48**, 1091-1106

MacKay, M.E., Jarrard, R.D., Westbrook, G.K. & Hyndman, R.D., 1994, Origin of bottom-simulating reflectors: geophysical evidence from the Cascadia accretionary prism, *Geology,* **22(5),** 459–462.

Makogon, Y.F., 1981, Hydrate of natural gas, *Pennwell Publishing Company*,

Malinverno, A., Kastner, M., Torres, M.E. & Wortmann, U.G., 2006., Gas Hydrate Saturations and Their Uncertainties From Chlorinity and Well Log Data at IODP Site U1325 (Exp. 311, Cascadia Margin)., *Eos Trans. AGU,* ***87*****(52),** Fall Meet. Suppl., Abstract OS11E-04

Malone, R.D., 1985. Gas hydrates. Technical Report DOC/METC/SP-218 *U.S. Department of Energy, Washington, DC.*

Marion, D., Nur, A., Yin, H., & Han, D., 1992, Compressional velocity and porosity in sand-clay mixtures, *Geophysics*, **57**, 554-563.

Marion, J.B. & Hornyak, W.F., 1982., Physics for Science and Engineering, *CBS College Publishing*.

Matsumoto, R., Uchida T., Waseda A., Uchida, T., Takeya, S., Hirano, T., Yamada, K., Maeda, Y., & Okui, T., 2000, Occurrence, structure and composition of natural gas hydrate recovered from the Blake Ridge, northwest Atlantic. In Paull, C.K., Matsumoto, R., Wallace, P.J., & Dillon, W.P. (eds.), *Proceedings of the Ocean Drilling Program, Scientific Results,* **164**, 13-28.

Mavko, G., Mukerji, T. & Dvorkin, J., 1998, The Rock Physics Handbook: Tools for Seismic Analysis in Porous Media, *Cambridge University Press.*

McCann, C., & Sothcott, J., 1992, Laboratory measurements of the seismic properties of sedimentary rocks, *Geological Society, London, Special Publications*, **65**, 285-297.

Mindlin, R.D., 1949, Compliance of elastic bodies in contact: *Journal of Applied Mechanics*, **16**, 259-268.

Minshull, T. A., Singh C. S. & Westbrook G. K., 1994. Seismic velocity structure at a gas hydrate reflector, offshore western Columbia, full waveform inversion, *Journal of Geophysical Research*, **99**, 4715-4734.

Minshull, T.A., Louden, K.E. & Dean, S.M., *in press*., Analysis of Gas Hydrate Provinces by Ocean Bottom Seismic Methods, *SEG monograph*.

Nobes, D.C., Villinger, H., Davis, E.E. & Law, L.K., 1986, Estimation of marine sediment bulk physical properties at depth from seafloor geophysical measurements, *Journal Geophysical Research,* **91**, 14033-14043.

Norris, A.N., 1985, A differential scheme for the effective moduli of composites, *Mechanics of materials*, **4**, 1-16.

Novosel, I., 2002, Physical and sedimentological properties of gas hydrate related sediments, offshore Vancouver Island. MSc Thesis, *University of Victoria*.

Novosel, I., Spence, G.D. & Hyndman T.R.D., 2005, Reduced magnetization produced by increased methane flux at a gas hydrate vent, *Marine Geology,* **216,** 265– 274.

Nur, A., Mavko, G., Dvorkin, J. & Galmudi, D., 1998, Critical porosity: A key to relating physical properties to porosity in rocks, *The Leading Edge*, **17**, 357–362.

O'Connell, R. & Budiansky, B., 1976., Reply, *Journal of Geophysical Research*, **81**, 2577-2578.

O'Connell, R.J. & Budiansky B., 1977, Viscoelatic properties of fluid-saturated cracked solids. *Journal of Geophysical Research,* **82**, 5719–5735.

Paull, C.K. Matsumoto, R. Wallace, P.J. *et al.,* 1996, Proceeding of the Ocean Drilling Program, in: *Initial Reports, College Station, TX.,* **164**.

Paull, C.K., Ussler III, W. & Dillon, W.P., 2000, Potential role of gas hydrate decomposition in generating submarine slope failures. Coastal Systems and Continental Margins. Natural Gas Hydrate in Oceanic and Permafrost Environments, vol. 5. *Kluwer Academic Publishers, Dordrecht,* 149–156.

Pearson, C.F., Murphy, J.R. & Hermes, R. 1986, Laboratory ultrasonic and resistivity measurements on sedimentary rocks containing tetrahydrofuran hydrates, *Journal of Geophysical Research*, **91**, 14,132–14,138.

Pearson, C.F., Halleck, P.M., McGuire, P.L., Hermes, R. & Mathews, M., 1983, Natural gas hydrate deposits: a review of in-situ properties, *Journal of Physical Chemistry,* **87**, 4180-4185.

Pellenbarg, R.E. & Max, M.D., 2000, Introduction, Physical Properties, and Natural Occurrences of Hydrate, In Max, M.D. (ed.), Natural Gas Hydrate in Oceanic and Permafrost Environments, *Kluwer Academic Publishers*, 1-8.

Petersen, C.J., Papenberg, C. & Klaeschen, D., 2007, Local seismic quantification of gas hydrates and BSR characterization from multi-frequency OBS data at northern Hydrate Ridge, *Earth and Planetary Science Letters,* **255**, 414–431.

Priest, J.A., Best A.I. & Clayton C.R.I., 2005, A laboratory investigation into the seismic velocities of methane gas hydrate-bearing sand, *Journal of Geophysical Research.*, **110**, B04102.

Priest, J.A., 2004. The effect of methane gas hydrate on the dynamic properties of sand. Ph.D. thesis, University of Southampton, Southampton.

Rad, N.S. & Tumay, M.T., 1985, Factors Affecting Sands Specimen Preparation by Raining, *Geotechnical Testing Journal*, **10(1),** 31-37.

Raynaud, D., Chapellaz, J. & Blunier, T., 1998. Ice-core record of atmospheric methane changes: relevance to climatic changes and possible gas hydrate sources. *Geological Society of London Special Publication.,* **137**, 327-331.

Rempel A.W., & Buffett B.A., 1998, Mathematical models of gas hydrate accumulation, Gas Hydrates: *Relev. World Margin Stab. Clim. Change* **137,** 63– 74.

Reuss. A., 1929. Berechnung der Fliessgrenzen von Mischkristallen auf Grund der Plastizitätsbedinggung für Einkristalle, *Zeitschrift für Angewandte Mathematik und Mechanik*, **9**, 49-58.

Riedel, M., Collett, T. S. & Hyndman, R. D., 2005, Gas hydrate concentration estimates from chlorinity, electrical resistivity and seismic velocity, *Geological Survey of Canada Open File Report*, 4934.

Riedel, M., Collett, T., Malone, M., & the Expedition 311 Project Team, 2005, Cascadia margin gas hydrates, *IODP Scientific Prospectus,* **311**.

Riedel, M., Collett, T., Malone, M., Akiba, F., Blanc-Valleron, M., Ellis, M., Guerin, G., Hashimoto, Y., Heuer, V., Higasi, Y., Holland, M., Jackson, P., Kaneko, M., n, M., Kim, J.-H., Kitajima, H., Long, P., Malinverno, A., Myers, G., Palekar, L., Pohlman, J., Schultheiss, P., Teichert, B., Torres, M., Tréhu, A., Wang, J., Wortmann, U. & Yoshioka, H. 2006. Proceedings of the Integrated Ocean Drilling Program, expedition reports, Casdadia margin gas hydrates. Ocean Drilling Program, College Station, Texas. 311.

Riedel, M., Hyndman, R.D., Spence, G.D. & Chapman, N.R., 2002, Seismic investigations of a vent field associated with gas hydrates, offshore Vancouver Island, *Journal of Geophysical Research*, **107**, 2200.

Riedel, M., Spence, G.D., Chapman, R.N. & Hyndman, R.D., 2001. Deep sea gas hydrates on the Northern Cascadia margin, *Leading Edge* **20**, 87–91.

Roe, J., 1993., Elementary Geometry., *Oxford Science Publications*.

Sassen, R. & MacDonald, I.R., 1994. Evidence of structure H hydrate, Gulf of Mexico continental slope. *Organic Geochemistry,* **22** 1029-1032.

Schlumberger, 1977, Log Interpretation Charts, *Schlumberger Limited.*

Schmeling, H., 1983, Numerische Modelle ueber den Einfluss partieller Schmelze auf elastiche, anelastische und elektrische Eigenschaften von Gesteinen mit Anwendung auf Labordaten und die Asthenosphare, *Disseration, Inst. Meteorol. Geophys., Frankfurt,* 268.

Schmeling, H., 1986, Numerical models on the influence of partial melt on elastic, anelastic and electrical properties of rocks. Part II electrical conductivity, *Physics of the earth and planetary interiors,* **43**, 123-136.

Schmuck, E.A., & Paull, C.K., 1993, Evidence for gas accumulation associated with diapirism and gas hydrates at the head of the Cape Fear Slide, *Geo-Marine Letters*, **13**, 145-152.

Schultheiss, P., Holland, M., Roberts, J Druce, M., IODP Expedition 311 Shipboard Scientific Party & NGHP Expedition 1 Shipboard Scientific Party, 2006, Gas Hydrate Investigations Using Pressure Core Analysis: Current Practice, *Eos Trans. AGU,* ***87*****(52),** Fall Meet. Suppl., Abstract: OS11E-03.

Schwalenberg, K., Willoughby, E.C., Mir, R., & Edwards, R.N., 2005. Marine gas hydrate electromagnetic signatures in Cascadia and their correlation with seismic blank zones, *First Break*, **23**, 57-63.

Semjonow, A.S., 1948, Der Einfluss der Gesteinsstruktur auf spesfischen *Winderstand, Materialien des UmonS-For-schungsintituts ErkundungS-Geophysik,* **12**.

Sheng, P., 1990, Effective-medium theory of sedimentary rocks, *Physical Review B***, 41**, 4507-4512.

Sheng, P., 1991, Consistent modelling of the electrical and elastic properties of sedimentary rocks, *Geophysics*, **56(8),** 1236-1243.

Shipley, T.H., Houston, M., Buffler, R.T., Shaub, F.J., McMillan, K.J., Ladd, J.W.& Worzel, J.L., 1979, Seismic reflection evidence for the wide-spread occurrence of possible gaS-hydrate horizons on continental slopes and rises, *American Association of Petroleum Geologists Bulletin,* **63,** 2204–2213.

Singh, S.C., Minshull T.A., & Spence G.D., 1993, Velocity structure of a gas hydrate reflector, *Science*, **260**, 204– 207.

Sloan, E.D., 1998, Clathrate hydrates of natural gasses, *Marcel Dekker, New York, 2nd edition.*

Spence, G.D. Hyndman, R.D., Chapman, N.R., Riedel, M., Edwards, N., & Yuan, J., 2000, Cascadia margin, northeast Pacific Ocean: hydrate distribution from geophysical investigations. In Max, M.D. (ed.), Natural Gas Hydrate in Ocean and Permafrost Environments: *New York (Kluwer Academic Publisher),* 183–198.

Stern, L.A., Kirby, S.H. & Durham, W.B., 1996, Peculiarities of methane clathrate hydrate formation and solid-state deformation, including possible superheating of water ice, *Science,* **273**, 1843– 1848.

Stokoe, K.H., Darendeli, M.B., Andrus, R.D. & Brown, L.T., 1999, Dynamic soil properties: Laboratory, field and correlation studies, paper presented at 2nd International Conference on Earthquake Geotechnical Engineering, *Portuguese Geotech*. Soc., Lisbon, Portugal.

Stoll, R.D. & Bryan G.M., 1979, Physical properties of sediments containing gas hydrates, *Journal of Geophysical Research.,* **84**, 1629–1634.

Stoll, R., Ewing, D.J., & Bryan G.M., 1971, Anomalous wave velocities in sediments containing gas hydrates, *Journal of Geophysical. Research*, **76**, 2090–2094.

Stoll, R.D., & Bryan G.M., 1979, Physical properties of sediments containing gas hydrates, *Journal of Geophysical. Research*, **84**, 1629–1634.

Stoud, K.A. & Booth, D.J., 2001., Engineering Mathematics (5th ed.)., *Palgrave Macmillan.*

Sultan, N., Voisset, M., Marsset, T., Vernant, A.M., Cauquil, E.,. Colliat, J.L., Curinier, V., 2007, Detection of free gas and gas hydrate based on 3D seismic data and cone penetration testing: An example from the Nigerian Continental Slope, *Marine Geology,* **240**, 235–255.

Timur, A., 1968, Velocity of compressional waves in porous media at permafrost temperature, *Geophysics,* **33**, 584-595.

Tipler, P.A., 1999., Physics for Scientists and Engineers (4th ed.)., *W.H. Freeman and Company*.

Tohidi, B., Anderson, R., Clennell, M.B., Burgass, R.W., Biderkab, A.B., 2001 Visual observation of gas hydrate formation and dissociation in synthetic porous media by means of glass micromodels. *Geology*, **29**, 867-870.

Torres M.E., Wallmann K., Trehu A.M., Bohrmann G., Borowskid W.S., Tomaru H., 2004, Gas hydrate growth, methane transport, and chloride enrichment atthe southern summit of Hydrate Ridge, Cascadia margin off Oregon, Earth and Planetary Science Letters, 226, 225– 241.

Tréhu, A.M., Bohrmann, G., Rack, F.R., Collett, T.S., Goldberg, D.S., Long, P.E., Milkov, A.V., Riedel, M., Schultheiss, P., Torres, M.E., Bangs, N.L., Barr, S.R., Borowski, W.S., Claypool, G.E., Delwiche, M.E., Dickens, G.R., Gracia, E., Guerin, G., Holland, M., Johnson, J.E., Lee, Y-J., Liu, C-S., Su, X., Teichert, B., Tomaru, H., Vanneste, M., Watanabe, M., Weinberger, J.L., 2004. Three-dimensional distribution of gas hydrate beneath southern Hydrate Ridge: constraints from ODP Leg 204. Earth Planetary. Science. Letters. 222, 845– 862.

Tréhu, A.M., Bohrmann, G., Rack, F.R., Torres, M.E., Bangs, N.L., Barr, S.R., Borowski, W.S., Claypool, G.E., Collett, T.S., Delwiche, M.E., Dickens, G.R., Goldberg, D.S., Gràcia, E., Guèrin, G., Holland, M., Johnson, J.E., Lee, C-S., Liu, Y-J., Long, P.E., Milkov, A.V., Riedel, M., Schultheiss, P., Su, X., Teichert, B., Tomaru, H., Vanneste, M., Watanabe, M. & Weinberger J..L, 2002., Leg 204, Preliminary. Report. **104**, *Ocean Drilling Program, College Station, Texas.*

Ussler, W., & Paull, C.K., 2001, Ion exclusion associated with marine gas hydrate deposits. In Paull, C.K., & Dillon, W.P. (eds.), Natural Gas Hydrates: Occurrence, Distribution, and Detection. *Geophysics. Monograph*, **124,** 41–51.

Vanneste, M., De Batist, M., Golmshtok, A., Kremlev, A. & Versteeg, W., 2001, Multi-frequency seismic study of gas hydrate-bearing sediments in Lake Baikal, Siberia, *Marine Geology,* **172**, 1–21.

Vanorio, T., Prasad, M. & Nur, A., 2003, Elastic properties of dry clay mineral aggregates, suspensions and sandstones, *Geophysical Journal International,* **155,** 319–326.

Voigt, W., 1928, Lehrbuch der Kristallphysik, *Teubner, Leipzig*.

Waite, W.F., Winters W.J. & Mason D.H., 2004, Methane hydrate formation in partially water saturated Ottawa sand, *American Mineralogist*, **89**, 1202–1207.

Walpole, L.J., 1969, On the overall elastic moduli of composite materials, *Journal of the Mechanics and Physics of Solids,* **17**, 235-251.

Wang, Z., & Nur, A., 1992, Elastic wave velocities in porous media: A theoretical recipe, (in) Seismic and Acoustic Velocities in Reservoir Rocks Volume 2, Theoretical and Model Studies, *Society of Exploration Geophysicists*, 1-35.

Waxman, M.H. & Smits, L.J.M., 1968, Electrical conductivities in oil-bearing shaly sand, *Society of Petroleum Engineers Journal*, **8**, 107-122.

Watson, R.T., Rode, H., Oeschger, H. & Siegenthaler, U., 1990, Greenhouse Gases and Aerosol, In Houghton, J. T., Jenkins, G. J., & Ephraums, J. J. (eds.),Climate Change, the IPCC Scientific Assessment, *Cambridge Univ.,* 1–40.

Weinberger, J.L., Brown, K.M., & Long, P.E., 2005, Painting a picture of gas hydrate distribution with thermal images, *Geophysics Research Letters,* **32(4),** L04609.

Weitemeyer, K.A., Constable, S,C., Key, K.W. & Behrens, J.P., 2006, First results from a marine controlled-source electromagnetic survey to detect gas hydrates offshore Oregon, *Geophysical. Research. Letters*, **33,** L03304.

Wellsbury, P., & Parkes, R.J., 2000, Deep biosphere: source of methane for oceanic hydrate, In Max, M.D. (eds.) Natural Gas Hydrate: In Oceanic and Permafrost Environments. *Kluwer, Dordrecht.*

Westbrook, G.K., & 21 others, 2005, Measurement of P and S velocities, and the estimation of hydrate concentration at sites in the continental margin of Svalbard and the Storegga region of Norway, *Proceedings of the 5th International Conference on Gas Hydrates*, **3**, 726-735.

Westbrook, G.K., Carson, B., Musgrave, R. & Shipboard Scientific Party, 1994, *Proceedings of the Ocean Drilling Program, Initial Reports*, **146**.

Westbrook, G.K., Chand, S., Rossi, G., Long, C., Bünz , S., Camerlenghi, A., Carcione, J.M., Dean, S., Foucher, J-P., Flueh, E., Gei, D., Haacke, R.R., Madrussani, G., Mienert, J., Minshull, T.A., Nouzé, H., Peacock, S., Reston, T.J., Vanneste, M., Zillmer. M., submitted, Estimation of gaS-hydrate concentration from multi-component seismic data at sites on the continental margins of NW Svalbard and the Storegga region of Norway. *Marine and Petroleum Goelogy*.

Willis, J.R., 1977, Bounds and self-consistent estimates for the overall properties of anisotropic composites. *Journal of the Mechanics and Physics of Solids.,* **25**, 185-202.

Winkler, K.W., & Plona, T.J., 1982, Technique for measuring ultrasonic velocity and attenuation spectra in rocks under pressure, *Journal of Geophysical Research,* **87(B13),** 10776-10780.

Winters, W.J., Dillon, W.P., Pecher, I.A., & Mason, D.H., 2000, GHASTLI: Determining physical properties of sediment containing natural and laboratory formed gas hydrates, In M. D. Max (ed.), Natural Gas Hydrates in Oceanic and Permafrost Environments, 311–322, *Springer, New York.*

Winters, W. J., Pecher I. A., Waite W. F., & Mason D. H., 2004, Physical properties and rock physics models of sediment containing natural and laboratory-formed methane gas hydrate, *American Mineralogist,* **89**, 1221– 1227.

Wood, A.B., 1941, A textbook of sound, *G. Bell and Sons, Ltd, London*,

Wood, W.T., Holbrook, W.S. & Hoskins, H., 2000, In situ measurements of P-wave attenuation in the methane hydrate- and gaS-bearing sediments of the Blake Ridge, *Proceedings of the Ocean Drilling Program, Scientific Results,* **164**, 365-272.

Wu, T.T., 1966, The effect of inclusion shape on the elastic moduli of a two phase material, *International Journal of Solids Structures*, **2**, 1-8

Wyllie, M.R.J., Gregory, A., & Gardner, G., 1958, An experimental investigation of factors affecting elastic wave velocities in porous media: *Geophysics*, **23**, 459-493.

Wyllie, M.R.J., Gregory, A.R., & Gardner, L.W., 1956, Elastic wave velocities in heterogeneous and porous media: *Geophysics*, **21(1),** 41-70.

Wyllie, M.R.J. & Southwick, P.F., 1954, An experimental investigation of the S. P. and resistivity phenomena in dirty sands, *Journal of Petroleum Techology*, **6**, 44-57.

Wyllie, M.R.J. & Spangler, M.B., 1952, Application of electrical resistivity measurements to the problem of fluid flow in porous media, *Bulletin of the American Association of Petroleum Geology*, **36**, 359-403.

Yuan, J., & Edwards R.N., 2000, The assessment of marine gas hydrates through electronic remote sounding: Hydrate without a BSR?, *Geophysical. Reseasrch. Letters.,* **27**, 2397–2400.

Yuan, T., Hyndman R.D., Spence G.D. & Desmons, B., 1996, Velocity structure of a bottom-simulating reflector and deep sea gas hydrate concentrations on the Cascadia continental slope, *Journal of Geophysical Research*, **101**, 13655-13671.

Yuan, T., Spence, G.D., Hyndman, R.D., Minshull T.A. & Singh, S.C., 1999, Seismic velocity studies of a gas hydrate bottom-simulating reflector on the northern Cascadia continental margin, Amplitude modeling and full waveform inversion: *Journal of Geophysical Research*, **104**, 1179-1191.

Yun T.S., Santamarina J.C. & Ruppel C., 2007, Mechanical properties of sand, silt, and clay containing tetrahydrofuran hydrate, *Journal of Geophysical Research*, **112,** B04106.

Yun, T.S., Narsilio, G.A., Santamarina, J.C. & Ruppel, C., 2006, Instrumented pressure chamber for characterizing sediment cores recovered at in situ hydrostatic pressure, *Marine Geology*, **229**, 285–293.

Yun, T.S., Francisca, F.M., Santamarina, J.C. & Ruppel, C., 2005, Compressional and shear wave velocities in uncemented sediment containing gas hydrate, *Geophysical Research letters*, **32**, L10609.

Zatsepina, O.Y. & Buffett, B.A., 1998, Conditions for the stability of gas hydrate in the seafloor, *Journal of Geophysical Research,* **103**, 24127–24139.

Zeller, R. & Dederichs, P., 1973, *Phys. Status Solidi B*, **55**, 831.

Zimmerman, R.W., 1991, Compressibility of sandstones, *Elsevier, New York.*